

SPACE POWER SYSTEMS ADVANCED TECHNOLOGY CONFERENCE

GPO PRICE \$ _____

CFSTI PRICE(S) \$ 3.75

Hard copy (HC) _____

Microfiche (MF) 1.50

ff 653 July 65

FACILITY FORM 602

N67 10261 N67 10271

(ACCESSION NUMBER)

(THRU)

(PAGES)

(CODE)

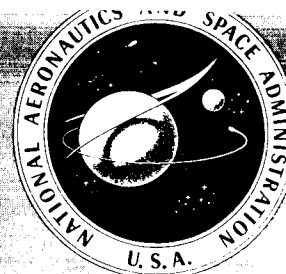
(NASA CR OR TMX OR AD NUMBER)

(CATEGORY)

LEWIS RESEARCH CENTER

Cleveland, Ohio

August 23-24, 1966



NATIONAL AERONAUTICS AND SPACE ADMINISTRATION

SPACE POWER SYSTEMS ADVANCED TECHNOLOGY CONFERENCE

*Lewis Research Center
Cleveland, Ohio
August 23-24, 1966*



Scientific and Technical Information Division

OFFICE OF TECHNOLOGY UTILIZATION

NATIONAL AERONAUTICS AND SPACE ADMINISTRATION

1966

Washington, D.C.

For sale by the Clearinghouse for Federal Scientific and Technical Information
Springfield, Virginia 22151 - Price \$3.75

FOREWORD

During the past several years, the Lewis Research Center has been engaged in a program to advance the technology of space power systems. The program has represented a substantial fraction of the overall NASA program in this area, although other NASA centers have made important contributions. During this same time the Department of Defense and the Atomic Energy Commission have also been conducting programs.

Presentation of an overall review of the progress in this field is timely. A few years ago, space power systems advanced technology was characterized by an abundance of ideas with very little data available on which to judge their true potential. Today, although much remains to be done, there exists a fairly considerable body of information which permits a more realistic assessment of the problems and potentials of the various power systems of interest.

This conference, under the chairmanship and cochairmanship of Bernard Lubarsky and Newell D. Sanders, respectively, has been prepared by NASA personnel, but the information presented includes important contributions by NASA contractors and by the Department of Defense, the Atomic Energy Commission, and their contractors.

Abe Silverstein
Director
Lewis Research Center

PRECEDING PAGE BLANK NOT FILMED.

CONTENTS

	Page
FOREWORD	iii
I. POWER SYSTEMS IN PERSPECTIVE	
Bernard Lubarsky	1 ✓
II. BATTERIES AND FUEL CELLS	
Harvey J. Schwartz, J. Stewart Fordyce, Robert B. King, James M. McKee, Daniel G. Soltis, and Lawrence H. Thaller	9 ✓
III. CONVENTIONAL AND THIN-FILM SOLAR CELLS	
Andrew E. Potter, Jr.	53 ✓
IV. ISOTOPES AND ISOTOPE THERMOELECTRIC GENERATORS	
Fred Schulman	73 ✓
V. BRAYTON CYCLE TECHNOLOGY	
Warner L. Stewart, William J. Anderson, Daniel T. Bernatowicz, Donald C. Guentert, Donald R. Packe, and Harold E. Rohlik	95 ✓
VI. SNAP-8 DEVELOPMENT STATUS	
Henry O. Slone	147 ✓
VII. POTASSIUM RANKINE SYSTEM MATERIALS TECHNOLOGY	
Louis Rosenblum, David R. Englund, Jr., Robert W. Hall, Thomas A. Moss, and Coulson Scheuermann	169 ✓
VIII. POTASSIUM RANKINE SYSTEMS TECHNOLOGY	
Robert E. English, Robert L. Cummings, Robert L. Davies, Thomas P. Moffitt, and Uwe H. von Glahn	201 ✓
IX. THERMIONICS	
Roland Breitwieser and Herman Schwartz	239 ✓
X. APPLICATIONS OF POWER SYSTEMS TO SPECIFIC MISSIONS	
Bernard Lubarsky and Lloyd I. Shure	269 ✓

PRECEDING PAGE BLANK NOT FILMED.

I. POWER SYSTEMS IN PERSPECTIVE

Bernard Lubarsky

A short introduction to place this overall review of progress in space power systems advanced technology in context is appropriate. Although many points are made which are obvious to anyone working in the space power field, they are necessary to place the whole conference in perspective. The discussion is in two parts: power systems that are currently in use and advanced power systems.

The chemical power system most used has been the battery. A brief survey revealed that from the time NASA was organized until May 1966 there have been 138 space flights and over 700 sounding rockets flown. Every booster and sounding rocket used a battery for power, and every payload had a battery aboard it somewhere. Even the two large Echo balloons had small supplies aboard to power radio beacons, and these included batteries. The first flight which did not have a battery in the payload was Pageos, the passive geodetic satellite, which was another large balloon flown in June 1966.

Another chemical power system in use recently is the hydrogen-oxygen fuel cell. The Gemini fuel cell (fig. I-1) is one of the two modules that together provide an average power of a little under 1 kilowatt. The Apollo fuel cell (fig. I-2) is one of three modules that provide an average power level of a little less than $1\frac{1}{2}$ kilowatts. Fuel cells are the lightest power supply for durations of a few days to a few weeks. About 5 years ago fuel cell technology was just being firmly established. Today the fuel cell power system is in use.

These are the chemical power systems in use. The only solar power system in use is the solar photocell. It has been the workhorse long-time power supply since NASA's inception and has been a very reliable power system. The solar cell arrays are lightweight, but energy storage weights for dark periods are heavy for some missions. An important trend in recent years has been a growth in the size of photocell arrays. In the early days of NASA, the power levels of photocell arrays were at the most a few tens of watts. Recently larger arrays have been flown. The largest array flown by NASA was on the Orbiting Astronomical Observatory (OAO) (figs. I-3 and I-4). The solar panels are 114 square feet in area and produce a power of somewhat under 1 kilowatt. A still larger array producing $1\frac{1}{2}$ kilowatts has been flown by the Air Force. An artist's sketch of that array on the Agena vehicle is shown in figure I-5. Figure I-6 shows one wing of the 19-foot-long, 5-foot-wide $1\frac{1}{2}$ -kilowatt array. The array, folded around the rocket engine of the Agena, is shown in figure I-7.

The only nuclear power system in use is the radioisotope thermoelectric generator (RTG). Isotope thermoelectric systems appear to be very reliable. Although heavier than the photocell arrays, they require no energy storage for dark periods and no orientation. However, nuclear safety must be assured for each application. SNAP-9A, a 25-watt RTG, has been flown on a

Navy navigation satellite. The first NASA use of isotope thermoelectric systems will be on Nimbus B. Nimbus B (fig. I-8) uses two SNAP-19 radioisotope thermoelectric generators (fig. I-9) for supplementary power to the main photocell supply. Each unit produces 30 watts of unconditioned power. The SNAP-19 is 22 inches across the radiator fins and 11 inches long and weighs about 30 pounds.

As in the case of fuel cells, 5 years ago the technology of radioisotope thermoelectric generators was just being firmly established. Today they are reaching mission use.

These are all the power systems actually in use. Rather conspicuous by their absence are any power systems using reactors and providing the large powers associated with reactor power systems. They are absent primarily because the development of large reactor power systems has been more difficult and time consuming than anticipated about 5 years ago. One reactor power system has flown; that is the SNAP-10A, a 500-watt reactor thermoelectric system, which has been flown on a test flight although it has not been used on missions. The 500-watt power level is low for reactor thermoelectric systems and therefore the probability is reduced that SNAP-10A will have mission use. However, the technology acquired is being used to develop larger systems.

The technology program work on these systems, batteries, fuel cells, solar cells, and radioisotope generators, is described in papers II to IV. Later presentations discuss power systems which are not in use, or advanced power systems.

The three principal power systems not in use on which the Lewis Research Center is working are the Brayton-cycle, gas-turbine power system; the Rankine-cycle, vapor-turbine power system; and the thermionic emitter. Some of the characteristics of these three power systems are as follows:

System	Characteristics
Brayton	High efficiency Large radiator area Considerable existing technology
Rankine	Lowest weight for given temperature level Smaller radiator area than Brayton cycle Two-phase, liquid metal system
Thermionics	Very high temperature High power density Smallest radiator area of the three systems

The thermionics system requires temperature levels considerably higher than the other two systems for its operation. However, if these temperature levels can be achieved, it offers high power density, the smallest radiator area, and a weight as good as the weight of the Rankine system at the lower temperature levels. In addition, it is a static system built of small modules with the redundancy of parallel connections.

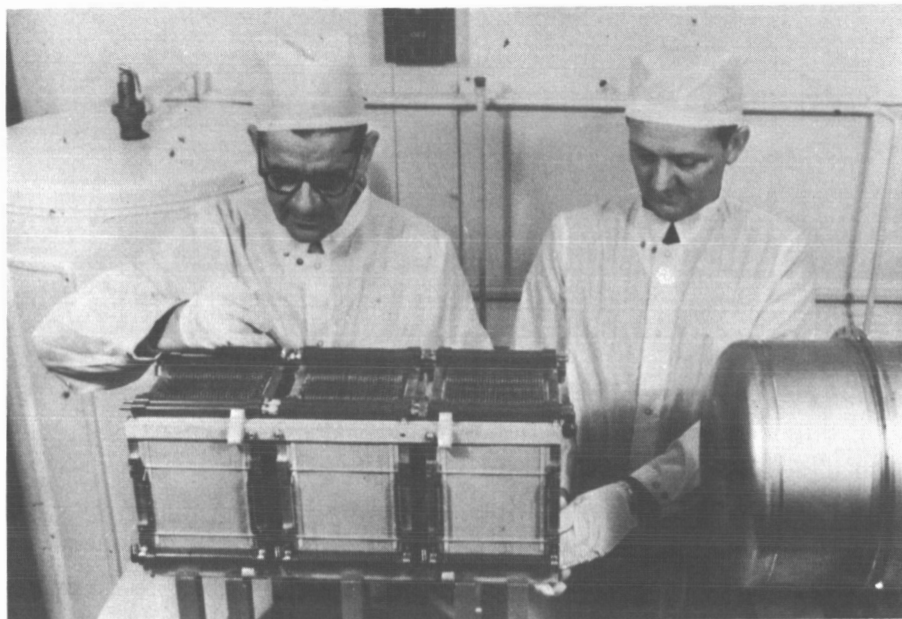
The three heat sources, solar, isotopic, and reactor, and the power conversion system or systems which currently appear to be the most interesting for these heat sources are as follows:

Heat source	Power conversion system
Solar	Brayton
Isotope	Brayton
Reactor:	
SNAP-8	Mercury Rankine, thermoelectric
Advanced	Brayton, potassium Rankine, thermionic

This listing is not meant to imply that these are the only power systems of interest in an absolute sense, but that, at this time, they appear to be the most attractive. Further technology work might very well change this viewpoint. For solar and isotopic heat sources, efficiency is important. In solar power systems, large collectors are required. The higher the efficiency, the smaller the area of the collector. Isotopes are of limited availability and high cost. High efficiency which will reduce the requirements for these isotopes is desirable. The desire for high efficiency leads to the interest in the Brayton cycle for these heat sources. In addition, power levels of interest for solar and isotope systems are from a few kilowatts to a few tens of kilowatts as compared with tens to hundreds of kilowatts for reactor systems. At these lower power levels, the large radiator area of the Brayton cycle is a lesser handicap.

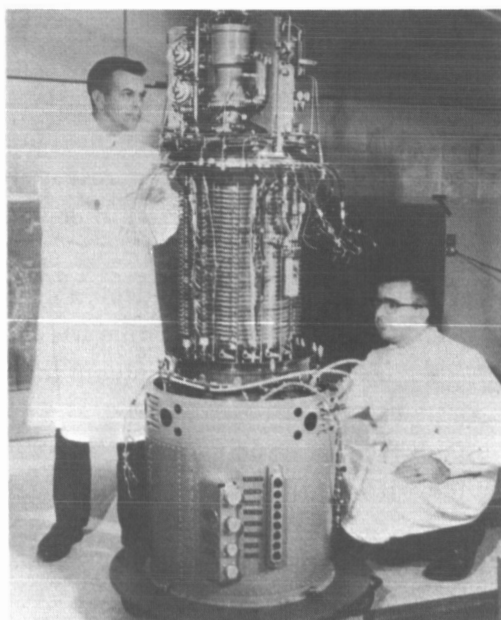
In considering reactor heat sources, an important feature arises immediately. Only one reactor, the SNAP-8, is sufficiently developed to be usable for missions of the 1970's. The technology of advanced reactors is not far advanced, and apparently it will be the late 1970's or 1980's before any of these reactors might appear in mission use. The SNAP-8 reactor is a liquid-metal-cooled reactor with a peak coolant temperature of 1300⁰ F. In the late 1950's, the mercury Rankine power conversion system was chosen as the power conversion system for the SNAP-8. The choice was made because the Rankine system had both low weight and small radiator area. The SNAP-8 is the only reactor power system fully committed to development at this time. Some technology work is being done on thermoelectric converters which could be used with the SNAP-8 reactor. For an advanced reactor, all three power conversion systems are possible choices. Not enough technology work has been completed to determine which system is best. Technology work is being conducted on all three power conversion systems in order to make this determination.

These various advanced systems, the Brayton cycle, SNAP-8, the potassium Rankine cycle, and thermionics, and how they might fit into the future missions of NASA are discussed in papers V to X.



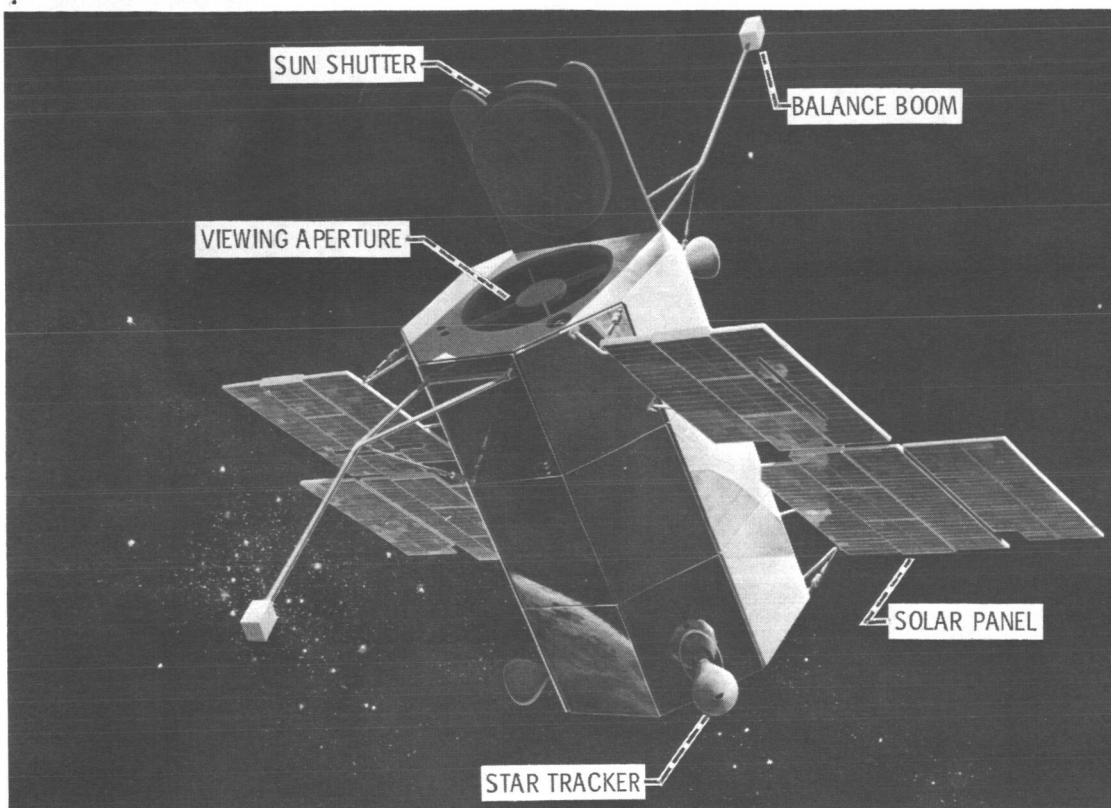
CS-40303

Figure I-1. - Gemini fuel cell.



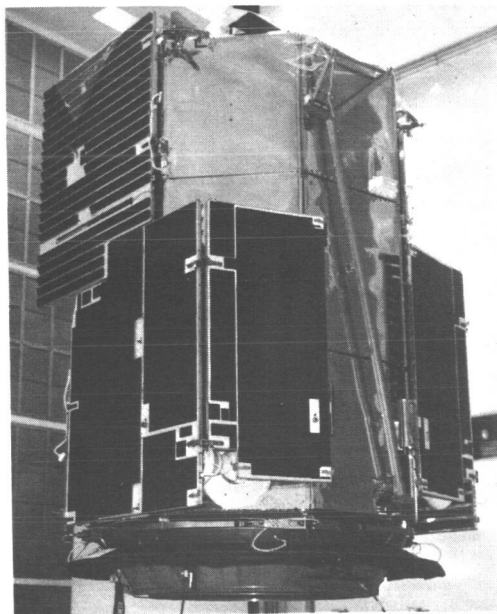
CS-40300

Figure I-2. - Apollo fuel cell.



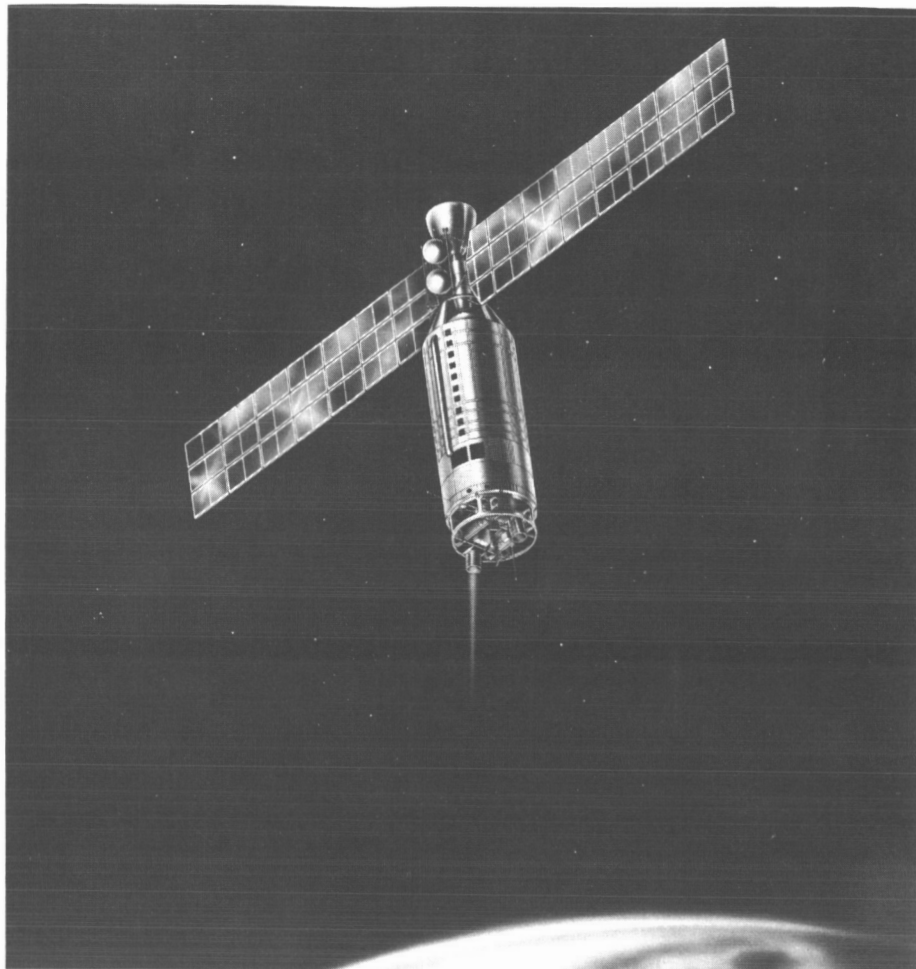
CS-40559

Figure I-3. - Orbiting astronomical observatory (OAO).



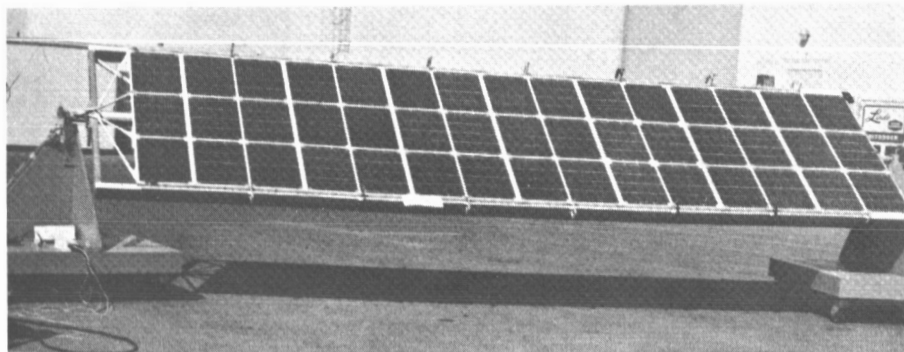
CS-40301

Figure I-4. - OAO with solar panels folded.



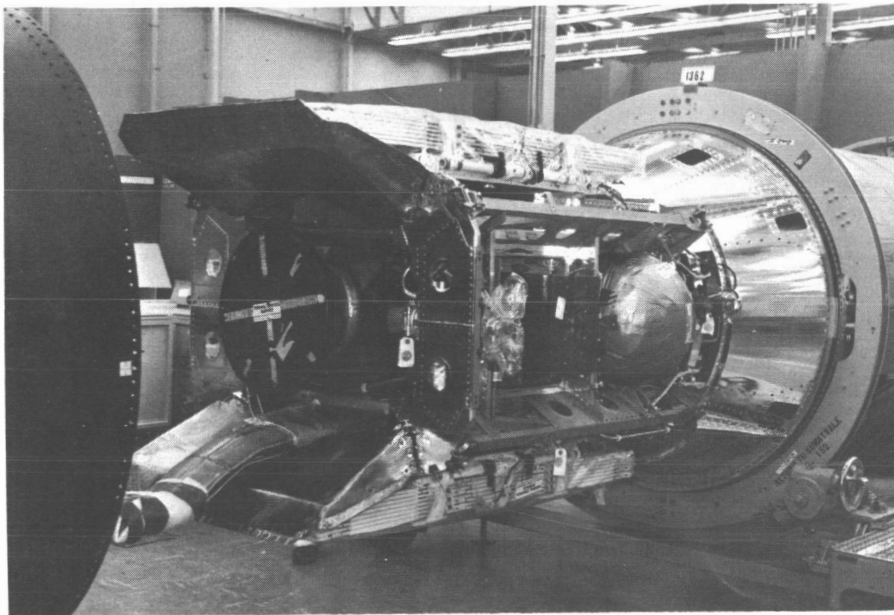
CS-39585

Figure I-5. - 1.5 Kilowatt solar cell array on the Agena.



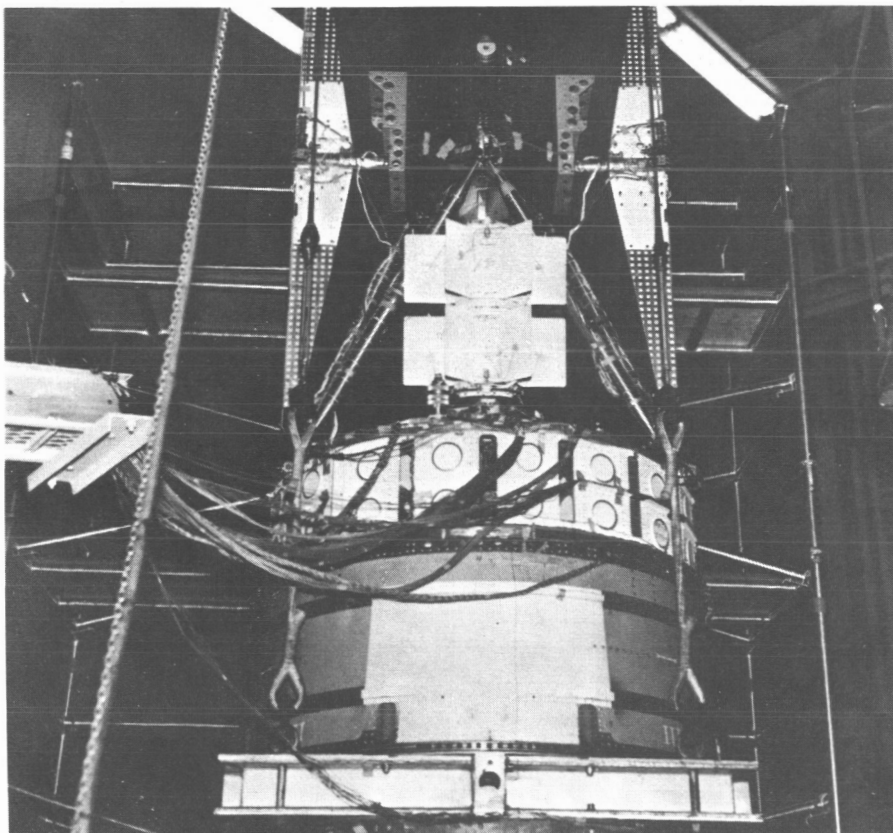
CS-40283

Figure I-6. - One-half of 1.5 kilowatt solar cell array.



CS-40284

Figure I-7. - Folded solar cell array.



CS-40339

Figure I-8. - Nimbus with SNAP-19 generator.

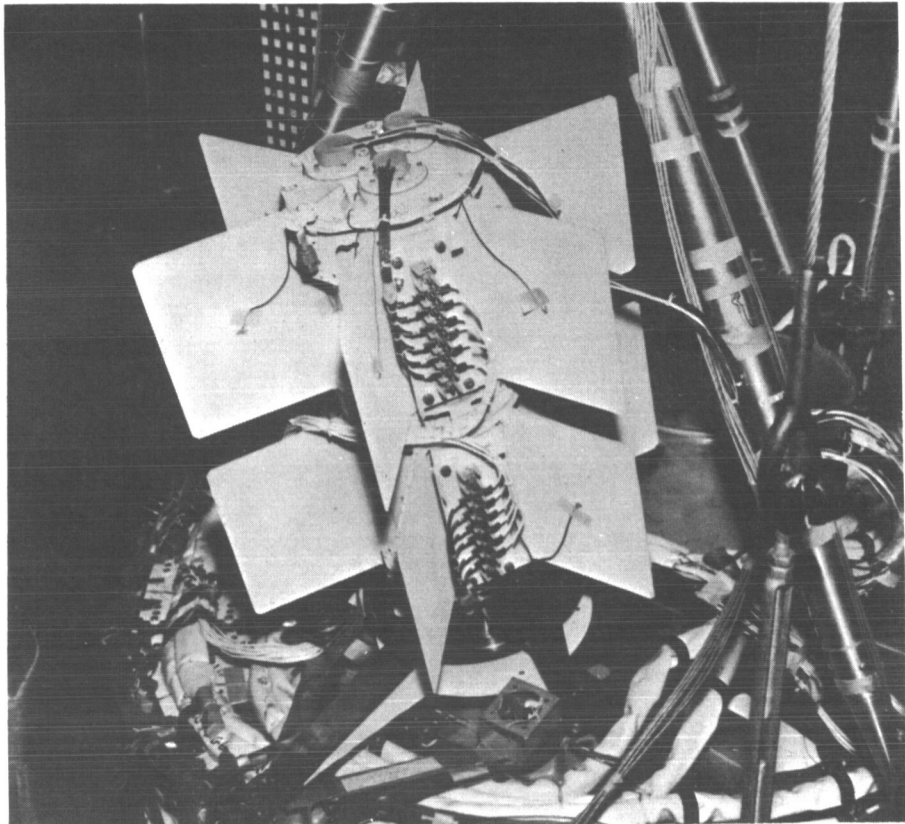


Figure I-9. - Closeup of SNAP-19 generator on Nimbus. CS-40340

II. BATTERIES AND FUEL CELLS

Harvey J. Schwartz, J. Stewart Fordyce, Robert B. King, James M. McKee,
Daniel G. Soltis, and Lawrence H. Thaller

INTRODUCTION

Since electrochemical systems will be used for a long time to come, it is worthwhile to discuss briefly what might be gained by improving these systems. First, consider the battery which is the main energy storage and conversion device in use today. One obvious area for improvement is in energy density, or the watt-hours of energy delivered per pound of battery weight. The silver-zinc primary battery, the main one used today, delivers from 30 to 90 watt-hours per pound depending on its discharge rate. This means that approximately 10 to 35 pounds of batteries must be supplied for each kilowatt-hour delivered. The situation is even worse for secondary or rechargeable cells. For this type of service the silver-zinc battery can not be used because of a variety of problems which will be discussed later. Therefore, the less energetic silver-cadmium and nickel-cadmium systems must be used. These have good cycle life, but the silver-cadmium cells are restricted to use in situations where low charge rates are acceptable. This leaves nickel-cadmium as the only proven, reliable battery system for long-term service where rapid recharge is needed, such as for low-altitude Earth-orbiting satellites. However, the nickel-cadmium cell only delivers a few watt-hours per pound, if long life is desired. It is apparent why this causes concern if one considers the 50-kilowatt solar-cell power system using nickel-cadmium batteries for energy storage. If lifetimes of several years are necessary, approximately 15 000 pounds of batteries would be required if a rather optimistic 2 watt-hours per pound were assigned as the energy density of the battery. It is obvious that 5000 pounds could be saved if the energy density delivered were 3 instead of 2 watt-hours per pound. Since expected cost per pound of material in orbit is roughly equivalent to its weight in gold (i. e., \$500/lb), this would represent a tangible "savings" of \$250 000 per application. Improving the energy density from 2 to 3 watt-hours per pound sounds easy, until one realizes that a number of years of research have not significantly increased the energy density of this system, and that at present, the mechanism of the reaction occurring at the nickel electrode is not known for certain.

It can be seen that much can be gained from improving energy density. Similar arguments can be made for improving other parameters, such as life, temperature capability, reliability, etc., for fuel cells as well as batteries. Our electrochemical technology program, which is aimed at improving the performance of all types of electrochemical systems, is divided into the following four areas:

- (1) Work on conventional batteries, such as nickel-cadmium or silver-zinc

- (2) Improvement in battery performance at extreme temperatures, both high and low
- (3) Research on new systems that promise major increases in energy density
- (4) Research and development on fuel cell systems and components of all types

Approximately 80 percent of the NASA spacecraft flown to date have carried nickel-cadmium secondary batteries. As noted previously, this nickel-cadmium system is characterized by long-life operation and unfortunately by low energy density where long service is required. Work on the nickel-cadmium system is an important part of the conventional battery improvement program.

STABILITY AND STRUCTURE OF NICKEL OXIDES

One way of improving performance of existing systems is to increase the efficiency of the reactants. In the nickel-cadmium system, one of the persistent problems is the loss of charge on the nickel oxide electrode on standing at open circuit. The mechanism for the loss of charge has been studied comprehensively by Conway and Bourgault (ref. 1) who concluded that the reaction is controlled by the electrochemical reaction of oxygen evolution, rather than the nonelectrochemical decomposition or oxygen desorption from the surface phase which had been advanced by others (ref. 2). The details of the mechanism are still not completely resolved. The technological problem remains, however, and work is being supported at Gulton Industries, Inc. to look into ways of stabilizing the charged electrode especially at elevated temperature where the loss of charge is severe. This is needed because the battery must perform under a variety of ambient conditions for space application. Two approaches have been taken so far. One is to charge the electrode at different rates and temperatures to study the influence of these variables on the stand characteristics. No really significant improvements have been obtained in this way. A second approach has been to introduce cations other than nickel into the electrode. The transition metal ions such as cobalt and manganese introduced at a level of 20 atom percent were found to have a marked improvement on retention characteristics as shown in figure II-1 where a comparison of percent charge retention is plotted against time in days on stand at 150° F. The electrodes used for these studies were loaded with the same total number of metal ions in each case. The upper curve is for electrodes containing 20 atom percent of cobalt or manganese and 80 percent nickel, while the lower curve is for 100 percent nickel. When metals of groups I and II of the periodic table were added, inferior results to the control positives were obtained. The change in the rate of charge loss after 1 day implies a change in the mechanism which is not understood at this time. The forming process used in the electrode preparation suggests that in the case of the manganese and cobalt doped system the charged electrode consists of the mixed oxides (or hydroxides) though this has not been proven or even examined. It should be noted that the divalent cobalt and manganese hydroxides have a structure identical to the nickel compound but with slightly larger lattice dimensions. The retention results suggest that the charged cobalt and manganese oxides are stable in contrast to the nickel oxide under these conditions, though this does not account for the whole effect. Nothing is known at present how much of the electrode capacity is due to the electrochemical reduction of cobalt or manganese oxides (or hydroxides) or in what form they exist. One further point should be made that even though the mixed oxide of manganese with

nickel imparts the same improved retention characteristics as the cobalt-nickel system there is a significant difference in the utilization efficiency in the two cases (ref. 3). This is shown in figure II-2 where the utilization efficiency (based on the capacity obtained for 100-mA discharge) is plotted against the discharge current in milliamperes. The dip in all the curves at 500 milliamperes is a real effect but is not yet explained. The manganese doped material follows the pure nickel control while the cobalt doped electrode shows enhanced utilization at all currents studied. This possibly indicates a preferred crystallite size for the mixed cobalt-nickel oxide system though this is by no means the only explanation. Much work remains to be done in this promising area.

In addition to the use of empirical methods such as those just described to improve stability, it is important to understand what occurs in the nickel oxide electrode on charging and to determine, if possible, the nature of the "charged state." Such studies provide a fundamental basis for potential improvements which are not even recognized yet. The identification and characterization of materials formed in the nickel oxide electrode at various states of charge have been the subject of much study with conflicting results (e.g., refs. 4 and 5). In view of this, the program with Gulton Industries also includes a substantial effort aimed at the elucidation of the structure of the nickel oxide in the sintered nickel plate electrode. The X-ray diffraction technique has been employed on wet plates and good diffraction data have now been obtained (ref. 6). Figure II-3 shows the diffraction intensity as a function of diffracting angle for plates charged to the level shown. The pattern of the discharged material at the top shows the three principal reflections at 38.3° , 32.8° , and 19° . These peaks are identified by their Miller indices, 101 - 002, 100 and 001, which describe the crystallographic planes. This material is nickel hydroxide ($\text{Ni}(\text{OH})_2$), which agrees with the conclusions of previous studies (ref. 7). As the charging level increases, there is essentially no major change in the diffraction pattern, and therefore, no change in structure occurs up to the 90-percent level. During the charging process, the active material is oxidized from Ni(II) to Ni(III) though Labat (ref. 5) has found magnetic evidence for the initial formation of Ni(IV). There is the simultaneous loss of a proton to the electrolyte solution. At 100-percent charge, the intensity of the 100 and 101 - 002 reflections begin to decrease. At 133-percent charge, the 100 reflection has completely disappeared and the 101 - 002 reflection is considerably reduced in intensity. These results, together with Kober's (ref. 7) infrared absorption data which show the formation of hydrogen bonds in the charged material relative to the discharged material where "free OH" exists, lead to the following description of the charging process. In figure II-4(a) is the unit cell of the hexagonal layer structure of nickel hydroxide ($\text{Ni}(\text{OH})_2$) showing the positions of the nickel, oxygen, and hydrogen atoms; the presence of free OH in the structure should also be noted. This is the discharged state. Up to 90 percent of charge, the only change that occurs is the loss of one of the protons and the formation of a hydrogen bond between the two oxygens as shown in figure II-4(b). As charging continues above the 90-percent level, the intensity data indicate (by comparison with calculated intensities based on postulated structures) that the ordered layer structure disappears and is replaced by a random stacking of the layers (ref. 8).

When charge input is twice the capacity, that is, at 200-percent charge, the intensity of all the reflections is very weak, which indicates that the material is amorphous in character but another phase is making its appearance at 12.7° . As charging continues, recrystallization to the

characteristic γ -NiOOH has occurred showing peaks at 37.5° , 25.5° , and 12.7° . The structure of this latter material is not known but is undergoing further investigation.

The success with these studies demonstrates the feasibility of using the diffraction pattern and its intensity as a means of characterizing a charged electrode and providing insight into the process involved in its operation. The application of these and other structural tools to electrochemical problems is a fertile field for further investigation.

IMPROVED SILVER-ZINC SECONDARY CELL

The nickel-cadmium cell because of its long cycle life and performance characteristics justifies considerable effort, but a secondary system that appears very attractive on the basis of energy density is the silver-zinc couple. A couple of this type would be most desirable as a long-life secondary cell. However, due to a number of problems, its usefulness is limited to short-term applications. A number of the problems which plague this cell are the following:

- (1) Soluble electrodes - silver oxide in charged state, zinc oxide in discharged state
- (2) Separators not inert to their environment
- (3) Zinc electrode susceptible to dendritic growth

These factors cause the cell to be limited in cycle capability. Elimination of all or some of these problems should give a cell which would find considerable use.

As a result of one of the contracts in which an attempt was made to develop an inorganic ion exchange membrane for a fuel cell, it was suggested that a similar type membrane, stable in potassium hydroxide (KOH) and of controlled pore size, could perform effectively as a separator in a secondary battery. Therefore, Astropower Laboratory of Douglas Aircraft began work to develop a membrane of this type. As a result of their investigations, a separator was developed that was inert in caustic, resisted the dendritic growth of the zinc electrode, and blocked the migration of the dissolved electrode materials. These factors alone warranted the development of this cell type. The separator is made from a combination of inorganic materials which after ball milling are compacted in the die shown in figure II-5 and then sintered. If the proper choice of materials and processing conditions is made, a controlled pore size membrane can be fabricated which will exclude the dissolved electrode materials.

The charge-discharge curves shown in figure II-6 are of a simple two plate cell that was tested during the feasibility study of the separator. This cell, which is one of the cells that indicated the potential of this development, was discharged at 77° F at 20 milliamperes per square centimeter for 30 minutes and charged at 12 milliamperes per square centimeter for 1 hour. The voltage curves of the discharge periods were quite constant throughout the cell's life. The test was discontinued at 2700 cycles because of the degradation of the zinc electrode. In fact, most of the problems encountered in these cells were due to poor seals and failure of the zinc electrode.

Another factor which evolved during testing was the ability of this cell to operate over a wide temperature range and to withstand sterilization temperatures with little or no degradation of capacity. Figure II-7 compares the performance of two cells cycled at 77° F on the 1/2-hour-charge, 1/2-hour-discharge cycle. Illustrated are cycles 1 and 220 of a sterilized and an unsterilized cell. The sterilized cell had been subjected to three periods of 36 hours each at 293° F

prior to testing at 77⁰ F. As can be seen, the performance of the cells compares favorably.

The next series of figures illustrates the cycling capability of the various cell types against temperature. Figure II-8 compares the standard silver-zinc cell against the experimental cell. The maximum cycle life of the standard cell is about 400 cycles compared to 1800 for the experimental, while the best obtained from this cell is 2700 cycles. The temperature range at which the experimental cell will operate is twice that of the standard cell (from approx. 30⁰ to 300⁰ F), and as can be seen, over 1000 cycles can be obtained over most of this range of temperature. These performance characteristics are a significant improvement over the state of the art. Figure II-9 shows how this performance measures up to the other systems. The nickel-cadmium cell undoubtedly has the best cycle life, but just as the other standard cells, it is limited as to the range of temperatures over which it can operate. The experimental silver-zinc cell, however, almost equals silver-cadmium performance and exceeds it considerably in respect to its operating temperature range. It is realized that the performance characteristics of all cell types are continually increasing; however, it is felt that the performance of the experimental silver-zinc cell will keep pace with these improvements and has a chance of exceeding them.

The development of the cell has progressed satisfactorily over the past 2 years and now a 9-plate, 5-ampere-hour cell is being fabricated. The construction of this cell differs somewhat from conventional types. Figure II-10 shows the basic assembly of the cell. The difference in the construction is the method in which the cell pack is assembled prior to insertion into the case. Each separator is sealed into the slotted frame to form discrete compartments, and then the electrodes are placed into these cavities. A complete seal is necessary to prevent species migration around the edge of the separator. The frame approach also facilitates assembly of the cell pack and insertion into the case. Electrolyte is added after the pack is inserted and the top seal closure made. The evaluation of these 5-ampere-hour cells has just begun.

The energy density expected from the cell should not differ significantly from standard silver-zinc cells; however, when compared with cycle life, there should be a significant difference in performance at each rate. A small weight penalty may occur because of the separator and frame construction, but other methods of encapsulation of the separator may bring this in line. In figure II-11 a comparison is made between the energy density and cycle life of the various systems. If long cycle life at low energy densities is desired, the nickel-cadmium battery should be used since as many as 10 000 cycles are reported. For shorter periods, however, the experimental silver-zinc cell would provide increased performance up to 3000 cycles. The curve for the silver-zinc cell shows a range of values with the uppermost line representing the best numbers obtained to date; the lower curve gives the average value. There is a significant difference when comparing the various cells at the higher rates for short times where on the basis of energy density the experimental silver-zinc cell exceeds them all. Any improvement in cycle life will only increase the advantages and subsequent utility of this development. Results of testing to date indicate that very few failures occur because of the separator; the major limiting aspect of this cell is the performance of the zinc electrode. A program has just been initiated to investigate what can be done to increase the efficiency and performance of this electrode. Any improvement here will surely increase the importance of this cell.

EXTREME TEMPERATURE BATTERIES

So far the discussion has been concerned with batteries that operate over the rather nominal temperature range of 0° to 300° F. In the space program, there are more severe operating conditions, and the nonaqueous systems for operation at extreme temperatures are being investigated. For the exploration of the surfaces of Mercury, Venus, and Mars and the possibility of close-in solar probes, a temperature range of -400° to 1000° F can be anticipated.

Figure II-12 illustrates the effect on battery capacity when operation is required outside of their normal temperature range. The batteries concerned are low-rate silver-zinc primary cells that were stored for 2 weeks at different test temperatures and then discharged while still at these temperatures. The percent of original capacity is plotted as a function of test temperature. Note that over the range of 0° to 80° F the 2-week wet stand does not reduce capacity significantly, but that at high and low temperatures the drop off is appreciably. At lower temperatures the fall off is due to poor utilization, while at elevated temperatures the phenomenon responsible is consumption of the active material due to direct chemical reaction.

There are two methods to cope with the problem of extreme thermal environments. The first is to protect the battery by thermal insulation and auxiliary heating in cold environments. The second, and preferred, is to build a battery system that will operate in the particular environment of interest.

The task of finding electrochemical systems that will operate at extreme temperatures is quite interesting. No longer will aqueous electrolytes be useful. It has been known for many years that molten mixtures of alkali halides are, in themselves, ideal nonaqueous electrolytes. They are very fluid, have high decomposition potentials, have conductivities much higher than any aqueous system, and are powerful solvents for almost any type of compound. However, the high melting points of even the eutectic mixtures of these compounds have prevented the widespread usage of this type of electrolyte.

Strangely enough there is one class of batteries which takes advantage of this fact. When batteries are made with these high-temperature electrolytes, they have literally years of room temperature shelf life, since the rates of self discharge at these temperatures are almost zero. When one wants to use these batteries one just melts the electrolyte and the battery is then ready. These cells or batteries, as the case may be, are used exclusively by the military and are referred to as thermally activated cells or simply thermal cells. In figure II-13 is a typical thermal battery.

The individual components of each cell have a layered arrangement. Calcium is usually employed as the anode. It reacts chemically with the melted electrolyte to form a liquid alloy of lithium and calcium at the anode surface. This makes an ideal electrode for high rates of discharge. The eutectic mixture of lithium chloride and potassium chloride is the usual electrolyte. A frequently employed cathode material is potassium chromate. The individual cells of the battery are brought up to the operating temperature by a pyrotechnic device that is interleaved between the individual cells. An electric match initiates the very rapid but almost gasless heat-producing chemical reaction that takes place in these layers. Thermal insulation helps keep down the heat losses from the activated battery. Because of the high solubilities of the cathode materials in the electrolyte, the rates of internal chemical reaction are very high. For this

reason, these cells can only operate a few minutes at the most. For their particular application, however, they can perform the job better than any other battery.

A few years ago NASA Lewis Research Center became interested in batteries that would operate for periods of several days at temperatures of about 800° F. One possible use would be for probes sent to the planet Venus where the surface temperatures are expected to be in that vicinity. In this application, internal heating devices to activate the battery are not too great a concern. A research program was started at Lewis to investigate possible electrochemical systems which might be useful for this application. The magnesium - copper oxide system was finally selected for intensive investigation. Figure II-14 illustrates one of several types of cells used in these studies. As to size, the cylindrical case has the same dimensions as a flashlight D cell. The copper can itself is the current collector for the cathode, and a stainless-steel shaft threaded into the anode conducts the current up through the insulated feedthrough. A woven glass separator material is employed in these cells.

The eutectic mixture of lithium chloride potassium chloride was picked for the electrolyte. It has a convenient melting point of 685° F, a high decomposition potential of about 3.5 volts, and an excellent ionic conductivity. Once the electrolyte had been picked, the electrode materials were selected on the basis of thermodynamic compatibility with it. Magnesium and cupric oxide both have high half-cell potentials, low equivalent weights, and were thought to have tolerable solubilities in the molten salt electrolyte. These hermetically sealed cells are placed in a furnace and discharged at a constant load. A typical discharge curve of this type of cell is shown in figure II-15. Here, the current, voltage of the cell under load, and the periodically observed open circuit voltage are plotted as functions of time. Two aspects of this plot are to be noted - one being the rather flat current against time curve at these light discharge rates, and the other the large step in the open circuit voltage curve. This large step is due to a change in the electrochemical reaction during the latter part of the discharge.

One of the important features being investigated in these studies is the average rate of self-discharge of different types of cell configurations. When five identical cells were discharged at different average currents and the anode efficiencies were plotted against these currents, it was found that although the anode efficiency increases with increasing current drains, the rates of self-discharge for all of these cells are about the same. From other preliminary experiments, it was deduced that this rate was controlled by the rate of diffusion of ions from the vicinity of the cathode to the anode. When cells were made that would hinder this diffusion, cells with lower rates resulted. Figure II-16 shows the value of the self-discharge rates for different cell configurations. It is seen that average rates decreased from about 200 to about 3 milliamperes as the distance was increased between the anode and cathode and other structural arrangements were made to decrease the surface area of the electrodes. The internal resistance of the cells with very high self-discharge rates is about 0.1 ohm, while for the cells with very low rates the resistance goes up to about 1 or 2 ohms. It is obvious that these latter cells cannot deliver currents as high as the former type. So it is seen that, as stated earlier, every cell made is a compromise between having low self-discharge characteristics and having the ability to deliver high current. However, from the results of these studies it will be possible to design cells which, for a given desired service life, will have the optimum balance of these two factors. The encouraging

results obtained thus far have prompted the NASA to award a contract to further study the magnesium - copper oxide system.

The next type of battery to be discussed would be useful at very low temperatures. These might be used on probes to cold environments such as the surface of Mars. Here again a non-aqueous electrolyte is called upon. These batteries, now under investigation, utilize liquid ammonia solutions as the electrolyte. The ground work for these low-temperature batteries was started some 20 years ago with what are referred to as the ammonia vapor batteries. Later with the introduction of stronger battery casings, higher vapor pressure cells offering higher performance were introduced. These higher vapor pressure cells also extended the range of low-temperature operation. Figure II-17 shows an up-to-date high pressure cell. As with the ammonia vapor cells, it is a reserve-type battery, which is one that is activated just before it is to be used. In this instance, the ammonia is contained in a reservoir above the battery section. Upon mechanical or electrical ignition of the percussion cap, the resulting pressure buildup drives the lance through the thin membrane located directly above the central ammonia manifold. The collapsing reservoir walls force the liquid into the manifold and on into the individual cell sections. The battery is now ready to deliver power. The technique of adding the electrolyte at the last minute is a common one used to bypass the problem of high self-discharge rates. The anode material is magnesium which has been plated onto silver foil; the solute for the electrolyte is potassium thiocyanate; and the cathode material is metadinitrobenzene. The wide operating range of -65° to 160° F results from the use of liquid ammonia in a strong battery case.

A study was initiated by the NASA to investigate batteries for use at about -130° F. These batteries are based on the general principles of the conventional high pressure ammonia cells just discussed and, in many respects, are similar. The first area that needed investigation was that of finding whether the potassium thiocyanate salt would depress the freezing point of the solution to the temperature of interest, and still serve as a suitable electrolyte. Figure II-18 shows the results of this investigation. It was found that the oxidizing agent used in the high temperature ammonia batteries was unsuitable for these low-temperature cells. Presently, mixtures of sulfur and mercuric sulfate are being investigated as the cathode materials. Concurrent with this is a study of different amounts of conductive additives for the cathode mix and their effect on the overall cell performance.

Specific requirements of the contract are for single cells that will operate for at least 3 days at a temperature of -130° F. Figure II-19 shows the discharge curve of one of these experimental cells. This particular cell had a bobbin-type construction and is characterized by a rather large drop in voltage during the first few hours of operation, followed by a gradual rise, and finally, the normal dropoff to the cutoff voltage of 1.35 volts. This large decrease in voltage at the start of operation is probably due to a change in the electrochemical mechanism at the cathode. The number of chemical and electrochemical reactions that can take place in this system is rather large and not too well understood as yet.

HIGH ENERGY DENSITY BATTERIES

Since the discussion on extreme temperature batteries is complete, attention can now be

turned to nonaqueous batteries of a different type which offer promise of major increases in energy density. It is easy to select combinations of reactants which have theoretical performance outputs that far exceed those in use today. One has only to go to the periodic table and pick the light metals on one hand as anodes and the halogens, or their compounds, on the other as cathodes. Simple free energy calculations (see table II-1) show that these are good choices. Note that the voltages for lithium anode combinations are above 3.0 volts, and that theoretical energy densities of between 500 and 750 watt-hours per pound are predicted. The magnesium-ACL system is of interest in the dry tape battery, which will be described later. While organic compounds tend to be heavy cathodes, the ACL shown here is representative of a promising class of compounds that are characterized by complex structures containing multiple positive chlorine atoms.

As attractive as these figures are, the materials are comparatively expensive and no large-scale commercial market has been evident, so that work, mainly under government support, on these systems has essentially started from scratch in recent years.

Once promising electrode couples have been chosen from the periodic table, the next problem to be faced is the selection of an appropriate electrolyte. The electrolyte in any dynamic electrochemical system is required to ensure charge neutralization at the electrode surfaces by giving or taking ions from the interfaces as electrons flow in the external circuit. It also completes the electrical circuit (as you have heard) and contributes a series resistance which conducts by the migration of ions in the potential gradient across the cell. These functions involve mass transport processes and are influenced by the physical properties such as the viscosity of the medium in which they occur.

For best performance, a battery electrolyte must have the following general properties:

(1) Good stability - It must not react chemically or electrochemically with the electrode materials or decompose under the conditions of operation.

(2) Good conductivity - It must permit reasonable current drain without excessive ohmic drop. Since they are ionic conductors, this implies the presence of a sufficient number of ions with adequate mobility.

(3) Low viscosity - This is desirable to maximize the diffusion of the reactants or products of the electrochemical reaction to or from the vicinity of the electrodes. If the rate of diffusion is slow compared to the rate of electrochemical reaction, severe concentration gradients can form. This leads to a decrease in the cell potential, the so-called concentration polarization, which is to be avoided wherever possible.

Now to the problem in a high energy density battery. First of all, since active metal anodes such as lithium are being used, any electrolyte containing water is ruled out since rapid reaction may occur with these metals to liberate hydrogen gas. One must go then to the so-called nonaqueous solutions, which in the moderate temperature range are based on organic materials as solvents for the most part. Of these materials, those which react readily with the active metals must be avoided of course. The most critical requirement, though, is the need to provide good conductivity. This implies that the organic solvent must be capable of dissolving ionic solids to form ions in solution. To guide the selection from among the many organic solvents, those properties of a solvent are considered that influence its ability to dissolve ionic solids to form a useful electrolyte system.

In order for an ionic solid to dissolve in any solvent, the ions in solution must represent a more stable state than the ions in the solid lattice. The magnitude of the difference in stability of these two states of the system will determine the extent of the solubility. (The process is described in fig. II-20.) For ionic solids, the lattice is held intact by strong forces; the energy needed to dissociate the solid to its ions is referred to as the lattice energy and is defined in such a way that the greater the lattice energy the more stable the solid. When ions go into solution, they combine with the solvent to form so-called solvated ions. These are ions that are tightly bound to one or more molecules of solvent. The energy liberated in this process, the so-called solvation energy, is defined in such a way that the greater the solvation energy the greater the stability of the solvated ions. If the solvation energy exceeds the lattice energy, then the solid will go into solution since this will be the most stable state of the system.

Most organic solvents have a handicap with regard to their solvation properties because those able to do so will solvate the positively charged cations to a greater extent than the negatively charged anions which are hardly solvated at all. This contrasts with the situation in water where both anions like the chloride ion and cations like the sodium ion are solvated to roughly the same extent. Since the solvation of both anions and cations contributes to the solvation energy leading to solution of the solid, the inability of the anion to contribute very much in the organic solvent leads to a lower solubility than in water for those solids with large lattice energies (ref. 9). The only way to overcome this handicap is to use solvents having very large ion solvation energies. Large solvation energies are associated with those molecules which are polar, that is, those which possess separated centers of positive and negative charge. This requirement is most stringent in the high energy density program since lithium anodes are being used and solvents are needed which will dissolve lithium salts, in particular the halides. These have large lattice energies because of the small size of the lithium ion.

It is indeed possible to find appropriate polar solvents to dissolve ionic solids of interest. However, it should be emphasized that even in dilute solution it is possible that the ions are not "free" but are associated by electrostatic forces to form nonconducting ion pairs in solution, as illustrated in figure II-21; thus, even though solubility has been achieved, conductance may be impaired. The extent of ion pair formation is a sensitive function of the dielectric constant of the solvent. The laws of electrostatics would predict that the force holding such an ion pair together is greater the lower the dielectric constant of the medium. Thus, the equilibrium shifts to the right in media of low dielectric constant and vice-versa. In figure II-22 are experimental results illustrating this (ref. 10), where the equilibrium constants for the formation of a typical ion pair are plotted as functions of the dielectric constant. It is noted that for this particular system the extent of ion pair formation drops rapidly and becomes negligible at a dielectric constant of 44 or a log of 1.63. In this case the ions involved (tetraisoamylammonium nitrate) are quite large, and the ion pair is unstable at this value of the dielectric constant. For smaller ions, an even larger dielectric constant is needed to prevent significant ion pair formation. This is a classic experiment which illustrates very well the advantage of high dielectric constant media to enhance conductivity. Though this simple consideration applies only in dilute solutions, it can be explained quantitatively by the electrostatic theory of ion pair formation developed by Bjerrum which provides the solid line through the points. The electrostatic aspects are only part of the picture, however; in any system of practical significance where high concentrations are en-

countered, many complex interactions involving both chemical and physical effects can occur.

The third requirement of a battery electrolyte, namely low viscosity, has to be considered. As far as the solvents are concerned, this means that the molecules should be symmetric and of relatively small size. However, the addition of a solute can drastically modify the structure of a liquid and change its properties. These influences must be kept in mind.

On the basis of the foregoing considerations, namely large ion solvation energy, high dielectric constant, which is typically in the range from 35 to 65 compared to water with a value of 80, and low viscosity, nonaqueous solvents that will all dissolve ionic solids to form electrolytes of value in high energy density systems can be selected. Some of these nonaqueous solvents, their abbreviations, and dielectric constants are as follows:

N-nitroso-dimethylamine	NDA	53
Methyl formate	MF	8.5
Dimethyl sulfoxide	DMSO	46
Acetonitrile	AN	37
Dimethyl formamide	DMF	37
Propylene carbonate	PC	64
γ -Butyrolactone	BL	39

Methyl formate though a suitable solvent is anomalous in that it has a dielectric constant of only 8.5. It serves to emphasize the importance of other factors.

Since the conductivity of the electrolyte must be as large as possible for battery application, it is instructive to examine the conductance, as a function of the concentration of solute over a wide range. In figure II-23 (ref. 11) are conductance-concentration plots for a couple of electrolytes in dimethyl formamide to show typical behavior. The increase in conductivity with larger ion size should be noted. The curves show a maximum value at approximately 1.5 molal concentration, which is typical for nonaqueous systems. This may result from either ion pairing or from the pronounced increase in viscosity of DMF containing high concentrations of salts. Remember that conductivity involves mass transport and is sensitive to any property which impedes ion movement.

For the case of KPF_6 , it is probable that the appearance of a maximum in the conductivity curve is predominantly due to the viscosity increase, not to ion pair formation. This is shown in figure II-24 where the viscosity and conductance are plotted together. The increase in viscosity coincides approximately with the drop in conductance. This may be a typical phenomenon in these types of concentrated electrolytes though the absence of quantitative data of this kind for practical systems makes it difficult to deduce what limitations are being imposed by nature in any given situation.

These limitations, which are rather specific for nonaqueous electrolytes, do have implications in the optimum design of high energy density batteries. As an example, a system is considered in which the products of the electrochemical discharge are soluble. To minimize the ohmic drop, it would be logical to choose an electrolyte concentration to provide maximum conductivity. As the cell discharges, there would be a pronounced increase in the electrolyte concentration since the amount of solution in the battery is minimized to achieve the highest energy

density. Because of this, the conductivity decreases and the viscosity increases. As a consequence, the cell potential drops for two reasons: increased ohmic resistance, and concentration polarization caused by the mass transport restrictions. As a trade off in actual battery design, it is desirable to start with an electrolyte concentration somewhere below that for maximum conductivity to achieve more uniform operating characteristics.

It is felt that if the limitations in nonaqueous electrolytes are identified and understood, then guidelines can be provided which will allow their influence to be reduced or avoided entirely. NASA and other agencies are funding programs to provide this insight.

Since theoretical considerations have been taken into account, some typical conductivity data will be examined. Table II-2 compares the conductivity of three popular electrolytes, one aqueous and two nonaqueous. If water is the solvent, potassium hydroxide (KOH) gives a maximum conductivity of $55 \times 10^{-2} \text{ ohm}^{-1} \text{ centimeter}^{-1}$; LiClO_4 with methyl formate gives $2.6 \times 10^{-2} \text{ ohm}^{-1} \text{ centimeter}^{-1}$ while with propylene carbonate, this is reduced to 0.5×10^{-2} . Note that the conductivity of the aqueous KOH electrolyte is over one order of magnitude greater than the MF system and two orders of magnitude greater than the PC system. Obviously, it would be desirable to use the aqueous KOH electrolyte, but a lithium anode reacts violently with it. It also reacts slowly with MF. Of the systems shown, only the PC electrolyte is stable. Table II-3 demonstrates the ohmic losses due to electrolyte resistance for the materials shown in table II-2 for an electrode spacing of 1 millimeter. For KOH in H_2O , the voltage loss at a current density of 10 milliamperes per square centimeter is about 0.002 volt. For LiClO_4 in MF, the loss is 0.0385 volt, and for LiClO_4 in PC, it is 0.2 volt. If the last system should operate at 100 milliamperes per square centimeter, it would suffer an ohmic loss of 2 volts, which would be an unacceptably high loss in performance.

From the previous discussion it is obvious that conductance alone is not a satisfactory basis for choosing an electrolyte. Sometimes trace amounts of materials apparently affect electrolyte properties. Figure II-25 demonstrates what may happen when a substance dissolves in a nonaqueous solvent. At the top of the figure is shown a cation, or positively charged ion, being solvated by a pure nonaqueous solvent. If a trace of water is present, it is seen that the cation may be preferentially solvated by the water. Both species, as well as intermediate forms, probably exist in the solution. In any case, the solvation energies will be different and will thus shift the position of any equilibria involved. Figure II-26 shows the effect of a trace amount of an unknown impurity upon a lithium anode performance. A technique called preelectrolysis, which involves passing a small current through the cell, was used to remove certain impurities from the electrolyte. Before preelectrolysis, the efficiencies are quite low. After overnight preelectrolysis, which apparently removed the unknown material, the efficiencies are dramatically improved. Note that before preelectrolysis, zero efficiency was obtained up to about 12 milliamperes per square centimeter. Apparently reduction of the impurity consumed the current instead of the desired process, reduction of Li^+ to Li^0 metal. Trace amounts of materials may be in the material as received or they may be accidentally added. Two cases of the latter may be cited from experience. In one case, traces of water were introduced by using presumably pure argon as an inert atmosphere. In a second case, foreign ions were introduced from a desiccant used to remove water. It is only fair, however, to note that trace amounts of certain materials may be necessary for satisfactory cell operation. It is felt that the solution to this problem is to carefully charac-

terize the materials - that is, to really identify them so that one can perform valid experiments. The general approach is to characterize the material before and after purification. All this leads to the rather disquieting conclusion that there is a great deal of uncertainty with respect to the nonaqueous data presently available. It is expected that the approach just described will better control the materials used and that the data generated can be reproduced and validly compared with other similarly obtained.

Some practical test results will now be discussed involving anodes, cathodes, and electrolytes. The electrolyte screening program produced significant numbers of nonaqueous solutions having conductivities greater than 10^{-3} ohm⁻¹ centimeter⁻¹. Lithium, calcium, and magnesium as anodes were characterized in the best of these and several interesting systems capable of supporting substantial current densities evolved. Table II-4 shows some representative lithium anode systems. The dimethyl formamide system gassed badly. The LiClO₄-PC system has a high polarization at significant current densities and is thus shown to be a low rate system with a fairly low conductivity. It is, however, the one that has received the most attention. Of the stable systems shown, only LiPF₆-NDA has exhibited a 100 milliampere per square centimeter capability. It, as well as LiClO₄-MF, is receiving considerable attention for medium rate applications.

Table II-5 shows the cathodes presently of interest in the high energy density battery programs being supported by the government. As a result of these studies, there is confidence that workable primary systems are possible with what is now known. Now consider the Li-CuF₂ system using a LiClO₄-PC electrolyte. Figure II-27 shows a present laboratory cell design. It consists of a CuF₂ cathode between two lithium anodes. A separator on either side of the cathode prevents contact with the anodes. The cell is sealed in a plastic envelope and the electrolyte is inserted with a hypodermic syringe. It is then discharged through a constant resistance. Figure II-28 shows a typical discharge curve, cell potential being plotted against discharge time. This cell for an average current density of 0.5 milliampere per square centimeter produces a very constant voltage throughout the major portion of its discharge. The 3-volt potential is very desirable since reasonable battery output potentials can be obtained with a minimum number of cells in series. Figure II-29 compares Li-CuF₂ performance using a low rate PC electrolyte at 95° F with a medium rate MF electrolyte at 5° and 95° F. Energy densities in watt-hours per pound for the plastic envelope cell are plotted against discharge time. Note that values as high as 210 watt-hours per pound at 0.5 milliampere per square centimeter have been obtained at 95° F using PC as the solvent. If MF is the solvent, values as high as 170 watt-hours per pound at 5 to 10 milliamperes per square centimeter have been obtained at 5° F. At 95° F, however, the MF system is reduced to 60 to 90 watt-hours per pound, possibly due to increased reaction between the cell components. The solid line compares a conventional AgO-Zn cell's discharge characteristics. The most serious problem with these systems is the lack of shelf life. The cell using PC loses capacity by dissolution of CuF₂ into the electrolyte, diffusing away from the electrode and reacting with the lithium anode. Either a separator to prevent diffusion to the anode or an environment that prevents or drastically limits the solubility of CuF₂ is needed. Figure II-30 indicates that coulombic efficiency is reduced from 75 to 60 percent in 6 weeks when stored at 5° F. When stored at 95° F for 2 weeks, there is a change from 75 to about 20 percent. The Li-CuF₂ cell using a MF electrolyte suffers a more rapid degradation since lithium reacts readily with it. This system would require a reserve construction if built according to present technology.

One rather unique reserve construction is the dry tape battery shown in figure II-31. The anode, cathode, and an encapsulated electrolyte are contained in a plastic film or tape. On demand for power, the tape is passed between rollers, which crush the electrolyte capsules and thus allow the electrochemical reaction to proceed. Electric power is removed by current collectors on either side of the tape.

The microencapsulated tape, shown at the right in figure II-32 contains the anode, a separator, and the cathode with the microencapsulated electrolyte. Capsule diameters range from 500 to 1700 microns. Three practical problems hamper microencapsulation: first, electrolyte loading of only 42 to 70 percent by weight has been achieved; second, electrolyte utilization of only 50 percent further complicates the problem; and third, an electrolyte evaporation rate of 0.4 to 2 percent per day results in rather limited shelf life.

The macroencapsulated tape on the left reduces or eliminates these difficulties. In this design, larger packets of electrolyte are contained in the center of the tape which, when crushed, permeate the area between the electrodes. This design has proven more satisfactory.

Figure II-33 compares present dry tape performance with that of a conventional silver-zinc battery. The dry tape battery operates between 90 and 120 watt-hours per pound, almost independent of discharge rate. Note that the apparent efficiency drop off at high drain rates is at least partially due to applying the entire system's weight over a short discharge period. It is estimated that energy densities possible with present dry tape systems will approach 150 watt-hours per pound.

There is great interest in the development of secondary high energy density batteries since they have many potential applications. Several programs have been funded by NASA and other agencies in the past several years; the results have not been too encouraging from the practical standpoint, since a maximum of 15 to 30 cycles is the best reported performance. A Li-AgCl battery has demonstrated several hundred cycles, but this is not really a high energy density system being only about 10 percent better than silver-zinc.

The very slow rate of progress in the development of secondary batteries is due in large measure to the primitive understanding of the chemistry in these systems. Clearly it is impossible to make reasonable gains with such systems until some progress is made toward the identification of the species, the characterization of their equilibria, and some understanding of their transport properties. A wide variety of physical chemical measurements are needed to obtain this information. The process actually going on at the electrodes must be characterized, of course; but electrochemical studies by themselves will not give an adequate description for further progress. Several new programs are now underway where the emphasis is being placed on providing this insight. This effort should give sound direction to further development work in this important area.

FUEL CELLS

The high energy density reactants that have been discussed so far offer theoretical energy densities in the 500 to 800 watt-hours per pound range. There is a common reactant combination which theoretically can produce outputs over 1600 watt-hours per pound, and that combination is

hydrogen and oxygen. However, since these materials are low density fluids, it becomes necessary to use a different type of conversion device, namely, the fuel cell.

Figure II-34 illustrates that a fuel cell is essentially a continuous operating battery, with the invariance of the fuel cell the main distinguishing feature. In a battery, all reactant materials and the ensuing products of reaction are contained within the case, and thus the composition continually changes. In a fuel cell, on the other hand, fuel and oxidant are fed continuously to the cell and the reaction products continuously removed along with any heat produced by the reaction. Since the electrodes are unchanged, proper balance of the flow process leads to a constant invariant condition within the cell. As a result, the operating time is limited only by the supply of reactants. For long operating periods, the energy density can approach the theoretical value for the reactants since the weight of supporting hardware is constant.

The successes of fuel cells on five Gemini flights, coupled with the early qualification of the fuel cell for the Apollo spacecraft, have greatly increased confidence in their use. Operating times are being increased from the 2-week lifetime of Gemini and Apollo to 21 to 30 days for the biological satellites and 30 days or longer for the Air Force's manned orbiting laboratory. The availability of proven flight hardware and increasingly attractive life data are causing discussion of fuel cells for several thousand hours of operation and power levels of a few tens of kilowatts. The need for fuel cells for missions either currently defined or likely to appear in the next several years can be met by the several systems already qualified or nearing flight hardware status; therefore, the fuel cell work here emphasizes improvements in the basic hydrogen oxygen fuel cell rather than construction of systems competitive with those already in existence. Efficiencies of the hydrogen-oxygen cells are high so that no large improvements in energy density are possible. As a result, the work done here has emphasized stable operation for long periods of time at the highest possible efficiency.

One of the critical areas demanding attention is the development of electrode materials capable of high power output and long life. The initial effort was directed toward improving the energy conversion capability and extending the operating environment of the lightweight-deposited catalyst nickel screen electrode.

New catalyst materials, including platinum blacks and platinum-rhodium mixtures were prepared and evaluated. A variety of nickel support screens was tested singly and in sandwich configurations. Levels of Teflon waterproofing between 8 and 50 percent were investigated.

This research activity resulted in an electrode, manufactured by the American Cyanamid Company and designated the AB-40, which uses a 40 milligram per square centimeter deposited platinum black catalyst supported on a 40-mesh nickel screen with 25 percent Teflon waterproofing. The nickel screen is gold plated to deter oxidation of the nickel when the electrode was used as a cathode in a hydrogen-oxygen fuel cell.

In the evaluation of these electrodes, single test cells were constructed using the AB-40 material for both anode and cathode. A matrix-separator, containing the electrolyte, was sandwiched between them.

Figure II-35 shows the performance obtained in single cell testing using the AB-40 electrode with a Johns Manville Quintera asbestos matrix containing a 50-percent KOH electrolyte concentration. The lower curve was run at a temperature of 160° F and atmospheric reactant pressure. The center curve demonstrates that increasing the operating temperature to 212° F results in a

10-percent improvement in cell output. An additional 10 percent is realized by increasing the reactant pressure to 45 pounds gage. The decrease in the rate of potential dropoff in the two top curves results from a decrease in the electrolyte concentration polarization due to increased ion mobility at higher temperature and a lower gas side polarization at higher reactant pressures.

The Quintera matrices of these cells have also demonstrated reliable life at current drains up to 300 amperes per square foot, as shown by figure II-36 in which cell potential against operating life in hours is plotted for several current densities.

The cell represented in the top curve was initially at a load of 100 amperes per square foot for 1450 hours after which the load was increased to 200 amperes per square foot. This cell is still operating after more than 4000 hours at a potential of 0.83 volt. For reference, it should be noted that 4000 hours is almost 6 months.

The cell operating at 200 amperes per square foot has run more than 1800 hours with a potential loss of only 2 percent, or 18 millivolts. Though the potential of the cell operating at 300 amperes per square foot is dropping off more rapidly, it has only decreased 5 percent, or 40 millivolts, in 1700 hours. This cell does, however, demonstrate that control problems increase at higher current levels.

In one of the earlier slides, the improved performance at higher temperatures was noted. It was found, however, that at temperatures above 212° F with electrolyte concentrations of 50 percent KOH, the asbestos matrix materials tended to dissolve, leading to cell failure.

In a search for higher temperature materials, the American Cyanamid Company has developed a ceria-Teflon material which resists electrolyte attack up to 300° F.

The performance of single cells using the ceria-Teflon matrix is shown in figure II-37. Here again, the improvement at higher temperatures and reactant pressure is evident. The dashed line is a comparison curve for a Quintera matrix run under the same conditions as the lower ceria-Teflon test. It is apparent that at temperatures of 212° F and below, the Quintera matrix offers superior performance and would be selected for applications in that range.

Life test with the ceria-Teflon matrix has not been as extensive as with the Quintera matrix since this is a development matrix and has only recently been characterized. Figure II-38 shows that 1000 hours of life has been demonstrated at temperatures of 260° F and 60-percent KOH concentration at current loads of 100 and 200 amperes per square foot. Two recently started tests at 100 and 200 amperes per square foot with reactant pressures of 45 psig are progressing quite satisfactorily after 500 hours. The increase in cell potential with increased reactant pressure at 200 amperes per square foot approaches 70 millivolts for a resultant 14-percent power gain.

Results to date with the American Cyanamid electrode have demonstrated that moderate and high current levels can be attained at reasonable cell potentials. Sufficient life test experience at moderate current density indicates that the electrode and matrix materials will hold up for 2000 to 4000 hours. The electrode-matrix development effort at Cyanamid is continuing and preparations are being made to evaluate these materials in a fuel cell module and in a complete system here at Lewis.

One unusual application for the hydrogen-oxygen fuel cell is as a secondary battery. Such a battery consists of a number of fuel cells, connected in series, which operate in the normal fashion during discharge and as electrolysis cells during charge. The gases generated on charging are stored in tanks which are an integral part of the battery. Figure II-39 shows a typical test vehicle.

There is a six-cell fuel cell stack in the center with the hydrogen storage tank on the left and the oxygen tank on the right. A pressure-balancing bellows, not shown here, prevents any appreciable pressure differential from being established across the cell.

This device offers a number of operational advantages. Cell reversal is impossible, and high overcharge rates can be sustained, limited only by the unit's ability to dissipate heat. This device has also operated satisfactorily after thermal sterilization. The most significant advantage, however, is that this is the only secondary battery in existence which gives a positive, accurate, state-of-charge indication. Figure II-40 shows a typical charge-discharge cycle. Note that the tank pressure increases linearly with charge and decreases linearly during discharge as a function of the current passed. By monitoring tank pressure, the exact state-of-charge can be determined.

Figure II-41 shows a 500-watt, 600 watt-hour battery that has been tested. The 34-cell stack is to the right of the center flange, and the pressure-balancing bellows to the left. The body of the unit is $8\frac{1}{2}$ inches in diameter and 37 inches long. It weighs 39 pounds as shown, but it is estimated that as a flight unit it would weigh 30 pounds and thus could deliver 10 watt-hours per pound in low-altitude orbit and 20 watt-hours per pound in a 24-hour orbit. The overall efficiency is 58 percent, which compares favorably with conventional secondary batteries. Power outputs over 1300 watts have been delivered for short times.

Like all experimental devices, this one has problems. For one, its volume is approximately three times that of an equivalent battery. Self-discharge occurs due to the high tank pressures, and charged-stand times beyond a few weeks appear impractical.

The most serious problem is life. The best results to date have been 300 cycle (500 hr) on multicell units and 725 cycles (6 weeks) on single cells. The present effort is concentrated on solving these life problems in order to enhance the usefulness of this battery.

The discussion on hydrogen-oxygen fuel cells thus far has studiously avoided mentioning a rather weighty problem - how the hydrogen and oxygen are to be stored. The problems of storing hydrogen and oxygen lead one to consider those materials which are easily stored on a spacecraft - that is, storable rocket propellants. An additional incentive for their use is the fact that they might just be along for the ride anyway and what is left over in the fuel cells can be used.

The first stage in the development of fuel cells using storable rocket propellants was to determine which, if any, were feasible electrochemically. Of the fuels only N_2H_4 , which was electroactive in acidic and basic electrolyte, showed feasibility. The UDMH was unreactive. Aerozine 50 is a 1:1 mixture of N_2H_4 and UDMH. As to be expected, only the N_2H_4 portion of it was active. Of the oxidizers, only N_2O_4 and HNO_3 showed feasibility. The H_2O_2 spontaneously decomposed at a too rapid rate. The potentials generally observed for hydrazine and hydrogen are similar. This is not unexpected since it is well known that hydrazine with its positive free energy of formation decomposes readily upon a suitable catalytic surface. Furthermore, the same general loss of potential occurs in acid electrolyte with both hydrazine and hydrogen. It is quite probable, therefore, that hydrazine functions as hydrogen when anodically oxidized. The choice of catalysts is quite critical since one that is too active causes excessive spontaneous decomposition and one that is not active enough reduces the electrochemical utilization. Since a very active catalyst decomposes N_2H_4 to hydrogen, the oxidizer can also be decomposed to oxygen and then used in any hydrogen-oxygen fuel cell. Thus, the present program has emphasized decomposing

N_2H_4 and Aerozine 50 to obtain hydrogen, and N_2O_4 to obtain oxygen. The Aerozine 50 reactor is shown schematically in figure II-42.

Aerozine 50 and water contact first a zinc catalyst, then a nickel oxide catalyst, and finally an iron oxide catalyst. The stream then passes through a palladium diffuser to produce ultrapure hydrogen. The reactor output composition is shown at the bottom of figure II-42.

Figure II-43 shows how the efficiency varies with time. Percent of hydrogen obtained is plotted against hours of continuous operation. Initially the process is about 99 percent efficient, but quickly levels off to slightly better than 95 percent for 1000 hours of continuous operation. Figure II-44 shows a N_2O_4 reactor. It uses 2 percent platinum on Al_2O_3 . This system starts out at a rather high value but after 80 hours has fallen to about 80 percent. It is apparently quite stable at this value up to 1000 hours of continuous operation. The oxygen inefficiency is caused by a deactivation of the catalyst to a constant level of performance and allows N_2O_4 to be admitted to the fuel cell cathode. This is undesirable, especially for an alkaline electrolyte system. Limited studies with zeolites indicate that they can effectively remove the N_2O_4 . Studies are now underway to demonstrate their useful life and efficiency.

CONCLUSIONS

A variety of programs has been presented herein. It might be well to consider what the future holds for some of the resulting systems.

In assessing the significance of the different types of battery work described, the natural tendency is to refer to the baseline values of 30 to 90 watt-hours per pound for primary cells, and perhaps 2 watt-hours per pound for long-life secondary cells, and to conclude that the most important programs are those which promise to raise these values the greatest amount. One would then assume that the nonaqueous work is of greatest significance, and in fact, a large part of our battery technology program is oriented in that direction. However, much research is needed and complete development of such batteries will take a long time, if it comes about at all. As a result, it may turn out that incremental improvements in existing batteries, which will be used over and over again, will be more important in the long run. Certainly the development of a long-cycle life silver-zinc cell will be a significant increase in the state of the art for secondary batteries.

In fuel cells, it is unlikely that any system will unseat the hydrogen-oxygen system from its prominent position, although others may be developed to meet special needs. Therefore, any technology work on this system is a good long-term investment.

Beyond that, one cannot guess which of the programs described herein will be of greatest value. It can only be said that several of these efforts will find eventual use in flight programs.

REFERENCES

1. Conway, B. E.; and Bourgault, P. L.: Electrochemistry of the Nickel Oxide Electrode. Part III. Anodic Polarization and Self-Discharge Behavior. Can. J. Chem., vol. 40, no. 8, Aug. 1962, pp. 1690-1707.

2. Pitman, A. L.; and Work, G. W.: Alkaline Storage Batteries - An Investigation of Nickel Oxide Positive Plate Characteristics. Rep. No. 5031 (DDC No. AD-149784), Naval Research Lab., Dec. 2, 1957.
3. Ritterman, P.; Lerner, S.; and Seiger, H.: Investigation of Battery Active Nickel Oxides. Gulton Industries, Inc. (NASA CR-72018), June 12, 1966.
4. Salkind, Alvin J.; and Bruins, Paul F.: Nickel-Cadmium Cells. I. Thermodynamics and X-Ray Studies. Electrochem. Soc. J., vol. 109, no. 5, May 1962, pp. 356-360.
5. Labat, Jean: Nickel Hydroxides. Ann. Chim., vol. 9, no. 7-8, 1964, pp. 399-427.
6. Ritterman, P.; Lerner, S.; and Seiger, H.: Investigation of Battery Active Nickel Oxides. Gulton Industries, Inc. (NASA CR-54957), Mar. 12, 1966.
7. Kober, Frederick P.: Analysis of the Charge-Discharge Characteristics of Nickel-Oxide Electrodes by Infrared Spectroscopy. Electrochem. Soc. J., vol. 112, no. 11, Nov. 1965, pp. 1064-1067.
8. Ritterman, P.; Lerner, S.; Seiger, H. N.; and Vaughan, P.: The Structure of the Battery Active Materials Existing on the Sintered Nickel Oxide Electrode at Various Stages of Charge. Paper to be presented at the Philadelphia Meeting of the Electrochemical Society, Philadelphia, Pennsylvania, Oct. 9-14, 1966.
9. Harris, William S.: Electrochemical Studies in Cyclic Esters. Rep. No. UCRL-8381, University of California, Radiation Lab., July 17, 1958.
10. Harned, Herbert S.; and Owen, Benton B.: Physical Chemistry of Electrolytic Solutions. 2nd ed. Reinhold Publ. Corp., 1950, p. 192.
11. Elliott, W. E.; Hsu, S. L.; and Towle, W. L.: The Development of High Energy Density Primary Batteries, 200 WATT Hours per Pound of Total Battery Weight Minimum. Final Rep. (NASA CR-54153), Globe-Union, Inc., Jan. 1965.

TABLE II-1. - THEORETICAL ENERGY
DENSITIES OF HIGH ENERGY COUPLES

Anode-cathode	Theoretical potential, V	Theoretical reactant performance, (W-hr)/lb
Li-CuCl ₂	3.07	503
Li-CuF ₂	3.55	749
Mg-ACL	2.92	785
Zn-AgO	1.86	205

TABLE II-2. - MAXIMUM CONDUCTIVITIES OF
SELECTED ELECTROLYTES

Solvent	Solute	Specific conductance, ohm ⁻¹ -cm ⁻¹
Water	KOH	55.0×10 ⁻²
Methyl formate	LiClO ₄	2.6
Propylene carbonate	LiClO ₄	.5

TABLE II-3. - VOLTAGE LOSS
DUE TO ELECTROLYTE
RESISTANCE

Electrolyte	Voltage loss at current density of 10 mA/cm ² , V
KOH-H ₂ O	0.0018
LiClO ₄ -MF	.0385
LiClO ₄ -PC	.2000

TABLE II-4. - LITHIUM ANODE PERFORMANCE

Electrolyte		Polarization, V		Compatibility
Solvent	Solute	10 mA/cm ²	100 mA/cm ²	
DMF	(n-C ₄ H ₉) ₄ NPF ₆	0.4	1.0	Gases vigorously
NDA	LiPF ₆	.2	1.6	Stable
PC	LiClO ₄	.6	>3.0	Stable

TABLE II-5. - CATHODE SYSTEMS

Cathode	Electrolyte	Application
CuF ₂	LiClO ₄ -PC	^a Low rate
CuCl ₂	LiAlCl ₄ -PC	^b Medium rate
CuF ₂	LiClO ₄ -MF	^b Medium rate
AgO	LiPF ₆ -NDA	^b Medium rate

^aCurrent densities to 1 mA/cm².^bCurrent densities from 1 to 10 mA/cm².

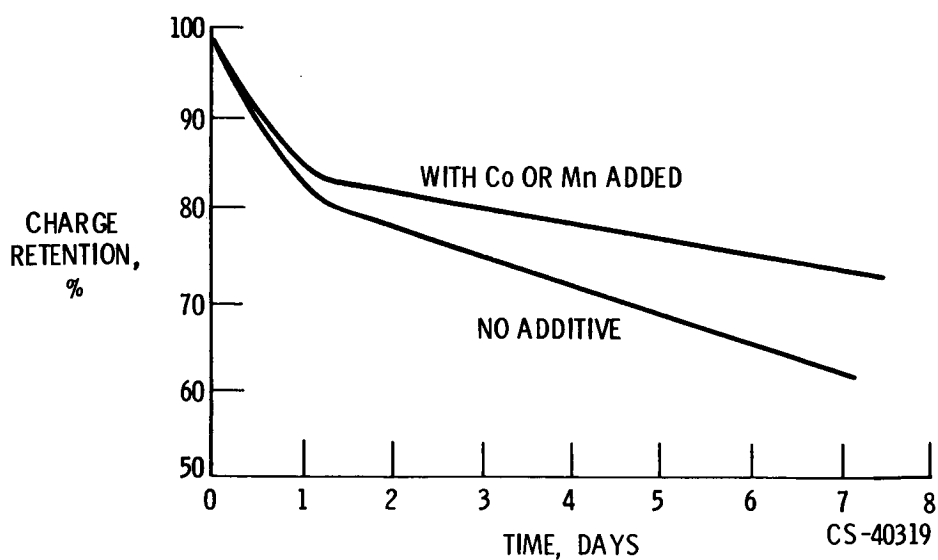


Figure II-1. - Stability of charged nickel oxide electrodes at 150° F.

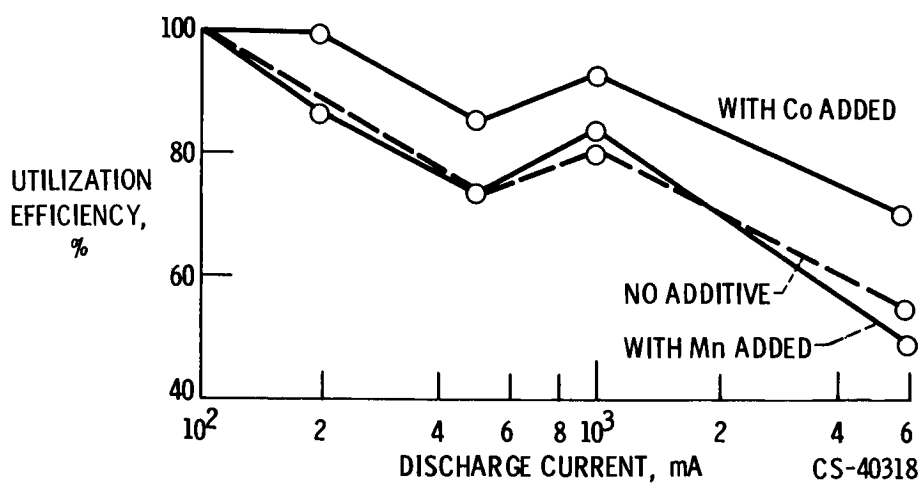


Figure II-2. - Utilization efficiency of nickel oxide electrodes as function of discharge current.

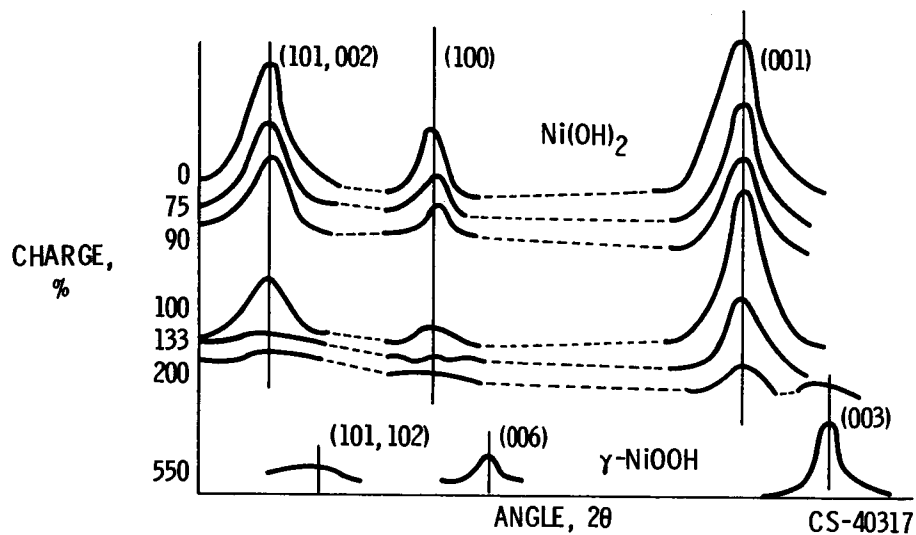


Figure II-3. - Nickel oxide electrode, X-ray diffraction.

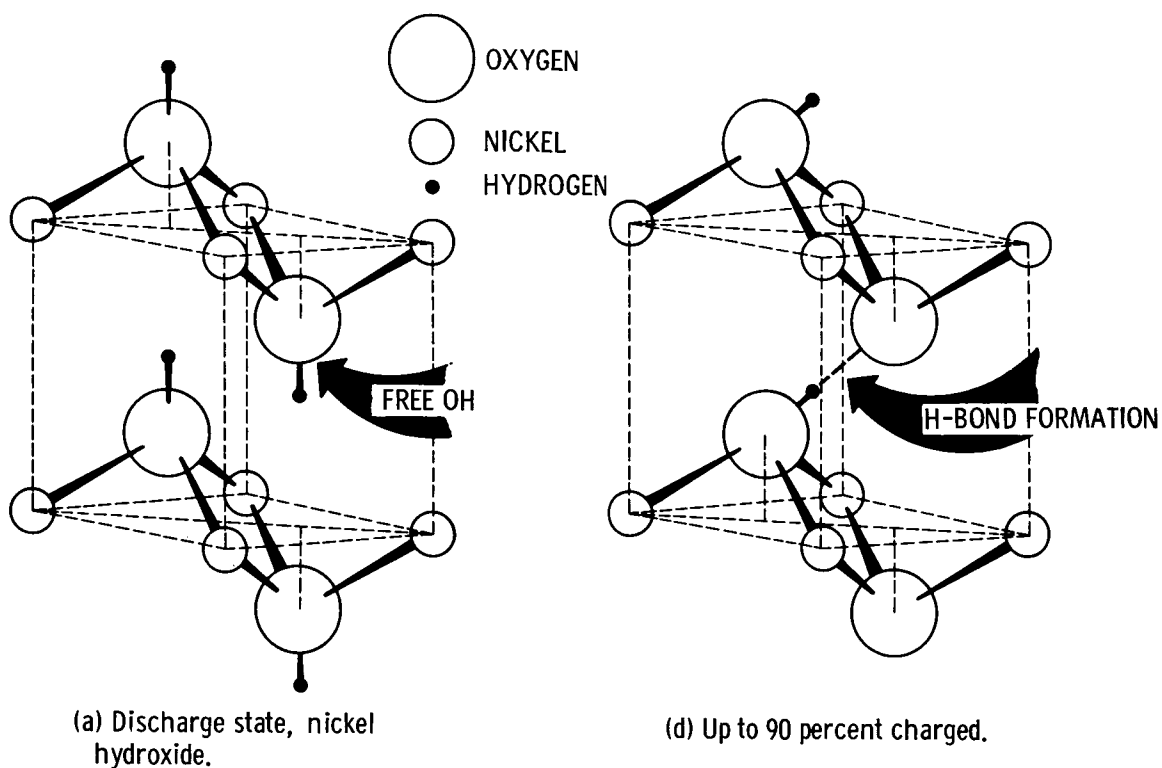
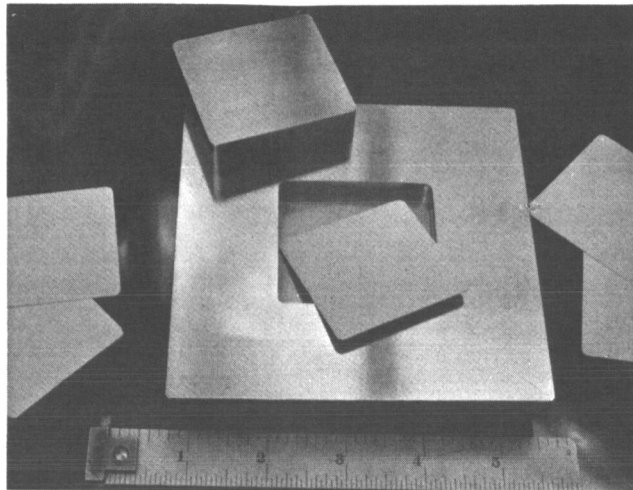
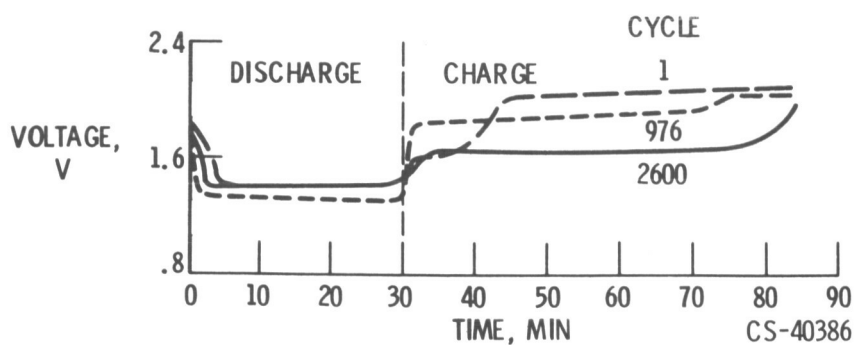


Figure II-4. - Structure of material in nickel oxide electrode.



CS-40390

Figure II-5. - Inorganic cell separator.



CS-40386

Figure II-6. - Experimental silver-zinc secondary cell. Charge-discharge cycle test at 77° F; depth of discharge based on 16-hour discharge, 17 per-cent.

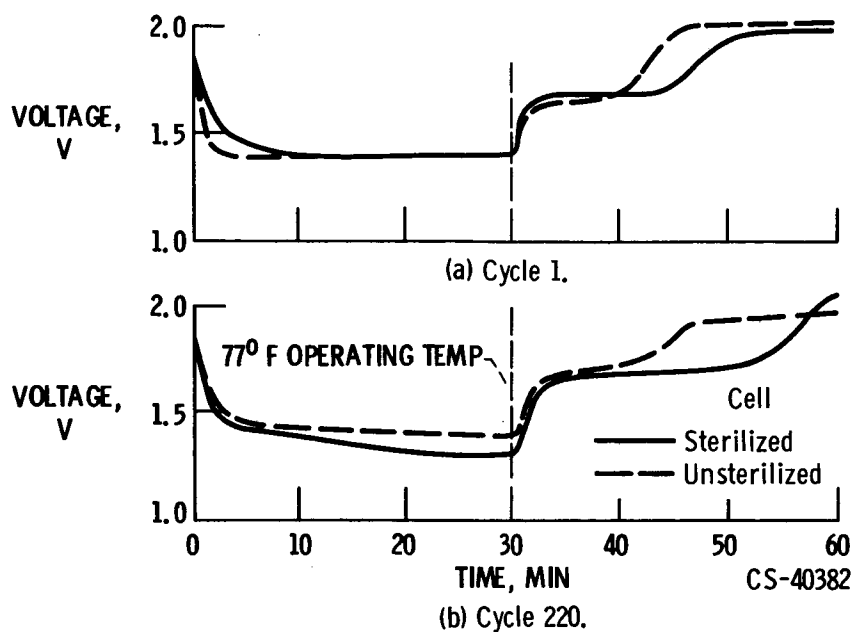


Figure II-7. - Experimental silver-zinc cell after thermal sterilization for 108 hours at 293° F.

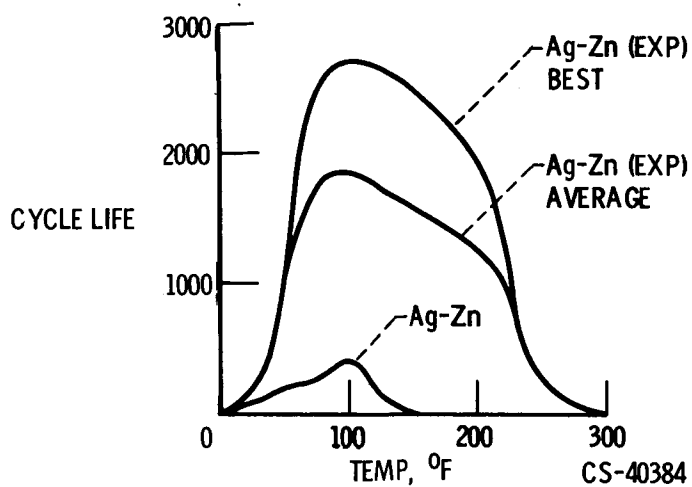


Figure II-8. - Comparison of cycle life of silver-zinc batteries. Depth of discharge, 25 percent.

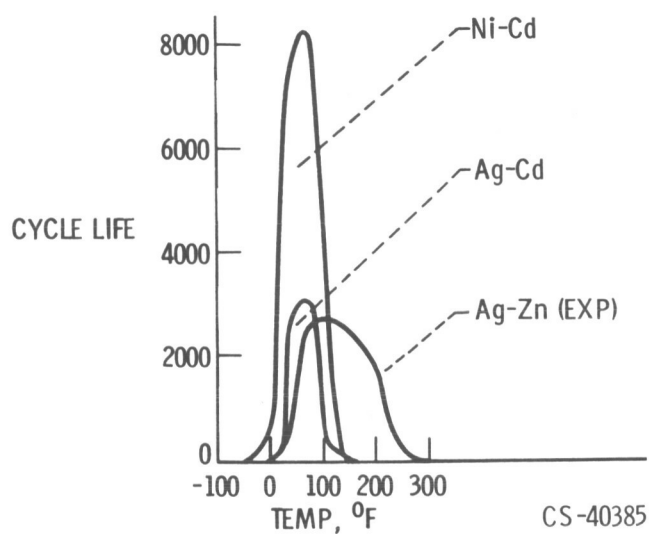
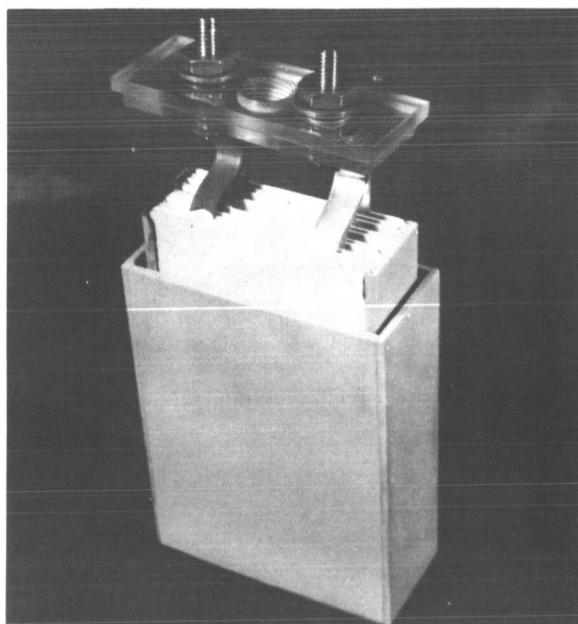


Figure II-9. - Comparison of cycle life of secondary batteries against temperature. Depth of discharge, 25 percent.



CS-40389

Figure II-10. - Silver-zinc cell assembly.

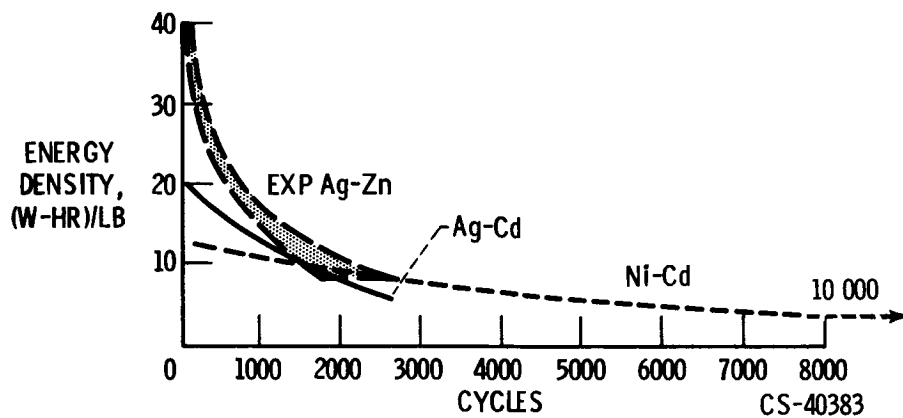


Figure II-11. - Comparison of energy density with cycle life.

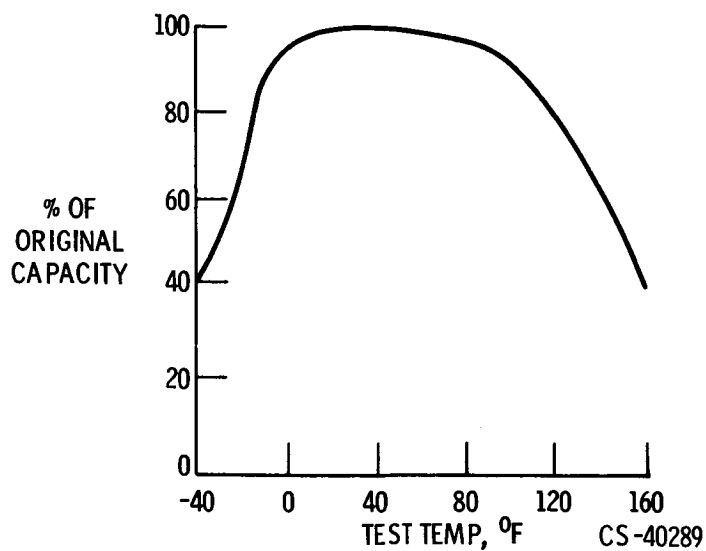
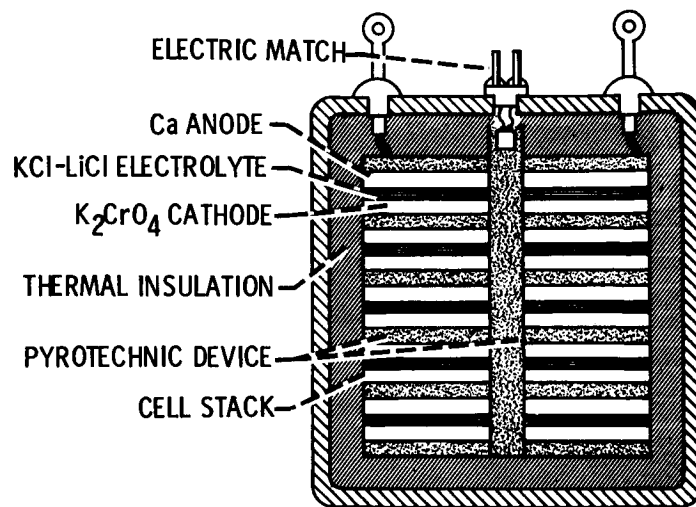
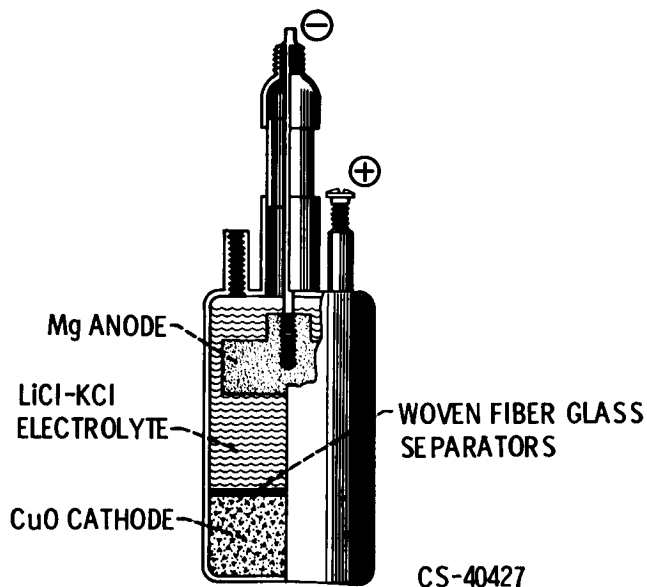


Figure II-12. - Loss of capacity of silver-zinc battery as function of temperature (after 2-wk wet stand at test temperature, fresh battery at 80° F equals 100 percent).



CS-40338

Figure II-13. - State of the art of high-temperature battery. Typical performance: service life, 5 minutes; operating temperature, 800° F.



CS-40427

Figure II-14. - NASA experimental high-temperature cell.

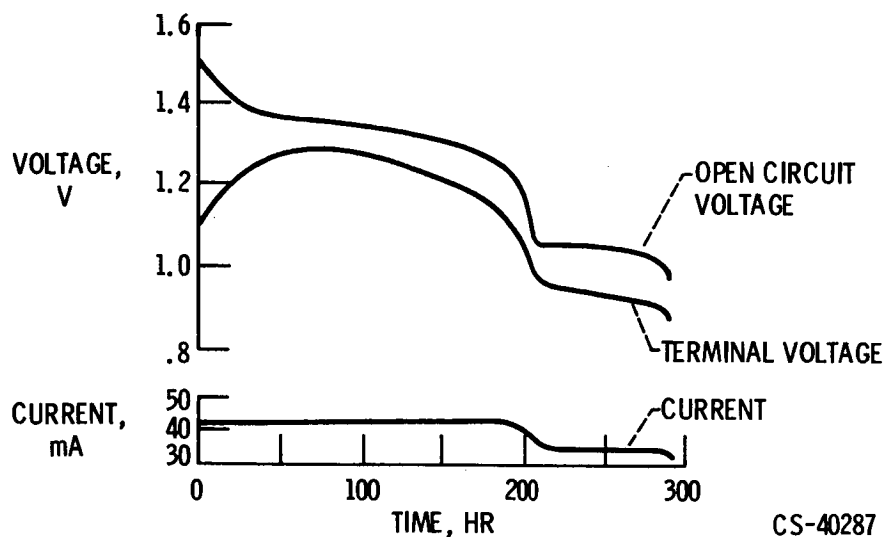


Figure II-15. - Performance of Mg-LiCl - KCl-CuO cell at 830° F.

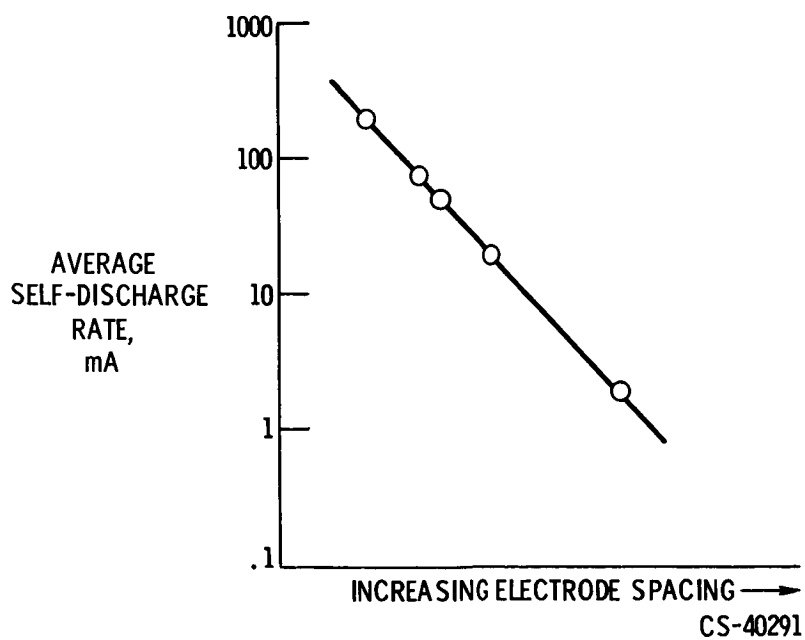


Figure II-16. - Effect of cell configuration on self-discharge rate.

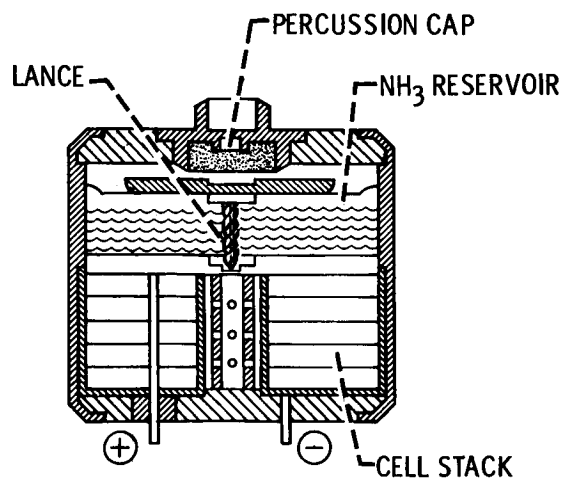


Figure II-17. - State of the art of low-temperature battery. Typical performance: service life, 36 hours; operating range, -65° to 160° F. CS-40337

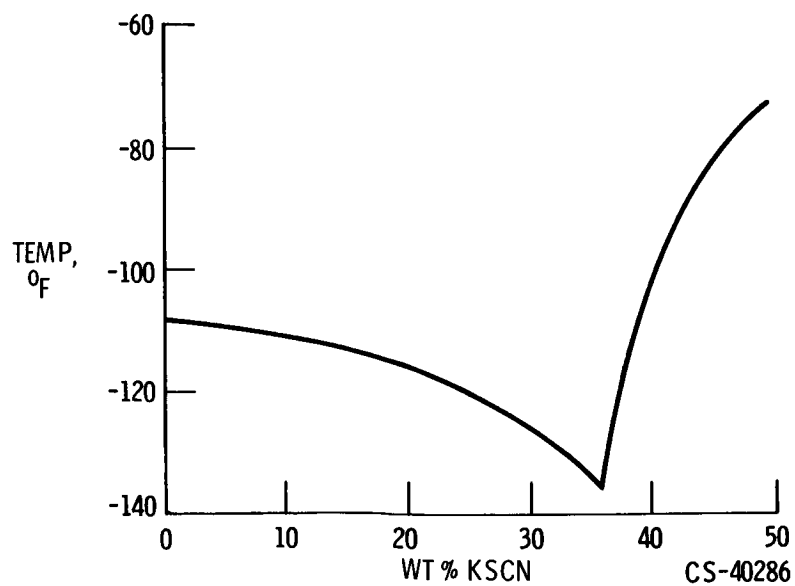


Figure II-18. - Freezing point diagram of NH_3 - KSCN. CS-40286

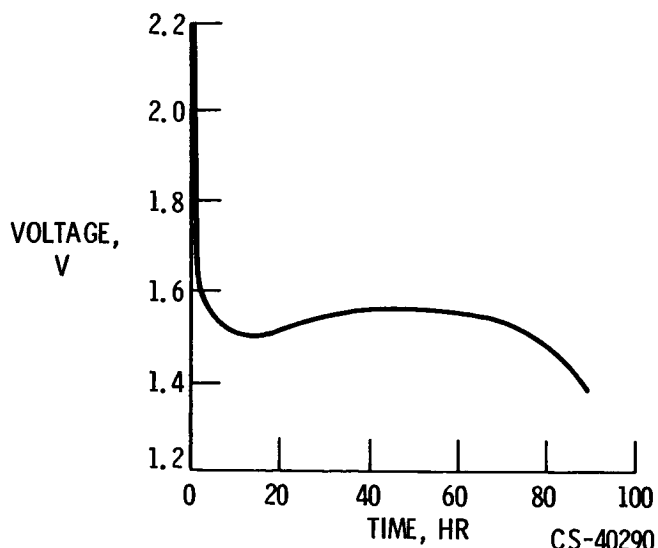


Figure II-19. - Performance of Mg-NH_3 - KSCN-S cell at -130°F .

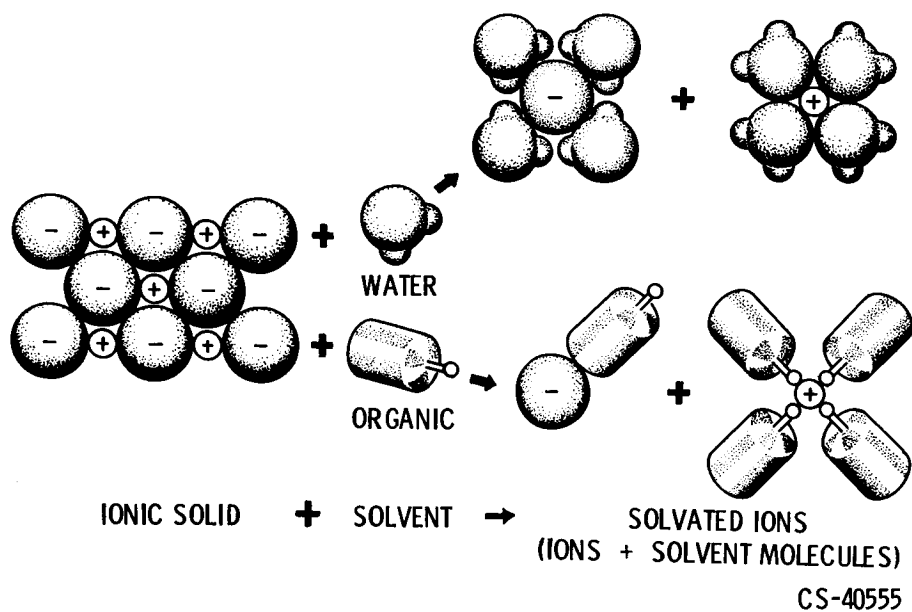
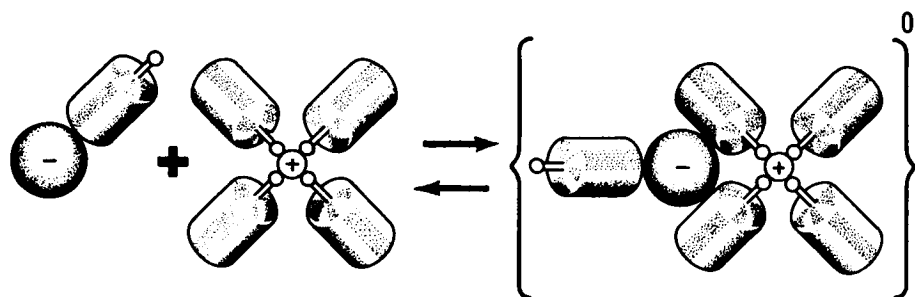


Figure II-20. - Dissolving an ionic solid.



FAVORED BY:

<u>CONDUCTING</u>	<u>LOW DIELECTRIC CONST.</u>	<u>NONCONDUCTING</u>
<u>SOLVATED IONS</u>	<u>HIGH DIELECTRIC CONST.</u>	<u>ION PAIR</u>

CS-40556

Figure II-21. - Ion pair equilibrium.

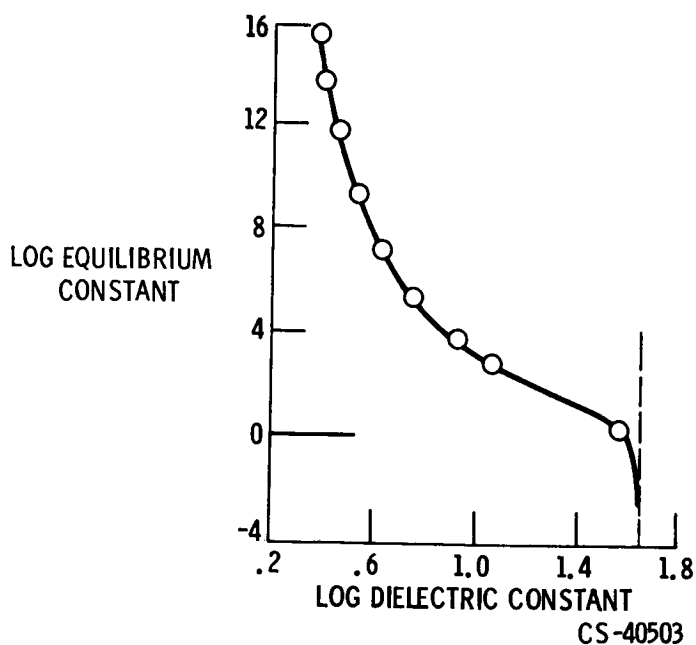


Figure II-22. - Ion pair formation as function of dielectric constant. $C^+ + A^- \rightleftharpoons [C^+A^-]^0$ (after Fuoss and Kraus).

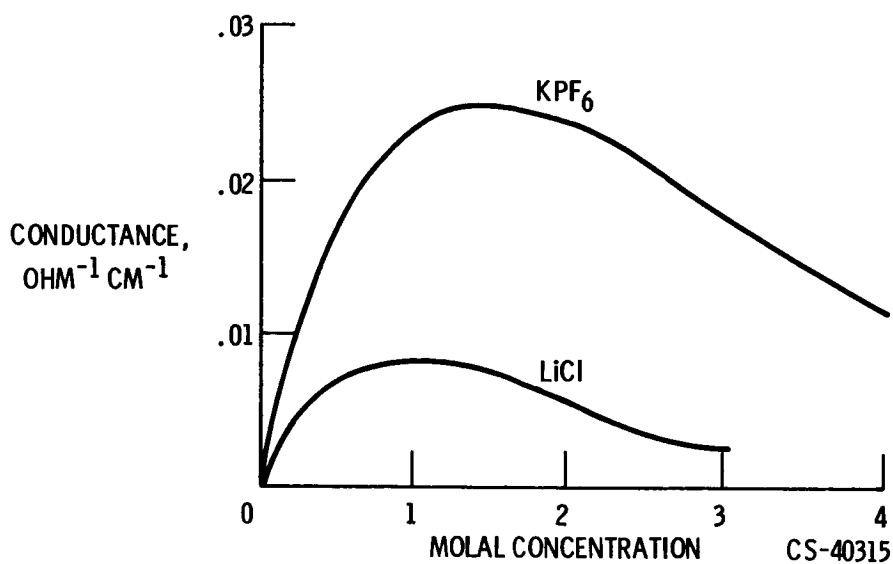


Figure II-23. - Conductance of solutions of salts in dimethyl formamide.

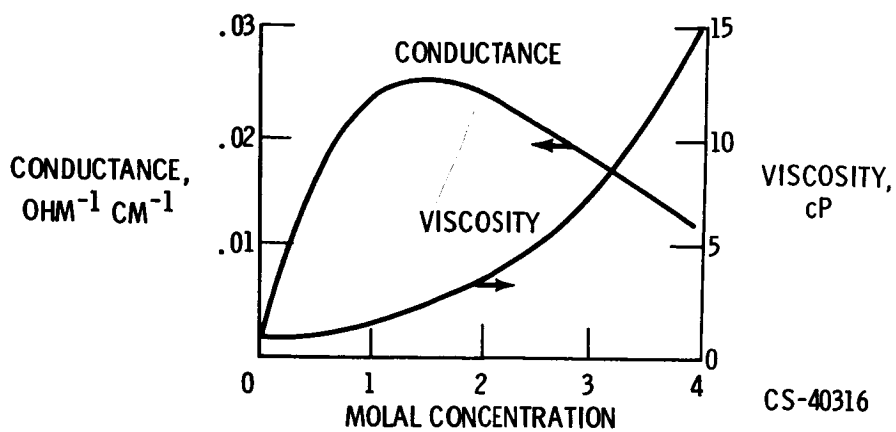


Figure II-24. - Conductance and viscosity of KPF₆ in dimethyl formamide.

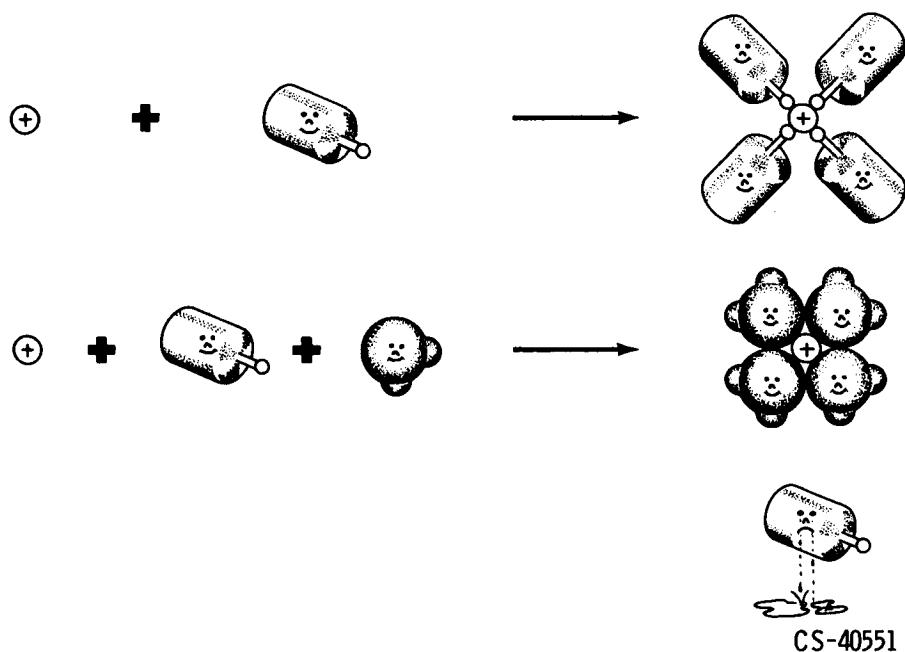


Figure II-25. - Preferential solvation.

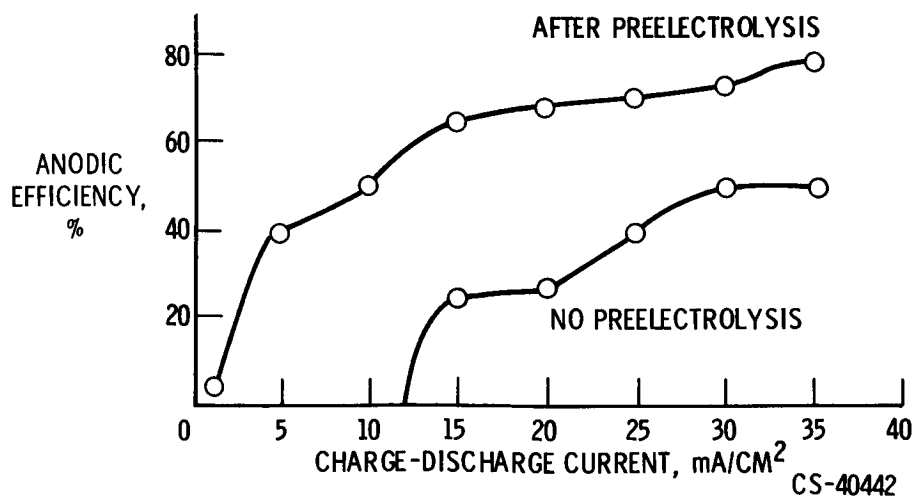


Figure II-26. - Effect of preelectrolysis on lithium anodic efficiencies. Preelectrolyzed and nonpreelectrolyzed electrolyte composed of propylene carbonate, 0.4M AlCl_3 , and 0.35M LiCl .

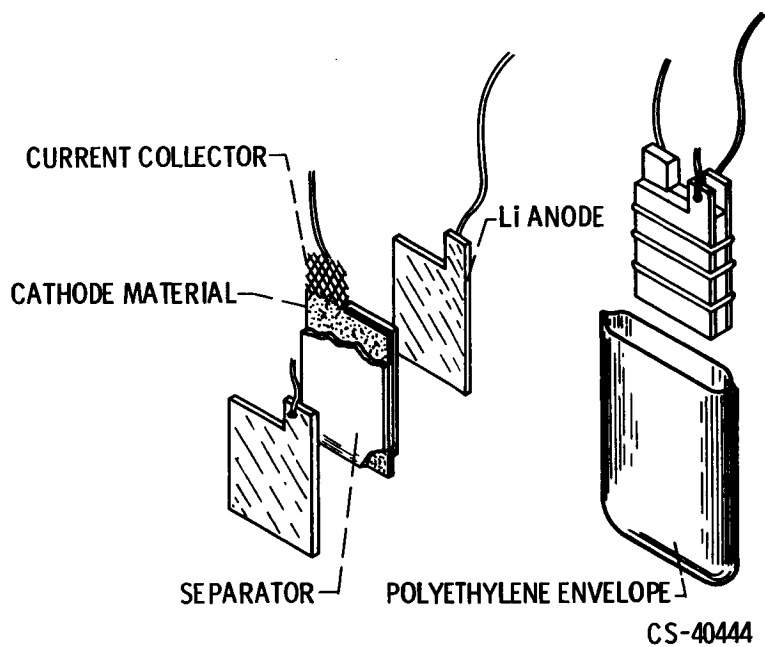


Figure II-27. - High energy density laboratory test cell.

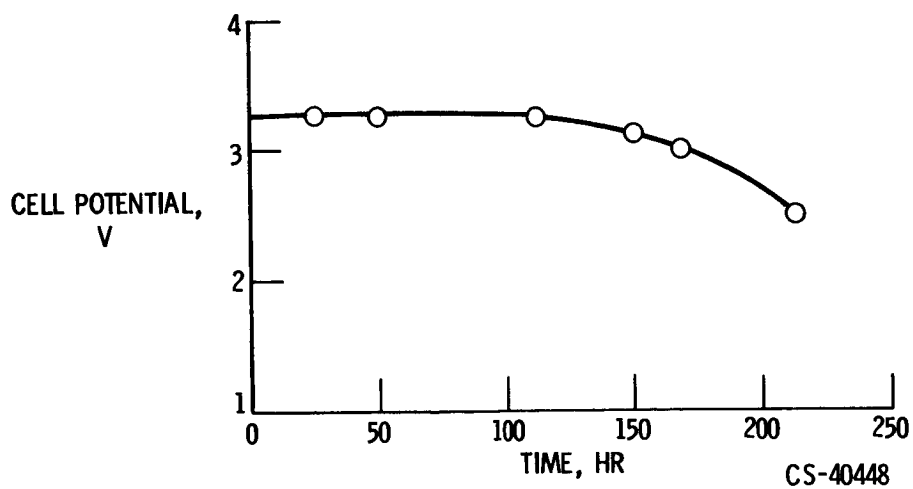


Figure II-28. - Discharge characteristics of Li-CuF₂ cell.

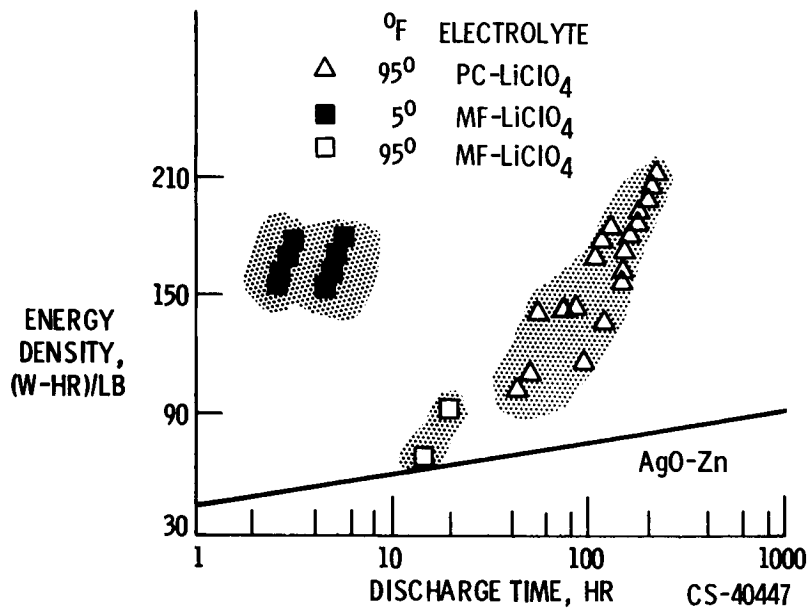


Figure II-29. - Cell performance of Li-CuF₂.

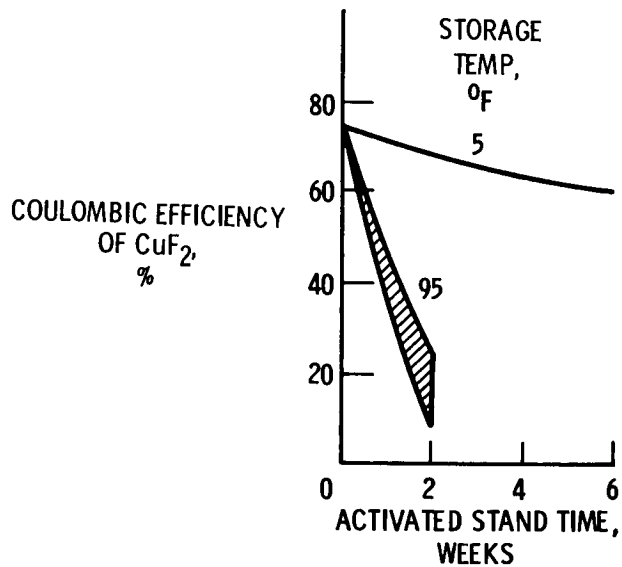


Figure II-30. - Shelf life of Li-CuF₂ cells stored at 5° and 95° F. Electrolyte, LiClO₄ - propylene carbonate.

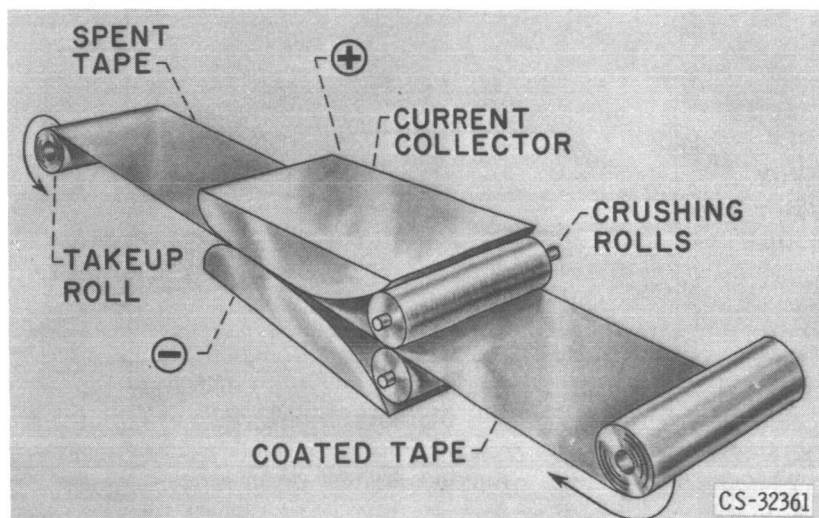


Figure II-31. - Dry tape battery concept.

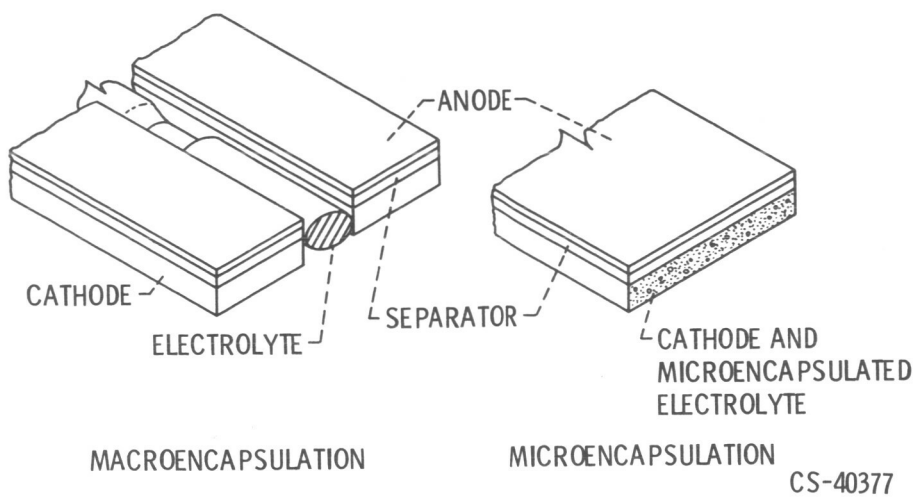


Figure II-32. - Dry tape concepts.

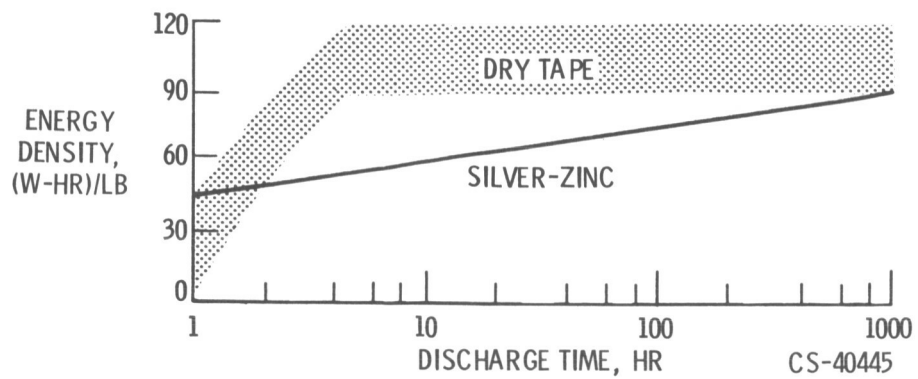


Figure II-33. - Aqueous dry tape performance.

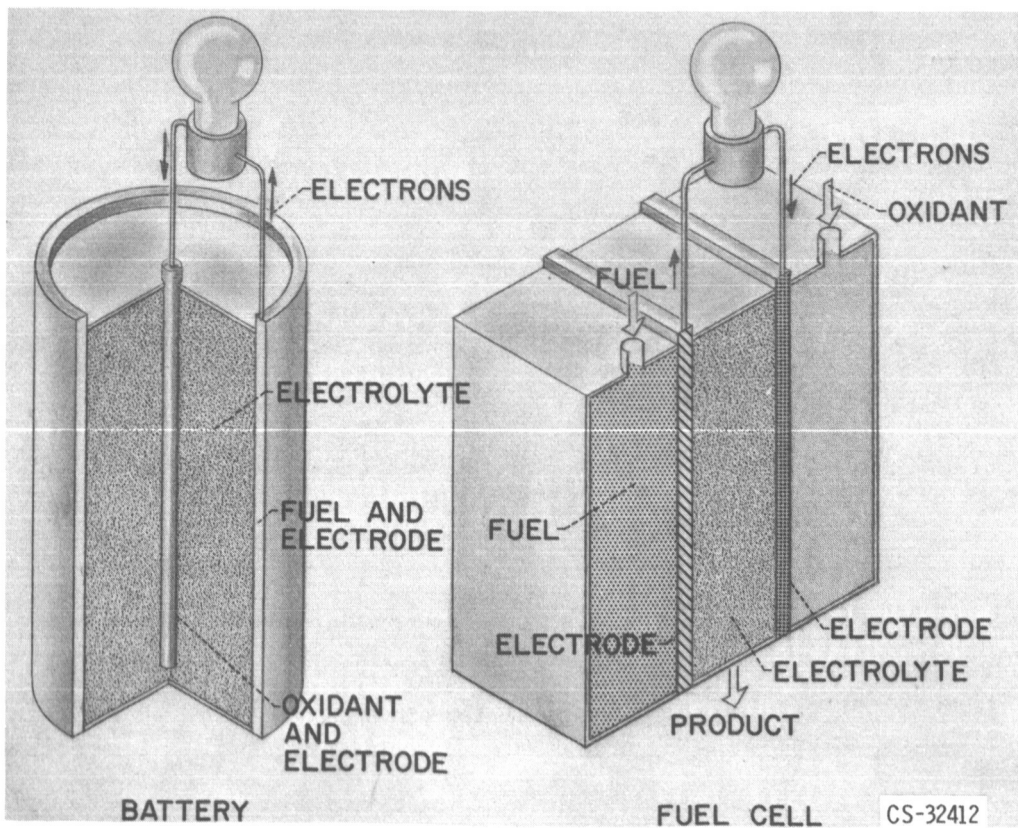


Figure II-34. - Comparison of battery and fuel cell.

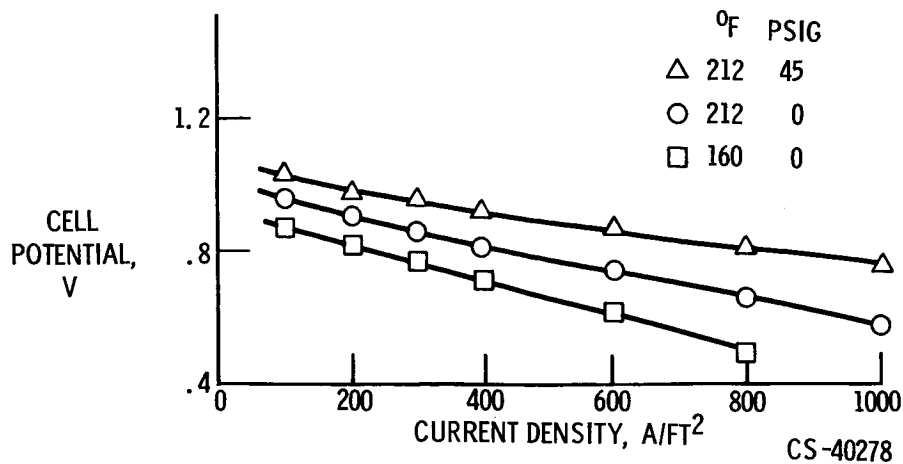


Figure II-35. - Single cell performance for cyanamid AB-40 electrode with Quintera matrix and 50 percent KOH.

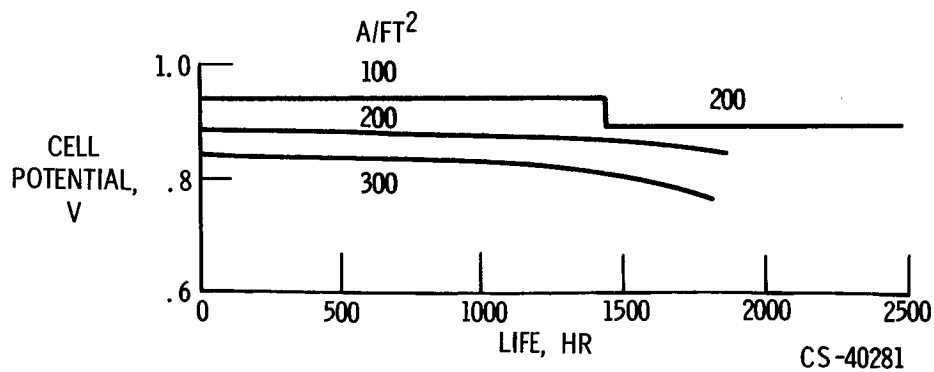
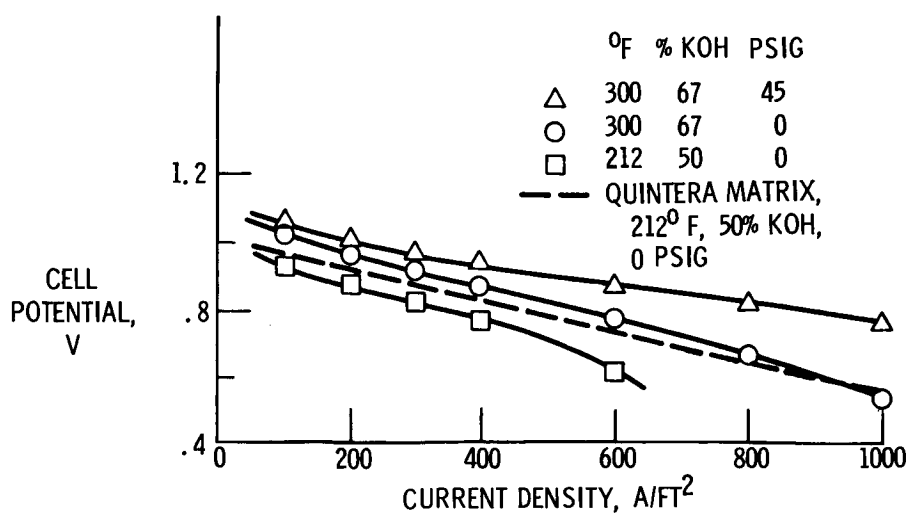
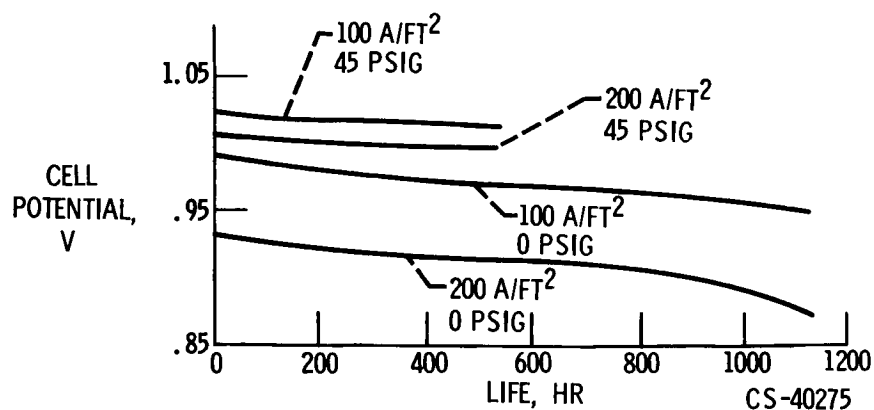


Figure II-36. - Life test for cyanamid AB-40 electrodes with Quintera matrix.
Operating conditions: 212°F, 50 percent KOH, 0 psig.



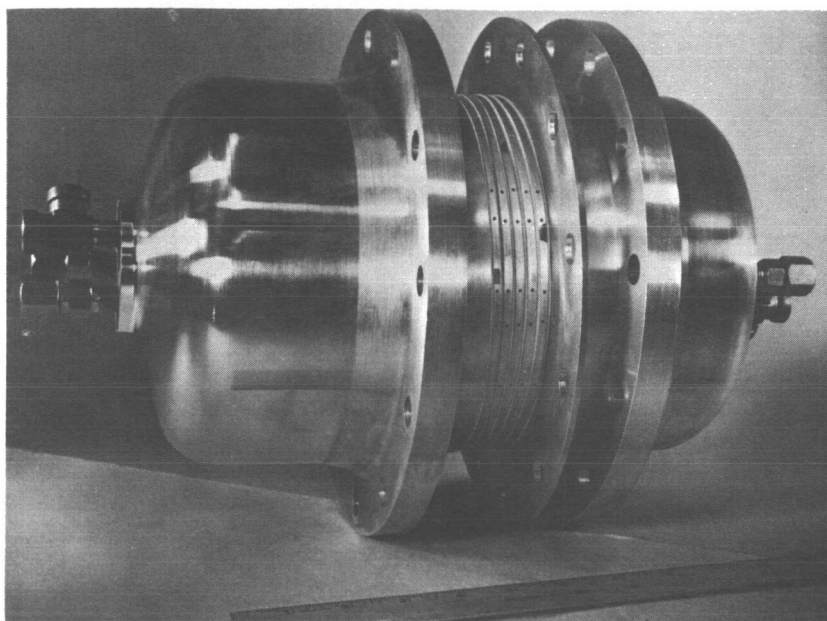
CS-40276

Figure II-37. - Single cell performance of cyanamid AB-40 electrode with ceria-Teflon matrix.



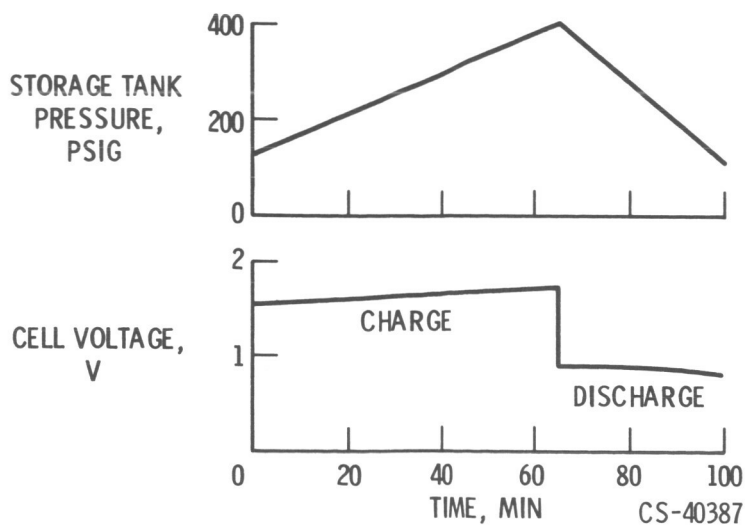
CS-40275

Figure II-38. - Life test for cyanamid AB-40 electrode with ceria-Teflon matrix. Operating conditions: 260°F; 60 percent KOH.



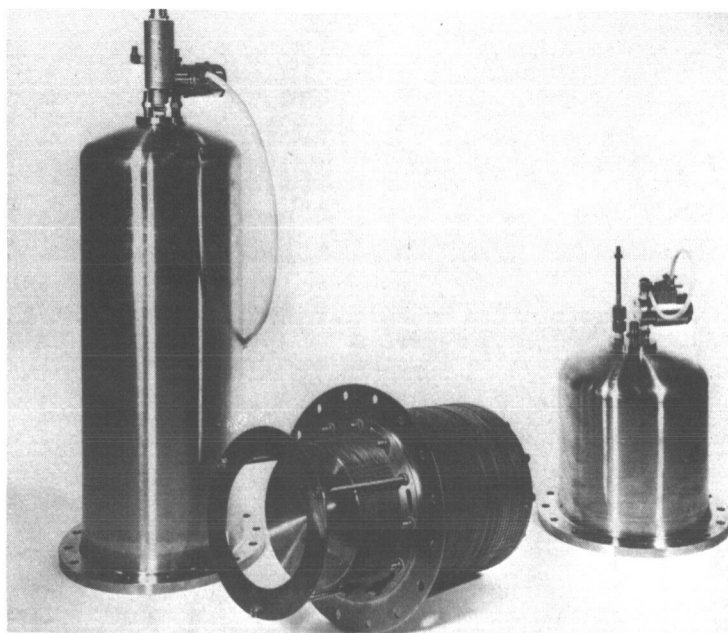
CS-40392

Figure II-39. - Six-cell regenerative hydrogen-oxygen unit.



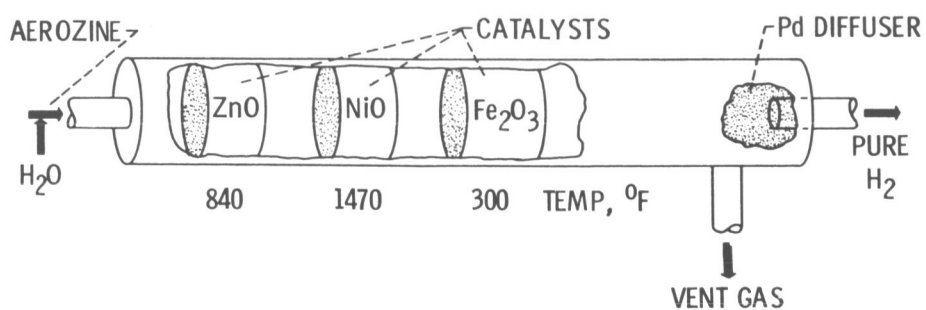
CS-40387

Figure II-40. - Performance of regenerative hydrogen-oxygen fuel cell.



CS-40393

Figure II-41. - 500-Watt regenerative hydrogen-oxygen battery.



CS-40378

Figure II-42. - Aerozine 50 reformer. Typical product composition, mole per-
cent: H_2 , 40.4 (99.5-percent yield); N_2 , 10.2; NH_3 , 0.3; H_2O , 42.9; CO , 0.4;
 CO_2 , 6.0; CH_4 , <0.1.

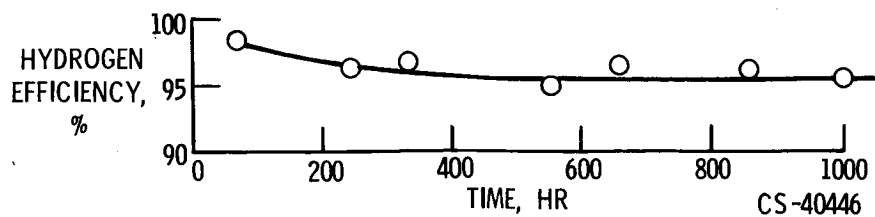
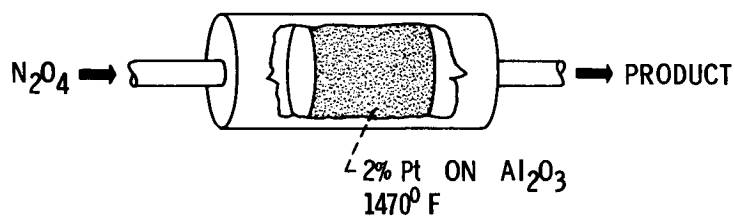


Figure II-43. - Life tests of Aerozine 50 reactors.



TYPICAL PERFORMANCE: $N_2O_4 \rightarrow N_2 + 2O_2$

TIME, HR	N_2O_4 CONVERTED, %
60	99
80	79
470	79
675	76
900	80
1000	79

CS-40376

Figure II-44. - N_2O_4 decomposition reactor.

III. CONVENTIONAL AND THIN-FILM SOLAR CELLS

Andrew E. Potter, Jr.

INTRODUCTION

At present, there appear to be four major trends in research and development on solar cells for space power:

- (1) Improved cell fabrication methods
- (2) Radiation damage resistance
- (3) Film cells
- (4) High-power arrays

Much work has been done and is being done on improved methods of silicon cell fabrication. The principal objective of this work is to lower the cost of cells; this kind of work includes the use of dendritic silicon to fabricate solar cells, the use of ion bombardment to produce the junctions in the solar cells, etc. Solar-cell power systems that must operate in the Van Allen belt are subject to damage by electron and proton radiation. Consequently, research on improving the resistance of solar cells to radiation damage is an important area. Thin-film solar cells such as those made from cadmium sulfide or cadmium telluride show promise of low-cost, lightweight solar cells that might be suitable for large solar power arrays. High-power arrays that use silicon cells are being seriously considered in powers up to 50 kilowatts. No attempt is made herein to cover all the work that is being done in these four areas. Instead, only the work of special interest to the Lewis Research Center is discussed, namely, radiation damage to solar cells, film cells, and high-power arrays.

RADIATION-DAMAGE-RESISTANT SILICON CELLS

The improvement of the resistance of silicon cells to radiation damage has been a major theme of the silicon cell research at Lewis. An effort is being made to improve the radiation-damage resistance by improving the blue response of the cells (refs. 1 and 2). The blue response is the current produced by the cell in response to the blue part of the solar spectrum. Figure III-1 shows why it is desirable to improve the blue response of the solar cell in order to improve its resistance to radiation damage. This figure shows the effect of radiation damage on the solar spectral response of a silicon cell. The current density yielded for a 0.1-micron interval of the solar spectrum is plotted against the wavelength of the solar spectrum. The effect of radiation damage is to reduce the current produced in the cell by the red wavelengths of light, 0.7 to 0.9 micron. The response of the cell to the blue part of the solar spectrum, 0.4

to 0.6 micron, is not changed. If the response of the cell to the blue part of the solar spectrum can be increased, the radiation-damage resistance of the cell will also be increased.

The reason that the blue response of the cell is only slightly affected by radiation damage can be explained by recalling some of the elementary features of a silicon solar cell. Figure III-2 shows a cross-sectional diagram of a typical n-on-p silicon solar cell. It consists of a thin layer of n-type silicon in contact with a thick layer of p-type silicon. The junction between the n- and p-type is located quite close to the surface. In most solar cells, it is about 0.5 micron deep. Each photon of sunlight produces a useful current carrier in the silicon. These current carriers diffuse through the silicon to the junction. When they cross the junction, they become excess current carriers, and thus produce a voltage. Figure III-3 shows that the depth at which light is absorbed in the silicon varies with the wavelength of the light. The absorption coefficient of red light in silicon is low, so that the percent of light absorbed changes slowly with the depth in silicon. A depth of 8 to 10 mils is required to absorb all the red light. Red light is absorbed deep in the body of the cell, far from the junction. Blue light has a high absorption coefficient and is absorbed almost completely at the surface of the cell, close to the junction.

The primary effect of radiation damage on the solar cell is to reduce the diffusion length of carriers in the crystal. The diffusion length is the distance that current carriers produced by light can diffuse before they are lost. The current carriers produced by red light must diffuse a long distance to the junction, so that the yield of these carriers is affected considerably by radiation damage. The current carriers produced close to the junction by blue light must travel only a short distance to reach the junction and, consequently, are affected little by radiation damage.

It is interesting to see what gains are theoretically possible in improving the blue response. In figure III-4 the actual response of a commercial silicon solar cell is compared with the theoretical response, which is calculated by assuming a 50-percent quantum efficiency. The actual response is seen to be close to the theoretical maximum response in the red part of the spectrum but falls far short of the maximum possible response in the blue part of the spectrum. Evidently, there is the possibility of a real gain in the response to the blue part of the spectrum; consequently, there can be a real gain in the radiation-damage resistance.

What can be done to improve the blue response of the cell? One thing is to bring the junction closer to the surface of the cell. Since the blue light is absorbed close to the surface, the closer the junction is to the surface, the more current that can be collected from blue light. There is considerable difficulty in moving the junction very close to the surface of the cell. When ordinary boron-doped crystals of silicon are used to make shallow-junction cells, the efficiencies of the cells are below acceptable values for space power systems. Figure III-5 shows that, when aluminum-doped oxygen-free silicon is used to make the cells, it is possible to make good junctions even though they are very shallow. The current output of the cell is the same whether boron-doped or aluminum-doped material is used. However, the aluminum-doped material yields a much superior junction characteristic and as a result, gives a higher open-circuit voltage, and an efficiency of 11.5 percent in space sunlight. The reason that aluminum-doped silicon is superior in this application is probably that aluminum introduces less strain into the silicon crystal lattice than boron does. Oxygen acts as an electrical damage center within the junction, and its removal is therefore beneficial. As a result, the crystal of oxygen-free

aluminum-doped silicon contains fewer defects and imperfections than a boron-doped silicon crystal. This means that a better quality junction can be made in the aluminum-doped material.

In addition to requiring the use of oxygen-free aluminum-doped material, shallow junction cells have other special construction requirements. One of these is the alloy contact to the cell. The conventional titanium-silver contact, which is used commercially to make contact to the cells, contains a material that diffuses into the shallow junction and poisons it. As a result, it was necessary to develop a new contact alloy in which cerium was used in place of titanium. Cerium does not contain harmful impurities, so that a silver-cerium alloy can be used to make contact with the shallow junction cells with considerable success. In fact, the silver-cerium contact has proved to be superior to the silver-titanium contact in terms of strength.

Solar cells require cover glasses in space power supplies for two reasons. One reason is to protect the cell against radiation damage, and another reason is to increase the infrared emissivity of the cell in order to lower its operating temperature in space. The cement used to attach the cover glass was undesirable for use in space because it degrades when illuminated in space sunlight, and then absorbs blue light. It was necessary, therefore, to devise a means of attaching the cover glass to the shallow junction cell without the use of cement, as shown in figure III-6. The cover glass has been provided with an evaporated silver-cerium pattern that exactly matches the top contact pattern on the cell. The cover glass and the cell are then clamped together, placed in a furnace, and heated. The solder on top of the contact pattern on the cell wets the silver pattern on the cover glass and bonds it firmly in place. After furnace brazing, the cover glass is firmly bonded to the cell without the use of light-absorbing cement.

Also shown in figure III-6 is one other effect of using a very shallow junction and that is the large number of grid fingers on the top contact. Ten grid fingers are used to collect current from the top of the cell, rather than the five or six which are commonly used. Having a shallow junction raises the electrical resistance of the surface layer of the cell. To avoid electrical losses due to this extra resistance, a greater number of grid fingers than usual must be applied.

The gain in blue response from the shallow junction is shown in figure III-7. Here, the response of a commercial type cell with the junction depth of about 0.5 micron is compared with the response of a cell with a junction depth of about 0.25 micron. This cell, of course, is an aluminum-doped cell with silver-cerium contacts. The improvement in the blue response of the shallow-junction cell is evident. However, there are still more gains to be made in the response, as can be seen by observing the theoretical maximum response, also shown in this figure. There is a way of improving the blue response still further by improving the anti-reflection coating of the cell. A two-layer antireflection coating is excellent for reducing reflection in the blue part of the spectrum. This coating consists of a layer of magnesium fluoride on the usual silicon monoxide antireflection layer. With this coating, reflection losses in the 0.4- to 0.5-micron region can be reduced. Thus, there is a considerable gain in the blue response of the cell (fig. III-8). The gain in blue response from the antireflection coating is about equal to the gain in blue response produced by using a shallow junction.

The result of these efforts in terms of radiation-damage resistance is shown in table III-1. Here a conventional cell is compared with the best Lewis cell that includes all the improvements

discussed previously. The efficiency of the conventional cell and of the Lewis cell is about the same. The blue response has been improved, but this improvement has been accompanied by some loss in total active surface area of the cell, with the result that the efficiencies are about the same. However, the resistance to radiation damage of the high-blue-response cell is about 3 times that of the conventional 10 ohm-centimeter n-on-p cell. This represents a considerable improvement in radiation-damage resistance. Use of this cell in place of a conventional cell will allow either a reduction of the array weight by use of thinner cover glasses, or an extension of array lifetime with the same thickness of cover glass.

THIN-FILM SOLAR CELLS

A thin-film solar cell can be defined as a solar cell made from a thin polycrystalline semiconductor film rather than from a single crystal of semiconductor, as is the silicon solar cell. Figure III-9 shows a cross section of a typical film cell. The cell shown happens to be a cadmium sulfide film cell, but a basic similarity exists for all film cells. The cell consists of a layer of polycrystalline semiconductor, cadmium sulfide here, which has been deposited on an electrically conducting substrate. On top of the polycrystalline semiconductor, there is barrier layer which is similar to the surface p- or n-layer in a silicon cell. In this case, the barrier layer is copper sulfide. The p-n junction in this solar cell is formed between the two materials, copper sulfide and cadmium sulfide. On top of the barrier layer a metal grid is placed to collect the current from the barrier layer. The cell is usually covered with a layer of transparent plastic that performs the same function that the quartz cover glass does for the conventional silicon cell.

Table III-2 shows a summary of the film cell research being done at present. RCA (ref. 3) has been working on gallium arsenide film cells. In these film cells, the semiconductor layer is gallium arsenide and the barrier layer is cupric selenide, or platinum. They have achieved efficiencies of 3 to 4 percent, but only in small areas - 1 centimeter square or so. Harshaw has been working on cadmium sulfide thin-film cells for many years (ref. 4). Their efficiencies in production are 3 to 4 percent in areas of 50 square centimeters. The Clevite Company (refs. 5 and 6) has also been working on cadmium sulfide cells. They have achieved production efficiencies of 4 to 5 percent in 50-square-centimeter cells. Their cells are not sensitive to moisture, remaining unchanged for long periods of time in moist atmospheres. Lewis has also been working on cadmium sulfide cells and has achieved efficiencies of 4 to 5 percent, but in small areas. The work here is aimed primarily at understanding the mechanism of the cell. The General Electric Company (ref. 7) has been working on cadmium telluride cells made from films of cadmium telluride with a barrier layer of copper telluride. They have achieved efficiencies of 4 to 5 percent, and occasionally somewhat more. These cells are reported to be insensitive to moisture but do appear to be damaged by exposure to moderate temperatures. The most advanced of the thin-film solar cells appears to be the cadmium sulfide cell, so the status of this cell is discussed in considerable detail.

Radiation damage is a serious problem for silicon cells, but this is not the case for cadmium sulfide cells. Data for radiation damage to cadmium sulfide film cells is shown in figure III-10 (ref. 8). The relative maximum power for film cells is shown as a function of radiation dose.

For electrons with energies of 0.6 to 2.5 million electron volts, there is not measurable damage to the cells up to doses of 10^{17} electrons per square centimeter. Proton damage can be detected but it is small and amounts to only 5 to 10 percent with doses of 10^{14} to 10^{15} protons per square centimeter. These are very large doses of electrons and protons. The largest doses shown here correspond to times in the Van Allen belt of 10 or more years. This means that the cell is extremely resistant to radiation damage and does not require the heavy cover-glass shielding required for conventional silicon cells.

The film cells do require a covering or encapsulation to protect their surfaces from abrasion and moisture, as well as to increase their infrared emissivity. Coverings are discussed in more detail subsequently, however the most successful coverings have been plastic films. The bombardments previously described were performed by using plastic-encapsulated cells. Kapton plastic encapsulation was not noticeably affected by the largest radiation doses given. Mylar plastic encapsulation darkened very slightly and became brittle after the maximum doses quoted previously. Delamination of the plastic did not occur for either plastic encapsulant.

It is interesting to look at the weight of cadmium sulfide film cells. The layers of cadmium sulfide, copper sulfide, plastic, etc. can be made very thin, so that the cells can be made very light. In figure III-11, cell weight is plotted in terms of pounds per square foot of cell against time in years. Several years ago, cell weights of 0.2 to 0.3 pound per square foot were observed. At this time, the cells were formed by depositing cadmium sulfide on 2-mil-thick molybdenum substrates. Most of the molybdenum substrate could be etched away to remove much of the unnecessary metal and reduce the weight to about 0.1 pound per square foot. More recently, Kapton plastic has been used as the substrate. This material allows further reduction in cell weight to the vicinity of 0.06 pound per square foot or about 1 ounce per square foot. It is interesting to compare these cell weights with the weight of silicon cells. The thinnest state-of-the-art silicon-solar-cell - cover-glass combination weighs about 0.17 pound per square foot, so that cadmium sulfide cells are presently about 3 times lighter than the lightest silicon cell.

While cadmium sulfide cells are superior to silicon cells with respect to weight per unit area and their resistance to radiation damage, silicon has a higher conversion efficiency. Figure III-12 shows the mean production efficiency that was observed for 3- by 3-inch cadmium sulfide cells shown as a function of time in years. The early film cells were very inefficient. From time to time during the past few years, the Clevite Company has achieved mean production line efficiencies of 5 percent at air mass one and 25°C .

Two hundred cells were delivered to NASA by Clevite in the period from July to September 1966. These cells were half the pilot production of plastic-substrate cells, with every other cell in the exact order of fabrication delivered to Lewis. Of this lot of cells, the average efficiency was 4.9 percent, with 68.5 percent of the cells having efficiencies from 4.5 to 5.5 percent, 8.5 percent with efficiencies from 5.5 to 6.0 percent, 20.5 percent from 4.0 to 5.0 percent, 1.5 percent from 3.5 to 4.0 percent, and 1 percent from 6.0 to 6.5 percent. While the highest cell efficiency in this period was less than 6.5 percent, several 50-square-centimeter cells showing efficiencies up to about 8 percent have been reported by Clevite (ref. 6). This fact is indicated in figure III-12 by a point at 8 percent. Cells with efficiencies in excess of 6.5 percent have not been stable, dropping in a few days to efficiency values near 6 percent.

At Lewis, a small 4-square-centimeter cell was made with an efficiency of 7 percent. In

6 months of desiccated storage, the efficiency had dropped to 6 percent. It should be mentioned that cell efficiencies reported at Lewis are based on airplane-flown standard cadmium sulfide cells.

At present, an efficiency of 5 percent at air mass one for the 3- by 3-inch size plastic-substrate cell is the value that is consistently available from a pilot production line. Further improvements in cell technology may eventually bring average efficiencies into the 6- to 6.5-percent range, where now only about 1 percent of the plastic-substrate cells fall.

It is interesting to make a point-by-point comparison of the cadmium sulfide cell with the silicon cell. In table III-3, the largest and lightest state-of-the-art cells are compared. This comparison considers only the cells and does not include any other parts of the solar array. It would be desirable to compare entire arrays of cadmium sulfide and silicon cells, including the supports and extension mechanisms for the arrays. In the author's opinion, however, insufficient information is available about the kinds of supports and extension mechanisms needed for an array of cadmium sulfide cells to make a valid comparison at this time. It appears naive and premature to assume that these factors should be identical for cadmium sulfide and silicon cells because of the greater flexibility and mechanical strength of the film cell, which should allow different methods of array construction.

When the weights per unit area are compared, the cadmium sulfide cell is about three times lighter than the silicon cell. As a result, in spite of the low efficiency of the cadmium sulfide cell, the weight per unit power of cadmium sulfide is less than the weight per unit power for silicon; 14 pounds per kilowatt for cadmium sulfide against 15 pounds per kilowatt for silicon. This difference is small enough so that it is really not significant in a discussion of this kind. It simply indicates that the weight per unit power is comparable for the two cells. The area per unit power shows clearly the low efficiency of cadmium sulfide relative to silicon; 220 square feet per kilowatt are required against 87 square feet per kilowatt for silicon. Another interesting feature of cadmium sulfide is the number of cells required to generate unit power. Cadmium sulfide requires 3400 cells to generate 1 kilowatt of power, while silicon requires 20 000 cells to generate 1 kilowatt of power. Consequently, the labor costs involved in assembling an array of cadmium cells will be much less than the cost to assemble an array of silicon cells.

Another advantage of the cadmium sulfide film cells is flexibility. A cadmium sulfide film cell array can be easily rolled to occupy a very small volume. Another desirable feature of the cadmium sulfide cell is its probable low cost of production. For example, the current price of cadmium sulfide cells is such that the cost of power is about \$125 per watt. This price is substantially the same price as power from silicon cells. However, this is the price for laboratory produced cells. In production, it is possible that the cost might drop to \$10 to \$50 per watt in units of 10 to 100 kilowatts production per year. If the production rate were increased to several million watts per year, the cost could probably be reduced to about \$1 per watt (ref. 6). With these advantages in mind, one may wonder why a number of large cadmium sulfide film cell arrays have not been constructed. The answer to this is that all the problems have not been solved that remain before the cadmium sulfide film cell can be used by the spacecraft power engineer.

The primary remaining problem of cadmium sulfide is that of stability. The major areas

where stability is a problem for cadmium sulfide cells are as follows:

- (1) Storage degradation
- (2) Humidity damage
- (3) Thermal cycling failure
- (4) Ultraviolet-light damage

In some cases, the cells degrade during storage. This problem seems to be under control except for high-efficiency cells. The damage to the cell by moisture has been, until recently, a severe problem. The cadmium sulfide cell is constructed of many different materials, and the thermal stresses that appear in the cell as a result of temperature changes as the cell goes in and out of sunlight can damage it considerably. Ultraviolet light causes damage to the plastic used to cover the cadmium sulfide.

The two main factors that control the stability of cadmium sulfide cells are the gridding of the cell and the encapsulant of the cell. The parts of the cell to which these refer are shown in figure III-9. The gridding of the cell refers to the metal screen grid electrode used to collect current from the barrier layer or surface of the cell. The encapsulant refers to the layer over the grid that serves to protect the surface of the cell from moisture, mechanical damage, ultraviolet light, and low-energy electrons.

The various techniques used for applying current-collecting grids to cadmium sulfide cells are shown in figure III-13. The oldest and simplest method uses a screen grid which is laid on the surface of the cell and is held in contact with the cell by pressure applied during lamination of the plastic. More recently, the screen grid has been held in place by a gold-filled epoxy cement. Grids can also be prepared directly on the surface of the cell by electroplating. In still another technique, the grid is bonded to the surface of the cell by heat and pressure to produce a compression-bonded screen grid.

The effect of these various types of grid on the stability of cadmium sulfide cells is shown in table III-4. Here are shown the various grid types and how they compare in stability against thermal cycling, moisture, and storage. The original pressure grid with a molybdenum substrate is poor in thermal cycling. The pressure grid with a plastic substrate seems to be quite good in its resistance to thermal cycling, but it is poor in its resistance to moisture. When the grid is cemented in place with a gold-filled epoxy cement, there is good resistance to moisture but problems with thermal cycling. The electroplated grid is very resistant to damage by thermal cycling, but it does not provide much resistance against moisture. The compression bonded grid is resistant to thermal cycling, but not much good in other respects.

The second factor that affects the stability of cells is the method used to encapsulate the cells. Three principal methods used for encapsulating cells are shown in figure III-14. The oldest method is the use of plastic and nylon cement. In this case, the grid is covered with a very thin layer of nylon plastic, which is covered by a thicker layer of another plastic that might be Mylar or Kapton. The whole assembly is laminated under heat and pressure. The nylon melts and flows, cementing the plastic cover to the grid and cadmium sulfide. In a variation, epoxy cement is used in place of nylon plastic. In this case, the heat and pressure of the lamination process cures the epoxy. The third type of encapsulation requires a grid that is electroplated or compression bonded. This coating, a transparent inorganic coating, does not provide any mechanical strength toward holding the grid in place.

Compounds such as silicon monoxide, aluminum oxide, and magnesium fluoride have been used for these transparent inorganic coatings. These encapsulants are compared in table III-5 with respect to their effects on cell stability. The Mylar-nylon encapsulant is poor against moisture. It is very poor in its resistance to ultraviolet damage, because the Mylar becomes brittle when exposed to ultraviolet light (ref. 9). If nylon is replaced by epoxy, the moisture stability is good, but the ultraviolet stability is still poor. The ultraviolet problem can be cured by using Kapton plastic film (ref. 9). This produces a cell that is good in all respects, except that the use of Kapton is accompanied by a 20-percent penalty in efficiency due to light absorption by the Kapton. This problem can be circumvented somewhat by using Mylar and coating it with a thin layer of Kapton. In a sense, Kapton acts as a sunburn cream and reduces the damage to the Mylar by ultraviolet light. After approximately 1 year of exposure to simulated space sunlight in a vacuum of 10^{-8} torr, Kapton coated Mylar cells were still flexible and undarkened. Still, a 5-percent efficiency loss is incurred as a result of light absorption in the Kapton layer. This is a good coating because it is resistant to moisture damage, stable in storage, and appears to resist ultraviolet damage. The inorganic coatings have been disappointing, primarily because they do not resist moisture probably because of small cracks in the film.

In summary, it appears that the problem of stability of these cells in use has not been solved. However, a solution seems imminent and in the author's opinion, a year or two more of work should yield stable space-worthy cells with efficiencies of 5 percent at air mass one. It is conceivable that the cadmium sulfide film cell might be useful for building large high-power arrays because of its expected low cost in production, its flexibility, and its lightweight.

HIGH-POWER ARRAYS

Presently, there are serious efforts to design, and eventually to construct solar power arrays that yield power up to 50 kilowatts (ref. 10). These high-power arrays use silicon cells. Silicon cells, of course, have the advantage that they are efficient, stable, and proven in the space environment. High-power solar arrays have definite disadvantages. First, there is their cost. They will be very expensive. The cost of a 50-kilowatt array is estimated to be \$20 million. Second, the arrays cannot be built for much more than 0.1 gravity, so that any propulsive maneuvers of a spacecraft equipped with a high-power array must be very slight. The principal advantages of high-power solar arrays are the facts that no major development problems must be solved for construction of such arrays, and the lifetime and reliability of solar arrays have been proved to be very good. A summary of some of the high-power solar arrays that are currently under active study is shown in table III-6. The largest of these is a 50-kilowatt array that has an area of 4500 square feet and uses very thin silicon cells as well as a number of lightweight construction features. The final array is expected to yield a specific weight of 50 pounds per kilowatt. This array is a folding semirigid structure in which the cells are mounted on rigid panels. A 1/4 segment of this array is under construction. Another large array is being studied by RCA. This array will yield approximately 20 kilowatts of power, and again it is a folding semirigid construction. Some smaller experimental arrays are also listed in the table because

they use a flexible rollup style of construction, rather than a folding semirigid style. The flexible rollup arrays can be easily expanded to larger powers, or adapted for thin-film solar cells.

CONCLUDING REMARKS

Solar cells have provided electric power on almost every satellite launched since the beginning of the space program. It appears that this state of affairs will continue for several years especially with the development of high-power arrays and high-radiation-damage-resistance cells. It is possible that, in the future, the use of film solar cells can reduce the cost of large high-power arrays to a relatively low price, accompanied by the disadvantage of increased array area. Insufficient information is now available to determine whether or not large film cell arrays can be made lighter than large silicon arrays.

REFERENCES

1. Mandelkorn, Joseph: Improved n on p Silicon Solar Cells. Paper Presented at the 19th Annual Power Source Conference, Atlantic City. May 18-20, 1965.
2. Mandelkorn, Joseph: A New Glass Covered Silicon Solar Cell for Space Application. Paper Presented at the 20th Annual Power Source Conference, Atlantic City, May 24-26, 1966.
3. Ellis, S. G.; Vohl, P.; Perkins, D. M.; Addiss, R. R.; and Hui, W.: Ga As Thin Film Solar Cells. Thin Film Solar Cells and Radiation Damage. Vol. II of the Proceedings of the Fifth Photovoltaic Specialist Conference, October 19, 1965. Rep. No. PIC-SOL-209/6.1 (NASA CR-70169), Pennsylvania Univ., Jan. 1966.
4. Griffin, T. A.; Krus, D. J.; and Schaefer, J. A.: Research and Development in CdS Photovoltaic Film Cells. Final Rep. (NASA CR-54481), Harshaw Chem. Co., Aug. 1965.
5. Shirland, F. A.; and Hietenan, J. R.: The Thin Film Cds Solar Cell. Thin Film Solar Cells and Radiation Damage. Vol. II of the Proceedings of the Fifth Photovoltaic Specialist Conference, October 19, 1965. Rep. No. PIC-SOL-209/6.1 (NASA CR-70169), Pennsylvania Univ., Jan. 1966.
6. Shirland, F. A.; and Augustine, F.: Thin Film Plastic Substrate CdS Solar Cells. Thin Film Solar Cells and Radiation Damage. Vol. II of the Proceedings of the Fifth Photovoltaic Specialist Conference, October 19, 1965. Rep. No. PIC-SOL-209/6.1 (NASA CR-70169), Pennsylvania Univ., Jan. 1966.
7. Massie, L. D.; and Wise, J. F.: Progress on Cadmium Telluride Thin Film Solar Cells. Thin Film Solar Cells and Radiation Damage. Vol. II of the Proceedings of the Fifth Photovoltaic Specialist Conference, October 19, 1965. Rep. No. PIC-SOL-209/6.1 (NASA CR-70169), Pennsylvania Univ., Jan. 1966.
8. Brandhorst, Henry W., Jr.; and Hart, Russell E., Jr.: Radiation Damage to Cadmium Sulfide Solar Cells. NASA TN D-2932, 1965.

9. Anagnostou, Evelyn: Effect of Ultraviolet Irradiation on Selected Plastic Films in Vacuum. NASA TM X-1124, 1965.
10. Ratcheson, W. I.: A Fifty Kilowatt, Twenty Watt Per Pound Solar Cell Array Feasibility Study. Solar Power System Consideration. Vol. III of the Proceedings of the Fifth Photovoltaic Specialists Conference, October 20, 1965. Rep. No. PIC-SOL-209/6.2 (NASA CR-70170), Pennsylvania Univ., Jan. 1966.

TABLE III-1. - RADIATION-DAMAGE RESISTANCE

Cell	Efficiency, percent	Relative radiation- damage resistance
Best conventional 10 ohm-cm	10 to 12	1
Best Lewis	10 to 12	3

TABLE III-2. - FILM CELL RESEARCH

Organization	Material	Approximate efficiency, percent	Remarks
RCA	Gallium arsenide	3 to 4	Small area
Harshaw	Cadmium sulfide	3 to 4	Moisture sensitive
Clevite	Cadmium sulfide	4 to 5	Moisture stable
NASA Lewis	Cadmium sulfide	4 to 5	Small area
GE	Cadmium telluride	4 to 5	Heat sensitive

TABLE III-3. - COMPARISON OF CADMIUM

SULFIDE CELL WITH SILICON CELL

[Temperature, 50° C; space sunlight at 1 AU]

Cell	Weight per unit area, lb/ft ²	Weight per unit power, lb/kW	Area per unit power, ft ² /kW	Cells per unit power, cells/kW
Cadmium sulfide ^a	0.065	14	220	3 400
Silicon ^b	0.168	15	87	20 000

^aPlastic substrate, plastic covered; 50-cm² cell; 5 percent efficiency at air mass one and 25° C.

^b8-mil-thick 4-cm² cell with 4-mil cover glass; 10.5 efficiency at air mass zero and 25° C.

TABLE III-4. - EFFECT OF GRID TYPE STABILITY

ON CADMIUM SULFIDE CELLS

Grid	Stability against-		
	Thermal cycling	Moisture	Storage
Pressure (molybdenum substrate)	Poor	Poor	Fair
Pressure (plastic substrate)	Good	Poor	Fair
Cemented (plastic substrate)	Poor	Good	Good
Electroplated (molybdenum substrate)	Good	Poor	Good
Compression bonded (molybdenum substrate)	Good	Poor	-----

TABLE III-5. - EFFECT OF ENCAPSULANT ON
STABILITY OF CADMIUM SULFIDE CELLS

Encapsulant	Stability against-		
	Moisture	Storage	Ultraviolet light
Mylar-nylon	Poor	Fair	Poor
Mylar-epoxy	Good	Good	Poor
Kapton-epoxy ^a	Good	Good	Good
Kapton-coated Mylar-epoxy ^b	Good	Good	Good
Inorganic (SiO, Al ₂ O ₃ , MgF ₂)	Poor	Fair (?)	Good

^aEfficiency loss due to light absorption by Kapton,
20 percent.

^bEfficiency loss due to light absorption by Kapton,
5 percent.

TABLE III-6. - DEPLOYABLE HIGH-POWER SOLAR ARRAYS
CURRENTLY UNDER ACTIVE STUDY

Nominal power, kW	Nominal area, ft ²	Silicon cell type	Company	Construction style
50	5000	0.008-in. thick	Boeing	Folding, semirigid
20	2000	Conventional	RCA	Folding, semirigid
0.5	50	Dendritic Conventional	Hughes Ryan	Rollup, flexible Rollup, flexible
0.2	20	Conventional	Fairchild-Hiller	Rollup, flexible

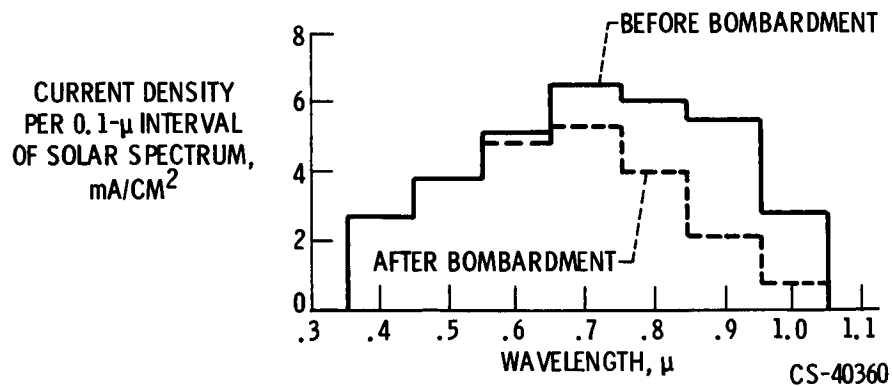


Figure III-1. - Effect of radiation damage on solar spectral response. Radiation dose, 10^{16} 1-million-electron-volt electrons per square centimeter; shallow junction; silicon oxide coated silicon cells.

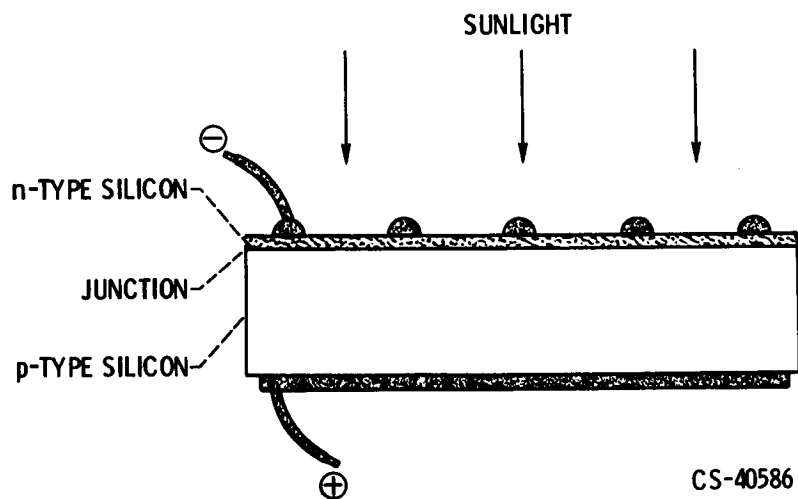


Figure III-2. - Cross section of silicon solar cell.

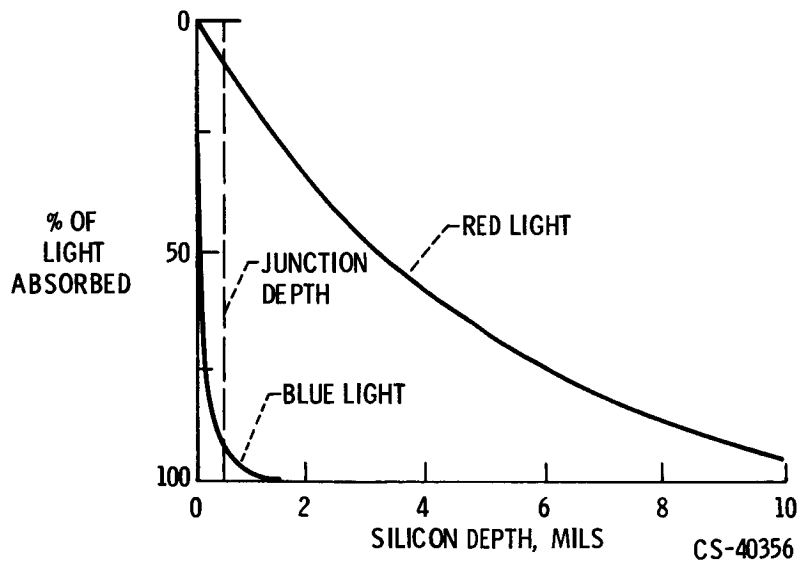


Figure III-3. - Dependency of absorption depth on wavelength in silicon.

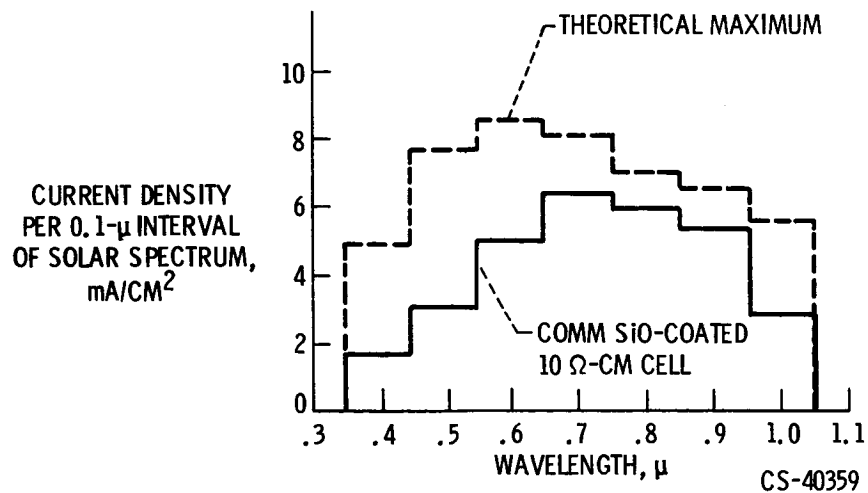


Figure III-4. - Comparison of actual response with theoretical solar spectral response for silicon cells.

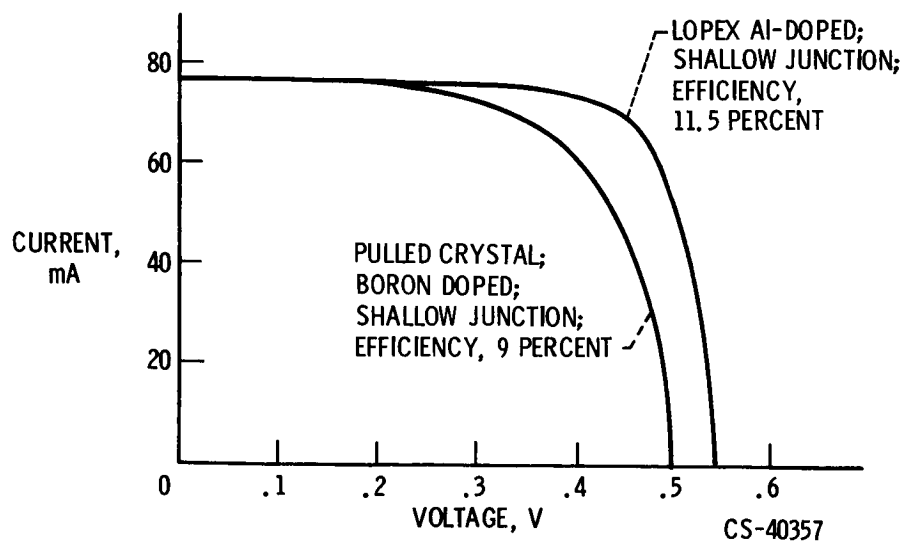


Figure III-5. - Effect of dopant on efficiency of shallow-junction cells. Current-voltage curves under simulated space sunlight. Cell area, 2 square centimeters.

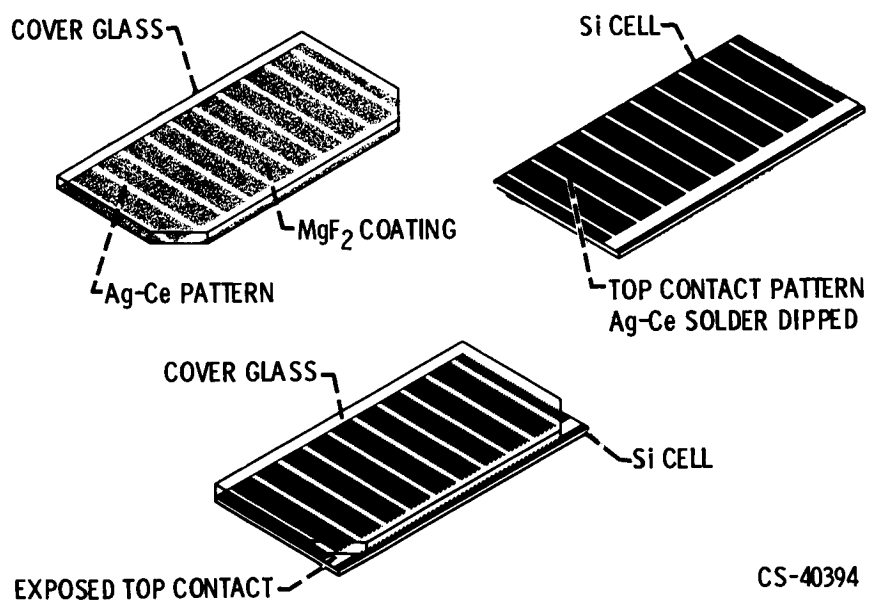


Figure III-6. - Lewis cover-glass attachment.

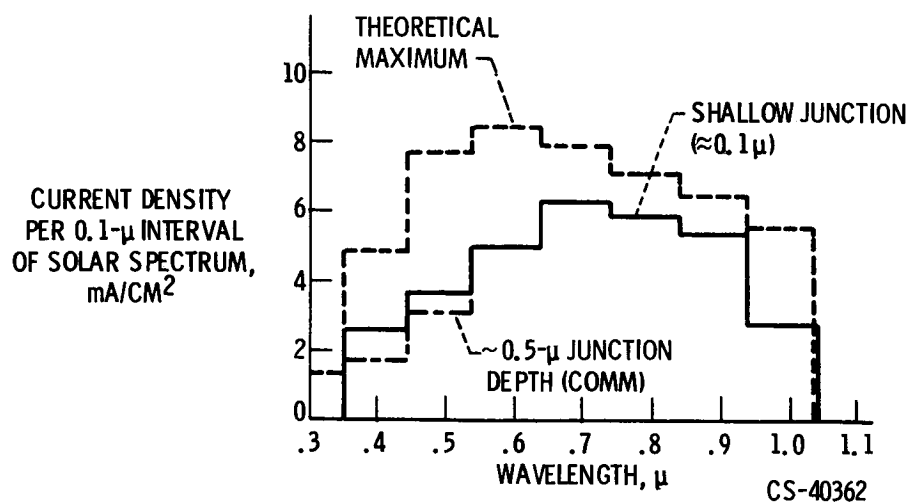


Figure III-7. - Effect of junction depth on solar spectral response for silicon oxide coated cells.

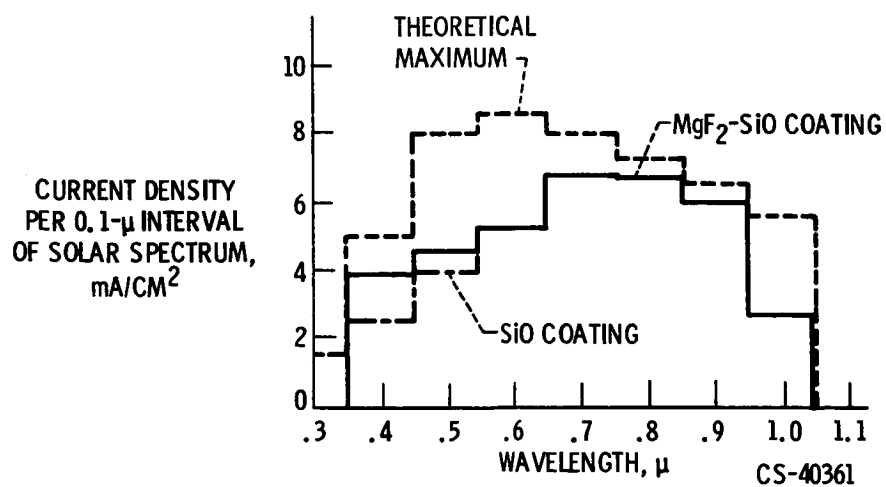


Figure III-8. - Effect of antireflection coating on solar spectral response for shallow-junction cells.

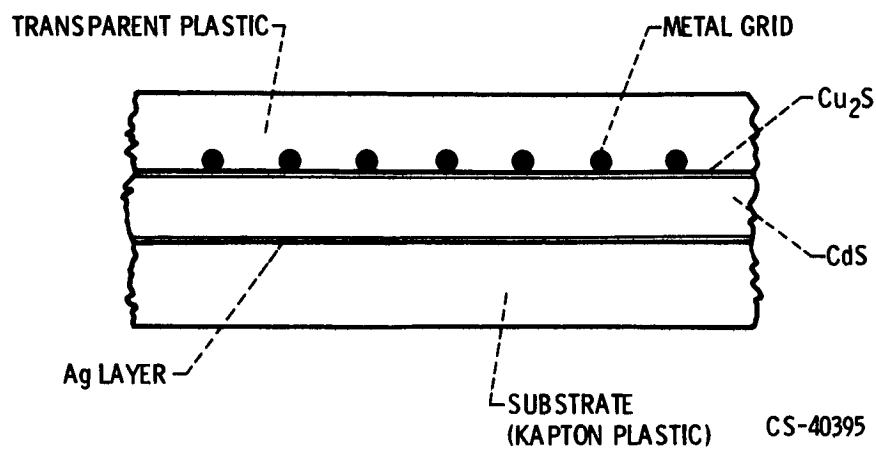


Figure III-9. - Cross section of typical cadmium sulfide film cell.

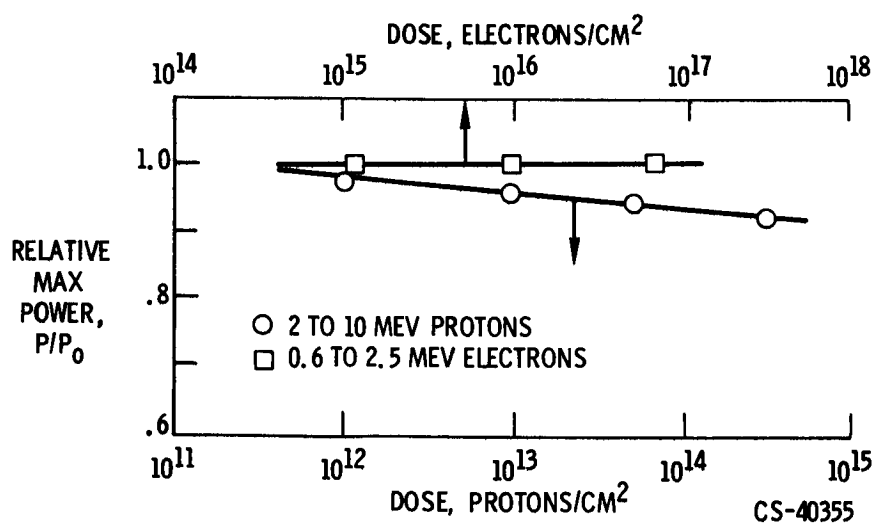


Figure III-10. - Radiation damage to cadmium sulfide film cells.

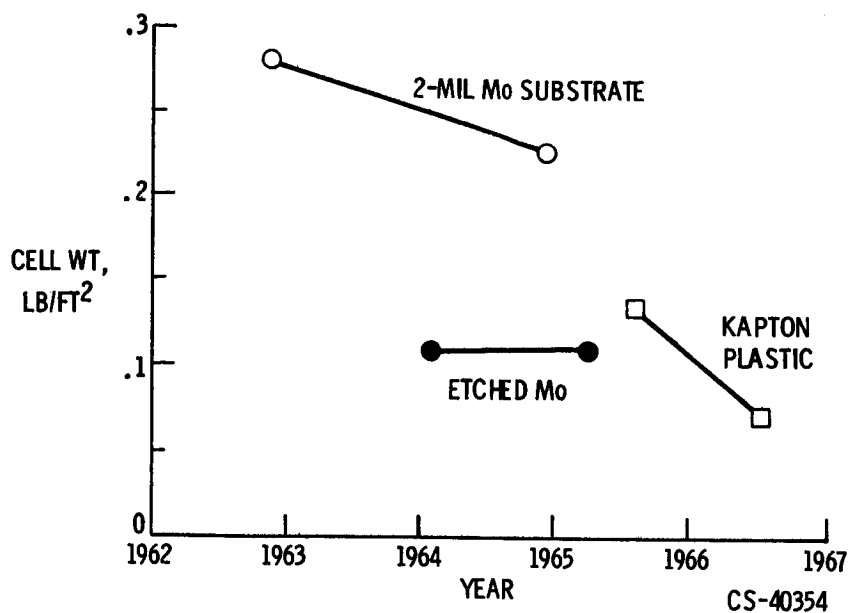


Figure III-11. - Improvements in cadmium sulfide cell weights.

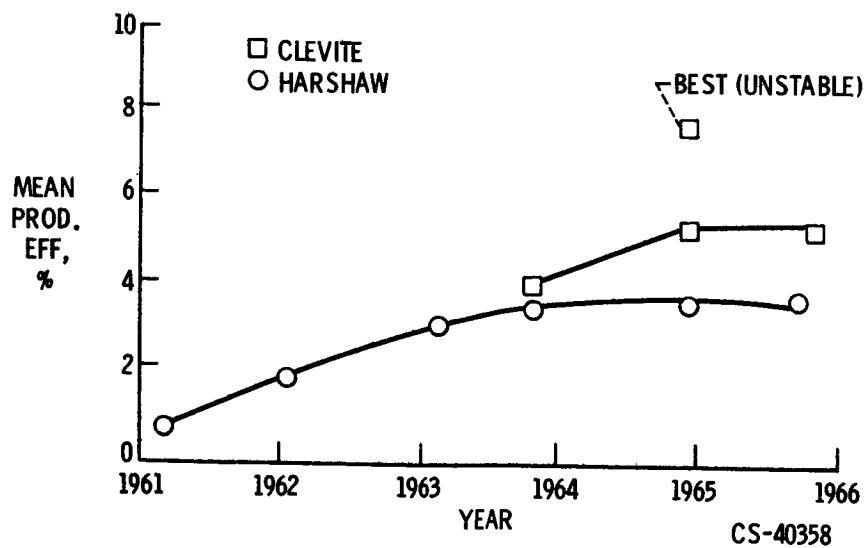


Figure III-12. - Efficiency improvements in cadmium sulfide film cells. Cell area, 50 square centimeters; air mass, 1; temperature, 25° C.

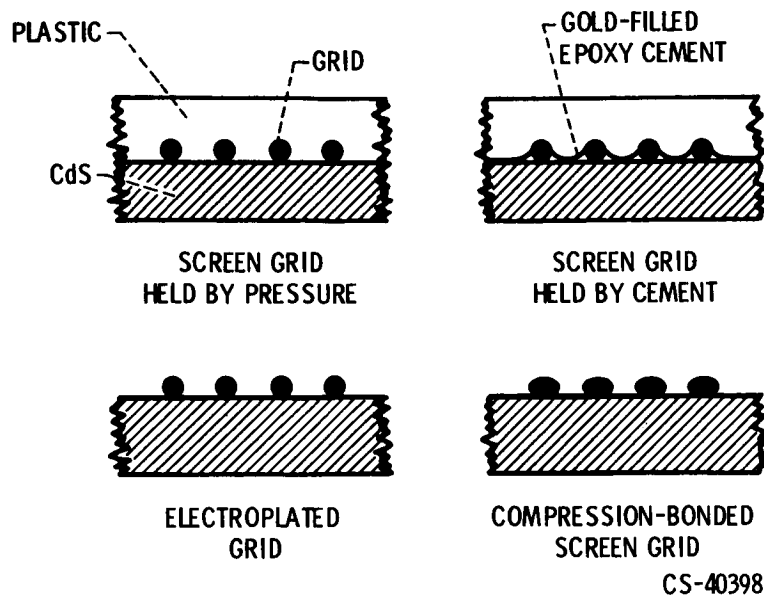


Figure III-13. - Gridding techniques for cadmium sulfide cells.

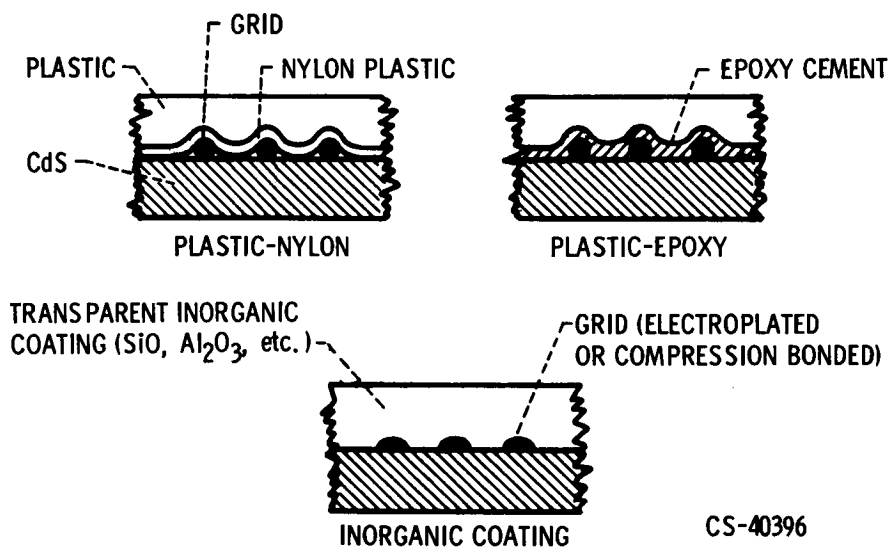


Figure III-14. - Encapsulant techniques for cadmium sulfide cells.

IV. ISOTOPES AND ISOTOPE THERMOELECTRIC GENERATORS

Fred Schulman*

INTRODUCTION

Isotope power systems are particularly attractive for missions in which relative freedom from environment, long life, and compactness are desirable. The properties of isotopes of interest to space, thermoelectric conversion, thermoelectric generators, and two NASA missions which illustrate this attractiveness are discussed briefly herein.

Isotope heat sources produce heat by stopping the alpha, beta, or gamma particles emitted by suitable radioactive nuclides. This heat can be used with many of the various power conversion cycles, which are discussed in detail in papers V, VIII, and IX. Because of availability, cost, and safety problems, isotope power will generally be limited to applications of a few kilowatts or less. Some of these problems are discussed in more detail in this paper.

ISOTOPIC POWER

Advantages and Disadvantages

Some of the principal advantages and disadvantages of isotopic power are as follows:

Advantages	Disadvantages
Can be used in any environment	Safety requirements
No power storage requirement	Availability
Flexible in operation	Possible costs
Long operational use	Unfamiliarity to users
Compact	Possible interference
Heat available to maintain equipment thermal balance	with experiments
Highly reliable	

Isotopes need no power storage system, and excess heat is available, if needed, to maintain equipment thermal balance and for thermal life support systems. However, isotopes can pose

*NASA Headquarters.

severe spacecraft integration problems because of the heat and radiation produced. Because of the potential usefulness of isotopes, NASA is considering an increasing variety of advanced missions, both manned and unmanned, since it is convinced that these problems will be solved. Such missions, in which isotopes are expected to play an important role in providing needed power, are Voyager, Manned Orbital Research Laboratories, Jupiter Flyby, and others. The AEC, which has the primary responsibility for providing the isotopes and developing the isotope sources, is conducting a vigorous program to increase availability, reduce costs, and provide needed information regarding fuel forms and heat sources.

Isotopic Power for Space Use

The beta-emitting isotopes, which have been considered for space use, are listed in table IV-1(a). They are cobalt 60 (Co^{60}), strontium 90 (Sr^{90}), promethium 147 (Pm^{147}), and thulium 170 (Tm^{170}). Beta emitters are usually easier to obtain than alpha emitters and hence could be more plentiful and less expensive. However, most of them have high shielding penalties that complicate spacecraft handling and safety problems. All of them have high bare-dose rates, as shown in table IV-1(a), and shielding is required. Promethium 147 is the best beta emitter with respect to shielding, and its 2.7-year half-life is attractive for many missions. Although unavailable at present for space power use, Pm^{147} will become available after 1970 from the Isochem purification plant being constructed at Hanford, Washington. Its capacity will be about 10 thermal kilowatts of aged Pm^{147} per year. The low shielded dose rate from Pm^{147} depends on the impurity content of Pm^{146} and Pm^{148} , as shown in figure IV-1. After about 700 days, the dominant radiation from Pm^{147} comes from the Pm^{146} impurity content. If Pm^{147} is appreciably contaminated with these active impurities, the dose rate will be higher than the bare and shielded levels of 100 roentgens per hour and 1 milliroentgen per hour, respectively, and in that case more shielding may be required.

The advantage of the alpha emitters over the beta emitters is that they generally require less shielding and can be more easily handled. The alpha emitters of principal interest are given in table IV-1(b). These include the short-half-life polonium 210 (Po^{210}) and curium 242 (Cm^{242}) and the longer half-life curium 244 (Cm^{244}) and plutonium 238 (Pu^{238}). Of all the isotopes, Pu^{238} is accompanied by the least external radiation, thus simplifying its handling and integration problems. Its half-life of 86 years makes Pu^{238} suitable for long-lived missions, and it can be stockpiled for later use with little loss from decay. It is, therefore, the isotope of choice for many missions, and all space flights with isotope generators to date have used Pu^{238} . All these isotopes have fuel forms that have high melting points, which make them suitable for consideration for higher temperature and more efficient conversion systems like thermionic or Brayton conversion cycles.

While shielding of isotope generators may be a disadvantage, most spacecraft will face radiation from other causes in space, and in many cases shielding will be required. The radiation levels that can be expected from the Van Allen belts, solar flare protons, and galactic cosmic rays are given in table IV-2. Radiation levels of thousands of rads per hour from primary electrons in the Van Allen belts can be virtually eliminated by a shield equivalent to 10 grams per

square centimeter. However, an appreciable fraction of the bremsstrahlung radiation remains. Other radiations except the high-energy galactic cosmic rays can be considerably reduced by shielding. Thus, some shielding will probably be aboard many spacecraft, and the most efficient design should take advantage of this to reduce any special isotope generator shield requirements, especially for manned missions.

ISOTOPIC-POWER GENERATORS

A considerable number of isotopic-power generators ranging from a few milliwatts to about 60 watts have been built. All of them have been built by the AEC. Table IV-3 gives the space units and, for completeness, the terrestrial units that have been built or are under development to date. The AEC has assigned odd numbers to its isotope Systems for Nuclear Auxiliary Power (SNAP) and even numbers to its reactor systems, such as SNAP-8 and SNAP-10A. Five generators of the SNAP-3 and 9 types have been launched into space. One of them, a SNAP-3 unit launched in June 1961, is still operating on isotope thermoelectric power, sending back telemetry signals through the isotope-powered circuit. This is the longest lived satellite operating in orbit since Vanguard I ceased. All these units were fueled with Pu^{238} and all of them used lead telluride thermoelectric conversion modules.

These early model generators experienced some power degradation in space because of various problems, such as leakage and increased contact resistance at the hot junction. Current designs incorporate many technical improvements, such as reduction in number of seals, improved thermoelectric materials, and better thermal and mechanical designs, which are expected to reduce degradation to within about 5 percent of initial power.

SNAP-19 and SNAP-27 are being developed for NASA missions. SNAP-19 will be flown on Nimbus B in late 1967, and SNAP-27 will be launched on the first Apollo mission before 1970.

One generator, SNAP-13, is a thermionic demonstration device. It was fueled with Cm^{242} at the Oak Ridge National Laboratory and operated for about 43 hours when a leak developed in the converter, and the test was terminated. Technology efforts are underway both at AEC and NASA to improve performance and life of isotope thermionic generators. One of the principal problems is the development of a suitable high-temperature heat capsule. The advantage, of course, is potential higher efficiency.

The SNAP-29 generator, whose development has been recently initiated by the AEC to meet the Department of Defense requirements is also under study by the Marshall Space Flight Center as a possible power supply to extend the usefulness of the Instrument Unit aboard the Saturn V launch vehicle. Under consideration are applications for a potential orbital workshop under the Apollo application program. In these applications, one or more generators could be used to satisfy increasing power needs. Many other studies are underway concerning isotope generators for future missions, including Voyager lander, Jupiter flyby, and galactic and solar probes. Obviously, long life and reliable operation of these generators must be achieved if they are to satisfy future mission requirements. For these space missions, the alpha emitters, particularly Pu^{238} , are desirable to minimize weight, shielding, and integration problems. On the other hand, the terrestrial units generally employ the less expensive and more abundant beta emitters, particularly Sr^{90} , since heavy shielding, of the order of tons, can be tolerated. In

both cases, however, the generators employ similar thermoelectric elements, and therefore the tests of these terrestrial generators contribute to the development of the long life and reliability so important to space thermoelectric power units.

Figure of Merit

One measure of thermoelectric material performance is the figure of merit. The figure of merit for lead telluride materials is shown as a function of temperature in figure IV-2. Similar data for silicon-germanium alloys are shown in figure IV-3. While many semiconductor materials have been examined during extensive research over the past 10 years, these two materials have been found to be most generally suitable for space power use. The figure of merit of a thermoelectric material is given by the equation $Z = S^2/\rho K$, where S is the Seebeck coefficient, ρ is the electrical resistivity, and K is the thermal conductivity. The figure of merit depends on the inherent properties of the materials and is very sensitive to impurities and temperature. As can be seen from the figures, lead telluride has a higher figure of merit at low temperatures, and silicon-germanium alloys have a higher value than lead telluride only when the temperature exceeds about 1000°K . Similar relations have been found for both n and p materials. This sensitivity to impurities is undoubtedly one of the reasons for some of the degradation noted in lead telluride thermoelectrics. Better quality control and improved bonding techniques will improve this condition. The good low-temperature performance of lead telluride is the principal reason it has been used in all space isotope power generators thus far. It will be necessary to qualify a fuel capsule for higher temperatures in order to obtain equal performance from silicon-germanium. On the other hand, lead telluride is brittle, oxidizes easily, and is volatile at 1000°K .

Heat Pipes Combined with Thermionic Converters

In addition to thermoelectric conversion, an interesting technology effort to improve conversion efficiency in low-power generators is the combination of heat pipes with thermionic converters. The heat pipe is an excellent thermal control device that can transfer heat from the isotope heat source to the cathode of a converter. In tests at the Radio Corporation of America (RCA), a heat pipe of TZM molybdenum alloy, which used lithium as a working fluid, successfully completed a 1000-hour life and compatibility test. It was also demonstrated that the heat fluxes could be concentrated up to a ratio of over 9.3 to 1. This limit existed because the heat-sink area of the heat-removal section of the heat pipe, which was progressively decreased while maintaining the input area constant, could not be reduced further.

Figure IV-4 shows a combination of the heat pipe with a thermionic diode. This equipment was used to determine the conversion efficiency of the heat pipe - diode combination, which was found to agree closely with the calculated value (14.5 percent).

A test setup combining the heat pipe, the thermionic converter, and a power flattening device

is shown in figure IV-5(a). This setup operated very well. Figure IV-5(b) shows the same test equipped with meters to demonstrate the constant diode output, automatically maintained by the power flattening device, although the input power, simulating the decay of an isotope, may be greatly reduced. In this experiment the power input was reduced from an initial 12 to 4 kilowatts, that is, a decrease of a factor of 3. As the heat is reduced, the hot length of the heat pipe is reduced, but the temperature of the diode emitter and hence the output of the diode remain essentially constant (from the 87 W shown in fig. IV-6 to 85 W). These tests suggest the practicality of using relatively low power density isotopes such as Pu^{238} for driving thermionic converters and of using short half-lived isotopes such as Po^{210} for missions of 2 or 3 half-life durations.

MISSIONS USING ISOTOPIC THERMOELECTRIC GENERATORS

The remainder of this paper discusses briefly two NASA missions that will use isotopic thermoelectric generators and the availability and cost of the isotopes that may be used for future space missions.

Nimbus B

The first mission is Nimbus B illustrated in figure IV-6. Two SNAP-19 generators will be aboard this spacecraft, each producing 25 to 30 watts to supplement the 185 to 200 watts of power produced by the two large solar paddles shown in the figure. Nimbus B is in reality designed for solar power, and the two SNAP-19 units are retrofitted to the Nimbus sensory ring. It is therefore not an optimum design, but it will nearly double the useful power aboard the satellite since about 120 watts are needed to keep the satellite operating in its high-noon sun-oriented mode. SNAP-19 also can be considered an important Nimbus B experiment that will provide useful experience and guidance for followup isotope powered missions. Figure IV-7 is a cutaway drawing of the SNAP-19 generator. A Pu^{238} fuel capsule, located in the center, provides heat to the lead telluride thermoelectric element hot junctions through the graphite heat-accumulator block. Rows of thermoelectric elements surround the fuel capsule and are interconnected, in much the same manner as solar cells, to provide extremely high reliability. Heat is rejected to space through the radiator fins. SNAP-19 is an improved generator design. It has fewer seals and leakage paths than either SNAP-3 or SNAP-9 and uses improved thermoelectric materials.

The SNAP-19 is shown in figure IV-8 while undergoing tests on the Nimbus spacecraft. Mechanical, mass, and electrical checkouts are underway in preparation for a late 1967 launch. The remaining schedule for the generators is as follows:

Event	Scheduled date
Development started	January 1964
Fueled-prototype qualification completed	October 1966
Electrically heated prototype made available	October 1966
Safety evaluation report submitted	December 1966
Fueled flight model qualified	January 1967
Fueled flight model backup made available	April 1967

In the next few months the fuel prototype system will be qualified. A total of seven power systems are in the program; each consists of two generators for a total of 14. Two sets of fuel capsules for ground checkout and flight use are provided. The first fueled model will be shipped and qualified about the beginning of 1967. A fueled flight backup system will become available about 3 months later. The important point is that the thermoelectric isotope power units can be used in flight programs in which tight schedules have to be met.

Apollo Lunar Surface Experiment Package

The second NASA isotope-powered mission is shown in figure IV-9. The SNAP-27 generator, which is under development by the AEC for the Apollo Lunar Surface Experiment Package (ALSEP), will provide power for a number of scientific experiments that will be left on the surface of the moon by the Apollo astronauts. This generator is the first one to be used by NASA where isotope power was specifically intended for the spacecraft application, rather than retrofitted to a solar power design, as in the case of Nimbus B.

Consequently, SNAP-27 is more efficient, and it produces more power for less weight. The generator is designed to be fueled on the lunar surface. The astronaut will take the single fuel capsule out of a special cask located on the Lunar Excursion Module (LEM) and insert it into the generator with the aid of a special lightweight tool. The fuel cask is located externally to the LEM and the fuel capsule is not part of the generator when it is aboard the spacecraft. This arrangement, which was decided upon after a complete detailed analysis of the entire system from the beginning to the end of the mission, minimizes the thermal problem within the shroud during the launch and parking orbital phases of the mission.

Figure IV-10 illustrates the SNAP-27 generator. Like SNAP-19, it uses Pu^{238} in a central fuel element. This design employs improved lead telluride elements and a lightweight beryllium radiator. It weighs 46 pounds, including the cask and handling tool, and produces 56 watts of power.

Some of the characteristics of this generator, which is designed to operate on the lunar surface for 1 year after 2 years storage on earth, are as follows:

Power (end of life), W	56
Voltage, V	14
Efficiency, percent	4
Diameter (over fins), in.	15.7
Length, in.	18.1
Temperature (maximum lunar day), °F:	
Fuel clad	1390
Hot junction	1100
Cold junction	525

AVAILABILITY AND COSTS OF ISOTOPES

Civilian Sources

The availability of isotopes, their production, and their cost are discussed briefly in this section.

Figure IV-11 shows the potential production of isotopes from civilian power only, not from AEC sources. It is very encouraging and significant to note the large upsurge in the introduction of civilian nuclear power in the past 2 years. In a 1962 report to the President, the Commission estimated that there would be 40,000 megawatts of electrical power installed in the United States by 1980. Further study resulted in an interim estimate given by the AEC at the Third Geneva Conference on Peaceful Uses of Atomic Energy in the range of 60 000 to 90 000 megawatts by 1980. Recent AEC estimates indicate an even larger potential, perhaps as much as 110,000 megawatts of electricity by 1980. As a matter of fact, the majority of large new powerplants that have been ordered in the United States during the past year have been nuclear. The important point of this discussion is that as the civilian nuclear industry increases, the potential for recovery of isotopes also increases. If proper steps are taken, approximately 1 thermal kilowatt of Pu^{238} , the isotope of choice, can be obtained for every 1000 megawatts of installed thermal power in the industry. It should be emphasized that the amounts of isotopes shown in figure IV-12 represent merely amounts potentially available from civilian industry. Proper incentives will have to be offered to ensure their becoming truly available. As is shown in figure IV-11, more than 500 thermal kilowatts annually of Sr^{90} might become available by 1980. For Pu^{238} , unfortunately, only minor amounts can probably become available until the late 1970's when about 100 thermal kilowatts might be produced annually. Promethium 147 production is low since much of that produced is destroyed by radioactive decay or by neutron absorption in the reactor. The figure indicates that curium 244 has a good production potential.

Atomic Energy Commission Sources

The second good source of needed isotopes is the AEC. The commission can respond to varying requirements through the management of its vast reactor and separation facilities.

Figure IV-12 shows how the isotope of choice, Pu^{238} , can be obtained. The key to Pu^{238} production is Np^{237} , a relatively stable isotope that has a half-life of about 2 million years. Neptunium 237 is obtained chiefly by two reactions. The first is the (n,γ) reaction on U^{235} , producing U^{236} , which is further irradiated to produce U^{237} , which decays rapidly to Np^{237} by beta emission. Yields of U^{237} are very low since U^{236} has a very small absorption cross section. The fuel is therefore recycled several times and upgraded when necessary to improve the yield of U^{237} . Since Np^{237} is different chemically and has a very long half-life, it can be separated and stored or irradiated in a special reactor to produce Pu^{238} . The other reaction is the $(n,2n)$ reaction on U^{238} to produce U^{237} . The entire process requires about 7 years. The fuel must be irradiated and reirradiated to build up the U^{236} content because of the small cross section until a reasonable yield of Np^{237} is obtained.

Furthermore, only about 10 to 20 percent of the Np^{237} can be converted to Pu^{238} per reactor cycle. Attempts to increase the yield by increasing the flux or the irradiation time are not practical, since the Np^{238} and Pu^{238} already formed have high fission and neutron absorption cross sections, respectively, and are readily burned out.

Thus, the production of Pu^{238} involves many variables that have to be considered if good yields at low cost are to be obtained. In short, the production of Pu^{238} is a very complex subject. The amounts obtained depend upon the amount of fuel consumption, its enrichment, the fast- to thermal-neutron flux ratio, the times of irradiation, and many other factors. The yields of products and the costs will change accordingly. In addition, there may be competing demands on the reactors for other purposes, thus reducing their optimum Np^{237} yields. To specify in advance just what will become available in any given year is therefore extremely difficult. However, since it takes about 7 years to complete a Pu^{238} production cycle, the amounts of isotopes that will ultimately be needed must be anticipated so that proper steps can be taken by the AEC to ensure that a sufficient amount of Pu^{238} will be available from civilian industries and their own reactor facilities.

Since Np^{237} is the key to Pu^{238} availability, the amounts of Np^{237} that might be produced in various types of civilian power reactors, both operating and proposed, should be estimated. Table IV-4 gives the amounts of Np^{237} that could be produced in a sodium-graphite reactor (Hallam), pressurized-water reactor (Yankee), boiling-water reactor (Dresden), heavy-water-cooled reactor (Douglas Point), gas-cooled reactor (Hinkley Point), and several advanced reactor designs. At low enrichments, most of the Np^{237} is produced by the $(n, 2n)$ reaction on U^{238} rather than by neutron absorption in U^{235} . The yield of Np^{237} increases rapidly with burnup so that the economy of the fuel cycle itself will greatly influence results. Obviously, some incentives to industry must be given if the Np^{237} in these reactors is to be recovered. It has been estimated that a credit value for Np^{237} of about 150 dollars per gram would be equivalent to a reduction in fuel cost of about 0.3 to 0.4 mill per kilowatt hour.

Figure IV-13 gives the possible AEC production of Pu^{238} for space use. The AEC probably could produce for space purposes between now and 1980 an amount ranging from somewhat over 200 thermal kilowatts to perhaps more than 400 thermal kilowatts. The key problem is that in the critical time period of the mid 1970's very little Pu^{238} will be available from civilian power; thus, the AEC reactors will be the primary sources. If a manned orbiting research laboratory were selected at this time period, only approximately 100 to 200 thermal kilowatts would be available. It is therefore most important that we design with care to get a highly efficient conversion system to utilize the isotopes that might be available in that period.

Figure IV-14 summarizes the possible cumulative availability of Pu^{238} for space use. The curve represents only possible civilian production. The AEC has been requested to provide a total of 500 thermal kilowatts by 1980. This production of Pu^{238} would be from their own sources or from a combination of their own and civilian sources. Obviously the AEC may have demands on plutonium other than NASA, such as those used for medical applications (heart pacers and heart pumps) and for military generators. By 1980, 800 thermal kilowatts could be available for NASA if the proper steps are taken. Again the difficulty is in the mid 1970's when civilian sources will be negligible and AEC sources will be dominant. Obviously the AEC could be producing material earlier, as was indicated in figure IV-13.

The estimated cost of the isotopes is as follows:

Radioisotope	Cost per thermal watt, dollars
Strontium 90	24
Promethium 147	93
Thulium 170	20 to 25
Polonium 210	30 to 40
Plutonium 238	500
Curium 244	700

Strontium 90 and thulium 170 are relatively inexpensive. Promethium 147 will cost about 93 dollars per thermal watt. But, in general, the long-half-life alpha emitters, Pu^{238} and Cm^{244} , are quite expensive. The short-half-life isotopes, such as Pm^{147} , Tm^{170} , and Po^{210} , are relatively inexpensive. Therefore, strong economic motivation exists for using either Pu^{238} very efficiently or the beta emitters if possible. The interest of NASA in the advantages of isotopes for future missions led to a comprehensive study last year at the Lewis Research Center on the selection of isotopes for NASA use. This study was the basis for the guidance given to AEC by NASA in March 1965. This guidance, summarized in table IV-5, was related to both availability of isotopes and additional technology efforts required to determine more adequately their usefulness in a wide variety of both manned and unmanned applications.

NASA asked the AEC for a minimum of 500 thermal kilowatts of Pu^{238} and also asked them to determine methods of producing more than 500 thermal kilowatts at low costs. NASA also agreed to support the current efforts of AEC on Cm^{244} , which is to produce 4.5 kilograms of Cm^{244} and to determine its properties and its suitability for space use. Requirements for Po^{210} were deferred pending mission selection because it appears Po^{210} apparently can be produced within a lead time that is shorter than the mission lead time. The short-half-life isotopes cannot be stored. Plutonium 238, on the other hand, can be stored since it has an 86-year half-life. It can be stored even more efficiently at less cost as Np^{237} since the Np^{237} has a 2-million-year half-life, which prevents any loss by decay.

Because appreciable amounts of all other isotopes are lost by radioactive decay, their production becomes rather mission dependent, and the timely scheduling of missions becomes very important in maintaining an adequate supply of short-lived isotopes. The AEC is also being supported by NASA in their current effort on Pm^{147} , which is to make available 10 thermal kilowatts per year. The use of Pm^{147} is very attractive provided, as discussed earlier, that it can be made free from highly radioactive contaminants. At present, Sr^{90} is not being considered for space use. It is, however, a highly attractive isotope for terrestrial applications, but NASA does not have any present interest in it until the AEC can demonstrate that Sr^{90} can be handled safely and that it does not unduly complicate spacecraft integration and launching procedures. In the area of technology, the AEC was asked to look into problems of high-temperature fuel forms, which will be needed if some of the higher temperature conversion systems, discussed in

papers V, VIII, and IX are to be used.

The AEC was also requested to determine the criticality limits of some of the alpha emitters, to investigate the safety problems of large heat sources because kilowatts of isotope power are being considered for manned missions, to define safety criteria, and to supply more information on the basic properties of the various fuel forms, such as thermal conductivity, vapor pressure, compatibility, radiation spectra, etc. NASA has given this guidance to the AEC because it is convinced that the advantages are so overwhelming that it is worth attempting to solve some of the problems that have been discussed.

In conclusion, isotopes will be available in sufficient quantities to be considered for many future space missions. The extent of their future use will be dependent on the programs now underway to improve performance and availability, to define properties, and to provide acceptable fuel capsules.

TABLE IV-1. - CHARACTERISTICS OF ISOTOPES
FOR POWER PRODUCTION

(a) Beta emitters

Isotope	Half-life	Compound	Compound power, W/g	Dose rate, mR/hr ^a	
				Bare	3-cm of uranium
Cobalt 60	5.27 yr	Metal	^b 3.0	3×10^8	6×10^6
Strontium 90	28 yr	SrTiO ₃	.2	6×10^6	1×10^4
Promethium 147 ^c	2.67 yr	Pm ₂ O ₃	.3	1×10^5	1.0
Thulium 170	127 days	Tm ₂ O ₃	1.75	4×10^6	50

(b) Alpha emitters

Polonium 210	138 days	Metal matrix	17.6	760	1.8
Plutonium 238	86 yr	PuO ₂	.35	5	.03
Curium 242	163 days	Cm ₂ O ₃ in metal matrix	15.5	280	2
Curium 244	18.4 yr	Cm ₂ O ₃	2.5	600	32

^aAt 1 m from 5-thermal-kW source.

^b200 Ci/g metal.

^cAged, 1 half-life.

TABLE IV-2. - RADIATION LEVELS IN SPACE

Radiation	Radiation level, rad/hr	
	Bare	10 g/cm ² shield
Van Allen belts:		
Electrons	10^3 to 10^5	~0
Bremsstrahlung	1 to 100	1 to 30
Protons	10 to 100	1 to 10
Solar flare protons	10 to 100	1 to 10
Galactic cosmic rays	$\sim 10^{-3}$	$\sim 10^{-3}$

TABLE IV-3. - ISOTOPIC POWER UNITS

SNAP	Power, W	Use	Fuel	Design life, yr	Status
Space applications					
3	2.7	Department of Defense navigation satellite	Plutonium 238	5	In orbit
9A	25	Department of Defense navigation satellite	Plutonium 238	5	In orbit
11	25	Surveyor	Curium 242	.25	Tested
13	12.5	Thermionic demonstration	Curium 242	.25	Tested
19	30	Nimbus B	Plutonium 238	5	Under development
27	50	Apollo Lunar Surface Experiment Package	Plutonium 238	1	Under development
29	500	Department of Defense application	Polonium 210	.25	Under development
Terrestrial applications					
Sentry	5	Weather station	Strontium 90	2	In use
7A	10	Light buoy	↓	10	↓
7B	60	Land light		10	
7C	10	Weather station		10	
7D	60	Boat weather station		10	
7E	7	Sonar		10	
7F	60	Navigation aid		10	
15A	.001	Department of Defense applications	Plutonium 238	5	Tested Tested
21	10	Advanced undersea	Strontium 90	5	Under development
23	60	Advanced terrestrial	Strontium 90	5	Under development

TABLE IV-4. - PRODUCTION OF NEPTUNIUM 237
IN SPECIFIC REACTORS

Reactor	Thermal power, MW	Initial enrichment, percent	Neptunium 237 production, kg/yr
Hallam	240	3.60	0.8
Yankee	485	3.40	1.4
Dresden	626	1.50	2.3
Douglas Point	693	.71	1.8
Hinkley Point	954	.71	2.5
Oak Ridge National Laboratory GCR-3	1908	3.00	4.7
Saline water reactor	8300	.71	24.0

TABLE IV-5. - GUIDANCE GIVEN TO ATOMIC ENERGY COMMISSION BY
NATIONAL AERONAUTICS AND SPACE ADMINISTRATION

[March 1965.]

Isotope	Availability	Technology
Plutonium 238	500 thermal kW by 1980	Develop high-temperature fuel forms; determine criticality limits; investigate large heat sources; define safety requirements; determine properties.
Curium 244	Support current efforts (3 to 4 kg)	
Polonium 210	Deferred pending mission requirements	
Promethium 147	Support current effort (10 thermal kW/yr)	
Strontium 90	No present interest	

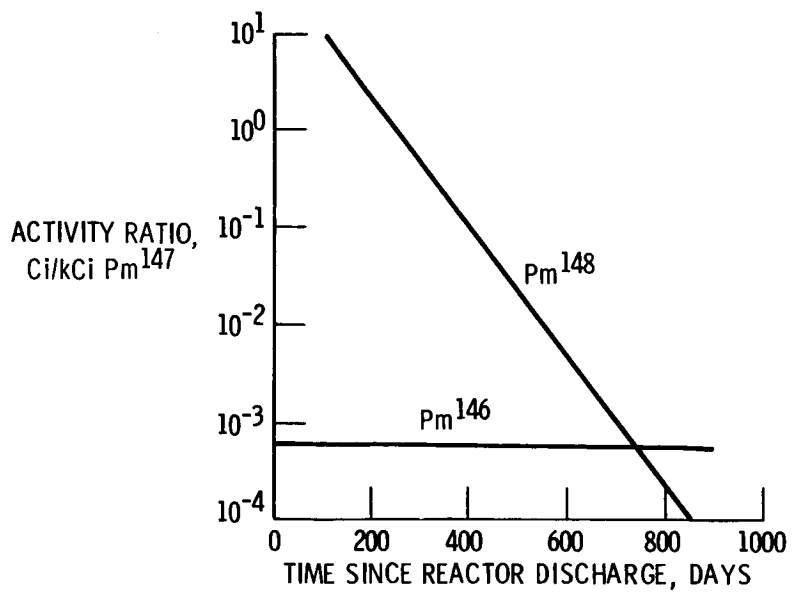


Figure IV-1. - Decay of promethium 146 and promethium 148 impurities relative to promethium 147. (From ORNL-64-709.)

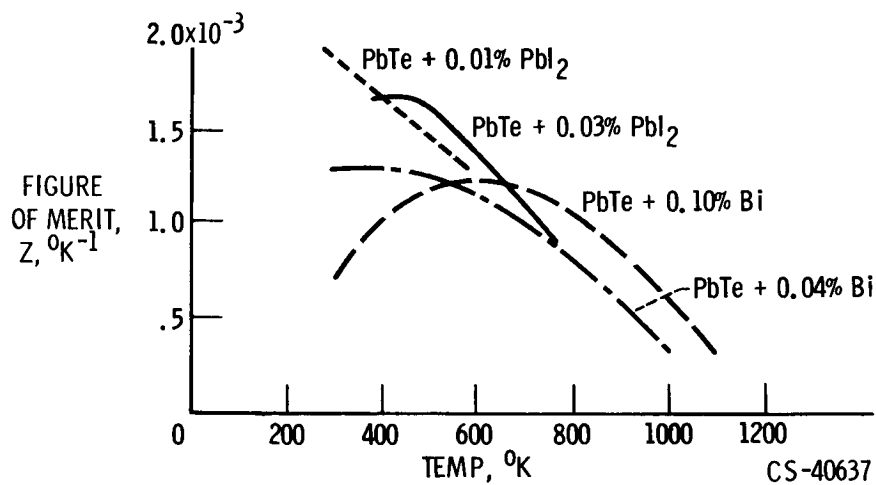


Figure IV-2. - Figure of merit of n-type lead telluride.

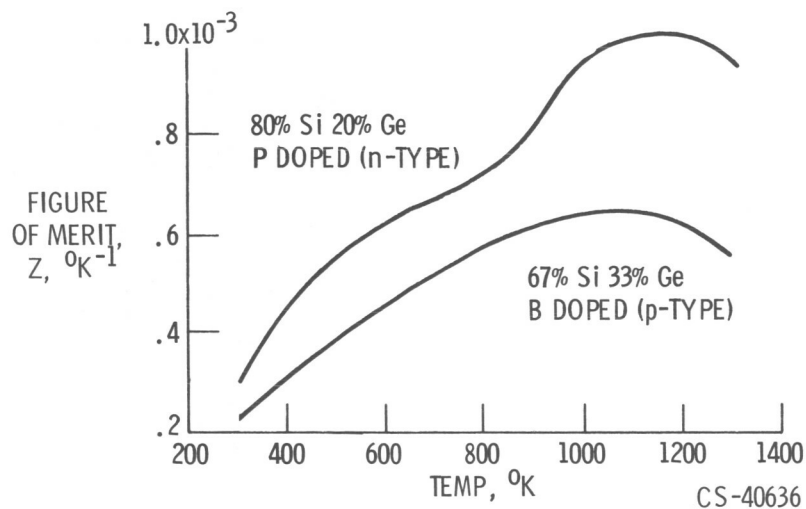
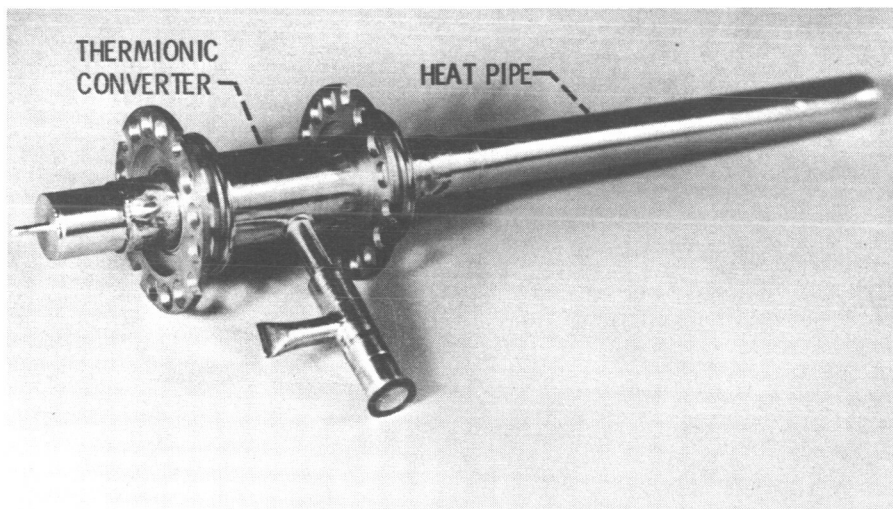
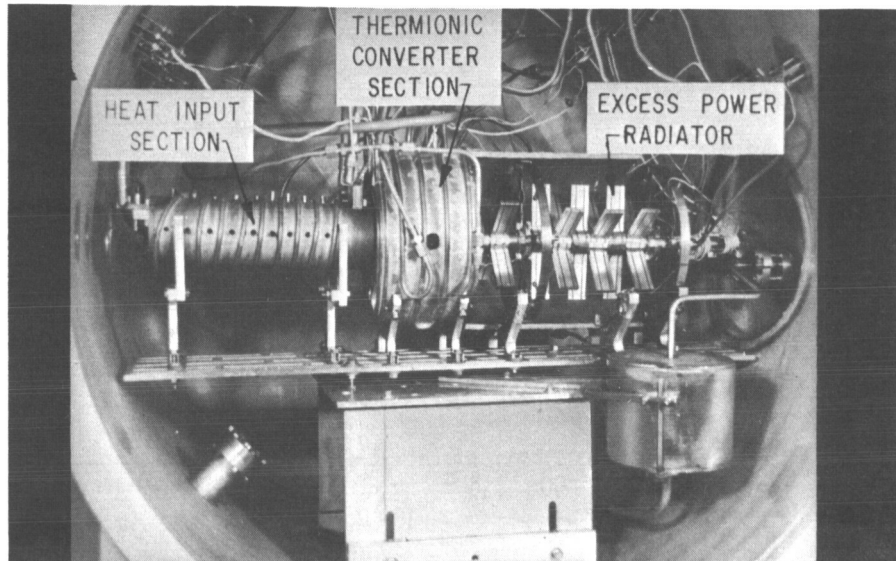


Figure IV-3. - Figure of merit of optimum silicon-germanium alloys.



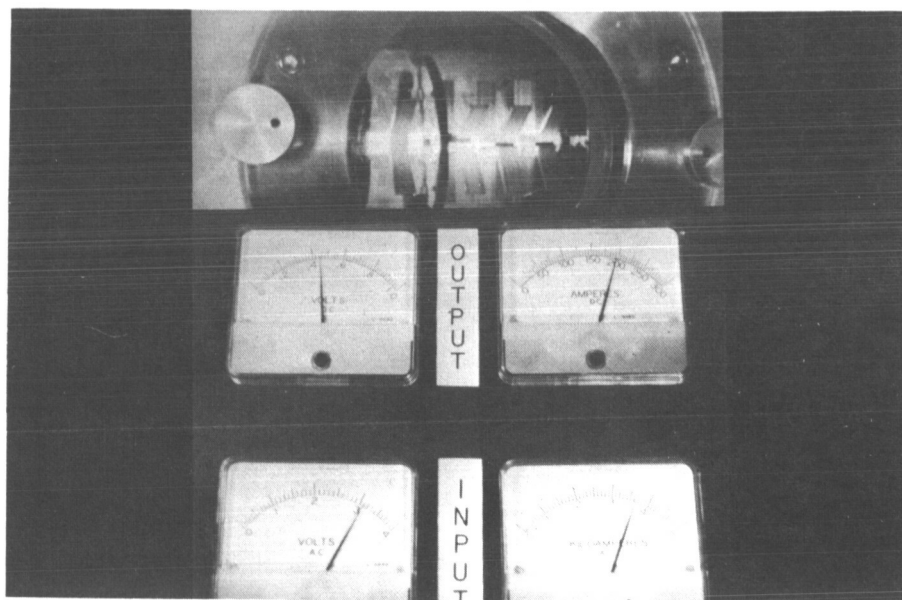
CS-40490

Figure IV-4. - Thermionic heat-pipe experiment. Heat pipe material, TZM molybdenum alloy; working fluid, lithium; test temperature, 1500°C ; thermionic converter, molybdenum; area, 50 square centimeters; measured efficiency, 14 percent; power output, 175 watts.



CS-40582

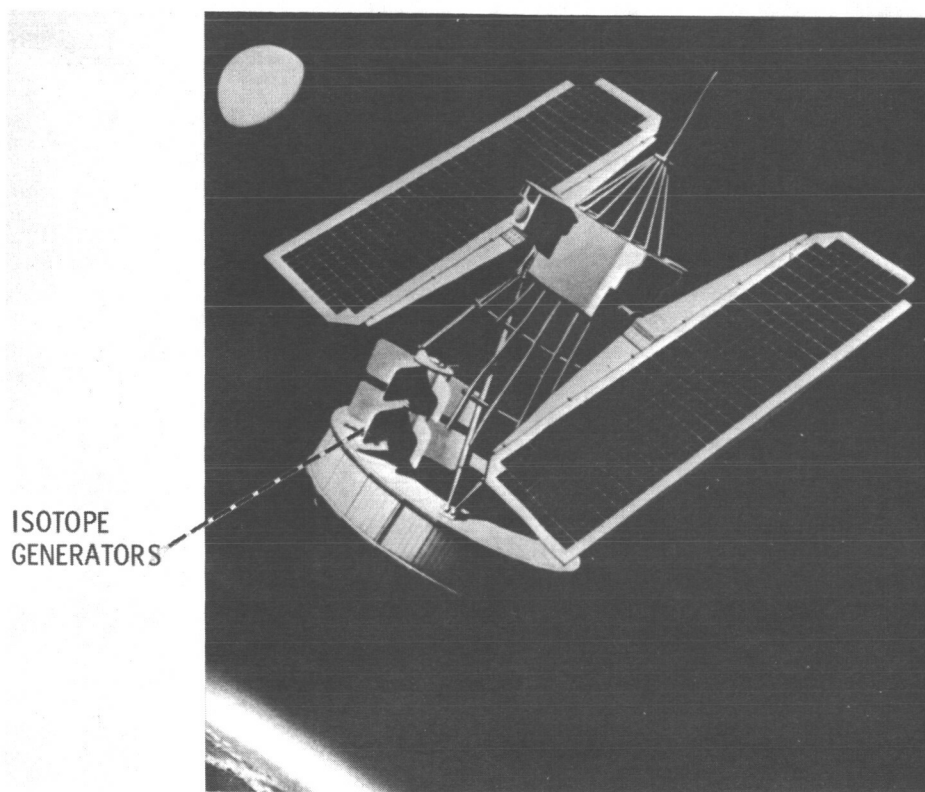
(a) System not operating.



CS-40583

(b) System operating.

Figure IV-5. - Thermionic heat-pipe experiment.



CS-40584

Figure IV-6. - Nimbus B.

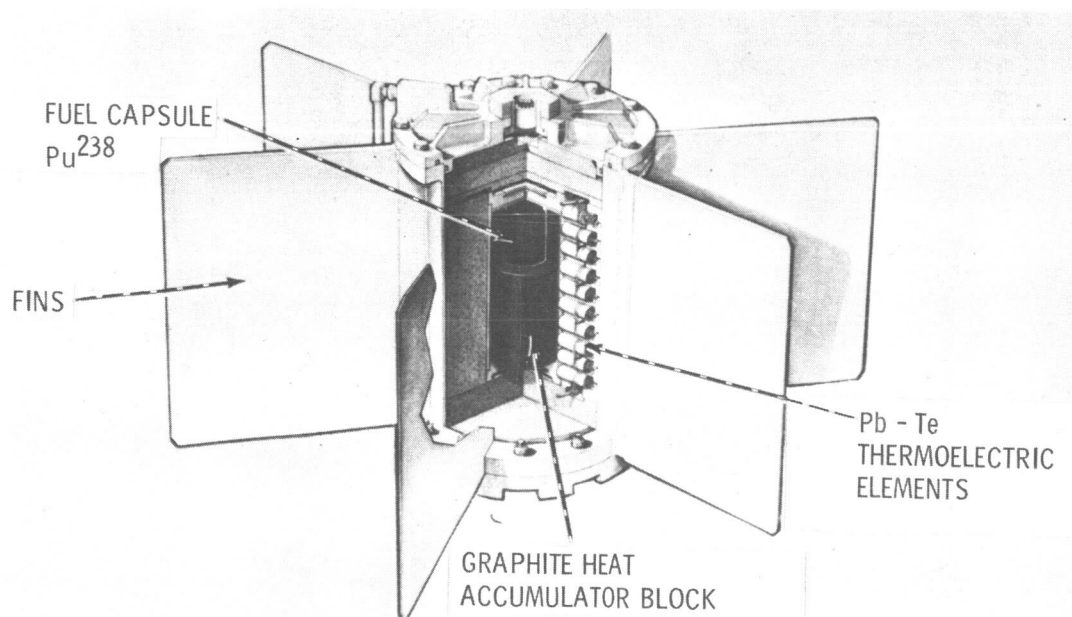
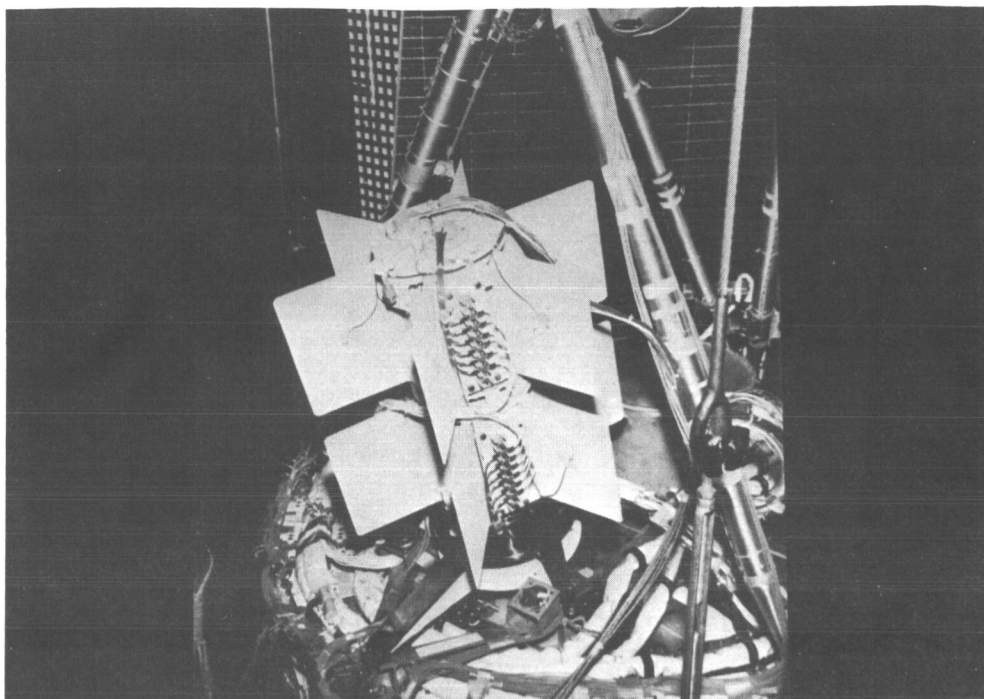
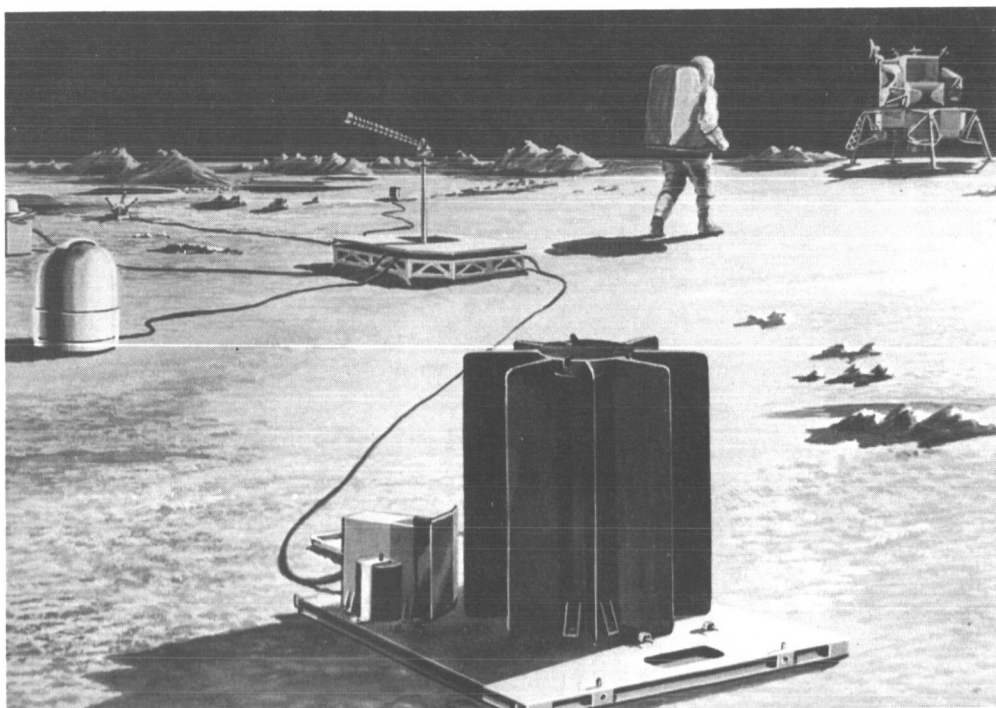


Figure IV-7. - SNAP-19 generator. Weight, 30 pounds; power output, 30 watts.



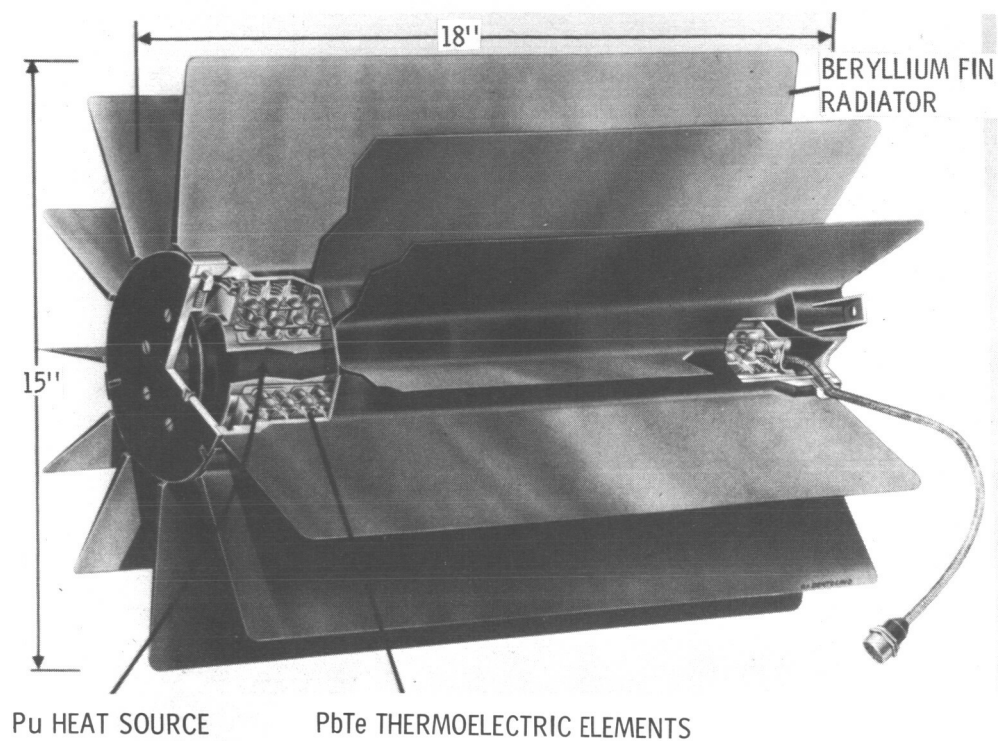
CS-40340

Figure IV-8. - SNAP-19 generator on Nimbus B.



CS-40341

Figure IV-9. - Apollo Lunar Surface Experiment Package (ALSEP) with SNAP-27 generator.



CS-40581

Figure IV-10. - SNAP-27 generator. Weight, 46 pounds; power, 56 watts.

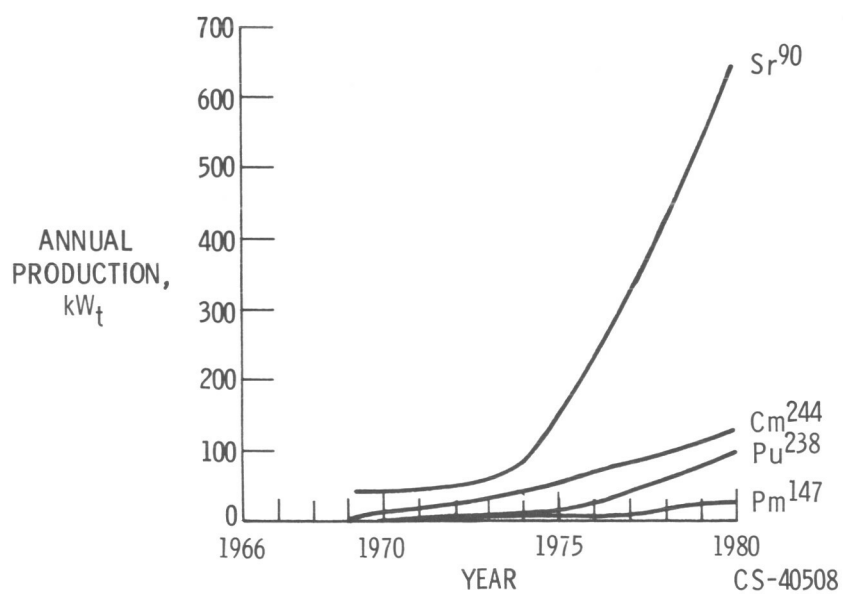
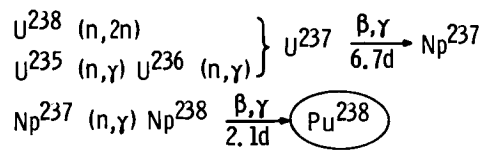


Figure IV-11. - Potential production of isotopes based on projected installed civilian power.

NUCLEAR PROCESS



FACILITIES FLOWSHEET

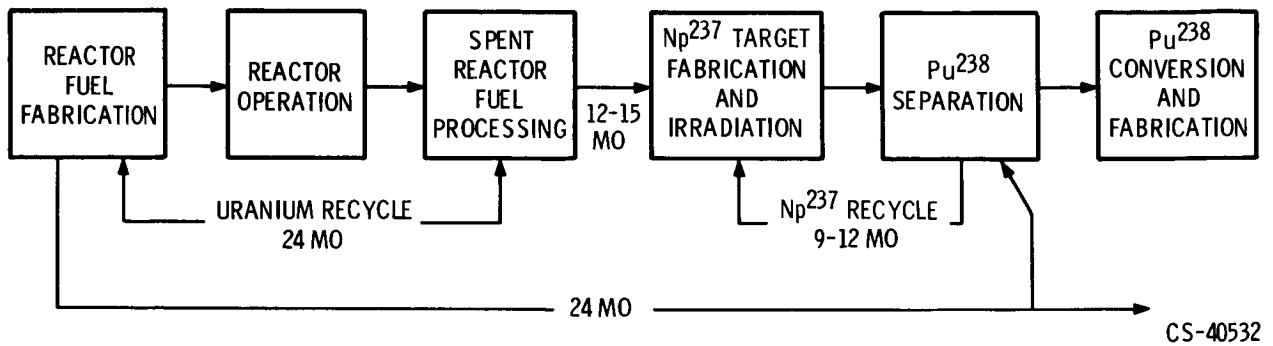


Figure IV-12. - Production of plutonium 238.

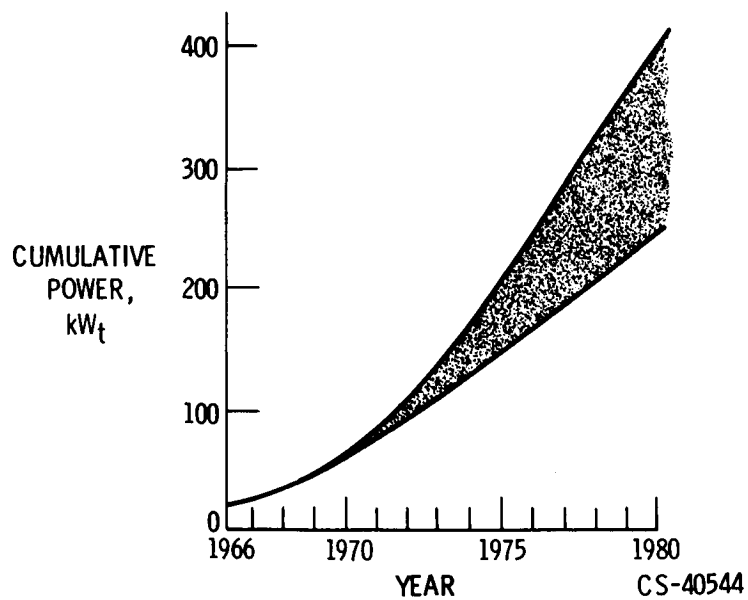


Figure IV-13. - Possible production of plutonium 238 by Atomic Energy Commission.

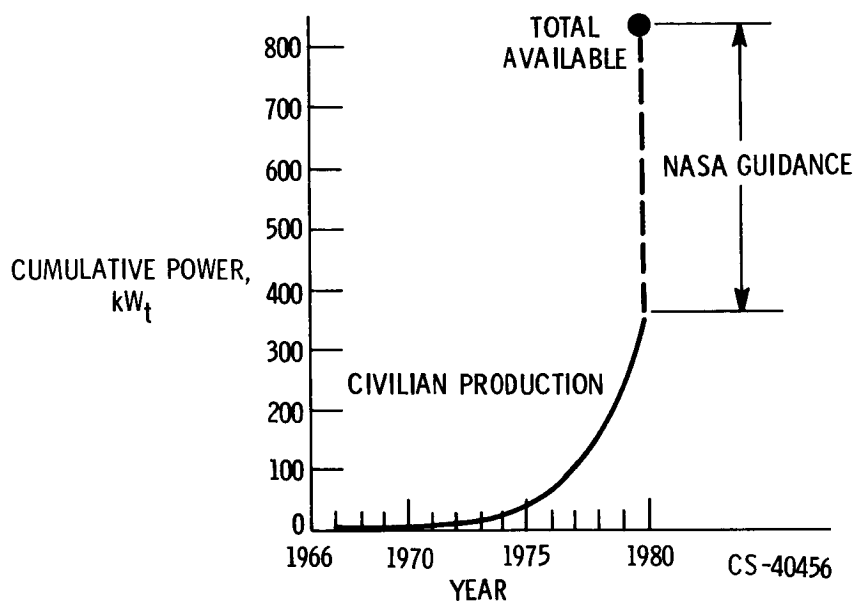


Figure IV-14. - Cumulative availability of plutonium 238.

V. BRAYTON CYCLE TECHNOLOGY

Warner L. Stewart, William J. Anderson, Daniel T. Bernatowicz,
Donald C. Guentert, Donald R. Packe, and Harold E. Rohlik

INTRODUCTION

The space power sources discussed in this conference can be divided into two general categories. The first, static sources, includes batteries, thermionic generators, solar cells, and fuel cells; it represents the direct-power conversion systems in which heat or chemical energy is converted directly into electrical current. The second, dynamic power sources, converts heat into electrical energy through an intermediate step that involves mechanical work. Power systems of this type include the familiar Rankine and Brayton systems and are of principal interest in the low kilowatt to megawatt level.

Although the Brayton cycle has been known for almost a century, the embodiment of its principles into practical engines occurred only in the last three decades through the development of the modern gas turbine engine. The principle by which this engine works is illustrated in figure V-1 where the major components required for airbreathing power applications are indicated. Air enters the compressor where its pressure is substantially raised. This high-pressure air then enters the combustor chamber, where fuel is added and burned. The high-pressure, high-temperature gas then expands through a turbine, spinning it, and producing mechanical work. Approximately two-thirds of this work is used to power the compressor, and the remaining one-third is used to drive the generator which, in turn, produces the useful electrical power.

When the Brayton cycle is applied to a space power system, the fundamental cycle as just described remains the same. However, since it is operating in a space environment, some modifications must be made. Such modifications can be noted in figure V-2 where the compressor, turbine, and generator previously described are shown in the lower right portion of the figure. The three major modifications include the following:

- (1) Since there is no air in space, the loop must be closed to reuse and to conserve the working gas. This closed-loop operation actually represents a considerable advantage, since it permits the use of working fluids with properties much more desirable than air.
- (2) Because of the closed-loop operation and the extended times of operation, the heat source must be of a different nature. Rather than burning fuel, heat sources such as solar and nuclear energy must be used. The heat so generated must then be transferred into the working loop by means of the indicated heat source exchanger.
- (3) Provision must be made to reduce the temperature of the gas prior to redirecting it back to the compressor. This is done by first passing the exhaust gas through a heat exchanger called

a recuperator, where heat is transferred back into the working fluid at the compressor exit. Such a step has the additional advantage of preheating the gas prior to going into the heat source and, thus, it improves substantially the efficiency of the cycle. Final cooling then takes place in the heat sink heat exchanger, where the remaining waste heat is transferred to a heat rejection loop. The heat is piped through a radiator where it is finally rejected to space.

From these considerations, it is evident that, although the basic cycle remains the same, additional components and considerable complexity arise when such a system is applied to space use.

The interest in the Brayton cycle for space power occurs for many reasons: (1) the extensive technology gained during the last 30 years in the gas turbine field can be drawn on and applied, (2) it has excellent prospects for applications where extended operation is required, (3) it is versatile in that a given system can cover a range of power levels and can be applied to a broad range of heat sources, and (4) it has potentially high cycle efficiency, thus making it a strong candidate for low-power applications where heat sources such as isotopic and solar energy are used and input energy is at a premium.

This interest has stimulated an extensive technology program at the Lewis Research Center aimed at obtaining a better understanding of its potential and exploring special problems that arise in its application. This paper reviews the technology program in terms of objectives, scope, and progress. Three general areas are discussed: (a) a review of the Brayton features as applied to a space power system, (b) a component technology discussion involving the performance and mechanical integrity of both rotating and heat transfer components, and (c) a system technology discussion directed at the questions of system control and startup.

BRAYTON POWER SYSTEM FEATURES

CYCLE DESCRIPTION

A better understanding of the features of the Brayton power system can be obtained by a comparison with the vapor, or Rankine, system. To do this, it is convenient to look at the temperature-entropy diagrams for the two cycles shown in figure V-3. In the Rankine cycle, a pump is used to pump the condensate returning from the radiator from a pressure corresponding with the condensing temperature up to a pressure corresponding with the boiling temperature. The liquid at high pressure is heated to boiling temperature, boiled along a constant temperature line, and expanded down to condensing pressure and temperature in a turbine that drives a generator. The vapor is then condensed and returned to the pump. It is important to note that the pressures in this cycle are determined by the vapor pressure - temperature relation of the working fluid and are not independent of the temperatures.

In the Brayton cycle, a compression process is followed by heating at approximately constant pressure, first in the recuperator and finally in the heat source where the gas is heated to the turbine inlet temperature. The gas is expanded through the turbine and is then cooled along an essentially constant pressure path, first through the recuperator and then through the radiator where the waste heat is rejected. The cycle is completed as the cooled gas from the radiator is

returned to the compressor. Because this is a gas cycle rather than a vapor cycle, the cycle pressure level is independent of the temperature.

In a comparison of the characteristics of the two cycles, it is first noted that the working fluids of interest in the Rankine cycle systems are liquid metals and involve a phase change. The working fluids in the Brayton cycle systems, on the other hand, are inert gases and involve no phase change. Certain problems or characteristics appear as a result of the nature of the working fluids involved in the two cycles.

The Rankine cycle, which utilizes a two-phase fluid, must contend with the problems of phase separation in a zero-g environment in both the boiling and condensing processes. The single-phase Brayton cycle is not subject to such zero-g effects. The liquid-metal working fluid of the Rankine cycle introduces problems associated with corrosion and mass transfer, while the use of an inert gas in the Brayton cycle eliminates such problems.

The two-phase Rankine cycle, however, offers a distinct advantage over the Brayton cycle in pump work, in that the pump work required to pump a liquid is much less than the compressor work required to compress the gas in the Brayton cycle. In a typical Brayton cycle system, almost two-thirds of the turbine work may be required to drive the compressor, leaving only one-third of the turbine work available as useful work. Because the useful work is rather small compared with the compressor or turbine work, a small percentage change in compressor or turbine work, resulting from small changes in efficiency or system pressure loss, will cause a relatively large percentage change in useful work. It can be seen, then, that the Brayton cycle performance is very sensitive to these factors, and there is a strong incentive to minimize system pressure losses and to maintain high turbomachinery efficiencies.

Another important difference between the Rankine and Brayton cycles is the cycle temperature ratio at which they operate. The cycle temperature ratio is defined as the ratio of the minimum temperature in the cycle, that is, the radiator discharge or compressor inlet temperature, to the maximum temperature in the cycle or the turbine inlet temperature. One minus this cycle temperature ratio is equal to the Carnot efficiency. As can be seen from the temperature-entropy diagram, the Rankine cycle operates at a much higher cycle temperature ratio than does the Brayton cycle. This is because of the pressure-temperature relation of a vapor in the Rankine cycle, such that low cycle temperature ratios are associated with very high expansion ratios, of the order of 100 to 1 at a cycle temperature ratio of 0.6. Thus, in Rankine systems of interest for space application, turbine problems associated with excessive expansion ratios and pump problems associated with low suction head place a lower practical limit on the cycle temperature ratio. The Brayton cycle, on the other hand, permits an independent selection of pressure and temperature, and the selection of turbine expansion ratio and cycle temperature ratio is reached through an optimization procedure involving tradeoffs between cycle efficiency and radiator area requirements. This procedure results typically in turbine expansion ratios around 2 to 1 or less and cycle temperature ratios around 0.25 to 0.30.

CYCLE EFFICIENCY

The capability of the Brayton cycle to operate at low cycle temperature ratios is favorable

from the standpoint of cycle efficiency, as shown in figure V-4. In this figure, cycle efficiency is plotted as a function of cycle temperature ratio for both the Brayton and the Rankine cycles. The crosshatched area represents the region of minimum practical cycle temperature ratio for the Rankine cycle, as previously discussed. Both curves show increasing cycle efficiency with decreasing cycle temperature ratio, but it can be seen that the Brayton cycle operates at cycle temperature ratios around 0.25 to 0.3, while the Rankine cycle is constrained to operate at cycle temperature ratios of around 0.65 to 0.7 or above. As a result, Rankine cycle efficiencies are lower than Brayton cycle efficiencies, even though the Rankine cycle is thermodynamically a more efficient cycle when operating between the same temperatures, that is, at the same cycle temperature ratio.

RADIATOR AREA

Although low cycle temperature ratios are favorable from the standpoint of high cycle efficiency, the associated low radiating temperature results in large radiator areas. This effect is shown in figure V-5, where specific prime radiator area is plotted as a function of cycle temperature ratio for a Brayton cycle and a Rankine cycle operating at a turbine inlet temperature of 1950°R and a sink temperature of 400°R . The crosshatched area again represents the region of limiting cycle temperature ratio for the Rankine cycle. It is seen that the Brayton cycle radiator area is quite sensitive to cycle temperature ratio as compared with the Rankine cycle and is an order of magnitude higher.

Because of this large radiator area requirement, a Brayton cycle operating at current turbine inlet temperatures in the range of 2000°R is of primary interest in relatively low power applications, measured in tens of kilowatts, where radiator area is not so dominant and high cycle efficiency may be important. Solar- and isotope-powered systems are examples of low power systems, where high cycle efficiency is desirable from the standpoint of minimizing the required size of a solar concentrator in a solar system or minimizing the isotope inventory requirements of an isotope-powered system.

It would be possible to reduce significantly the radiator area requirement of the Brayton cycle if turbine inlet temperatures could be increased. This effect is shown in figure V-6 where minimum specific prime radiator area is plotted as a function of turbine inlet temperature in $^{\circ}\text{R}$ for a sink temperature of 400°R . If the turbine inlet temperature could be increased to 3000°R , the specific radiator area could be reduced to one-third of that area required at present turbine inlet temperatures of about 2000°R . If material properties can be improved to a point where such increases in turbine inlet temperature can be achieved, the Brayton cycle may become of interest at higher power levels.

PRESSURE LEVEL AND MOLECULAR WEIGHT EFFECTS

It has been pointed out that the pressure level of the Brayton cycle can be selected independently of the cycle temperatures. Freedom to adjust pressure level is useful in two ways. First,

it permits the use of the same turbomachinery over a range of power levels through changes in pressure level. For example, the power of the compressor and turbine can be doubled by doubling the pressure. In this way, one set of turbomachinery could be the heart of a variety of power systems. Second, it permits a choice of the size of the components for any particular power range. In particular, it permits the use of more nearly optimum-sized turbomachinery. At low power levels where mass flows are small, the pressure level can be reduced to keep volume flows at reasonable levels. In this manner, extremely small turbomachinery diameters for which it is difficult to maintain high efficiency can be avoided. At low pressure levels, however, a penalty is paid in the form of larger heat exchanger components.

Another important variable affecting turbomachinery geometry in terms of both number of stages and size is the gas molecular weight. Figure V-7 shows the number of turbomachinery stages required and the relative size or diameter as a function of molecular weight. The number of stages shown is for an application for which one stage is required with argon (mol. wt, 40), and the size is shown relative to that required with argon. As molecular weight is decreased, the number of turbine stages required increases rapidly. Thus, an application requiring a single turbine stage with argon (mol. wt, 40) would require 2 stages with neon (mol. wt, 20) and 10 stages with helium (mol. wt, 4). At higher molecular weights, less than 1 stage is shown to be required. For these higher molecular weights, a single stage would be used, but it could be operated at lower speeds and stresses with obvious benefits.

Figure V-7 shows that, as molecular weight is increased, the turbomachinery diameter increases. For low power machinery, this can be a helpful trend. For example, a compressor that would be only 3 inches in diameter if argon were used, would be 20 percent larger, or 3.6 inches in diameter, with krypton (mol. wt, 83).

Gases of high molecular weight, therefore, are favorable to the turbomachinery, but these benefits are not obtained without some penalty. Here, a penalty is paid in increased heat exchanger size. This effect is shown in figure V-8, in which the bars indicate relative heat exchanger size (volume) associated with each of five inert gases, helium, neon, argon, krypton, and xenon, with the size normalized to 1 at helium's molecular weight of 4. The heat exchanger size associated with each of the pure gases increases with increasing molecular weight. A heat exchanger designed for use in argon is about 6 times as large as one designed for use in helium to meet the same requirements, while one designed for use in xenon would be almost 15 times as large. It is apparent, then, that the choice of the working fluid involves a tradeoff between the turbomachinery and the heat exchanger components.

It is possible to achieve the benefits of high molecular weight from the standpoint of the turbomachinery without such a large sacrifice in heat exchanger size through the use of mixtures of these inert gases rather than the pure gases. As long as the molecular weight is the same, the mixture and the pure gas behave the same in the turbomachinery, and the previous discussion about number of stages and diameter applies as well to mixtures. However, the thermal conductivity can be substantially improved by mixing the highly conductive helium with a heavy gas, like xenon, to give the desired molecular weight. The curve labeled helium-xenon gas mixture shows that, for each intermediate molecular weight (neon, argon, krypton), the improved conductivity of the mixture reduces the heat exchanger size to almost half.

Current interest is in gases with molecular weights in the range of 40 to 80 for power levels

from a few kilowatts to a few tens of kilowatts. In this range, the use of gas mixtures appears to be an attractive method for improving the heat transfer characteristics of the Brayton cycle working fluids, if problems such as possible preferential leakage of helium from the system are not encountered.

COMPONENT TECHNOLOGY

From the cycle discussion, it is evident that the components must have high performance in order to exploit the performance potential afforded by the Brayton cycle. In addition, these components must have within them the ingredients that give them high mechanical integrity and long life capability. These two concerns, performance and mechanical integrity of the components, are discussed herein. The section is divided into two major subareas, rotating components, which have more general application, and heat transfer components, some aspects of which must be tied to more specific applications.

ROTATING COMPONENTS

The discussion of the rotating components is divided into four parts. The first two deal with the performance aspect of the turbomachinery and generator involved, whereas the last two are concerned with the packages involved when these components are put together. The first of these sections discusses the use of gas bearings applied to Brayton packages, and the last part describes the results obtained to date in the investigation of one such package.

Turbomachinery Aerodynamics

Design considerations. - In the selection of turbomachinery for Brayton space power systems, two candidate compressors appear suitable, the single-stage centrifugal and the multistage axial. On the drive end of the shaft, radial- and axial-flow turbines may also be considered. The units shown in figures V-9 and V-10 are the rotors of two matched sets of turbine and compressor designed for a particular Brayton system. The compressor rotors (fig. V-9) includes a 6-inch-diameter radial-blade centrifugal unit and a six-stage 3.5-inch-diameter axial unit. The radial in-flow turbine rotor (fig. V-10) is about 6 inches in diameter and was designed to drive the centrifugal compressor. The axial turbine shown drives the six-stage compressor and has a tip diameter of 5.1 inches. The size of these components brings up several questions regarding fabrication and performance, and the importance of high component efficiency indicates careful consideration of the factors that influence efficiency. These have been explored in a program combining in-house and contract efforts.

There are several areas that must be considered before the turbine and compressor components of a given system are designed. Three major areas of concern include the selection of design point conditions consistent with high efficiency, the use of optimum geometry, and the

influence of small size and low Reynolds number on performance.

The selection of the design point operating conditions involves the use of optimum velocity diagrams, and selection of an optimum velocity diagram involves the use of curves such as that shown in figure V-11. In figure V-11, turbine efficiency, based on total pressures at the inlet and outlet, is shown as a function of the ratio of turbine tip speed to the isentropic gas velocity corresponding to the turbine expansion process. This ratio is commonly used to identify turbine velocity diagrams and the shape of the curve is typical of both radial and axial turbines. Efficiency goes to zero at zero speed and also at a high speed where the blades overspeed the gas flow to the extent that no turning takes place in the rotor.

The data points on the curve were obtained with the 6-inch radial turbine. The peak efficiency of 0.88 is quite satisfactory for this application and compares favorably with much larger turbines. The occurrence of peak efficiency at a velocity ratio of 0.7 is consistent with previous work in radial inflow turbines.

After selection of the optimum velocity diagram, the influence of overall geometry must be considered. Figure V-12 shows how geometry considerations affected the selection of rotative speed for the 6-inch radial turbocompressor. In figure V-12, compressor efficiency and tip radius are shown to vary with shaft speed for a given set of gas conditions and flows. The cross sections are compressor impellers corresponding to various combinations of radius and shaft speed when tip speed is fixed by the required pressure ratio and velocity diagram considerations. The inlet is about the same in each cross section. This results from an essentially constant volume flow as governed by cycle conditions. The impeller shape is, therefore, a function of speed. Past experience in the field has produced the illustrated efficiency variation, showing, for this example, an optimum speed near 35 000 rpm. The cross section here, then, shows the optimum overall geometry. The speed range shown in figure V-12 (35 000 to 60 000 rpm) includes the speeds of interest in Brayton space power systems.

Another consideration in the selection of the design point is associated specifically with the compressor. This may be seen in figure V-13, which shows experimental performance in argon of the 6-inch centrifugal compressor. Pressure ratio is plotted as a function of weight flow, ratioed to the design flow, for lines of constant speed. Efficiency is shown as contours superimposed on the speed lines. The location of the design point shows that the design combination of pressure ratio, speed, and flow was achieved in this design. The operational boundary on the left is the compressor surge line, which represents a condition of violent flow fluctuations with induced shaft and blade vibrations. Figure V-13 shows that the maximum efficiency at each speed occurs near the surge line. Safe operation of the compressor, however, requires a margin between surge and the design point. This involves a sacrifice in efficiency of about 2 points.

The selection of design point velocity diagrams, therefore, is made on the basis of an optimum blade-to-gas velocity ratio which yields maximum efficiency. Optimum geometry, also corresponding to maximum efficiency, is the influencing factor in the selection of rotating speed. In addition, to ensure safe operation of the compressor, there must be a safe margin between surge and any programmed operation.

Reynolds number and size effects. - The effect of Reynolds number on boundary layer behavior has been studied rather extensively. As Reynolds number is reduced in the turbulent regime, a progressive thickening of the boundary layer occurs. As Reynolds number is reduced further,

the flow in the boundary layer becomes laminar, and separation and increased loss are likely to occur. In order to determine the extent to which Reynolds number influences performance, experimental investigations were made over a wide range of Reynolds number using the 6-inch radial turbine and the 6-inch centrifugal compressor. Results of these tests are shown in figure V-14, in which total efficiency is plotted against Reynolds number based on rotor blade chord. Although a wide range in Reynolds number was covered, no sharp decreases in efficiency were observed. This indicates that there were no pronounced effects of laminar flow separation. The design Reynolds number for the compressor is about 300 000, and the maximum experimental efficiency was 0.79 at design speed.

The turbine efficiency was 0.88 at design speed, pressure ratio, and Reynolds number. The drop in efficiency, therefore, was only 0.02 in decreasing Reynolds number from 150 000 to the design value. The difference in efficiency levels between the compressor and turbine reflects the fact that turbines benefit from the accelerating internal flow, while the compressor must cope with appreciable flow decelerations and consequent higher losses. It can be pointed out that there is some concern regarding the performance of the axial flow machinery. The very short blade chords in both turbine and compressor result in design Reynolds numbers of 20 000 and 75 000, respectively. These axial flow machines are now being tested to determine the extent to which these low Reynolds numbers influence the efficiency levels.

Reynolds number and size are related directly by the characteristic length in the Reynolds number equation. There are other considerations, however, that obscure this relation when Reynolds number loss correlations are attempted. Other size factors include contour coordinate accuracy, flow area control, running blade tip clearances, and surface roughness. Therefore, a size study was initiated in the Lewis technology program. Figure V-15 shows the impeller of the 6-inch centrifugal compressor described previously and a similar compressor 3.2 inches in diameter. The tip diameter ratio is almost 2 to 1, and the flow area ratio is about 3.5 to 1. Also, a radial inflow turbine was made geometrically similar to that described in the Turbo-machinery Aerodynamics section. The two rotors are shown in figure V-16. The tip diameters are 6.0 and 4.6 inches and result in a diameter ratio of 1.3 and an area ratio of 1.7. These machines were tested over a range of Reynolds number, and the efficiencies are shown in figure V-17. Turbine total efficiencies plotted were measured at design equivalent speed and pressure ratio and, consequently, at the design value of blade-to-ideal-gas velocity ratio. The compressor efficiencies, however, are the maximum values of efficiency at design equivalent speed. Earlier correlations using design flow or pressure ratio at design speed were questionable because of the effects of thickened boundary layers on flow and also impeller-diffuser mismatch as Reynolds number was reduced. Both the compressor and the turbine show some size and Reynolds number effects. The differences associated with size vary from only a point or so in the compressor to two or three points in the turbine. From this, it can be concluded that size and Reynolds number can be important in space power system components, so some care must be exercised in selecting these parameters. The efficiency levels being achieved, however, are satisfactory for low-power Brayton applications.

Electric Generator

The electric generator converts the available shaft power into electric power to supply the many and varied loads that are typical of space power systems. In order to be applicable for a space power Brayton system, a generator must meet the following two criteria: it must be very reliable in order to operate over extended periods of time with zero maintenance, and it must convert mechanical to electrical power with high efficiency. In general, all other factors such as weight and size are of secondary importance in this application.

Reliability. - The question of reliability will be considered by first reviewing the conventional alternating current generator or alternator concept. Figure V-18 shows a simplified diagram of a conventional two-pole alternator with the field winding on the rotor. This machine has both brushes and slip rings on the shaft to carry current through the rotating field windings. The brushes are a continuous point of friction and wear and a source of contaminant particles for a space power system and are, therefore, a potential cause for unreliable operation. Because of the stringent reliability requirement, the brush slip ring concept is considered unsuitable for space power applications. While it is true that brushes can be eliminated by an additional winding and rotating rectifiers, as is popular in the aircraft industry, it is desired to improve further the inherent reliability of a space power system alternator by removing the windings entirely from the rotor, leaving only a solid magnetic path.

In an alternator, voltage is generated by the time rate of change of flux through the armature windings. Thus, any arrangement that causes flux variation with rotation will induce voltage in an armature coil. One such arrangement is shown in concept in figure V-19. This machine has both field and armature windings on the stator, the stationary magnetic element. The rotor has no windings. As the shaft rotates, once each revolution, the rotor pole faces become aligned with the stationary pole faces and, at this point, maximum flux through the iron occurs; at 180° rotation from this maximum, a minimum flux condition occurs. The changing flux thus induces armature voltage. Also, the flux through the rotor is always unidirectional because of the axial offset of the pole faces. In a real machine of this type with a cylindrical stator, the flux is not only unidirectional but constant as well. This constancy of flux all but eliminates eddy current heating losses in the rotor iron and, except for the pole faces, permits solid rather than laminated construction. One additional advantage of the solid rotor is that the field losses, which result in heat, occur on the stator in this type of machine, where cooling can be more easily provided.

Therefore, even though the conventional wound rotor alternator is lightweight and more efficient, the overriding reliability requirement indicates that the solid rotor alternator has the best potential for space power application.

There are many variations of solid rotor alternators. The choice of which variation to use depends on the system requirements. In the Turbomachinery Aerodynamics section, it is pointed out that, in order to achieve good performance, the turbocompressor shaft speed must run typically between 30 000 and 60 000 rpm. Solid rotor alternators, on the other hand, are better suited to a lower speed range, typically 10 000 to 40 000 rpm. In addition, the lower speeds are more desirable on the basis that power at 400 cps, which is a standard aircraft frequency for which there exists a vast technology and a wide variety of off-the-shelf devices, can be generated directly only at the lower speeds, for example at 12 000 rpm in a four-pole alternator. Depending

therefore on the requirements, the configuration of the Brayton system may be either a one-shaft or a two-shaft system, as shown in figure V-20.

The single-shaft system, shown in figure V-20(a), combines the turbine, alternator, and compressor on the same high-speed shaft, while the two-shaft system (fig. V-20(b)) has only the compressor and its turbine on a high-speed shaft and the alternator with a second turbine on a low-speed shaft. The single-shaft system has the advantage of being compact in size and easily integrated into the system. The two-shaft system is somewhat larger in total size and more difficult to integrate into the system; however, it provides lower output-power shaft speeds and allows independent development of both rotating packages.

Efficiency. - Efficiency is, of course, influenced by many factors. For the high speed alternators, windage losses are a significant element of efficiency. Thus, for high-speed operation, it would be desirable to design a rotor with a smooth surface. Figure V-21 shows a two-pole alternator rotor of this type. The bottom view shows the two-pole pieces before assembly. In the assembled rotor shown at the top, magnetic pole piece separation has been achieved by the use of a nonmagnetic filler material, in this case, Inconel. As can be seen, the rotor surface is smooth, which tends to minimize windage losses in the machine at high speed.

Where the system requirements permit a lower speed alternator configuration, a machine of the type shown in figure V-22 may be used. In figure V-22 is a view of the disassembled alternator. In this machine, pole separation is achieved on the rotor both by axial displacement and by elevation of the pole faces. Windage losses are minimized by end plates. It may be noted that this is a four-pole alternator, as opposed to the two-pole conceptual machine shown in figure V-18. The use of four-pole construction on the rotor permits mechanical balancing, but it also has the effect of doubling the output frequency for the same shaft speed. This machine is rated at 12 kilowatt output at a speed of 12 000 rpm and a frequency of 400 cps.

As part of the Lewis Research Center program to investigate their performance, two solid rotor alternators have been built. Both are 12 000 rpm, 400 cps machines of similar design. They include the aforementioned Brayton system 12-kilowatt machine and a 60-kilowatt machine for the SNAP-8 Rankine system. Figure V-23 plots the performance of these two machines at a power factor of 0.8. The solid line is a curve generated from loss measurements made on the 12-kilowatt Brayton machine. The data points are measured efficiencies of the 60-kilowatt SNAP-8 machine. It can be seen that the efficiency of both machines is essentially flat at about 91 to 92 percent over a wide power range. These efficiencies are electromagnetic efficiencies and do not include bearing losses.

Tests to date show that the lower speed solid rotor alternators have satisfactory performance and, although the performance of the high-speed machines has not been demonstrated, no significant problems are anticipated.

Magnetic unbalance. - Magnetic unbalance is of concern in a Brayton alternator because of the use of gas bearings. Figure V-24 is a schematic view of one end of the rotor shaft. The problem in this machine arises from the fact that the two diametrically opposite pole faces are of the same magnetic polarity. When the rotor is centered, as in figure V-24(a), the flux is uniform on both pole faces and balance is achieved. If the centerline of the rotor is displaced as shown in figure V-24(b), however, the flux through the small gap will increase while the flux through the large gap will decrease, thereby creating a net force of attraction toward the smaller gap. As

an example of the magnitude of the problem, analytical studies have shown that for the 12 kilowatt Brayton machine, a periodic force of attraction of up to 20 pounds would result from a 0.002-inch displacement in a machine with a 0.040-inch radial gap. The bearings would be required to supply an opposing force of equal magnitude. Studies, both analytical and experimental, are underway to fully evaluate this problem.

Gas Bearings

Design considerations. - Some of the system characteristics and operating conditions have a profound influence on bearing selection and design. (1) The system is required to operate for several thousand hours with a high degree of reliability and, during this time period, the inert gas working fluid must be kept clean. This makes it advantageous to use gas bearings. The use of oil-lubricated rolling bearings would result in greater power loss, weight, and complexity because of the need for seals and oil scavenge and separation systems. (2) The low pressure level and pressure ratio of the system dictate the use of self-acting or hydrodynamic bearings, which generate their own load capacity, as opposed to externally pressurized or hydrostatic bearings. Because of the low pressure drop available, purely hydrostatic bearings would not have sufficient load capacity unless the bearings were made quite large. (3) It is necessary for the power system to operate at high speeds and low loads to zero loads in a zero-gravity environment. This combination of operating conditions makes the stability characteristics of the bearings extremely important. Stable operation of the rotor or shaft in the bearing implies the absence of any motion of the shaft axis relative to the bearings other than simple synchronous eccentricity caused by shaft unbalance.

Journal bearings. - A conventional circular journal bearing, such as illustrated in figure V-25, is not suited for high-speed, low-load operation because of its tendency to be unstable. Under the action of a load, the journal center O_J deflects to form a fluid pressure wedge, but it does not move in the direction of the load. The resulting fluid film pressure force can therefore exert a moment about the bearing center O_B so that, if a momentary imbalance of forces occurs, it can drive the journal center into an orbital motion around the bearing center. This so-called whirl can destroy the bearing if its amplitude becomes great enough to cause a rub.

The most effective type of gas journal bearing in resisting whirl instabilities is the tilting or pivoted pad bearing. A four-pad pivoted journal bearing is shown in figure V-26. It consists of a journal and four pads, each of which is free to pivot so that it can adjust itself to the position of the shaft. Under zero external load conditions, a pivoted pad bearing can be set up geometrically so that each pad applies restoring forces to keep the shaft centered in the bearing. A wedge-shaped film is formed between each pad and the shaft, similar to that of a highly loaded ordinary journal bearing.

In addition to stability, load capacity, power loss, and running clearance are also important. The performance characteristics of a single pad of a typical three-pad bearing used in a Brayton turbocompressor are illustrated in figure V-27. Pad load capacity in pounds and pad friction in watts are shown as functions of minimum film thickness. The operating minimum film thickness is of the order of 0.0004 inch. At this minimum film thickness, the power loss is about 20 watts

for one pad, or 60 watts for a three-pad bearing. This is reasonable but, in small machines of only a few kilowatts, output bearing power loss can be a problem, so care must be taken to maintain adequate film thickness.

A problem that must be considered with self-acting bearings is that they have no load capacity at startup when there is no relative motion of the surfaces. Therefore, to avoid surface contact at startup, which could result in damage to the critical bearing surfaces, a system of external pressurization is used. The arrangement used, shown in figure V-28, consists of a bearing pad mounted on a diaphragm with a ball and socket pivot. Pressurized gas is fed through the pivot to avoid attaching lines to the pad; attachments would increase pad restraint, which is detrimental to bearing stability. The fitted ball and socket pivot is used to minimize leakage of the pressurizing gas. Pressurized gas is fed to four orifices on the pad surface. Figure V-29 shows the three journal bearing pads. The four orifices for hydrostatic jacking can be seen in each of two pads, and the pivot socket can be seen on the back side of the third pad.

Thermal considerations. - As might be surmised from the small film thicknesses, the gas journal bearings are quite sensitive to thermal distortion and differential thermal growth of the shaft and pad carriers. Minimum film thickness must be maintained within rigid limits, as can be seen in figure V-30. The permissible limits of minimum thickness are shown in the area bounded by the crosshatching. The minimum film thickness at the operating point is of the order of 0.0004 inch. With the pad pivots rigidly mounted, it would require a differential temperature of only a few degrees Fahrenheit to either completely take up all the bearing clearance and get into the overload area shown on the left or to increase the bearing clearance and get into the unstable operation area shown on the right. In a hot machine, this is obviously unacceptable.

One way to overcome these problems of maintaining pivot film thickness within rigid limits in a hot machine in which the parts undergo drastic changes in temperature is by mounting one or more of the pads on a soft spring, such as the diaphragm shown in figure V-28. This makes the journal bearings quite tolerant to otherwise hazardous thermal conditions. The effect of pad mount stiffness on thermal tolerance is shown in figure V-31. The relative thermal growth that can be tolerated is shown in the area bounded by the crosshatching. With rigid pad mounts, only a small amount of relative thermal growth can be permitted, since all of it appears as a change in the film thickness. With a spring mount, however, a large relative thermal growth can be permitted, since very little of it appears as a change in film thickness. Practically all of it is taken up as a deflection in the spring mount. A soft spring mount thus makes the bearing very tolerant to thermal conditions.

Thrust bearings. - Two types of thrust bearings being considered for application in Brayton machinery are illustrated in figure V-32: these are the Rayleigh step bearing and the spiral groove bearing. The Rayleigh step bearing is composed of a number of segments (the bearing shown in fig. V-32(a) has eight), each with a feed groove, a step, and a land area. Clockwise rotation of the smooth-faced mating runner drags gas across each of the eight steps where it is compressed. Four jacking orifices, used for external pressurization at startup, are located on the lands of alternate sectors.

The spiral groove bearing utilizes a large number of very shallow spirally cut grooves. Counterclockwise rotation of a smooth-faced runner causes gas to be pumped radially inward. A pressure rise is created, which supports the load. In the spiral groove bearing, the jacking

orifices are placed on the land area inside the grooves.

A photograph of the hydrodynamic thrust bearing used in a Brayton turbocompressor is shown in figure V-33. It is an eight-sector step bearing. The feed grooves, steps, and lands, as well as the four jacking gas orifices are visible in the figure.

Operating experience. - The operating experience to date with the Brayton turbocompressor at turbine inlet temperatures to 1250° F indicates that the bearings operate stably. Pains have been taken, however, to control the bearing thermal environment carefully. The magnetic loads imposed on the bearings in the turboalternator are still an unknown factor since this unit has not been operated. More work is required to develop bearings that are less thermally sensitive and generally more rugged.

In other machines such as helium blowers, gas bearings have demonstrated several thousand hours of reliable operation, although at lower temperatures than those in Brayton machinery.

Packaging

Temperature control. - The bearing considerations already discussed lead to numerous packaging problems, which include thermal isolation of the hot turbine area, minimum temperatures and temperature gradients in the bearing area, and flexibility in the bearing mounts. In order to explore and solve these problems, the turbocompressor component of a twin-shaft system is being operated at Lewis Research Center. This unit is shown in figure V-34. Visible are the compressor volute on the left, the turbine inlet scroll on the right, and the shell housing the bearing cavity between the two. The turbine and compressor are the radial units previously discussed. The package interior is shown schematically in figure V-35. Here again, the compressor is shown on the left and the turbine on the right. The thrust bearing, with a gimbaled stator, is mounted between the two journal bearings. The journal bearing cross section shows the low-spring-rate diaphragm mount of one pad in each journal bearing array of three pads. Three struts or columns, as shown at the bottom of figure V-35, support the compressor and turbine housings and the bearing carriers and thus control all running clearances.

Thermal isolation of the turbine area was accomplished with three major heat barriers; these include the thin-wall hollow section in the shaft adjacent to the turbine rotor, the two coated radiation shields, and the thin-wall hollow sections in each column at the hot end. These heat barriers interrupt the major heat paths as much as possible without sacrificing structural integrity.

Steps were also taken to minimize temperature gradients in the bearing area. Copper inserts in the shaft and column serve this purpose. The heat that does get through the heat barriers and the heat generated by bearing friction are removed by a small quantity of cooling gas and conduction to the compressor end of the package.

Preliminary investigation of the operating characteristics of the package has been made in a test facility that permitted slow starts and fine control of speed and flow. Figure V-36 shows the test installation with the shaft vertical in order to prevent gravity loads on the journal bearings. The compressor is at the top. About 70 instrument leads connect internal instruments with display and recording equipment in the control room. The investigation was made with turbine inlet

temperatures up to 1000° F, and successful self-acting operation of the bearings was obtained. Measured temperatures in all bearing parts showed a range of 27° with an average of about 300° F. These tests indicate that temperature controls designed into the unit have been fairly effective. The level of all internal temperatures will increase, of course, as turbine inlet temperature is increased to the design value of 1500° F.

Critical speed and shaft vibration. - An important factor in the design and operation of any rotating machinery is critical speed. Care must be taken to ensure that none of the natural frequencies of the system coincide with or are even near the design speed. The first two critical speeds are the rigid body criticals; one involves a conical motion of the shaft while the other is a cylindrical motion. These frequencies depend to a large extent on the spring rates of the bearing mounts. A third critical speed involves shaft bending, and the speed at which it occurs depends largely on shaft stiffness. The radial turbocompressor was designed to have the first two criticals occur at very low speeds and the third well above the design speed. A rotating mass cannot be perfectly balanced; consequently, there will be some exciting force at the critical speeds that will result in rotating loads and shaft excursions within the bearings.

Since it is important to know both the location of critical speeds and the magnitude of shaft excursions, shaft displacement probes were mounted near each journal bearing. Figure V-37 shows the arrangement of the probes relative to the hard- and soft-mounted pads. The probes are located in radial planes just outboard of the bearing pads, and the two at each journal are spaced 90° apart so that their outputs can be fed into the x-y inputs of an oscilloscope to provide an image of shaft motion. Figure V-38 shows a group of shaft orbits as observed during a recent test run. Speed is shown in the upper right corner of each frame in hundreds of rpm. Figure V-38(a) shows stable rotation with little or no eccentricity. Figure V-38(b) shows an elliptical orbit with a major axis of 0.001 inch. This was observed as the shaft accelerated through one of the critical speeds. Figure V-38(c) is a near-circular orbit indicating simple eccentricity with a diameter of 0.0005 inch.

The taped record of an acceleration was used to prepare a plot of the shaft motion as a function of speed. Figure V-39 shows maximum shaft center displacement plotted against rotative speed. Five distinct peaks were measured with two of these corresponding to the first and second critical speeds calculated with the high spring rate of the gas film in series with the hard mount. Two additional peaks at lower speeds may be attributed to the low spring rate of the diaphragm mount and gas film. There are, therefore, four distinct rigid body criticals corresponding to the translatory and conical modes with the hard- and soft-mount spring rates. The reason for the fifth peak is not clear, but it appears to be a test rig resonance. There is very little shaft displacement as the rotative speed increased from about 16 000 rpm to the design speed of 38 500 rpm. The third or bending critical occurs at 56 000 rpm, well above the design speed.

The main observations made to date are that the first and second criticals occur well below the design speed and that the very small shaft displacement obtained near design speed should not cause any trouble in sustained design operation. High-temperature and long-term operations have not yet been attempted. During all operations to date, however, the bearings have operated satisfactorily and, on one occasion, a valve malfunction caused a rapid deceleration from 80 per cent speed to zero through the compressor surge region of operation. The bearings, pressurized

at the time, maintained running clearances and suffered no apparent damage.

HEAT TRANSFER COMPONENTS

The discussion of the Brayton components associated with the transfer of heat is divided into two parts. The first part will discuss the recuperator and heat rejection system whereas the second part will cover the heat source component. The three sources discussed include solar, radioisotope, and nuclear reactor.

Recuperator and Heat Rejection

It has been mentioned that, for the Brayton cycle, a recuperator with high effectiveness and low pressure drop is needed. Fortunately, the technology in heat exchangers is far enough advanced that such high performance heat exchangers are not a special problem. Presently a recuperator is being fabricated for use with argon and designed to give an effectiveness of 90 percent and a pressure drop of about 2 percent. The core geometry is of the counterflow, plate-fin type, and the core performance has been validated by tests on air.

The heat rejection subsystem shown in figure V-2 consists of a liquid loop coupled to the gas loop by a heat exchanger. Cooling the gas in the radiator, without a liquid loop, was also considered. It was found that the extra gas pressure drop would cause a drop in output greater than the power needed to pump the liquid, and that the gas radiator would be heavier despite the elimination of the temperature drop in the heat exchanger.

Also, any changes in the gas radiator would tend to change the gas pressure drop and directly affect system output, thereby making conversion system performance quite dependent on radiator location and configuration. With the liquid loop, however, the radiator shape and location could be changed to meet different vehicle integration constraints without affecting conversion system performance.

The only apparent disadvantage of the liquid loop is that it adds complexity to the system and would tend to reduce reliability. Generally, however, a liquid cooling loop is needed to cool other components, such as the alternator and electric components, and adoption of a liquid loop for the main heat rejection system means only an enlargement of the loop rather than an incorporation of additional components.

Therefore, it appears to be preferable to use the liquid loop rather than the gas radiator.

Heat Sources

The Brayton cycle can be used with any energy source that can provide heat at the proper temperature. For space applications, the energy sources of principal interest are the Sun, radioisotopes, and nuclear reactors. Each has its advantages and disadvantages, and these factors vary in importance with the application. The nuclear sources are compact and require no special orientation, but they are hazardous. The solar heat sources do not have the hazards that the nuclear ones do and require less technology advancement to make a usable system. However,

they require orientation, special means to operate during shadow periods, and large areas to intercept the solar flux.

Solar heat source. - Figure V-40 shows a conceptual picture of a solar Brayton cycle system. The large concentrator or mirror focuses the sunlight into a receiver, in which the energy is transferred to the cycle gas. The conversion equipment is clustered around the receiver. The large, squat cylinder is the radiator and, in this concept, the concentrator could be stowed within it during launch.

To provide heat to a Brayton cycle furnishing 5 to 10 kilowatts of power, a concentrator 20 to 30 feet in diameter is required. In order to heat the cycle gas to 2000°R , the mirror surface accuracy required for high collection efficiency is moderate. To explore the problems of building a concentrator for the Brayton cycle, a prototype 20-foot-diameter unit is now being made. The approach in this program was to use conventional manufacturing techniques as much as possible and to avoid leaving residual stresses in the material to minimize changes in shape that might occur because of relief of stresses with time.

The concentrator consists of 12 magnesium sectors bolted together. A sector is seen at one step of the processing in figure V-41. The process is as follows: 1-inch-thick flat magnesium plates are polished on one side. Pockets are then machined into the back, leaving a ribbed structure that provides stiffening. These flat, machined sectors are placed on an accurately machined aluminum form, as in figure V-41. The form and sector are then heated and the load is applied to the sector, first mechanically by clamps (some of which are shown in fig. 41) and then by vacuum ports in the form. The sector is held at about 550°F under load for about 1 hour, and it deforms plastically and takes the shape of the form. The edges are machined to final dimensions and bolt holes are drilled.

An assembly is shown in figures V-42 and V-43, in which can be seen the ribbed back side and polished front. The polished magnesium surface is smooth but not shiny. The sectors are now being coated to make them mirrorlike. An epoxy layer is applied to the magnesium to give a glasslike surface on which the actual reflecting surface of aluminum is vacuum deposited.

The weight of this prototype is 1 pound per square foot. The geometric accuracy of this concentrator has not been fully evaluated yet, but preliminary measurements are encouraging.

The other solar heat source component is the receiver, which captures the concentrated solar energy and transfers it to the cycle gas. To provide the capability for power generation in the dark, some of the captured energy is stored in the receiver. The storage and release of this energy are accomplished by melting and freezing a material with a high heat of fusion, such as lithium fluoride.

Several different requirements must be met in the design of a receiver if it is to perform all its functions satisfactorily. The heat transfer into the cycle gas, the solar input, and the stored heat must be properly matched with respect to time as well as location. This can be accomplished only if the distribution of the fluoride is properly controlled. The distribution must be controlled in such a fashion that it is the same in zero g (for the ultimate use) and in 1 g (for meaningful ground testing). This distribution problem is difficult and crucial because lithium fluoride contracts 24 percent when it freezes. Therefore, the receiver must be designed to accommodate this contraction and expansion of fluoride. It is important to control the location of the fluoride, not only to provide the proper distribution of the stored heat but also to avoid the

danger of rupturing the container when the fluoride melts and expands. The receiver must also be able to tolerate the repeated temperature transients and accompanying thermal stresses as it passes through the many Sun-shade cycles.

A program to build a receiver using the concept shown in figure V-44 is now in its early phases. The gas enters the header at the bottom, is heated as it passes through the array of tubes, and exits at the top. The solar energy enters through the aperture and shines on the tubes.

A cutaway of a portion of one of the tubes is shown in figure V-45. The gas passes through the central tube, and rosette fins inside the tube improve the heat transfer to the gas. A bellows-type tube surrounds the gas tube, and the fluoride is contained within it. Clearance is provided between the bottom of each convolution and the central tube. The type of freezing pattern expected is also shown. The contours indicate the freeze line at different times. When the fluoride is completely melted, it fills the bellows. When the receiver enters the shade period, the gas will cool the fluoride. The first freezing will occur on the surface of the inner tube, and the solid will form a seal at the bottom of each convolution. Freezing will then progress in sealed compartments and, when fully frozen, each compartment will have a void. Without the sealing, liquid from one compartment could flow into voids in other compartments and overfill them. On melting, the overfilled compartment would rupture. It is hoped that this compartmentalizing will control the fluoride distribution, and the bellows geometry will ease thermal stresses and provide a finning effect to reduce hot spots. Work is now being initiated to evaluate this concept.

Radioisotope heat source. - Figure V-46 shows a possible future space station with a radioisotope Brayton cycle power supply. The radioisotope fuel is located in the two small rectangles at the far end of the vehicle. Two Brayton conversion units behind them furnish a total of 13 kilowatts. The radiator is in the vehicle skin. The system is very compact and requires no special orientation.

It was pointed out in Paper IV that the availability of attractive isotopes is limited. Therefore, the Brayton cycle with its high efficiency is attracting considerable attention for use with radioisotopes. Power outputs up to 10 or 15 kilowatts can be foreseen for radioisotope Brayton systems.

The present effort on radioisotope heat sources for use with a Brayton cycle consists primarily of studies. A fully acceptable design has not yet been evolved, but the effort is progressing in that direction. Figure V-47 schematically illustrates the basic elements that are felt to be required in a radioisotope Brayton system. The heat source contains the radioisotope fuel and radiates heat to a heat exchanger in the conversion system. This heat exchange by radiation allows independent handling, replacement, and disposal of the heat source.

A shield protects the crew or payload. One of the principal problems is that of hazard, not only prior and during actual use, but even after use; that is, how is the spent heat source to be disposed of? The best means of disposal appears now to be intact reentry from orbit and recovery on Earth. A reentry body for disposal is shown attached to the heat source (fig. V-47).

A door is shown as a means of cooling the fuel block by radiation in the event the conversion system fails and no longer draws heat. Such auxiliary means of cooling will also be necessary for shorter lived isotopes, which release excess power early in life. Heat sink material that

may be needed to prevent melting of the heat source in certain accidents such as a fire on the launch pad is also shown in figure V-47.

These then are the basic elements that now appear to be required, and studies are continuing to define these elements more fully.

Reactor heat source. - Figure V-48 shows a possible configuration for a 150-kilowatt nuclear reactor Brayton system. The reactor, shield, radiator, and redundant Brayton conversion equipment including the turbomachinery, recuperator, and waste heat exchanger are shown. In this concept, the reactor coolant is a liquid metal, and a liquid-metal-to-gas heat exchanger is buried in the shield.

All reactor systems require a heavy shield, which is relatively independent of power level. Therefore reactor systems are not of interest for powers below 20 or 30 kilowatts. As power level increases, the reactor systems become more and more attractive and, at 100 kilowatts or more, reactor power systems are the leading candidates.

It will be recalled, however, that the Brayton cycle requires a large radiator (typically several times larger than a Rankine cycle). At the higher powers, integration of the Brayton radiator into the launch vehicle envelope becomes a serious problem. Therefore, there is more incentive with the reactor Brayton system to raise the turbine inlet temperature as high as possible, up to the limit set by reactor technology.

The leading concern at this time is the definition of the reactor for a Brayton cycle system. Several important questions must be resolved: should the reactor coolant be gas or liquid-metal? What is a practical target for reactor operating temperature? What fuel and cladding materials should be used? More study is required before the picture can be clarified and the best reactor Brayton system defined.

SYSTEM TECHNOLOGY

In a complex system such as the Brayton space power generating system, certain problems arise due simply to the assemblage of a large amount of equipment into an integrated, coordinated, functioning machine. These problems cannot be identified exclusively with any one component but rather with the interactions among the components of the system. Thus, there is indeed a technology associated with an assemblage of components, which is known as system technology.

System technology seeks to understand the important variables in system operation so as to configure and control the system to an optimum performance. Of particular concern in system technology are the establishment and maintenance of a suitable system operating point, safe and reliable start and shutdown procedures, control of critical operating variables such as alternator frequency, and the identification and specifications for all peripheral hardware components necessary to perform these tasks.

Three areas of system technology for Brayton systems are discussed herein, namely, alternator speed control, system power level control, and system start. This section is an attempt to give the reader an insight into system technology and therefore does not cover all the problems that may arise. It is intended, however, to be descriptive in significant system technology study areas.

ALTERNATOR SPEED CONTROL

Fundamentally, the speed is controlled by balancing the turbine and alternator torques at the design speed. Practically, however, the electrical load on the alternator may not be constant and may switch, for example, as much as full on to full off and back at any time. In order to achieve a continuous torque balance at design speed, one of two choices must be made, as illustrated in figure V-49. As shown in the top portion of the figure, speed control may be achieved by controlling the total alternator load to balance at all times the power input to the turbine. For this type of control, alternator output power, which is not consumed as useful load, is diverted to a parasitic load and dumped overboard. In the lower portion of the figure, speed is controlled by varying the input power to the turbine in correspondence with the electrical power consumption by the useful load. In this method, high performance valving can be employed to control turbine input power on an instantaneous basis, thus diverting transient excess power away from the turbine, while a secondary control can adjust the average primary heat source power level on a long term basis to conserve energy. For reliability, the alternator load method is preferable since it has no moving parts and can be built from very reliable solid-state electronic or magnetic elements. It can be seen, however, that unused power from the alternator is wasted. This wasted power is of no consequence if the primary heat source is either infinite energy, such as a solar source, or continual decay, such as an isotope heated source. If, however, the energy source is finite and conservable (e.g., a nuclear reactor), a control responsive to load demand like the turbine input method would be desirable.

As part of the Brayton technology program at Lewis, an alternator load-type speed control was built and tested using solid-state current switching. Figure V-50 shows the experimental transient response of this speed control on a turboalternator. The useful load was switched from full off to full on and then, a few moments later, back to full off. The transient is the most severe that the speed control must accommodate. In the lower trace, it can be seen that, for both load changes, the maximum transient error in frequency was very small, in this case less than 1.5 percent of design frequency of 400 cps and lasting about 0.5 second. The final steady-state error is less than 1 percent. Thus, the alternator load-type speed control is able to maintain speed adequately within close tolerance limits.

The speed control, in effect, matches the alternator power to the turbine power. Matching the system power to the heat source power is now considered.

POWER LEVEL CONTROL

It has been pointed out that control of Brayton system power level is important in order to efficiently convert the power available from the prime heat source to electrical output. The motivation for this control is somewhat different depending on the particular heat source used, that is, isotope, solar, or reactor. The peculiarities of each of these heat sources are shown in figure V-51. For the isotope, the power level decays exponentially with time typical of isotope behavior. For the solar source, the available power oscillates between zero and some maximum as the system orbits the Earth and passes through the Earth's shadow. In the solar

system, a heat storage device, the receiver, which is discussed in the Solar Heat Source section, is introduced between the solar source and the conversion system in order to average out the power over the Sun-shade cycles. It is also expected that, over the system lifetime, the net solar input to the system may degrade, because of concentrator surface deterioration, for example.

The reactor is directly controllable in power level; however, it is energy limited and, as figure 51 shows, it may be operated either at a design power level for a fixed period of time or at a reduced power level for a longer period of time.

Before power level matching with these three power sources is discussed, it is necessary first to examine a characteristic that is peculiar to the solar energy source and is due to the requirement for a heat storage device. Figure V-52 illustrates the system behavior for the case where there is a deficit of solar input energy; that is, there is less solar energy per orbit than the system consumes at rated power. Since the receiver (or absorber) concept is to store heat as heat of fusion, the temperature of the storage material will remain constant only as long as the material stays between a fully melted and a fully frozen condition. Where a solar input energy deficit exists, however, the heat storage material will become fully frozen before the end of the shade period and will enter the sensible heat region where the temperature drops rapidly. As a result, the absorber outlet temperature, or turbine inlet temperature, begins to fall and will continue to drop until the system reenters the sunlight.

This drop in turbine inlet temperature, with consequent reduction in cycle efficiency, results in a drop in alternator output power, as shown in figure V-52, with a minimum occurring at the end of the shade period. Because of the aforementioned effects, the drop in alternator output with the solar system is more severe than that for the other energy sources, as can be seen in figure V-53.

The solar curve shows that, for a 10 percent decrease in solar input, the alternator output power drops to about 65 percent of rated output at the end of the shade period (fig. V-52). This is obviously an undesirable situation.

For the isotope curve, the alternator power does not drop linearly with source power but has a curvature upward. This trend results from variations in cycle efficiency caused by the combined effects of increasing heat transfer component effectiveness and decreasing turbine inlet temperature as source power decreases, as well as by changes in turbomachinery performance as their operating point changes.

The reactor system does not show any deviation since the power level of the reactor can be independently controlled. However, as mentioned in the alternator speed control section, it would be desirable to be able to efficiently throttle back on reactor power when it is not needed in order to extend the lifetime of the system. These three curves (fig. V-53) indicate that some means of controlling system power level would be highly desirable.

Analog computer system studies were undertaken to determine the most effective control for this purpose. The dashed curve in figure V-53 shows the benefits resulting from the use of a system pressure level control to match the system power demand to the available heat source power. Relative system pressure level is shown as a parameter along the curve. Through the use of such a pressure control, a 20 percent decrease in heat source power can be accommodated with a decrease in alternator power of less than 10 percent. For the solar source, the use of a

system pressure level control results in maintaining the receiver in the heat of fusion region at all times. For the isotope source, it is a means of maintaining turbine inlet temperature as power degrades, thus maintaining high cycle efficiency. For the reactor, it is a means of efficiently reducing power demand in order to extend operating time.

While figure V-53 shows data for a two-shaft Brayton system, preliminary investigations of a one-shaft configuration have shown a similar benefit from pressure control. Thus, Lewis computer studies have shown that system pressure control is an effective means of matching the Brayton conversion system to the power source.

On the basis of the results of analog studies, it has been concluded that there is no fundamental reason that will prevent adequate control of the Brayton power system. However, work on system hardware is just getting underway, and problems may still arise.

SYSTEM START

The final item of system technology to be discussed is system start. The method of start is, of course, dependent on the particular system configuration. For a two-shaft Brayton system, various start procedures have been studied using an analog computer dynamic system simulation. The start method finally chosen utilized an injection of the cycle gas through the turbine into the evacuated system to bring the turbocompressor up to speed. This method requires some peripheral equipment shown in figure V-54. In this figure, the solar Brayton configuration is illustrated as an example, and the peripheral components are indicated by the numbers: (1) A primary heat source control, to start the system, is given the command to bring the source to working temperature. (2) The alternator field must be externally powered during start to ensure that electrical power will immediately be available to control speed. (3) The application of jacking gas to lift off the gas bearing occurs next for the turboalternator and turbocompressor. The bearings are operated hydrostatically until the rotating units are up to speed; (4) The gas bottle and injection valve, the isolation valve to prevent back flow during gas injection, and the exhaust valve used to evacuate the system are shown.

Various start procedures have been studied, including various injection flow rates and with and without the system exhaust valve open. These studies show that, because of the volume of the heat exchanger components, the system can be started successfully at 20 percent of rated flow with the exhaust to space valve closed. This particular start procedure is shown in figure V-55. Note the expanded insert on the time axis for a 1 minute period during the start. Time zero is taken, using the solar Brayton system as an example, as the moment the system enters the sunlight.

The step by step sequence is as follows: once in orbit, the system is given the command to bring the primary heat source up to temperature, in this case, to bring the absorber melt quality to 1.0 as shown by the top trace. After an appropriate period of time, injection of gas inventory into the system is begun, as shown by the second trace. The isolation valve is closed at this time to prevent backflow of the injected gas. The gas exits from the absorber and enters the turbine at rated temperature, bringing the turbocompressor up to speed in about 15 seconds. At some point in the turbocompressor speedup, the compressor discharge pressure exceeds the injection pressure downstream of the isolation valve, and the valve is driven full open. The

compressor flow then adds to the injection flow, and the system bootstraps itself up to rated conditions. The turboalternator speedup follows the turbocompressor speedup with the speed control taking over when the alternator reaches rated frequency. The turboalternator power overshoots, however, for about the first 30 minutes of operation because of initially cold radiator and, therefore, higher cycle efficiency.

The single-shaft Brayton system may be also started in the manner just described. In addition, however, it may be possible to start the single-shaft system by running the alternator as a motor on an inverter from battery power. This start scheme has not been fully studied as yet.

As part of the Lewis in-house study of Brayton systems, a breadboard loop has been built into which the turbocompressor discussed herein has been placed. Progress in this program has been made to a point where the system has been started through closed-loop injection several times. One such time history of a start sequence is presented in figure V-56. At the 2-second point, the injection valve was opened, forcing the gas through the heater and turbine and spinning it up rapidly to over 17 000 rpm. At the 4-second point, the isolation valve was opened, permitting the gas to circulate through the loop. The temperature level into the turbine had risen to 1100° R in the meantime. This temperature is insufficient for self-sustained operation so the speed is noted to drift off. However, the inlet temperature continued to rise as rig parts approached equilibrium temperatures and, at the 50-second point, it had risen to 1250° R where it was sufficient for development of net work from the system. From this point on, the turbocompressor proceeded to accelerate in a self-sustained manner up to equilibrium speed. The equilibrium speed ultimately reached was approximately 25 000 rpm. These results are very encouraging, and it appears that the start of a Brayton system should be a rather straightforward process with the prospect of closed-loop starting being reasonably good.

CONCLUDING REMARKS

From the Brayton technology discussion it is evident that this type power system embodies a wide variety of technology areas. Although all cannot be summarized, some of the major points brought out can be reviewed.

1. From the cycle discussion, it was indicated that relatively large radiator areas are required. This factor, together with the high potential cycle efficiency, results in the principal emphasis being placed on low and intermediate power level applications where cycle performance dominates. Also it was indicated that working fluid pressure levels and the use of inert gas of varying molecular weights are extremely valuable tools in the selection of optimum component geometry for a given application.

2. From the component investigations to date, it can be concluded that acceptable performance can be obtained, particularly with respect to the most critical turbomachinery involved. The gas bearing program has indicated that they work stably and with acceptable loss. From the packaging program, control of the internal thermal conditions appears to be of major concern.

3. The system studies have indicated that control of pressure level through inventory modulations is an extremely valuable tool in the control of power output. Starting studies have also

indicated that this aspect of operation should be relatively straightforward.

It should be emphasized that there is still much ground to cover before the assessment of the Brayton system is complete. The package program, for example, has not progressed to a point where major conclusions regarding mechanical integrity and life can be drawn. The study of magnetic unbalance in the alternator component and its effect on gas bearing design and operation has only begun. It was also indicated herein that much progress must still be made in the area of the heat sources. Thus, it is evident that, although substantial advances have been made and results obtained to date are encouraging, considerable effort is still required before ultimate conclusions can be recorded regarding the Brayton cycle for space power.

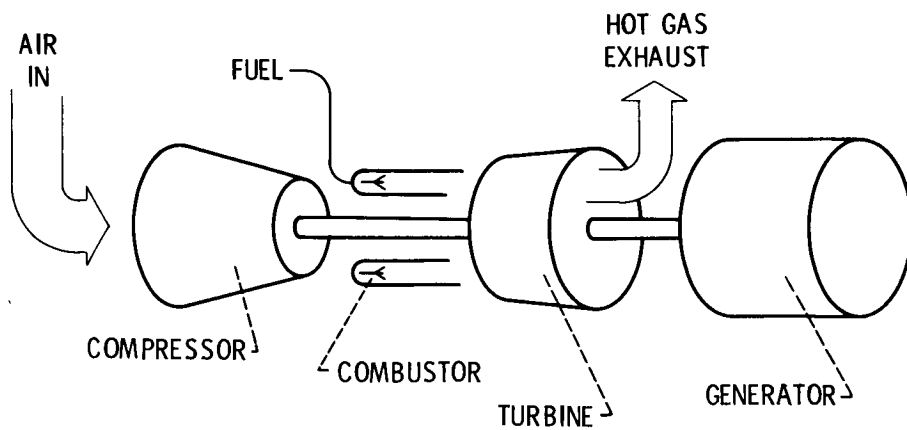


Figure V-1. - Gas turbine Brayton power system. CS-40258

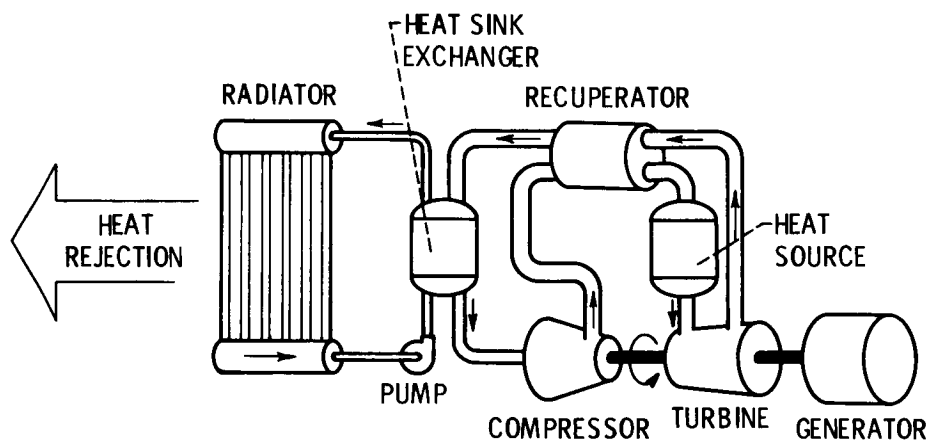
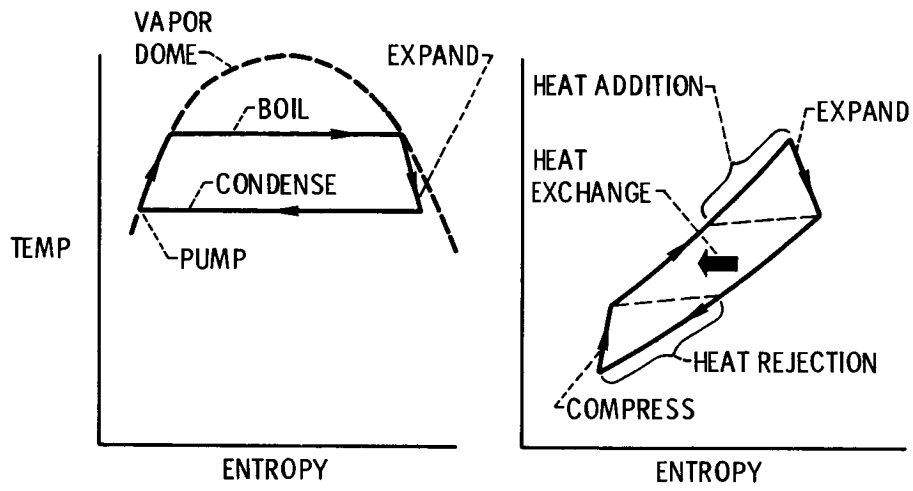


Figure V-2. - Brayton cycle space power system. CS-40312

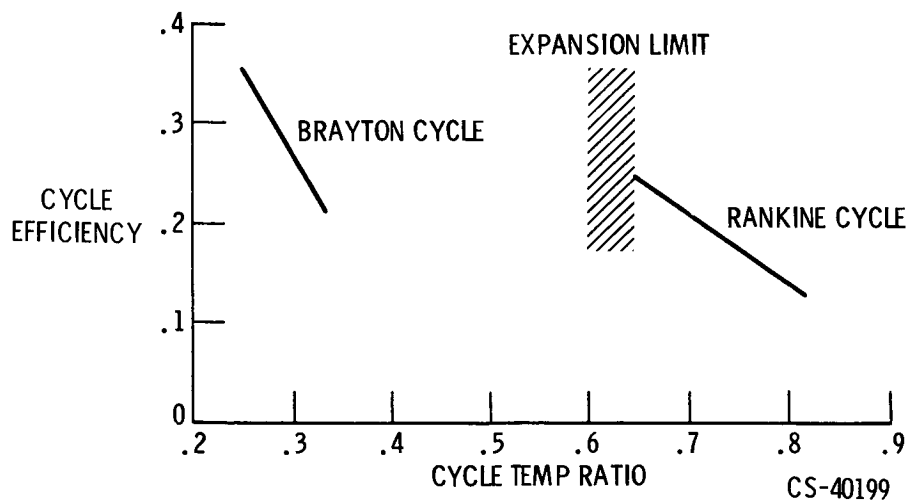


CS-40200

(a) Rankine system.

(b) Brayton system.

Figure V-3. - Cycle thermodynamic comparison.



CS-40199

Figure V-4. - Cycle efficiency comparison.

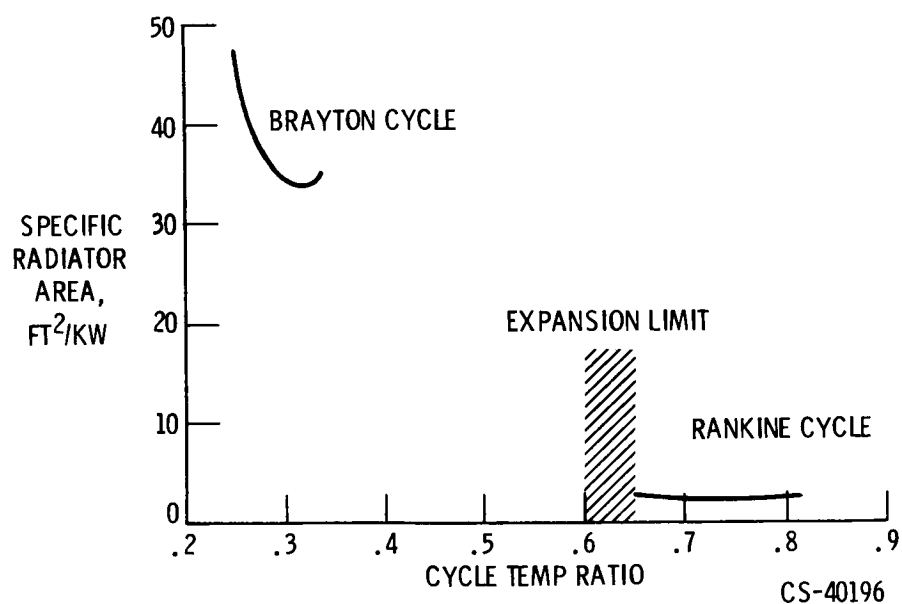


Figure V-5. - Radiator area comparison. Turbine inlet temperature, 1950°R ; sink temperature, 400°R .

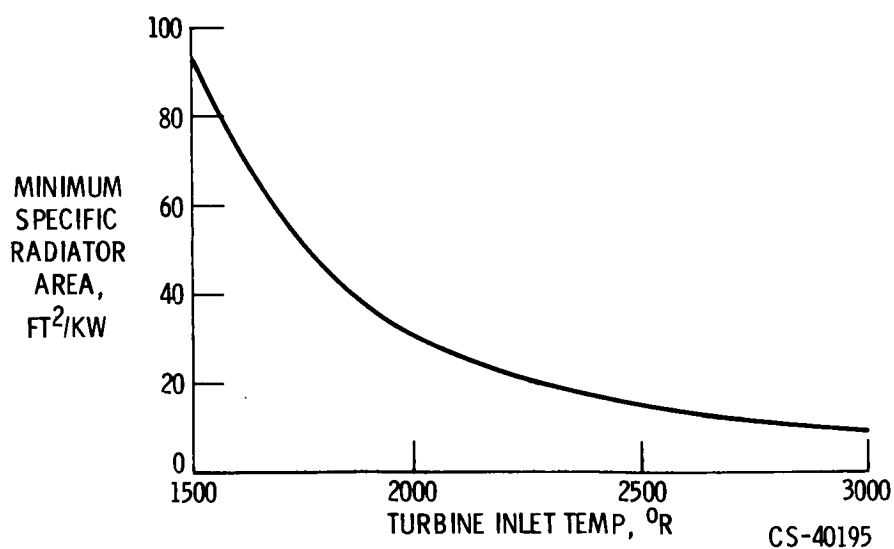


Figure V-6. - Effect of turbine-inlet temperature on radiator area. Sink temperature, 400°R .

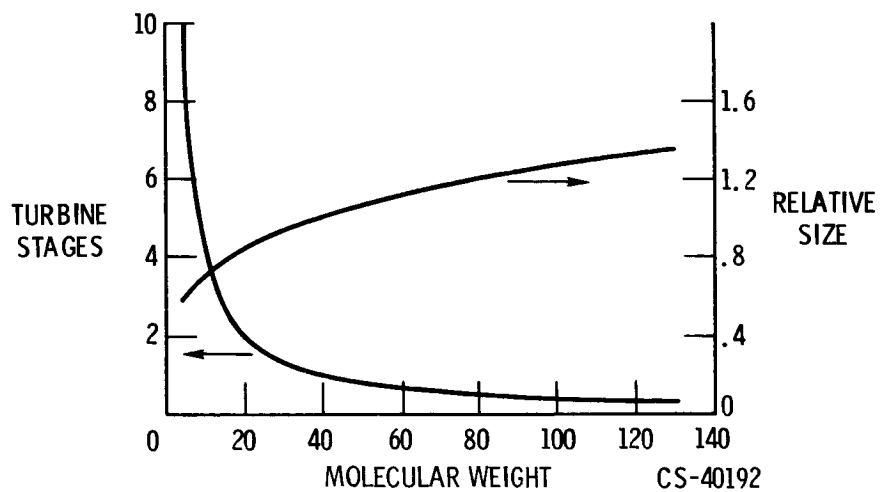


Figure V-7. - Effect of molecular weight on turbomachinery.

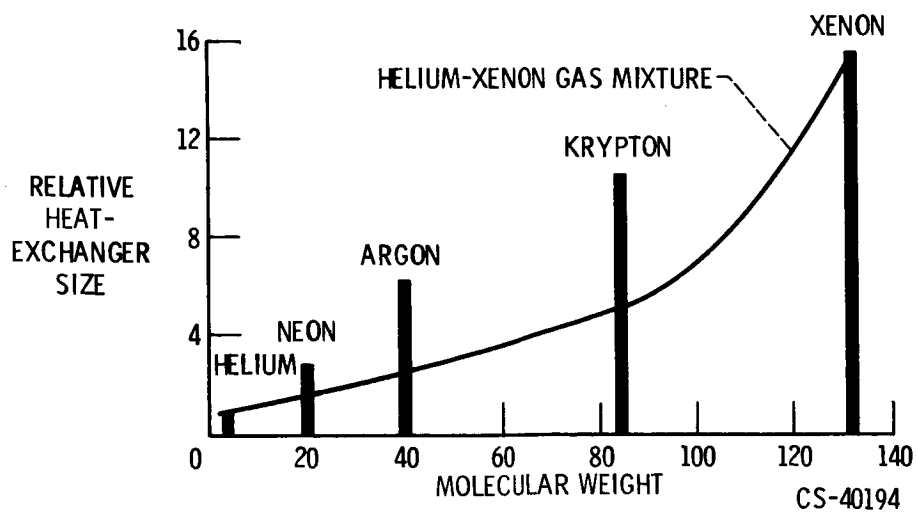
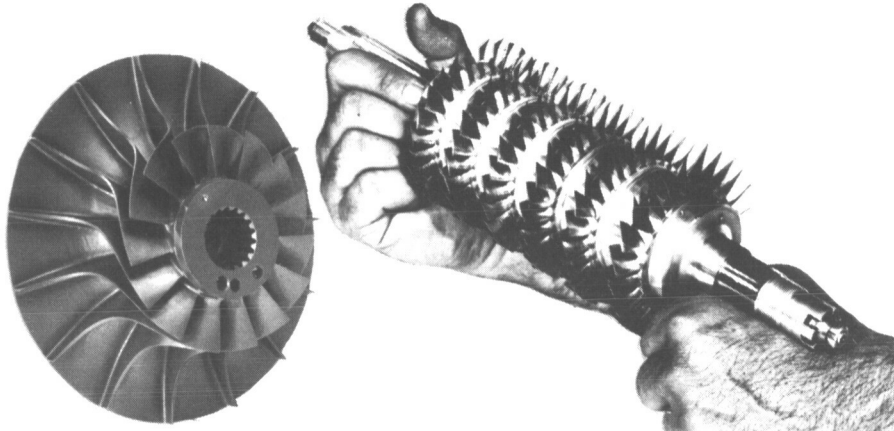


Figure V-8. - Effect of molecular weight on heat-exchanger size.

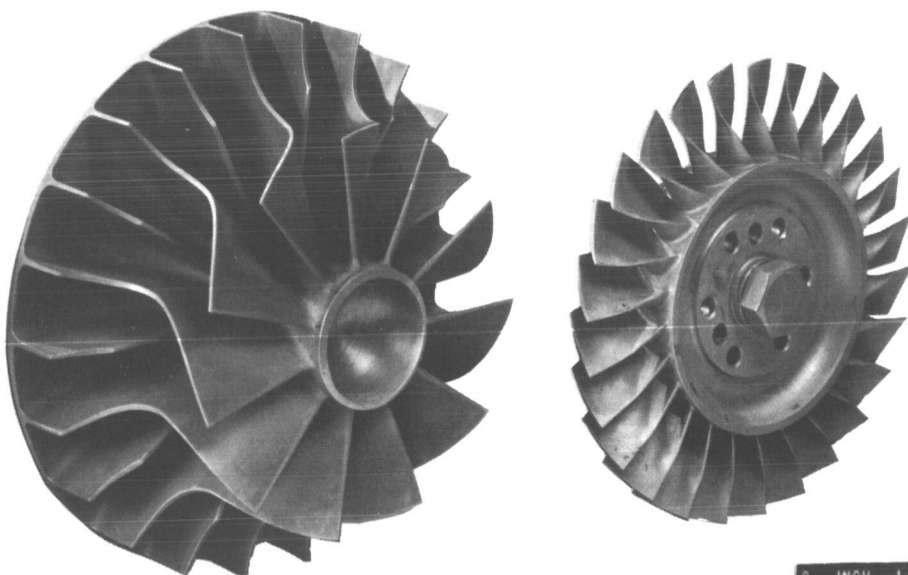


CS-40274

(a) Centrifugal.

(b) Axial.

Figure V-9. - Brayton-cycle compressors.

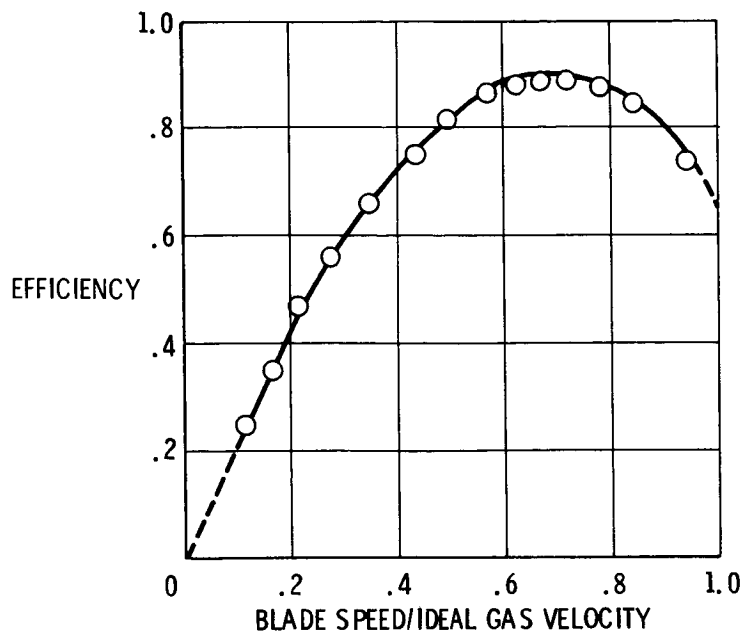


CS-40265

(a) Radial.

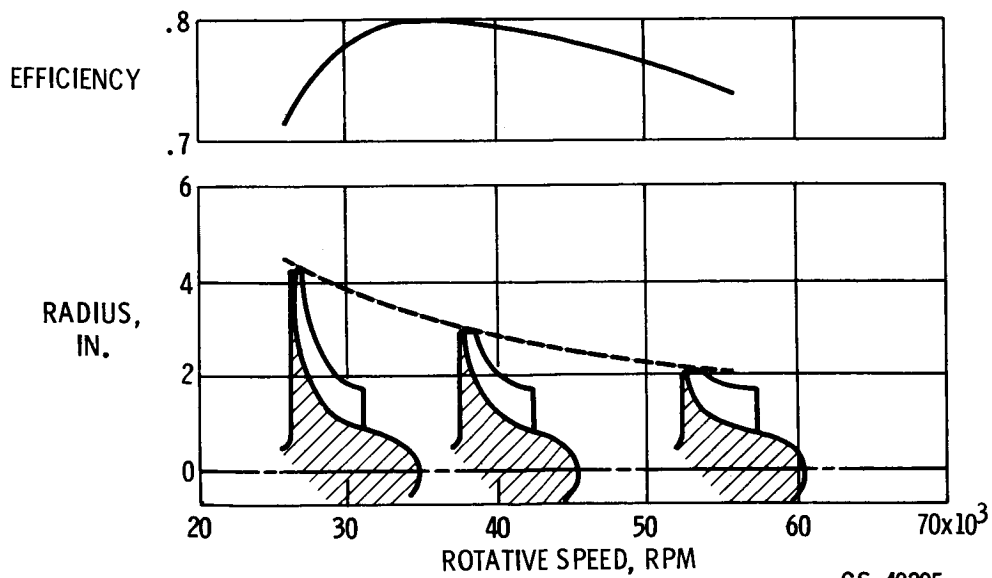
(b) Axial.

Figure V-10. - Brayton-cycle turbines.



CS-40209

Figure V-11. - Radial turbine performance. Diameter, 6 inches; fluid, argon.



CS-40205

Figure V-12. - Centrifugal compressor efficiency - geometry relation.

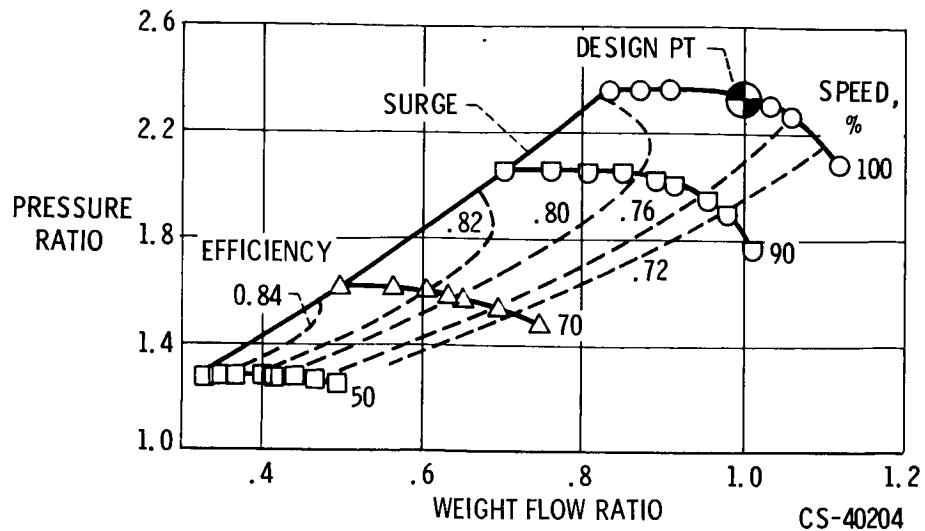


Figure V-13. - Centrifugal compressor performance. Diameter, 6 inches; fluid, argon.

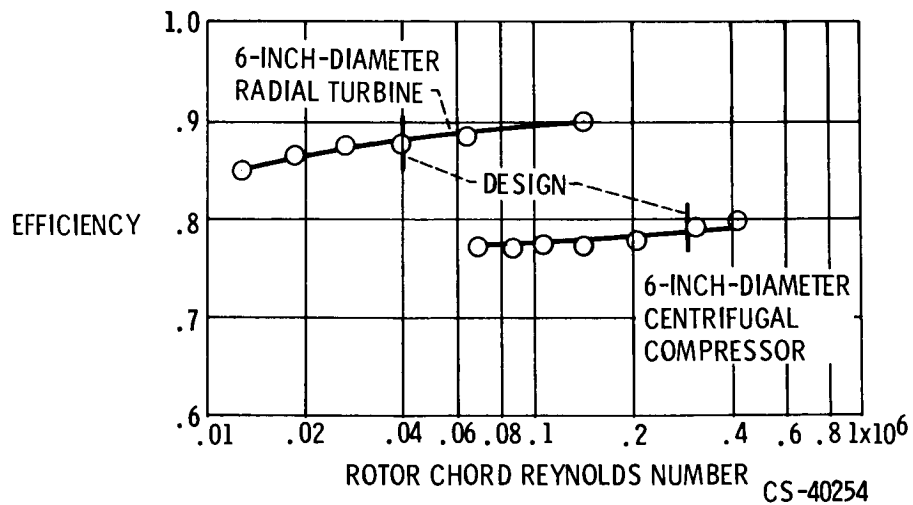
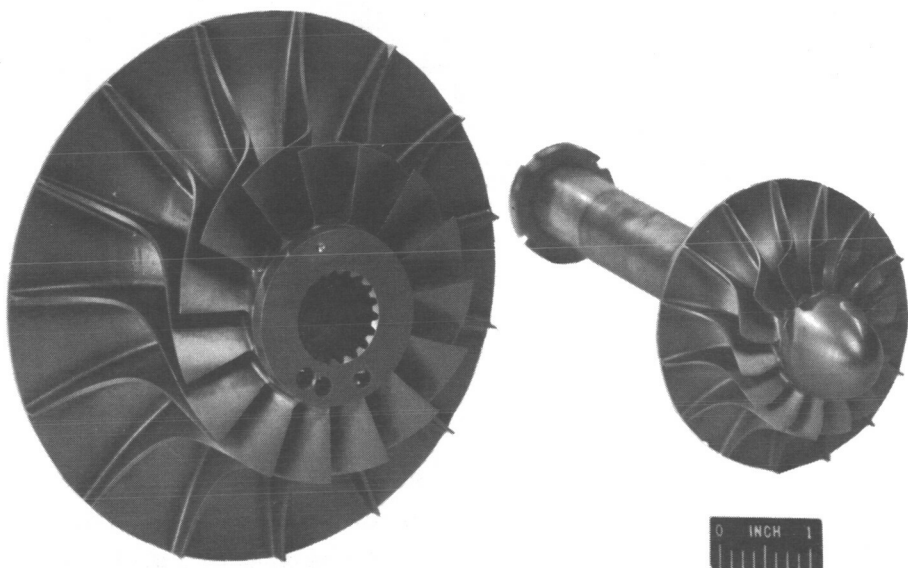


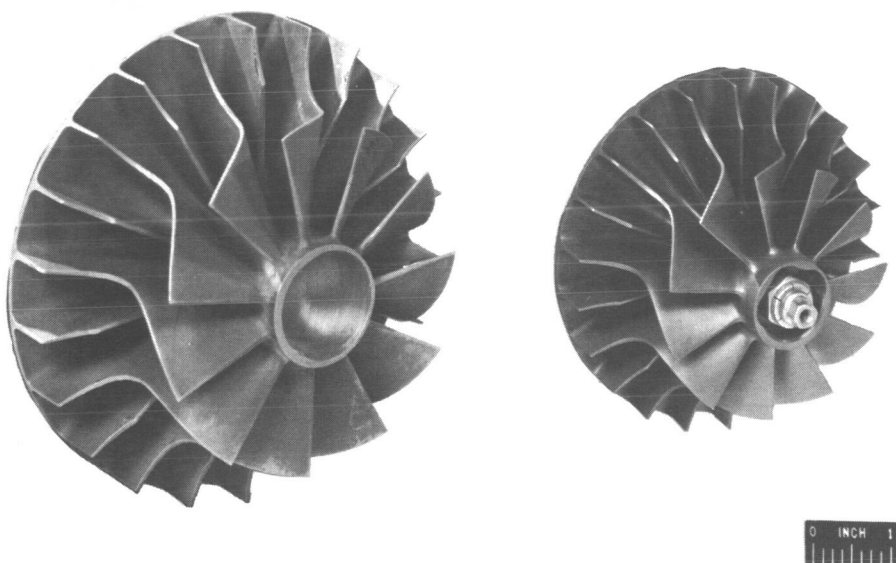
Figure V-14. - Effect of Reynolds number on efficiency. Turbine fluid, argon; compressor fluid, air.



(a) 6.0-Inch diameter.

(b) 3.2-Inch diameter. CS-40268

Figure V-15. - Compressors for size effect study.



(a) 6.0-Inch diameter.

(b) 4.6-Inch diameter. CS-40267

Figure V-16. - Turbines for size effect study.

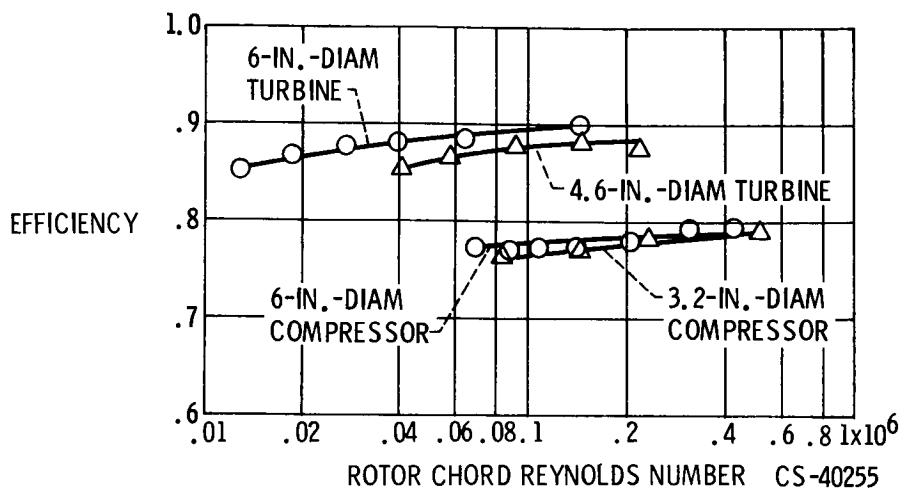


Figure V-17. - Effects of Reynolds number and size on efficiency. Turbine fluid, argon; compressor fluid, air.

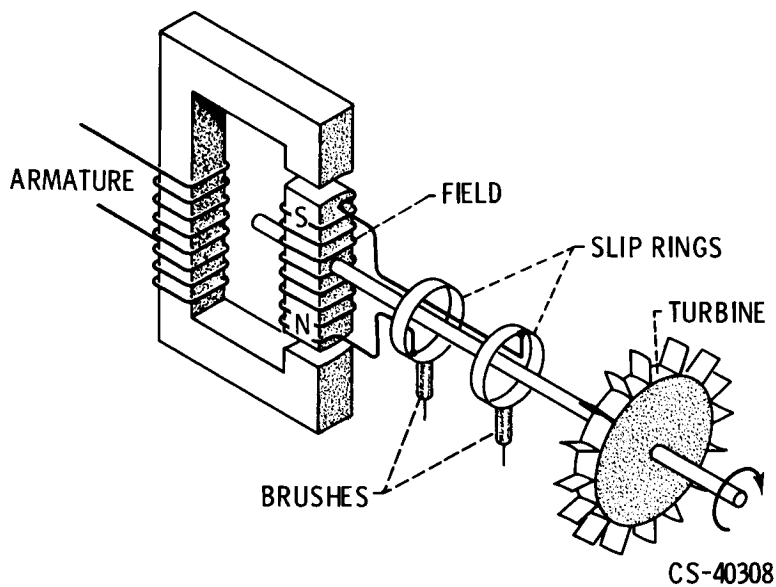


Figure V-18. - Conventional wound rotor alternator.

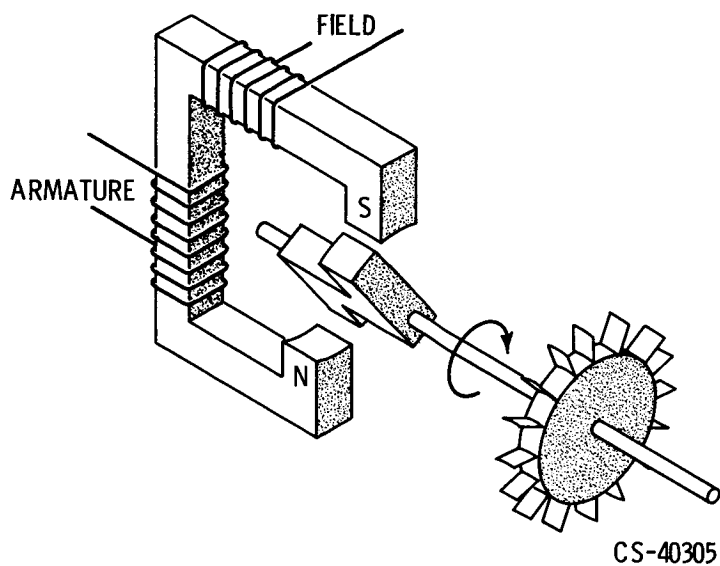


Figure V-19. - Brushless solid rotor alternator.

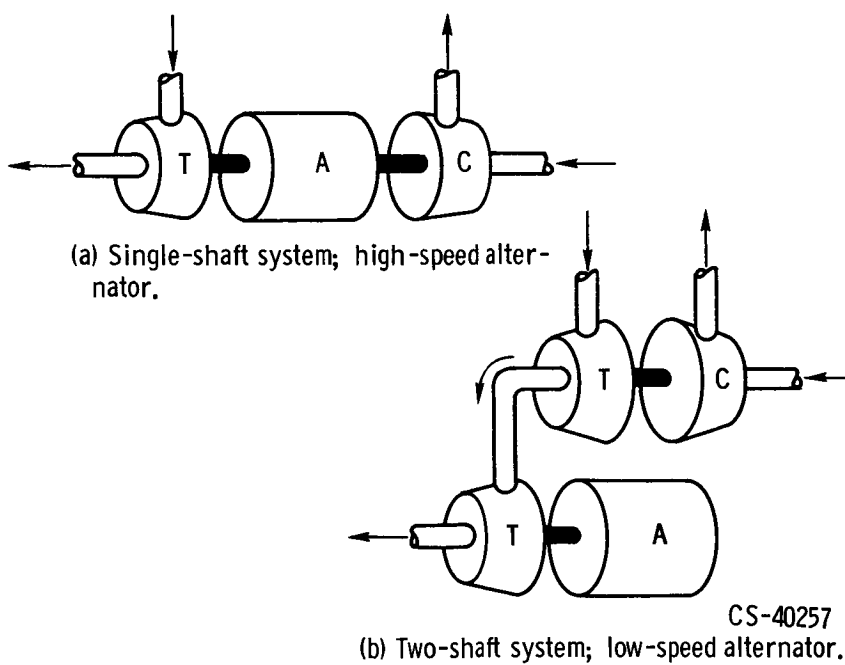
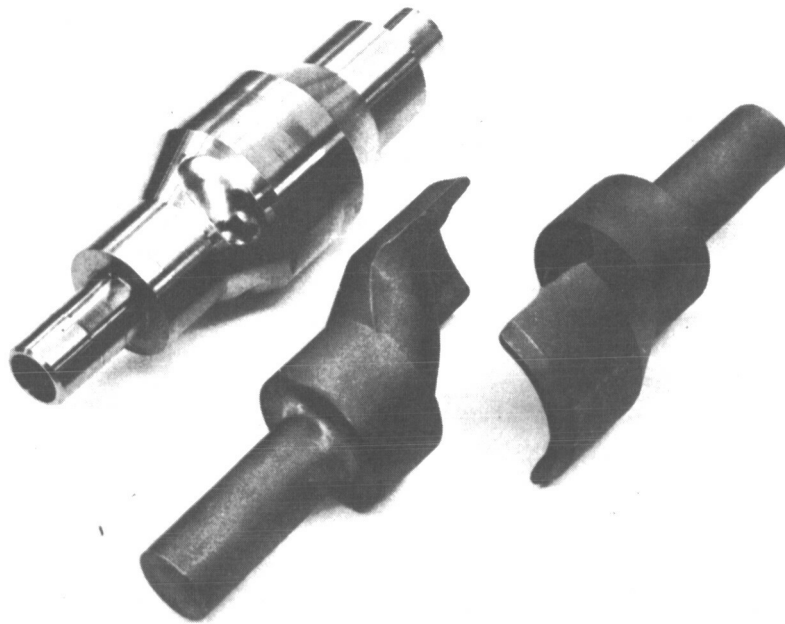
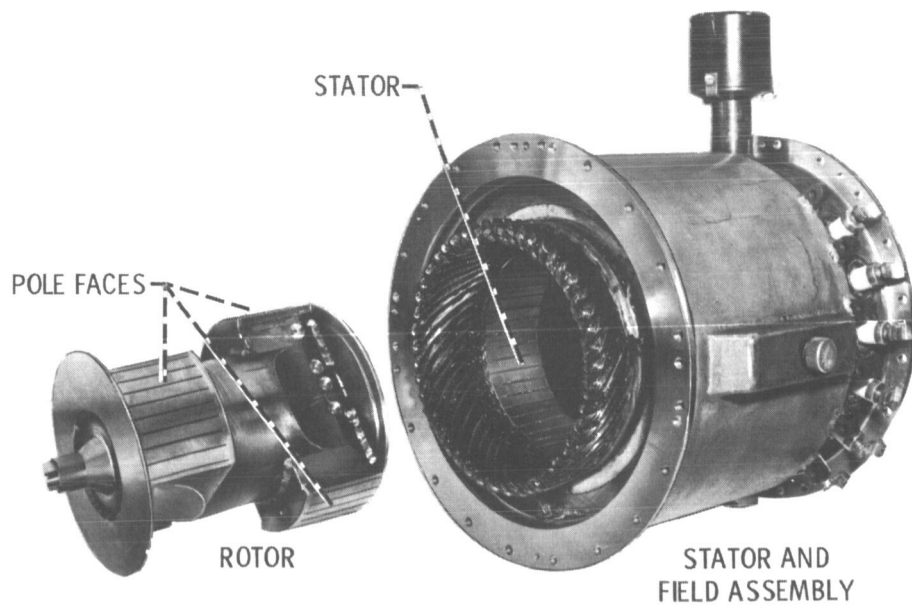


Figure V-20. - Shaft arrangements.



CS-40369

Figure V-21. - High-speed solid rotor.



CS-40367

Figure V-22. - Brayton solid rotor alternator.

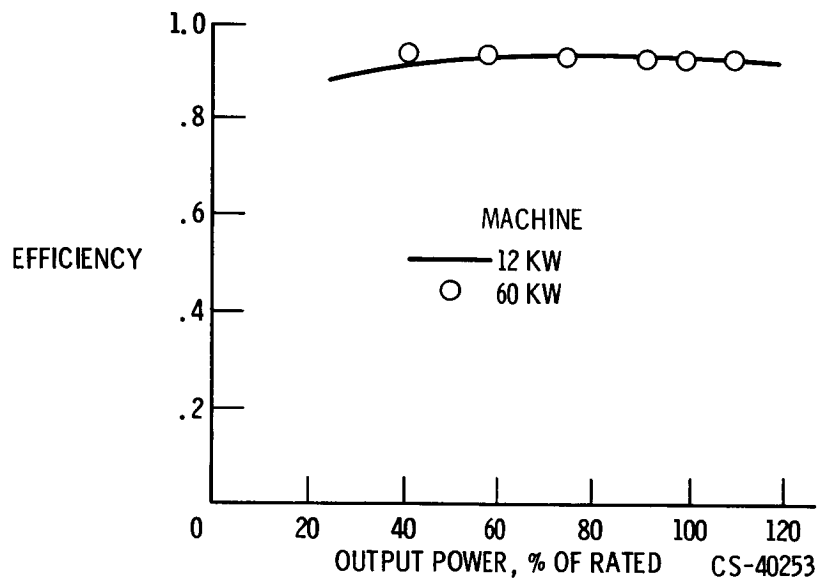
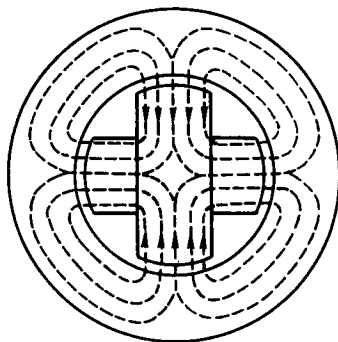
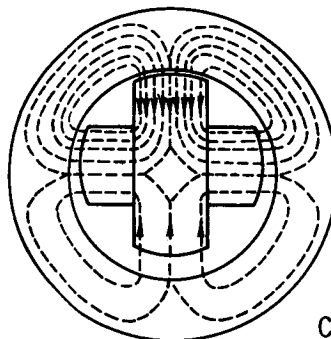


Figure V-23. - Solid rotor alternator performance. Power factor, 0.8.



(a) Uniform flux.



CS-40189

(b) Distorted flux.

Figure V-24. - Magnetic unbalance.

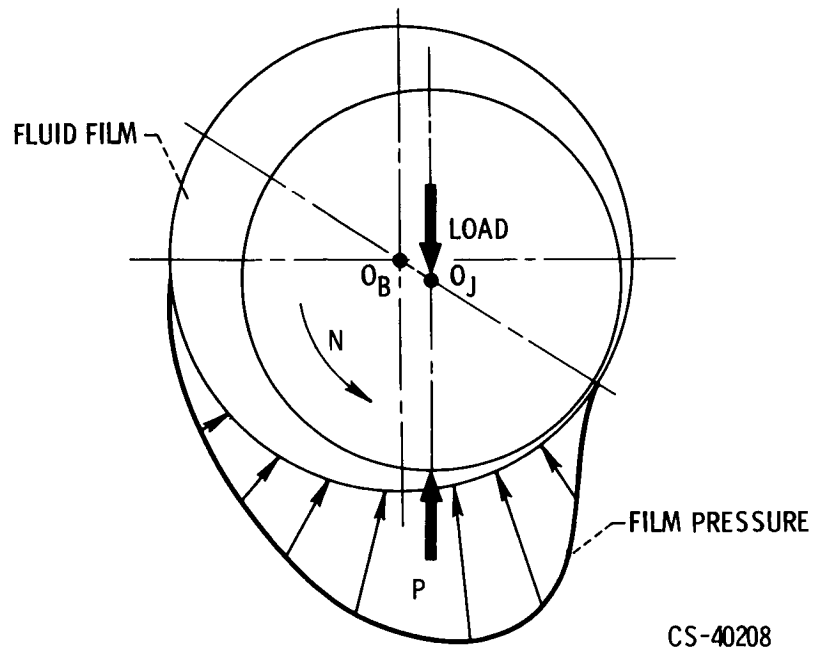


Figure V-25. - Journal bearing.

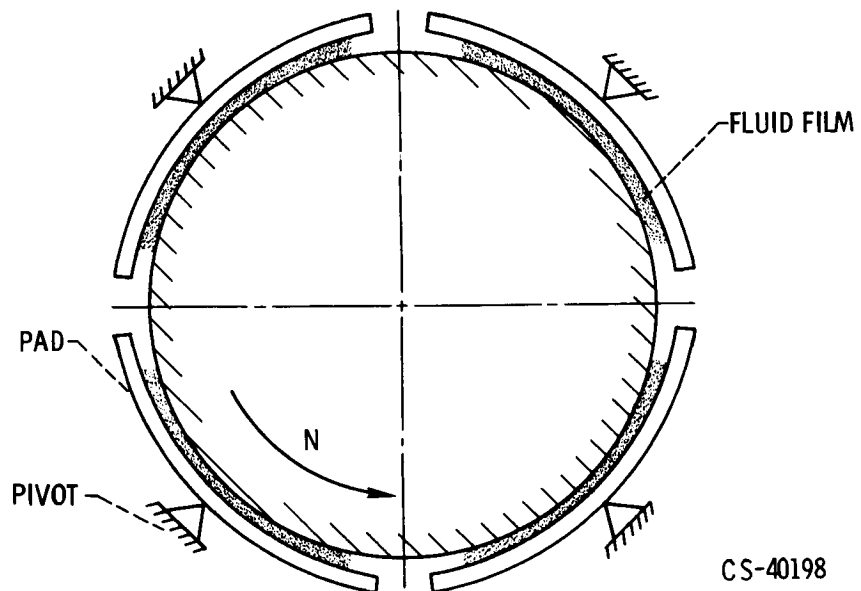


Figure V-26. - Pivoted pad journal bearing.

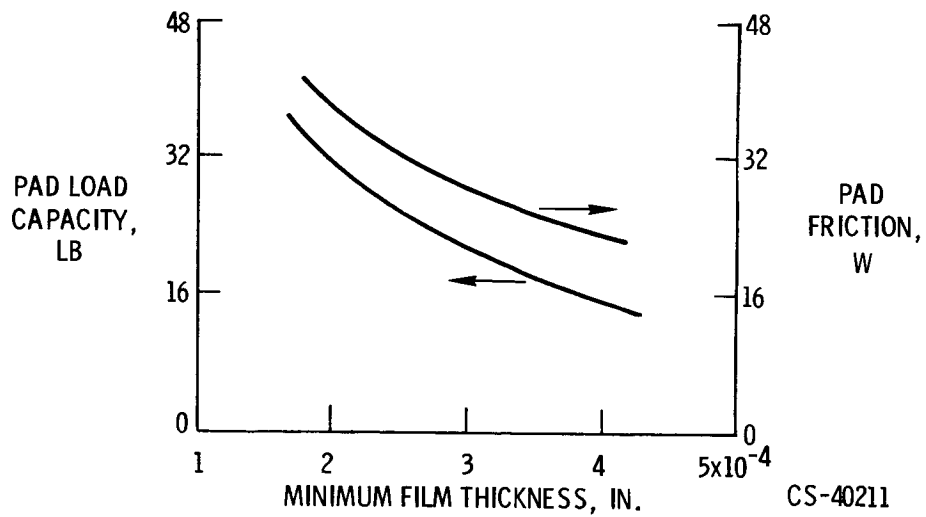


Figure V-27. - Typical journal bearing pad performance.

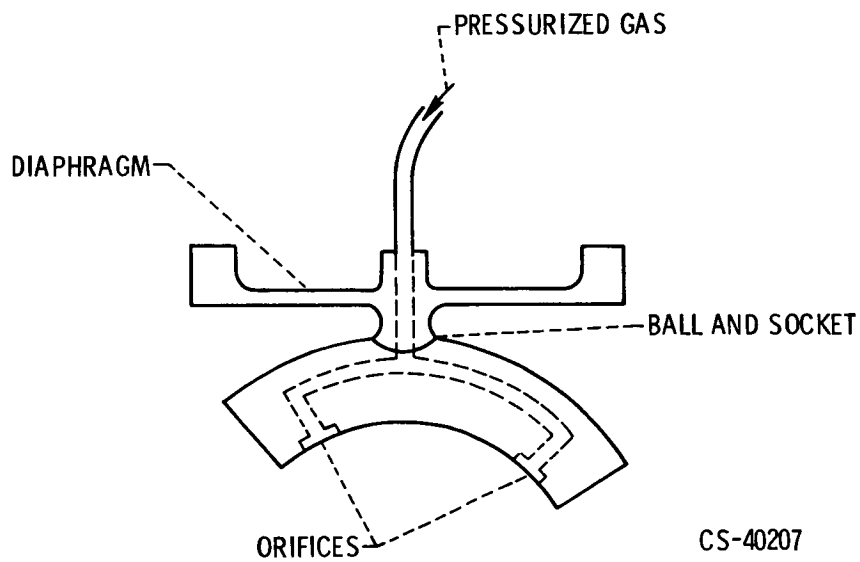


Figure V-28. - Pivot and external pressurization arrangement.

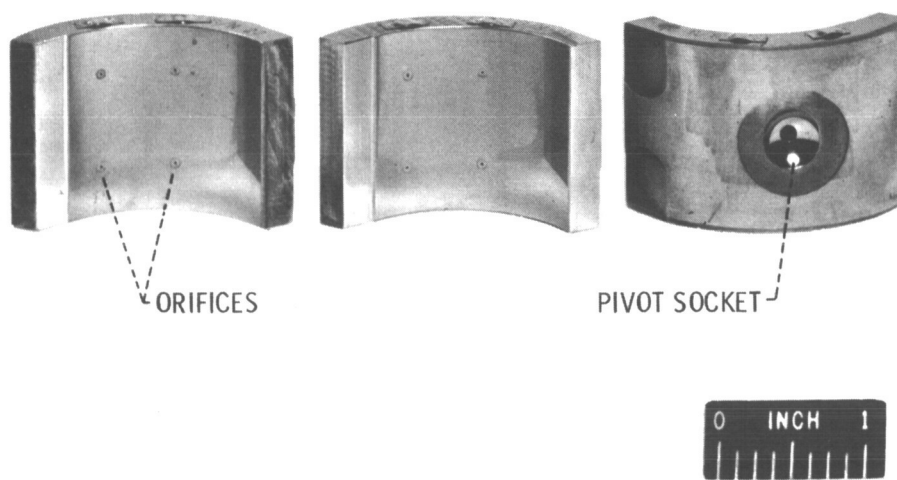
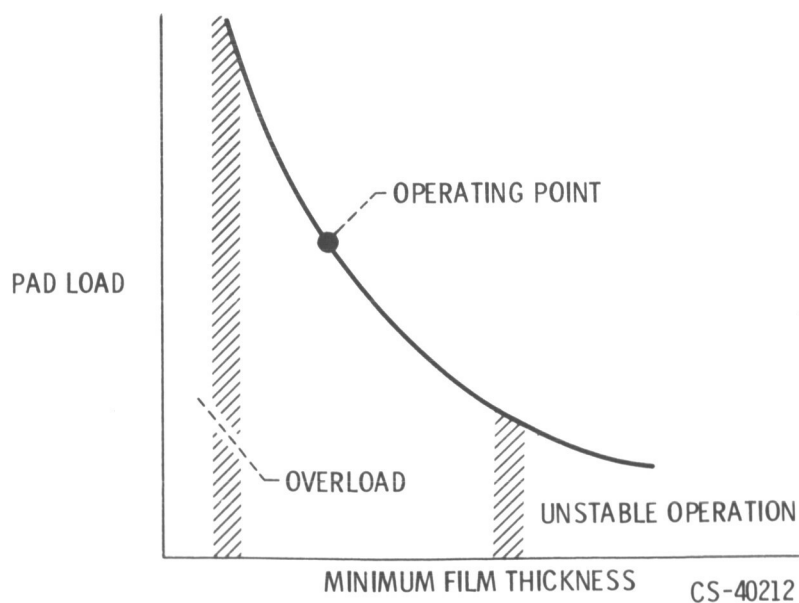


Figure V-29. - Journal bearing pads.

CS-40313



CS-40212

Figure V-30. - Pad loading at various film thicknesses.

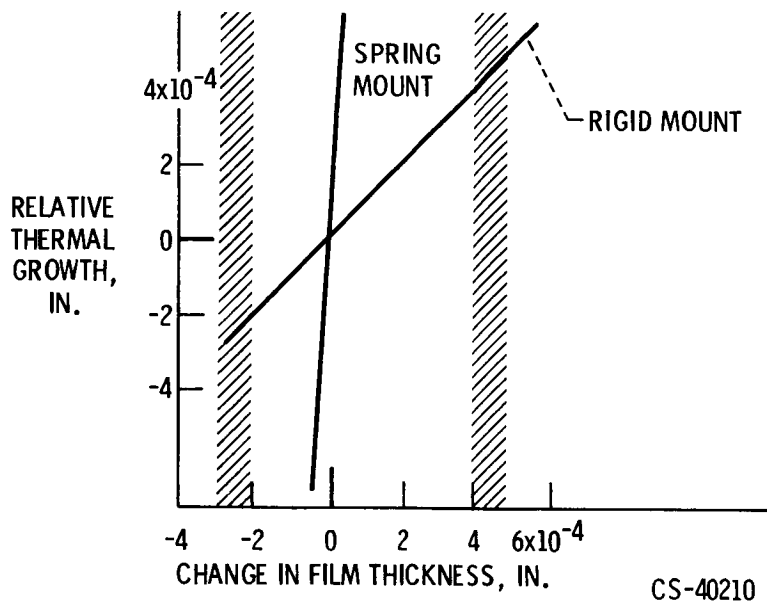


Figure V-31. - Effect of pad mount stiffness on thermal tolerance.

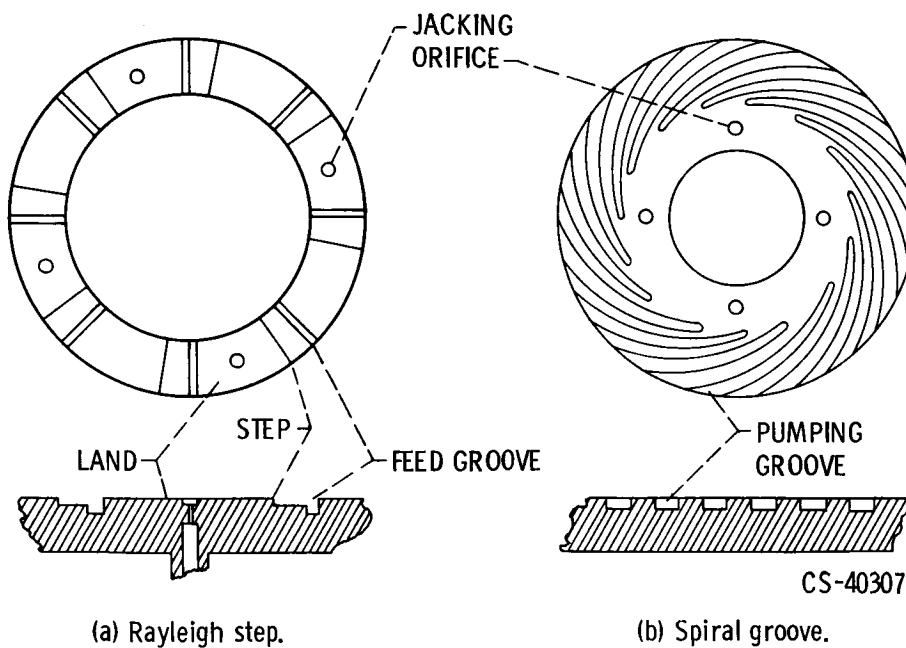
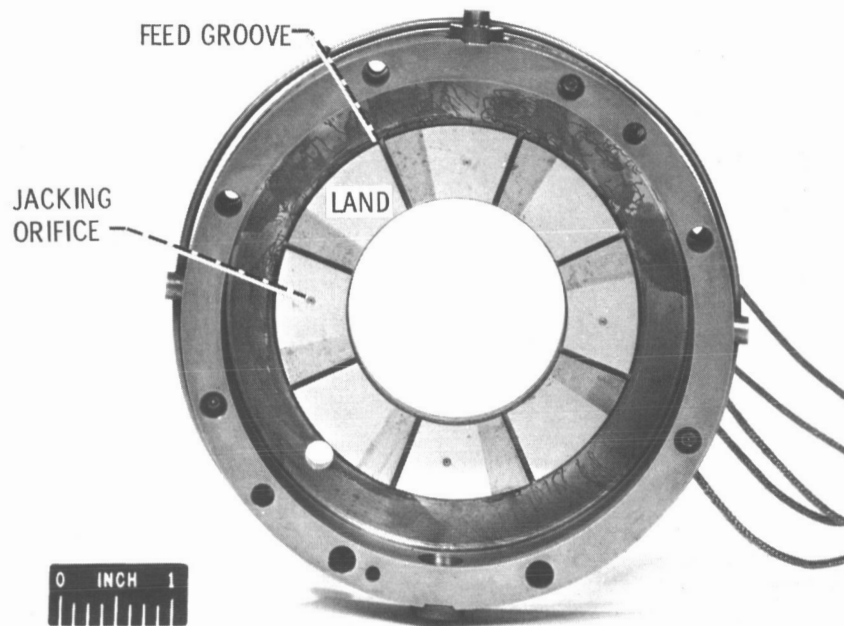
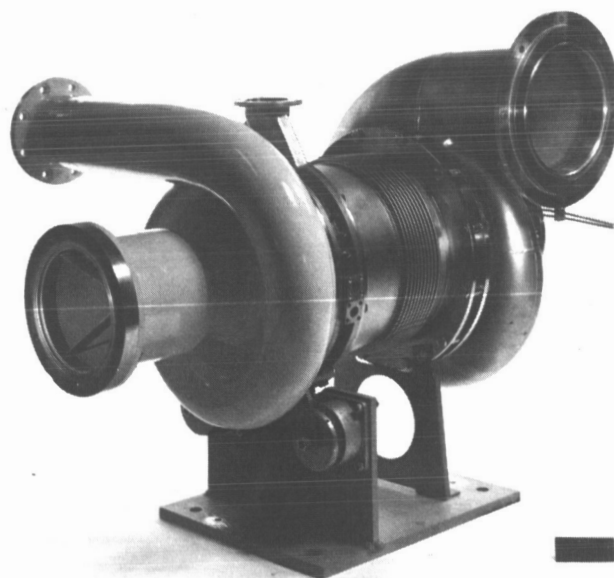


Figure V-32. - Thrust bearing types.



CS-40272

Figure V-33. - Rayleigh step thrust bearing.



CS-40271

Figure V-34. - Research turbocompressor.

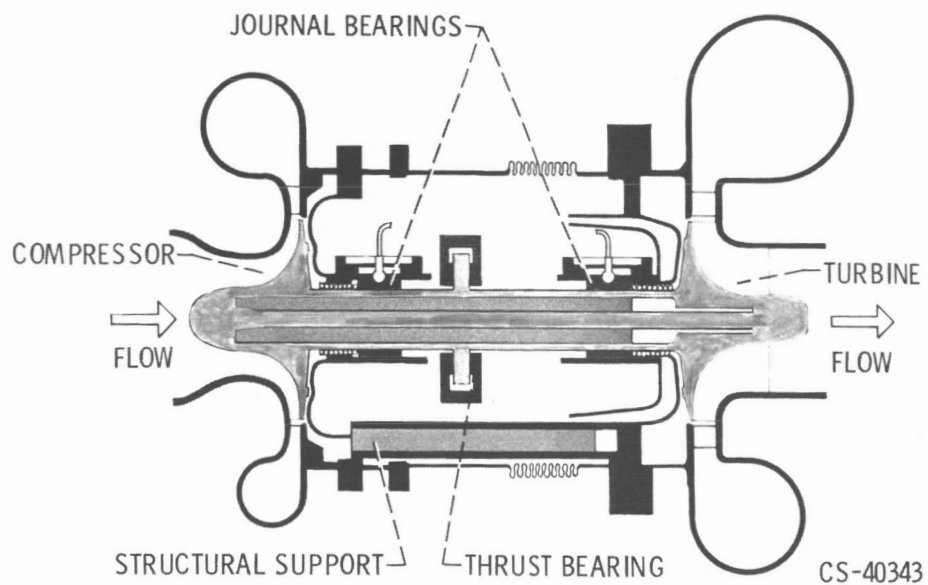


Figure V-35. - Schematic of turbocompressor.

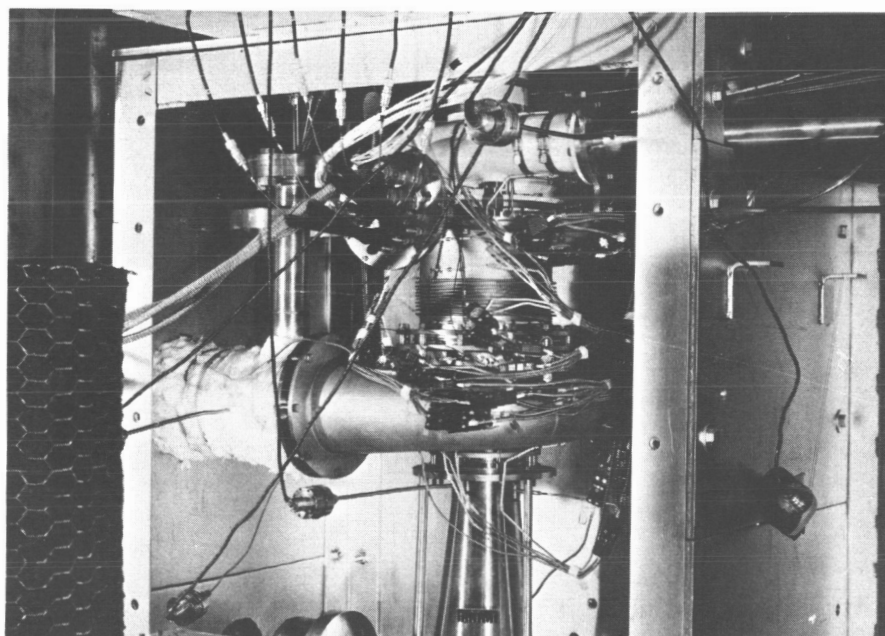


Figure V-36. - Turbocompressor installation.

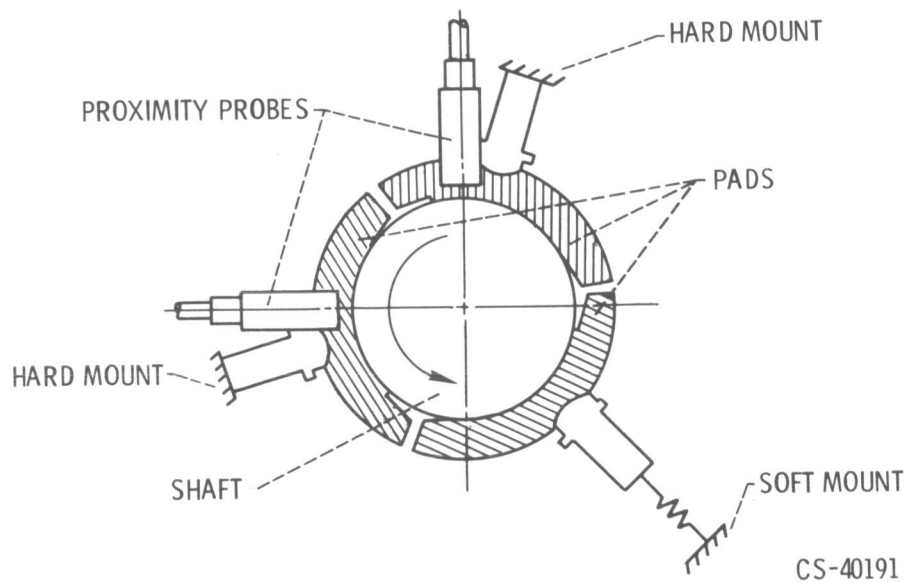


Figure V-37. - Journal bearing arrangement.

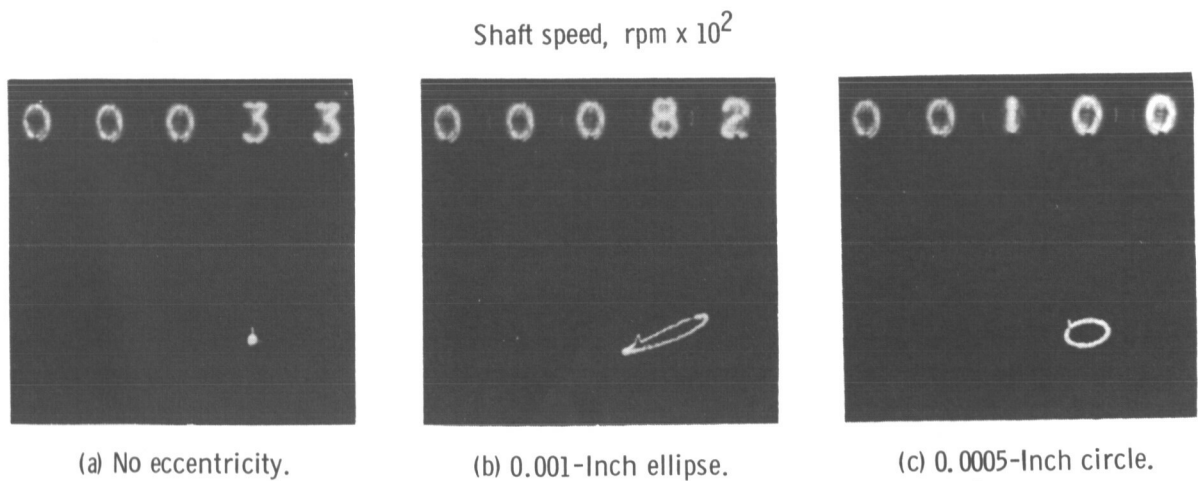


Figure V-38. - Shaft orbit patterns.

CS-40171

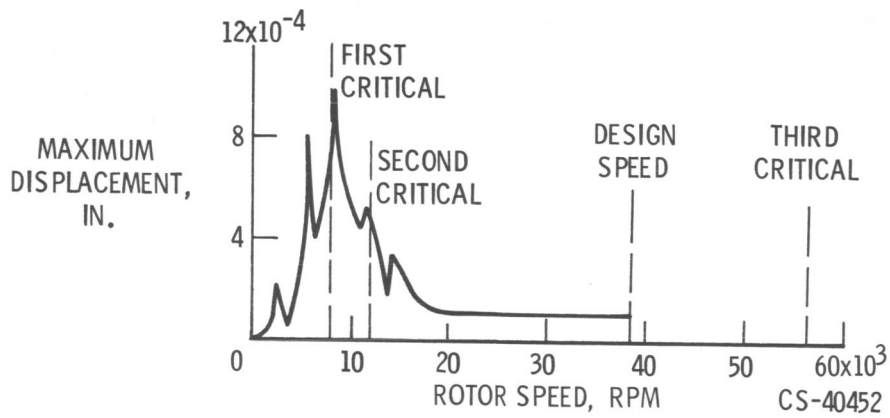
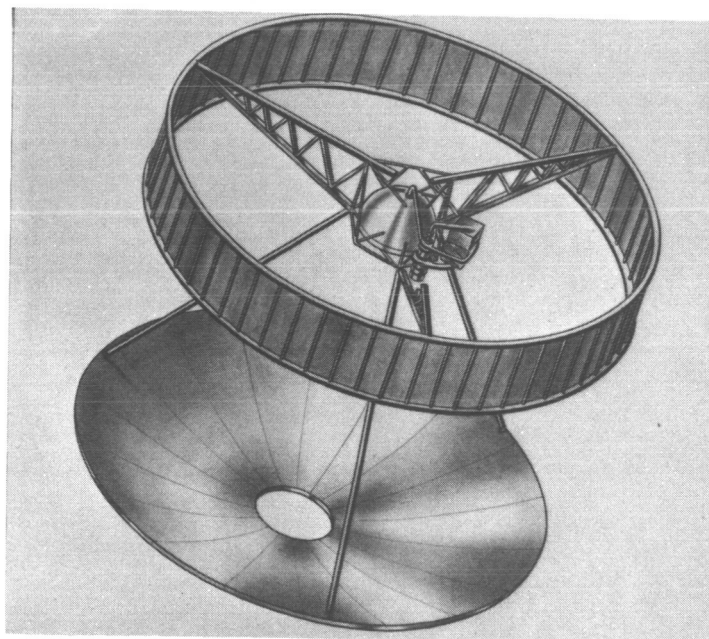
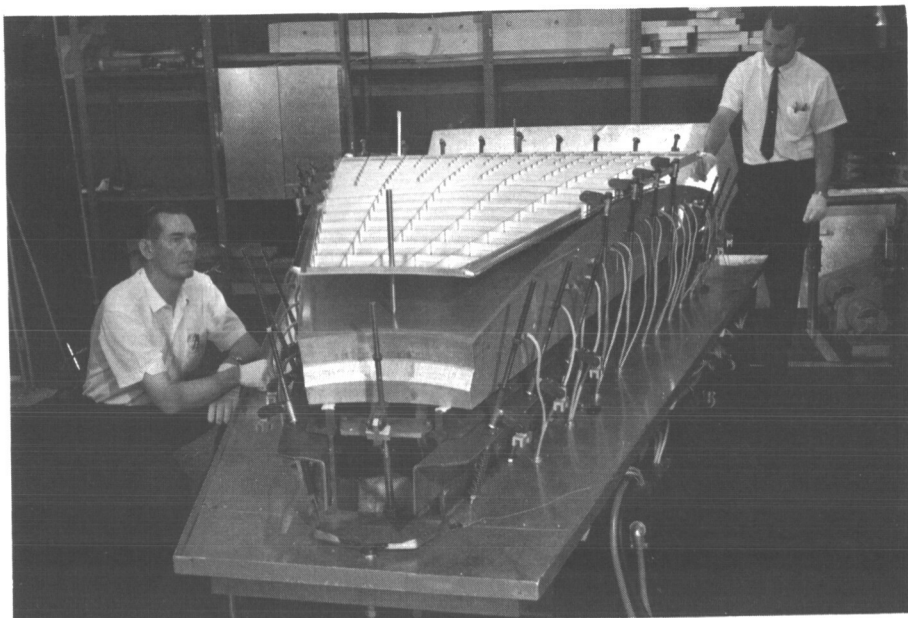


Figure V-39. - Turbocompressor shaft displacement.



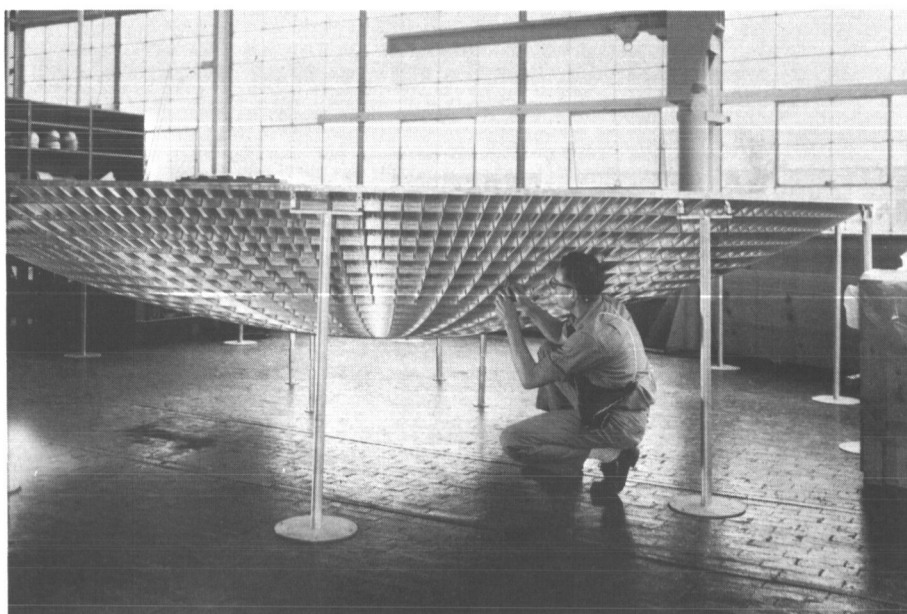
CS-40201

Figure V-40. - Solar Brayton cycle space power system.



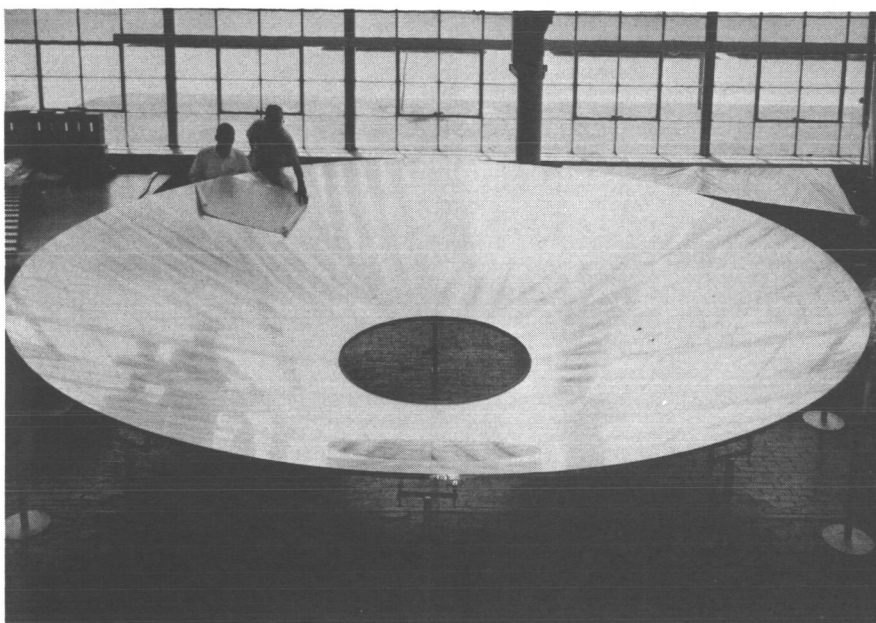
CS-40263

Figure V-41. - Formation of concentrator sector.



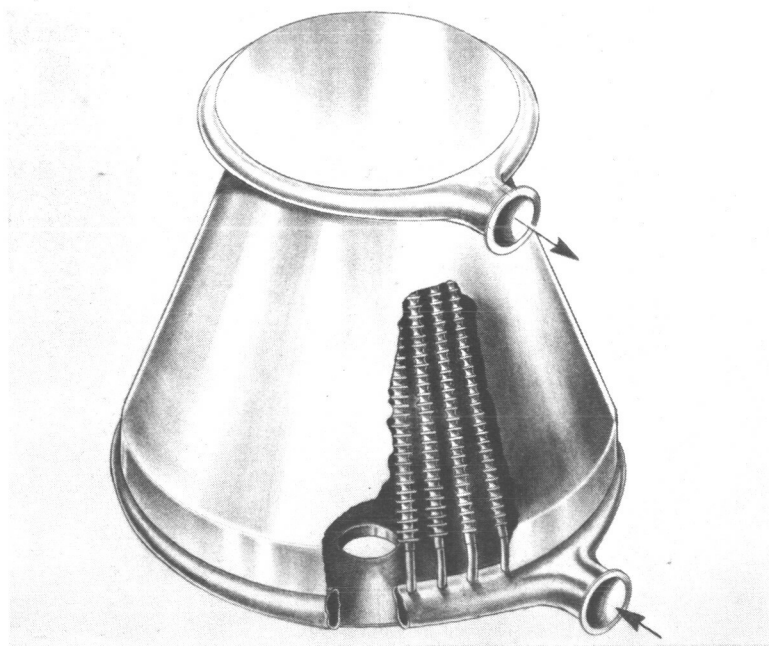
CS-40264

Figure V-42. - Ribbed back of 20-foot concentrator.



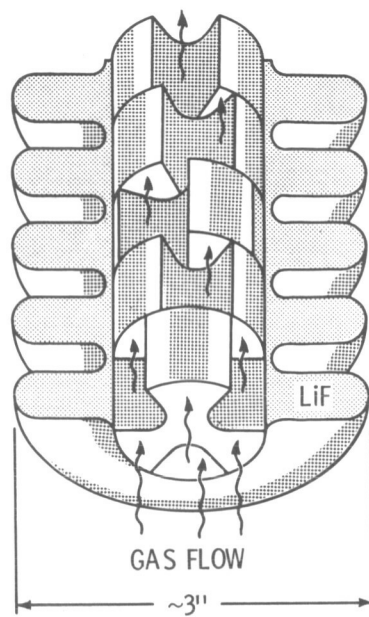
CS-40270

Figure V-43. - Polished front of 20-foot concentrator.

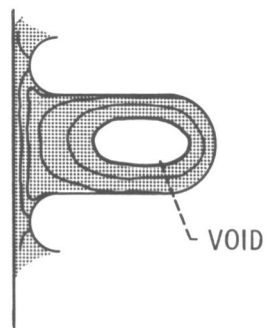


CS-40368

Figure V-44. - Heat receiver.



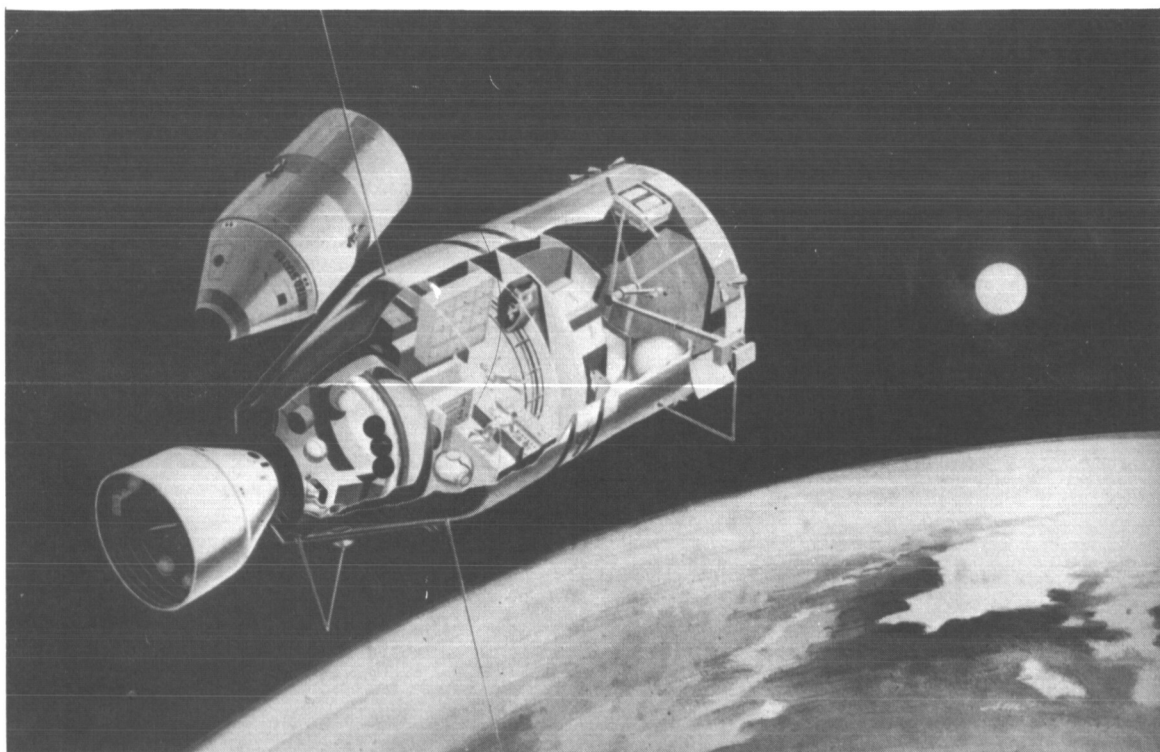
(a) Cutaway of tube.



(b) Expected freeze pattern.

CS-40259

Figure V-45. - Receiver tube concept.



CS-39850

Figure V-46. - Isotope Brayton space station concept.

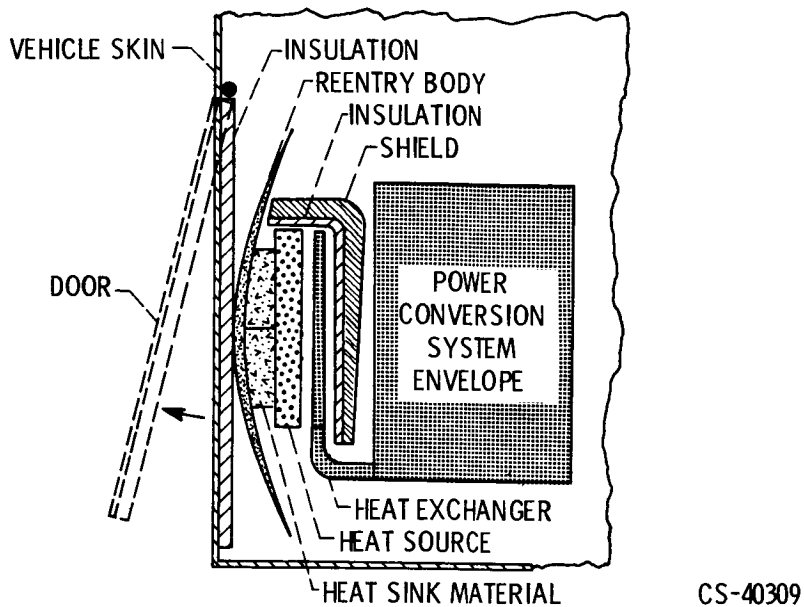


Figure V-47. - Radioisotope Brayton cycle concept.

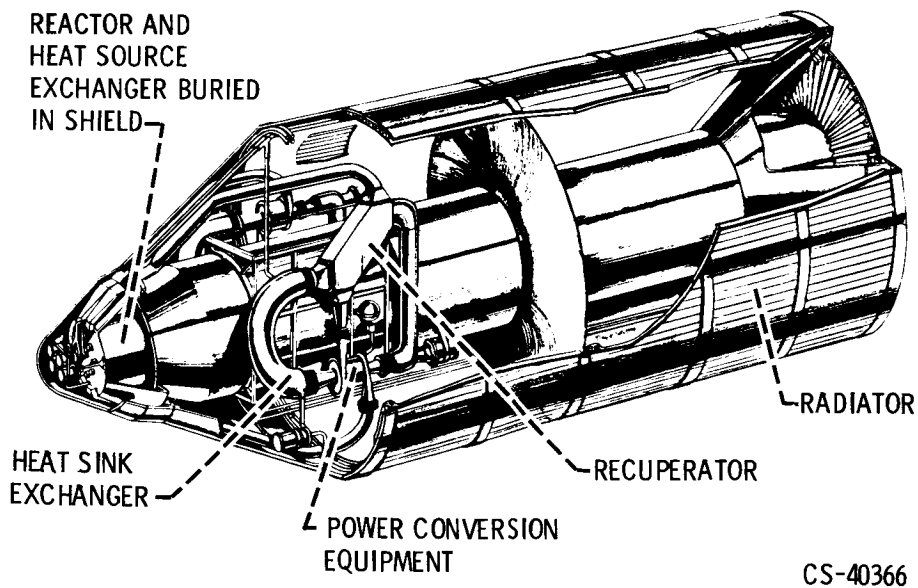
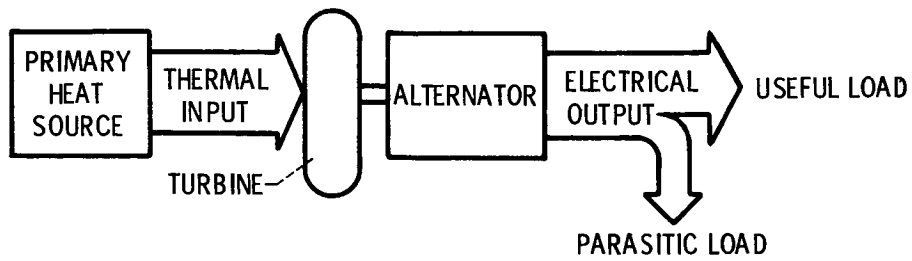
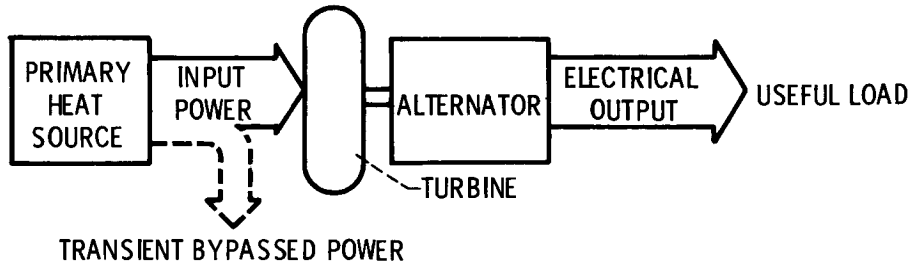


Figure V-48. - 150-Kilowatt-electric nuclear Brayton system.



(a) Alternator load.



(b) Turbine input.

CS-40187

Figure V-49. - Speed control techniques.

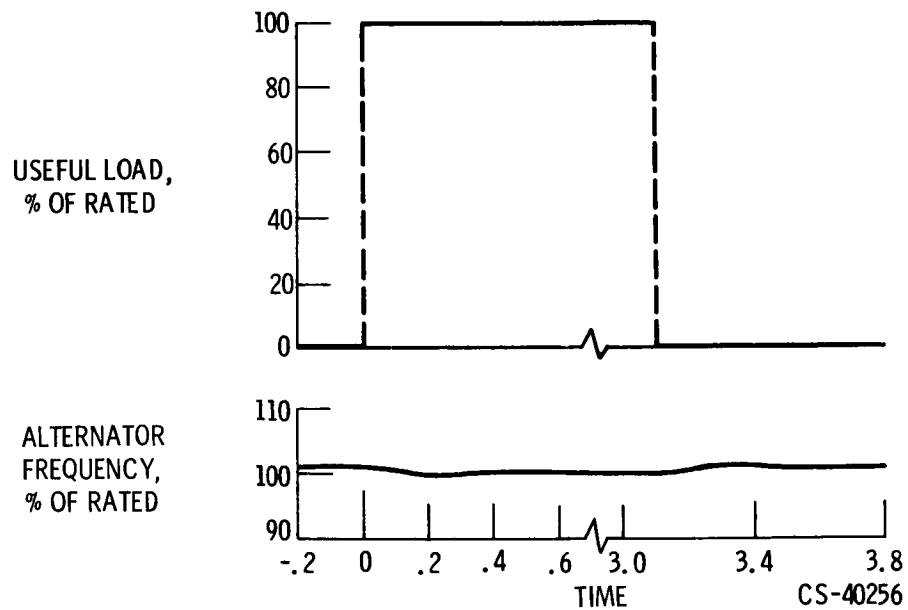


Figure V-50. - Experimental performance of speed control.

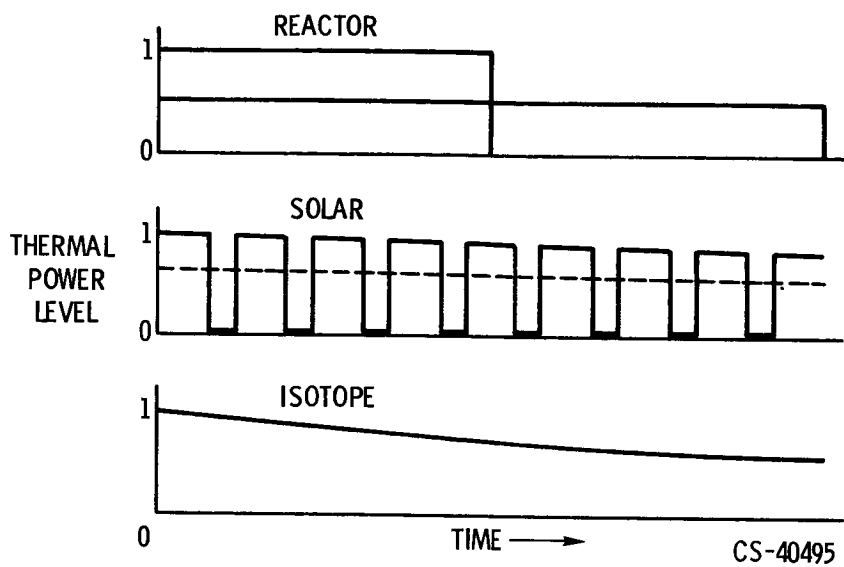


Figure V-51. - Heat-source characteristics.

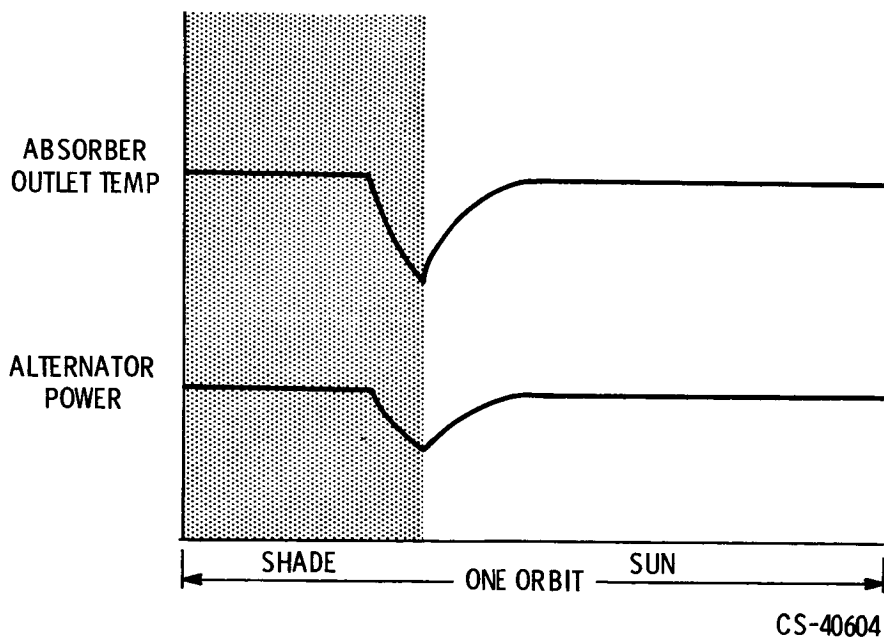


Figure V-52. - Energy imbalance effects.

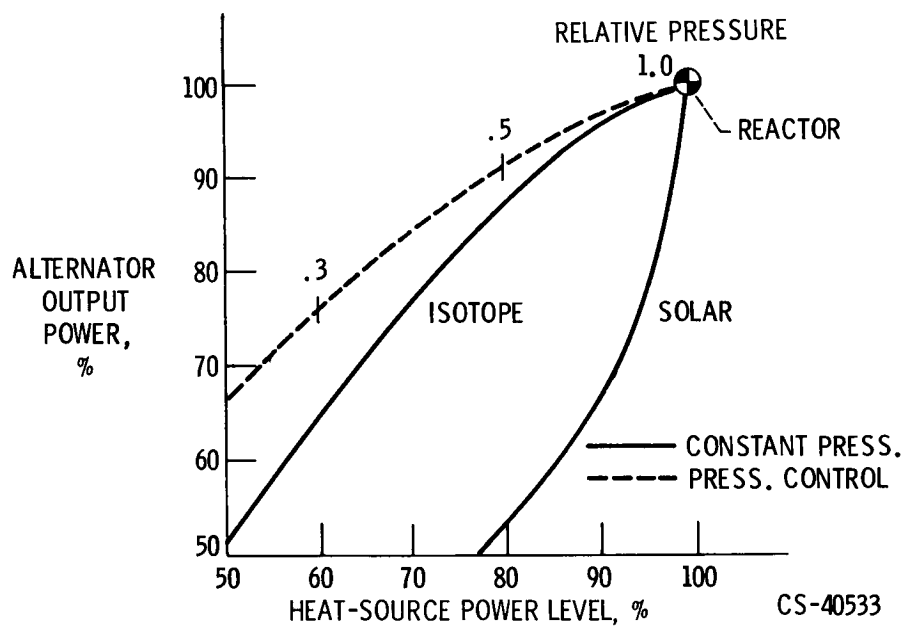


Figure V-53. - Pressure control effectiveness; two-shaft system.

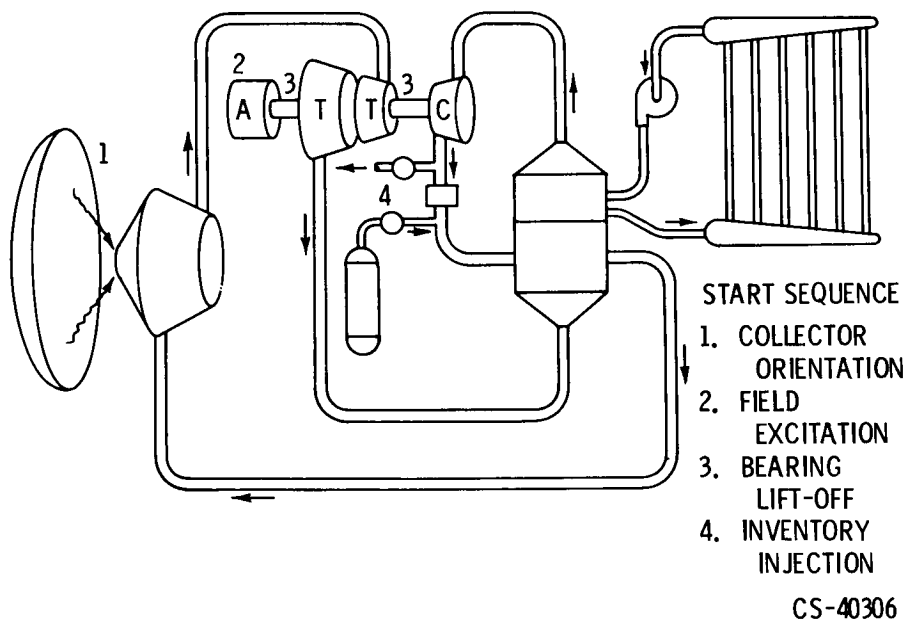


Figure V-54. - System configuration for start.

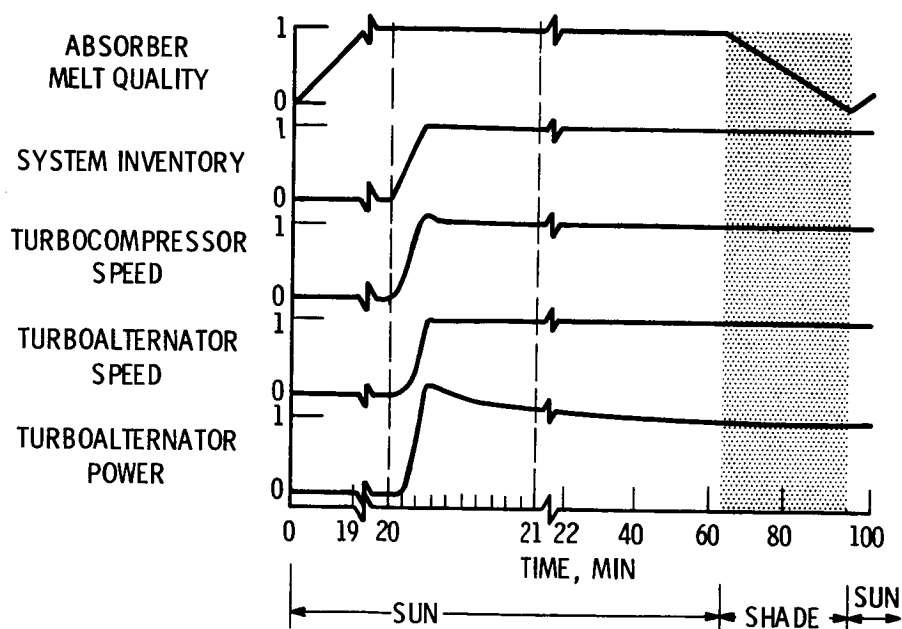


Figure V-55. - Two-shaft system start.

CS-40311

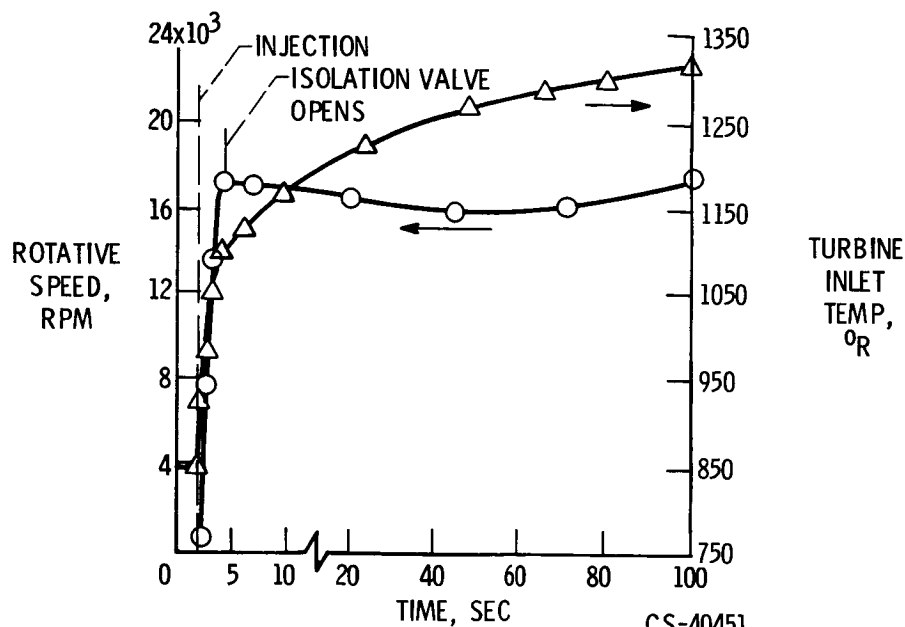


Figure V-56. - Turbocompressor experimental start.

CS-40451

VI. SNAP-8 DEVELOPMENT STATUS

Henry O. Slone

INTRODUCTION

The SNAP-8 is a turboelectric nuclear space power system using a mercury Rankine cycle. It is being developed jointly by the NASA and the AEC to produce a minimum electrical power of 35 kilowatts, to have high reliability, and to be capable of unattended full-power operation for 10 000 hours.

The SNAP-8 electrical generating system comprises three major subsystems, as shown in figure VI-1: a nuclear system consisting of a reactor, reactor controls, and a shield; a power conversion system consisting of a boiler, a turbine-alternator assembly, mercury- and sodium-potassium-pump-motor assemblies, a condenser, and the necessary electrical controls, piping, and structure; and a flight radiator assembly consisting of radiator heat exchangers required to remove heat from the liquid cooling loops and reject it to space. As indicated, Atomics International under AEC contract is responsible for developing the nuclear system, and Aerojet-General under NASA contract is responsible for developing the power conversion system. Since SNAP-8 is not being designed for a specific space mission at this time, the development of the flight radiator assembly and flight shielding is not a part of the current SNAP-8 program. The prime objective of the SNAP-8 development effort at this time is to develop SNAP-8 components and subsystems and system technology to the point at which the major system performance and development uncertainties are understood and resolved.

The NASA Lewis Research Center has project management responsibilities for the development of the power conversion system and for the integration of the nuclear system and the power conversion system. In addition, Lewis is engaged in experimental and analytical programs which are an integral part of the SNAP-8 development program. The project management responsibilities for the nuclear system are within the AEC Space Nuclear Systems Division.

This paper discusses the current status of the technical development of the SNAP-8 reactor and the power conversion system. Both technical accomplishments and difficulties are included.

SNAP-8 SYSTEM DESCRIPTION

The SNAP-8 program was started by NASA and AEC in 1960. The initial design, based on the technology existing at that time, included two loops and a direct-condensing radiator. After a thorough technical evaluation by NASA, the AEC, and their respective contractors in late 1962, the SNAP-8 system was redesigned in January 1963 in order to separate and to simplify the devel-

opment problems being experienced. The resulting four-loop concept is shown in figure VI-2. Also shown in figure VI-2 are typical temperatures, pressures, and flow rates required to produce a minimum net electrical power of 35 kilowatts. The systems operate as follows.

A liquid sodium-potassium alloy (NaK 78) flowing at about 46 000 pounds per hour is used in the primary loop to transfer heat from the reactor to the boiler; the alloy enters the boiler at about 1300° F. Mercury is used as the Rankine cycle working fluid in the second loop, wherein thermal energy is converted to mechanical energy. The mercury, flowing at about 11 600 pounds per hour, is boiled and superheated in the boiler. The superheated mercury vapor enters the turbine at 1250° F and 265 pounds per square inch absolute, is expanded through the turbine, condensed, and pumped back to the boiler. The turbine drives the alternator and thus provides the desired electrical power. All the pumps are motor driven, and they are powered by the alternator. A third loop, the heat-rejection loop, uses NaK to transport waste heat from the mercury condenser to a radiator from which it is rejected to space. The fourth loop in the SNAP-8 system, the lubricant-coolant loop, uses an organic fluid, a mixture of polyphenol ethers, at about 210° F to cool the pump motors, the alternator, the space seals in the turbine-alternator assembly and the mercury pump, and the electrical controls; this loop also lubricates the turbine-alternator and mercury pump bearings. The heat from this fluid is disposed of through a separate space radiator. As mentioned previously, development of the radiators is not part of the current development program.

The SNAP-8 electrical controls, not shown in figure VI-2, can be divided into two areas: the start system and those components that operate for 10 000 hours. The start system includes a 28-volt chemical battery, a start programmer, and an inverter which provides alternating-current starting power to the pump motors. The 10 000-hour electrical components, which are hermetically sealed, include a voltage regulator, a speed controller, and a parasitic load resistor. The SNAP-8 control system is based on constant-power-level operation independent of the electrical load supplied to the space vehicle. The parasitic load resistor, located in the heat-rejection loop, is capable of absorbing the entire net electrical output of the power conversion system.

Much progress has been made in the SNAP-8 program since January 1963. All the components and subsystems which comprise the SNAP-8 system have undergone testing. In February 1966, the first power conversion system went on test, and it has operated for over 400 hours to date. During operation of this system, 35-kilowatt net electrical power was delivered to a dummy space vehicle load. Thus, the SNAP-8 program has finished its preliminary phases and is now ready for intensive performance and endurance tests.

In the following sections all the major components shown in figure VI-2, are described and their test results discussed. In addition, there is a discussion of the mercury loop containment material, 9-percent chromium - 1-percent-molybdenum (9 Cr - 1 Mo) steel, since mercury corrosion is considered to be a potential problem for 10 000-hour operation.

Reactor

The SNAP-8 reactor, shown in figure VI-3, is designed to produce 600 kilowatts of thermal power at a NaK coolant outlet temperature of 1300° F for 10 000 hours. This compactly designed

reactor utilizes hydrided zirconium-uranium fuel-moderator rods clad with Hastelloy N. There are 211 fuel elements in the reactor core vessel. The reactor is controlled by movable beryllium reflector control drums, which by their position control the amount of neutron leakage. There are a total of six beryllium control drums, three of which are used during startup and three of which are used for long-term control. Each control drum has its own drive mechanism.

The overall reactor dimensions are a diameter of about 27 inches and a height of about 30 inches; the reactor weight is about 600 pounds.

The SNAP-8 experimental reactor (S8ER), which was developed to demonstrate and measure performance of the reactor core at design conditions of 600 kilowatts of thermal power and a 1300° F NaK coolant outlet temperature, went on test in May 1963. Figure VI-4 shows the S8ER reactor core, control drum assembly, and test shield being lowered into the test facility containment vessel.

The reactor went critical in May 1963, and testing continued until April 15, 1965. The energy output during this period was 5 154 332 kilowatt-hours out of a possible design output of 6 000 000 kilowatt-hours. A total of 11 990 hours of operating time was accumulated, of which 8800 hours were at the design temperature of 1300° F and thermal powers between 400 and 600 kilowatts (table VI-1). The remaining operating hours were obtained at lower NaK outlet temperatures and/or thermal powers less than 400 kilowatts. The longest continuous run was about 5000 hours, and about 2400 hours were accumulated at 600 kilowatts and 1300° F.

The results of the S8ER test program were generally satisfactory; and they showed that the reactor core had sustained power operation capability. However, upon disassembly of the core, it was discovered that about 80 percent of the 211 fuel elements had cladding cracks. A critical technical evaluation of the fuel-element cracking has been completed, and corrections will be made in the design of the next reactor, which will be mated with a power conversion system.

Boiler

The SNAP-8 mercury boiler is the interface between the nuclear and nonnuclear systems and is subject to the most significant perturbation that occurs in operation, a variation in NaK inlet temperature as the nuclear reactor responds to its temperature control system. The boiler must continually maintain vapor superheat, an acceptable fluid inventory variation, and minimal outlet pressure fluctuations over a 50° F band of NaK inlet temperature.

The boiler, shown in figure VI-5, is a second-generation design. The boiler is a single-pass counterflow tube-in-tube heat exchanger wound into a helix with a protruding inlet and outlet. The mercury flows through seven parallel 0.652-inch-inside-diameter tubes 30 feet long. The NaK flows, in the opposite direction, through the annulus passage between the mercury tubes and the outside tubular shell which has an outside diameter of 4.25 inches. Spacers are used to center the seven mercury tubes in the NaK annulus. The mercury tubes are made of 9 Cr - 1 Mo steel, and the shell is made of type 321 stainless steel. The boiler weight, including the mercury and NaK inventories, is about 480 pounds.

Boiler operation is shown schematically in figure VI-6. Here the NaK and mercury temperature profiles are plotted against boiler length. Also shown in figure VI-6 is a cross section of a

mercury tube. An inlet plug is inserted into each of the seven mercury tubes. The inlet plug is a solid rod spaced from the inside of the tube by a wire spring forming a spiral flow path for the mercury. This insert continues through the boiler tube for about 5 feet. Downstream of the plug, the spiral flow is maintained by another wire spring (spring turbulator) that is wound at a larger pitch to reduce the pressure drop. The inlet plug is inserted to increase the liquid-mercury and low-quality velocity, while the spring turbulator serves to separate the high-density liquid from the vapor, and makes boiler operation insensitive to gravitational field forces and increasing heat-transfer rates.

Since the boiler is a once-through heat exchanger, four regions are ideally defined on the mercury side of the boiler. The first region, called the preheat region, is where the sensible heat is added to the liquid mercury and the mercury temperature is heated to the saturation temperature which corresponds to the pressure at the liquid-vapor interface. The second region is where the majority of evaporation occurs and is termed the boiling region. The mercury vapor from the boiling region is superheated in the third region to a temperature approaching the NaK temperature. The fourth region, called the excess superheat length, exists to dry the vapor, and represents the surface area margin in the boiler design. Note that the liquid region occurs in the plug insert, as does a portion of the boiling. On the NaK side, a minimum of heat is transferred in the excess superheat region. There is a slight drop in NaK temperature through the superheat region followed by a relatively steep drop through the boiling region. A final drop in NaK temperature represents the sensible heat addition. Another parameter of importance in defining boiler performance is the "pinch point ΔT ," which is the temperature difference between the NaK and the mercury at the boiling or liquid-vapor interface. As the pinch point ΔT approaches 0°F , little or no heat is transferred, and test data have shown undesirable variations in boiler pressure and an increase in liquid carryover from the boiler.

Five full-scale SNAP-8 boilers have been tested for a total accumulated operating time of over 3600 hours. In addition, over 6000 hours have been accumulated on subscale SNAP-8 single-tube boilers. During this testing a phenomenon termed boiler "conditioning" has been observed. The term "conditioning" is defined as a time-dependent change in boiler performance. Three modes or regimes of boiler conditioning have been observed. These are (1) fully conditioned operation as typified by the NaK temperature profile shown in figure VI-6, (2) partially conditioned operation, and (3) deconditioned operation.

Figure VI-7 illustrates the three conditioning regimes obtained during a particular test of a SNAP-8 boiler. Temperature of NaK is plotted against boiler length. The NaK temperature profile is used to determine the conditioning regime, because the derivative of the profile (temperature plotted against length) is proportional to the heat flux. After 35 hours of boiler operation, the lower NaK temperature profile indicates the deconditioned operation. The extended flat portion in the first 15 feet of the boiler represents a region of low heat flux. With continued operation, note that the local heat-transfer rates increase, as shown by the increase in the slope of the profile. Also, the region of excess superheat length becomes apparent. Finally, after 51 hours of boiler operation, the fully conditioned NaK temperature profile obtained. Continued operation results in no further improvement in performance. The amount of time required to fully condition a boiler has varied from a few hours to a few hundred hours.

The curves shown in figure VI-7 indicate the effects of conditioning on boiler performance.

Other performance parameters found sensitive to conditioning are boiler outlet pressure stability, boiler exit temperature, and boiler pressure drop. For example, a deconditioned boiler shows outlet pressure fluctuations of ± 10 percent compared to pressure fluctuations of ± 2 percent in a conditioned boiler.

Thus far, boiler conditioning has been defined and its effect on the boiler has been noted. Two logical questions are

- (1) What causes this phenomenon?
- (2) What can be done to minimize its effect?

Dr. L. Rosenblum of the Lewis Research Center has demonstrated that small amounts of oil contamination on an otherwise clean surface can prevent mercury droplets from wetting the surface. Tests at Aerojet-General have verified that oil contamination of forced-convection mercury boilers can cause boiler deconditioning. Boilers can be contaminated because of oil exposure during fabrication and/or installation in a test loop, or because of turbine and mercury pump ball-bearing lubricant entering into the mercury during abnormal system operation.

Thus far, three methods have been successfully employed to obtain fully conditioned boilers. These are (1) the chemical cleaning of the boiler prior to operation, (2) continued operation or "wear-in" of the boiler such as illustrated in figure VI-7, and (3) the use of the additive rubidium in the mercury. All boilers tested were fully conditioned by one of these methods. In addition, once a boiler was fully conditioned, it did not decondition during continued operation.

The boiler tests have shown that the boiler can meet SNAP-8 system requirements and that the conditioning problem is not limiting. However, in order to understand, minimize, or, hopefully, eliminate the conditioning phenomenon, heat-transfer and materials programs have been recently initiated.

Condenser

The SNAP-8 condenser, shown in figure VI-8, is a NaK-cooled tube-in-shell counterflow heat exchanger in which the mercury vapor discharging from the turbine is condensed and subcooled. The mercury flows axially through 72 tubes with inside diameters tapered from 0.44 to 0.20 inch, while the NaK flows through the tapered shell in the opposite direction to the mercury. The tubes and shell are tapered to maintain vapor velocity and provide a continual movement of condensate to the liquid-vapor interface in zero-gravity operation by the drag of the vapor on the condensate droplets. The overall length of the condenser is about 61 inches, and its wet weight is 120 pounds. The tubing and headers are made of 9 Cr - 1 Mo steel, and the shell is made of type 410 stainless steel. Since the thermal expansion coefficients of both materials are compatible, the thermal stresses between tubes and shell are minimized, and fixed header design is possible.

The operational requirements of the condenser in the SNAP-8 system are threefold:

- (1) To provide a back pressure (condensing pressure) on the turbine commensurate with system power requirements
- (2) To provide subcooling to assure adequate net positive suction head to the mercury pump
- (3) To provide mercury inventory storage capacity to make up for space-seal leakage from the turbine-alternator assembly and the mercury-pump - motor assembly

(The space seal is discussed later.)

Over 3600 test hours have been accumulated on three SNAP-8 condensers, and the test results have been very satisfactory. A typical NaK and mercury temperature profile plotted against condenser tube length is shown in figure VI-9 for a particular test condition. The mercury temperature profile was calculated; the NaK profile was measured. The NaK enters from the right, and the initial relatively flat slope moving from right to left represents the subcooling area of the condenser with relatively low heat-transfer rates. The steep gradient represents the high-heat-transfer-rate area characteristic of condensing. The flat portion of the profile at the left represents an area of no heat transfer. The tube schematic indicates the relative tube lengths for the saturated mercury vapor, the mercury condensate, and liquid mercury.

Data obtained from single tapered tube condensing experiments conducted at the Lewis Research Center were used in the design of the SNAP-8 multitube condenser.

In testing to date, the performance of the condenser has been good, and it has met all its operational requirements.

Turbine-Alternator Assembly

The heart of the SNAP-8 power conversion system is the turbine-alternator assembly. A simple schematic of the turbine-alternator assembly is shown in figure VI-10, and a photograph of the actual assembly in the clean room at Aerojet-General is shown in figure VI-11 to give some idea of its size.

Two major assemblies comprise the turbine-alternator assembly: a turbine assembly and an alternator assembly. The two assemblies are bolted together with the turbine rotor shaft directly coupled to the alternator rotor by means of a splined quill. Both the turbine and the alternator assembly use conventional design ball bearings which are lubricated by polyphenol ether.

The turbine assembly, which is cantilevered, is a four-stage impulse turbine with the first two stages operating with partial admission and the last two stages with full admission.

The alternator, supplied by General Electric, is a four-pole, brushless, radial-air-gap, homopolar-inductor machine. There are no rotating windings, the rotor being a one-piece steel forging mounted on ball bearings. A cooling jacket surrounds the electrical windings.

To prevent intermixing of the turbine working fluid (mercury) and the bearing lubricant (polyphenol ether), a low-leakage seal to space was designed and developed. Intercontamination of the two fluids is avoided by venting a section of the shaft to space and permitting limited leakage of mercury and polyphenol ether to space. Leakage rates are controlled by creating a liquid-vapor interface in each seal, through which liquid cannot pass. The interfaces are established by a screw pump on the mercury side and a disk slinger on the polyphenol ether side. Loss of vapors emanating from the liquid-vapor interfaces is further restricted by molecular screw pumps on each side. In the mercury seal, a heat exchanger built into the housing serves the dual function of cooling the liquid-vapor interface and assuring that mercury condensate, instead of vapor, fills the adjacent seal section.

The turbine design conditions are output, 63 kilowatts; efficiency, 60 percent; speed, 12 000 rpm. The alternator design conditions are output, 80 kilovolt-ampere at a power factor of

0.75; efficiency, 87 percent; frequency, 400 cps. The turbine assembly weighs about 151 pounds, and the alternator weight is about 430 pounds.

The first turbine-alternator assembly went on test in a mercury test loop in November 1964. Since then, four other units have been operated. Figure VI-12 shows a performance comparison of the first four turbine assemblies tested to date. Also shown in figure VI-12 are the accumulated test hours obtained for each turbine-alternator assembly and the number of starts made on each unit.

Tests on turbine-alternator assembly 1 were terminated after 820 hours of operation because of a mechanical failure which occurred when a locking device from the floating shaft seals escaped from its location. Posttest examination indicated a number of other mechanical deficiencies and a materials problem. The cobalt base material Stellite 6B, chosen as the turbine wheel and diaphragm material because of its excellent mercury erosion resistance, went through a metallurgical transformation which caused extreme reduction in ductility and increased notch sensitivity.

Subsequent turbines that went on test were modified in varying degrees to correct for the minor difficulties encountered in turbine-alternator assembly 1. Also, some design changes were made to accommodate the notch sensitivity of Stellite 6B. About 400 hours of test time were accumulated on turbine-alternator assemblies 2, 3, and 4, and although some mechanical problems were encountered with these units, no testing was terminated because of a turbine failure as in the case of turbine-alternator assembly 1.

As indicated, none of the turbines met the design efficiency goal of 60 percent. The variations in efficiency among the four units are due mainly to interstage leakages and the fact that the first-stage nozzle areas were different for each unit. The performance degradation shown for turbine-alternator assembly 2 was due to a movement of the first-stage nozzle block insert that effectively increased the nozzle area, which caused a loss in efficiency. At present, a new turbine aerodynamic and mechanical design is under way in order to improve the performance and mechanical integrity of the turbine assembly. It is anticipated that these improvements will allow the turbine efficiency to approach the design level of 60 percent. The new turbine will be available for testing early in 1967.

Four alternators have been tested, and a performance map of alternator capability has been generated. Some results of the alternator tests are shown in figure VI-13. Alternator efficiency is plotted against power at the alternator terminals for three power factors. The data show an alternator efficiency of about 87.8 percent at the design power factor of 0.75, compared to the design efficiency of 87.0 percent. In general, no problems have been encountered with the SNAP-8 alternator.

The space-seal configuration which is used in the turbine-alternator assembly and the mercury-pump - motor assembly are the result of a separate development effort in which extensive theoretical and experimental work was done. Testing during this effort revealed that the total leakage of mercury and polyphenol ether to space can be expected to be less than the design goal of 10 pounds over the 10 000-hour life of the system. This is illustrated in figure VI-14, which shows data obtained for the mercury seal operating in a simulator test rig. Mercury leakage in pounds per 10 000 hours is plotted against heat-exchanger coolant inlet temperature. The data were obtained during a 1000-hour run by taking leakage samples in 1- to 20-hour runs and in 100- to 200-hour runs and extrapolating to 10 000 hours. Note the reasonably good agreement

with the theoretical leakage curve. Also, note that the data indicate a leakage of less than 1 pound in 10 000 hours at the design operating temperature, which is considerably less than the design goal of 10 pounds in 10 000 hours.

Lubricant-Coolant-Pump - Motor Assembly

The lubricant-coolant-pump - motor assembly, provided by TRW and shown in figure VI-15, consists of a single shaft with a straddle-mounted motor rotor and an overhung, single-stage impeller. The assembly is self-cooled and lubricated by the polyphenol ether which bleeds from the pump discharge, flows through the motor and bearing area, and returns to the eye of the impeller through the hollow shaft. The pump-motor assembly dimensions are mean diameter, about 6 inches, and length, about 12 inches. The weight is about 25 pounds.

Seven units have been built and tested and have accumulated over 7700 test hours. One unit has accumulated over 4500 test hours. A typical test performance curve is shown in figure VI-16. Note that the pump has exceeded its SNAP-8 design requirements and its mechanical integrity has been demonstrated during over 7700 hours of operation.

Mercury-Pump - Motor Assembly

The mercury-pump - motor assembly, shown in figure VI-17, consists basically of a one-piece solid shaft supported by two ball bearings mounted in a central transmission housing. The bearings are lubricated with polyphenol ether, and mercury sealing is effected by pump seals similar to the sealing configuration used in the turbine-alternator assembly discussed previously. A 400-cycle, three-phase induction motor is overhung from the bearing housing at one end, and a combination jet and centrifugal pump is overhung on the other end. The jet pump is incorporated upstream of the centrifugal pump to provide positive suction head to the centrifugal impeller at very-low-flow starting conditions. The pump-motor assembly dimensions are mean diameter, about 8 inches, and length, about $2\frac{1}{2}$ feet. The weight is about 150 pounds.

Six units have been built, and four of these units have been tested and have accumulated about 2000 hours. A test performance curve is shown in figure VI-18. As can be seen from the curve, the mercury-pump - motor assembly has met or exceeded SNAP-8 design requirements. In general, no difficulties have been encountered in testing.

Sodium-Potassium-Pump - Motor Assemblies

As discussed previously, the SNAP-8 system requires two NaK-pump - motor assemblies, one for the primary loop and one for the heat-rejection loop. Because of the similarity of requirements, one design is used in both loops.

The NaK-pump - motor assembly, shown in figure VI-19, is a self-contained hermetically sealed unit. It incorporates on a single shaft a centrifugal pump, a hermetically sealed 400-cycle,

three-phase induction drive motor, an internal lubricant-coolant circulating pump, and NaK-lubricated hydrodynamic bearings. Included with the pump-motor assembly, but not shown in figure VI-19, are heat exchangers, a cold trap, and a NaK filter for the circulating NaK. Polyphenol ether is used as the coolant in the heat exchanger. The NaK lubricant-coolant circuit is independent of the process pumping circuit. The pump-motor assembly dimensions are mean diameter, about 8 inches, and length, about $1\frac{1}{2}$ feet. The weight is about 200 pounds.

A total of 10 NaK-pump - motor assemblies have been tested and have accumulated over 4000 hours of test time. One unit has operated for 3028 hours. A test performance curve is shown in figure VI-20 for a NaK-pump - motor assembly operating at 1170° F, the operating temperature of the primary loop. As shown by the curves, the NaK-pump - motor assembly meets SNAP-8 design requirements. It should be noted that the SNAP-8 NaK-pump - motor assembly design is the first of its kind, and the results of the test program have been most satisfactory.

Mercury Containment Material

A potential problem in a mercury system is that of mercury corrosion of the containment material. Of the current materials, low-additive iron-base alloys exhibit minimum corrosion potential in mercury. This is illustrated in figure VI-21, where the corrosion rates of an iron-base alloy, 9 Cr - 1 Mo steel, and a cobalt-base alloy, HS-25, are shown. These data were obtained at the Lewis Research Center in refluxing mercury capsules operating at 1100° F. Individual capsules fabricated from the two materials were operated for time increments of 300, 1000, 2000, and 5000 hours. After testing of each capsule was completed, it was metallurgically examined to determine its resistance to mercury corrosion, expressed as corrosion penetration. The data curves were then extrapolated to 10 000 hours. On the basis of these data, 9 Cr - 1 Mo steel was selected in early 1963 as the SNAP-8 mercury containment material. The predicted penetration in 10 000 hours is about 3 to 4 mils for 9 Cr - 1 Mo and about 17 mils for HS-25. It should be noted that the stainless steels exhibit a higher corrosion penetration than HS-25 and that the refractory metals such as columbium and tantalum exhibit no mercury corrosion. A refractory material was not selected for SNAP-8 in 1963 because of the difficulties encountered in handling the material.

Since the selection of 9 Cr - 1 Mo steel was made in early 1963, three subscale corrosion loops and five boilers fabricated from 9 Cr - 1 Mo have been operated. Figure VI-22 shows the results obtained after metallurgical examination of a first-generation-design SNAP-8 boiler which operated for 1425 hours. The NaK temperature profile is plotted against length of one of the mercury tubes in the boiler. The two profiles shown indicate the change from partial conditioning to full conditioning with test time. Also plotted is the maximum pit depth observed in the tube wall at various locations along the tube. The maximum depth observed was about 5 mils, which occurred in the liquid section of the boiler tube. The test results from the subscale corrosion loops indicate pit depths greater than 5 mils.

Based on the test data, the following observations are made:

- (1) The maximum attack which occurs is apparently associated with the liquid-mercury section and high-heat-flux area of the boiler tube.
- (2) The attack pattern seems to depend on the conditioned state of the boiler during operation.

(3) It is not clear whether the pits observed in the tube wall are due to corrosion or cavitation-erosion or both.

In summary, the current test data do not allow an accurate prediction of the life of 9 Cr - 1 Mo steel as a mercury containment material in the SNAP-8 system. The life could be greater or less than 10 000 hours. As a result, tests are continuing in order to establish the life capability of 9 Cr - 1 Mo steel. In addition, work is under way to establish the feasibility of using a bimetal refractory material, such as tantalum clad with a stainless steel, or a bare refractory material for the mercury containment material.

SUMMARY

The major technical accomplishments and problem areas of the SNAP-8 program are summarized in table VI-2.

Test times, as of August 1, 1966, are tabulated for the major power-conversion-system components. Listed are the number of units tested, the accumulated test time for all units, and the longest test time accumulated on a single unit. Only one unit, the turbine-alternator assembly, has had a failure, and its performance has been somewhat lower than expected.

The results obtained on SNAP-8 components and subsystems have been most encouraging in that no fundamental problems have been encountered which might prevent development of the SNAP-8 system. However, much effort is required before it can be said that the SNAP-8 is ready to be selected for a given mission. The endurance and reliability of SNAP-8 for 10 000 hours must be demonstrated. For example, the 10 000-hour life of the boiler material (9 Cr - 1 Mo steel) is uncertain. The first power conversion system, which began tests in February 1966, has accumulated a total operating time of only about 400 hours. In addition, the three major subsystems which comprise the SNAP-8, that is, the nuclear system, the power conversion system, and the flight radiator assemblies, must be integrated and operated. Currently, testing is continuing on the first power conversion system and on components. In the future, a second power conversion system and a combined system (i. e., a reactor mated with a power conversion system) will be tested. All systems will be operated for 10 000 hours.

TABLE VI-1. - OPERATING TIME OF SNAP-8

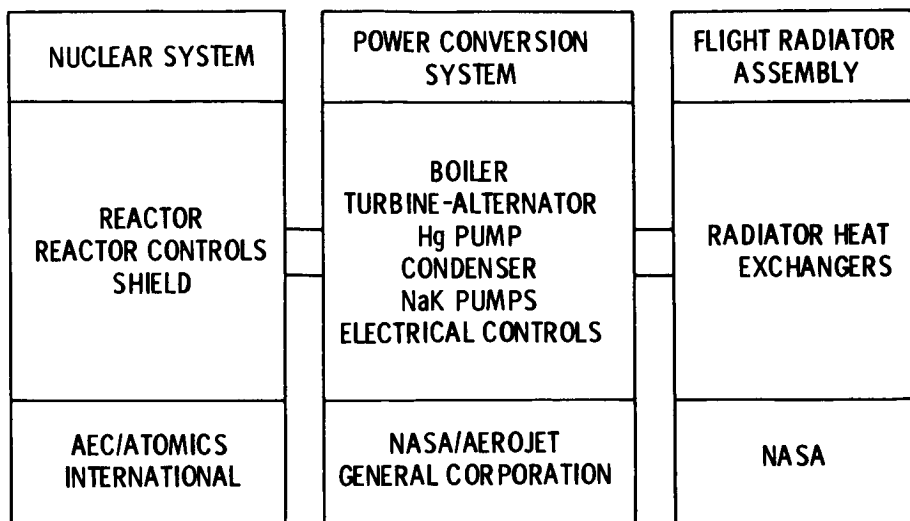
REACTOR AS OF APRIL 15, 1965

Temperature, °F	Thermal power, kW		Total operating time, hr
	400 to 600	Other than 400 to 600	
	Operating time, hr		
1300	8 800	470	9 270
1300 and other	10 320	1670	11 990

TABLE VI-2. - SUMMARY OF SNAP-8 PROGRAM AS OF AUGUST 1966

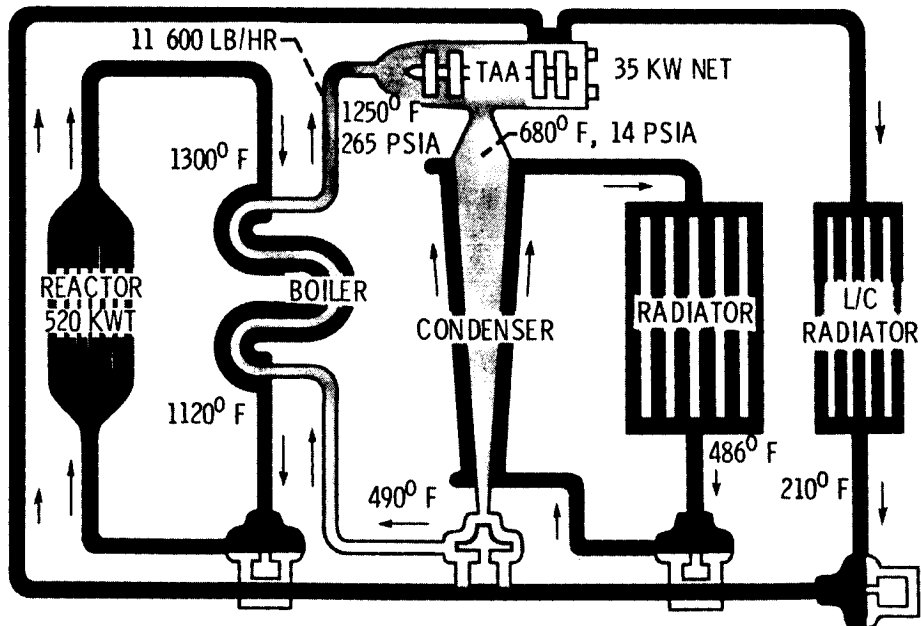
Component	Number of units tested	Test time for all units, hr (a)	Longest single- unit test time, hr
Turbine-alternator assembly	4	1122	820
Sodium-potassium-pump - motor assembly	10	4157	3028
Mercury-pump - motor assembly	3	1975	1099
Lubricant-coolant-pump - motor assembly	4	7727	4552
Boiler	5	3694	1429
Condenser	3	3694	1851

^aPower conversion system delivered 35 kW net electric power with all pumps on alternator power during 1966 testing.



CS-40215

Figure VI-1. - SNAP-8 electrical generating system. Electrical power, 35 kilo-watts; life, 10 000 hours.



CS-40234

Figure VI-2. - Schematic drawing of SNAP-8 system.

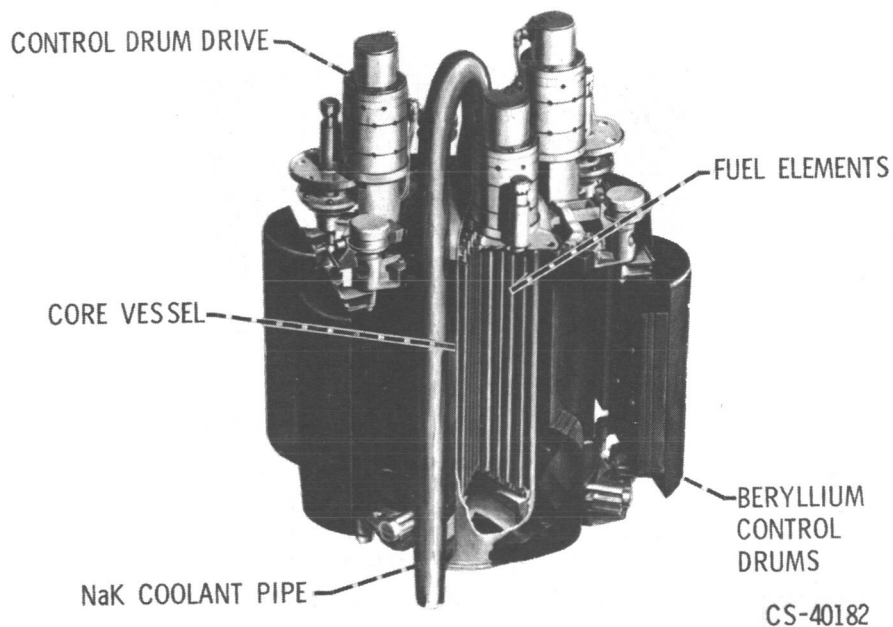
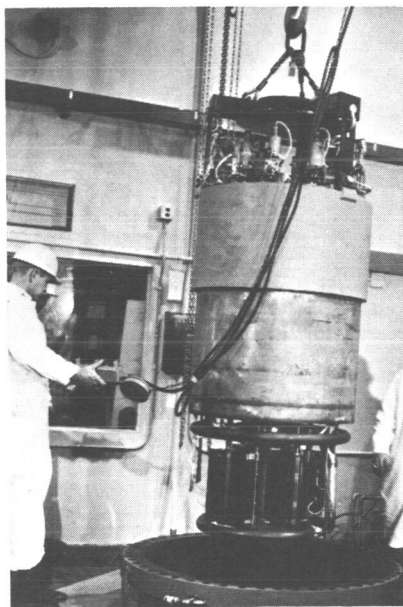
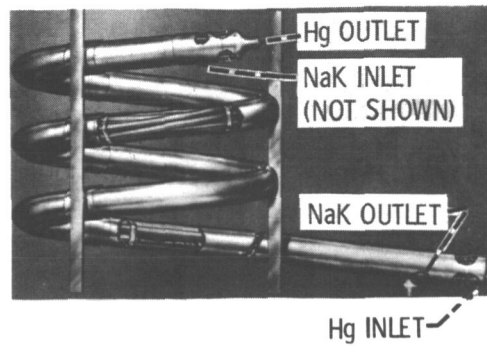


Figure VI-3. - SNAP-8 reactor assembly.



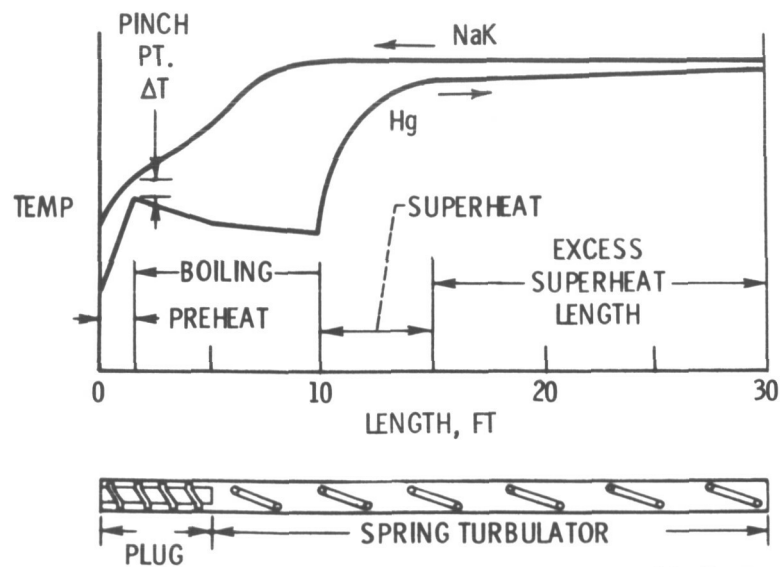
CS-40220

Figure VI-4. - SNAP-8 experimental reactor. Critical operation reached in May 1963; thermal power, 600 kilowatts; sodium-potassium outlet temperature, 1300° F; energy output through April 15, 1965, 5 154 332 kilowatt-hours.



CS-40218

Figure VI-5. - SNAP-8 tube-in-tube boiler. Sodium-potassium and mercury flow in opposite directions; shell dimensions: outside diameter, 4.25 inches; wall thickness, 0.125 inch; length, 30 feet; tube dimensions (seven tubes): inside diameter, 0.652 inch; wall thickness, 0.09 inch; length, 30 feet; wet weight, 480 pounds.



CS-40175

Figure VI-6. - Temperature profile of SNAP-8 tube-in-tube boiler.

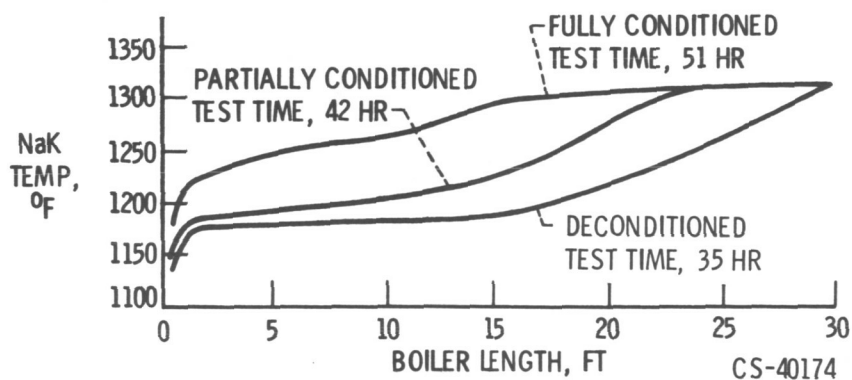
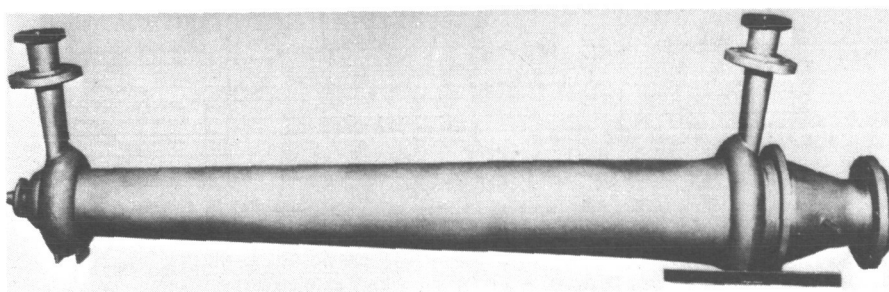
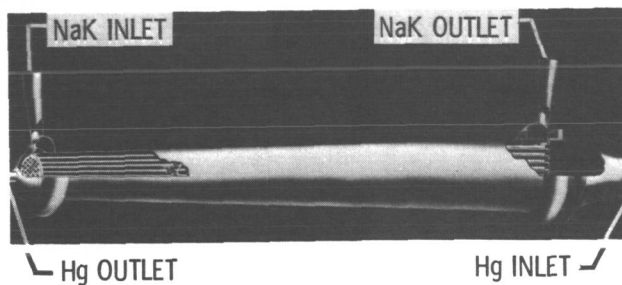
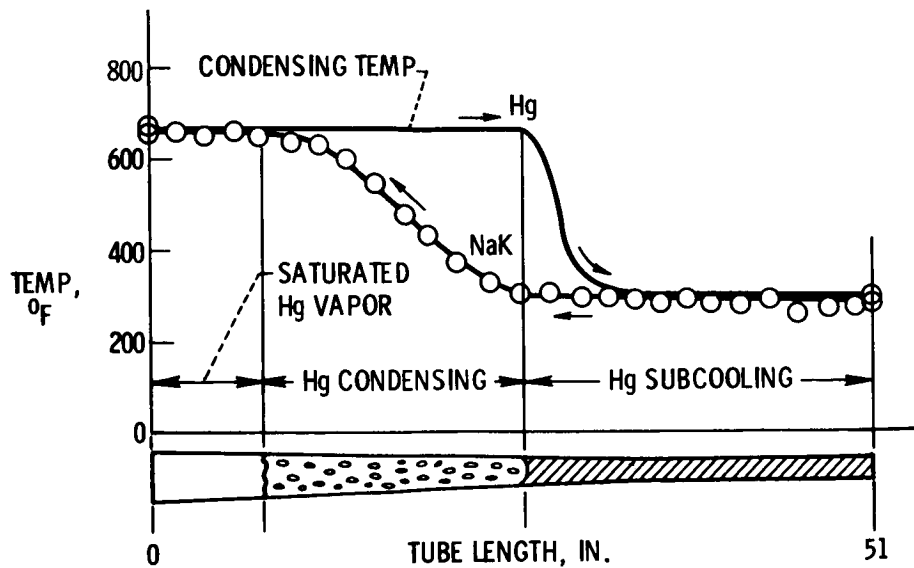


Figure VI-7. - Conditioning history of SNAP-8 tube-in-tube boiler. Mercury flow rate, 11 500 pounds per hour; mercury exit pressure, 265 pounds per square inch absolute; mercury inlet temperature, 450° F; sodium-potassium flow rate, 45 000 pounds per hour; sodium-potassium inlet temperature, 1310° F.



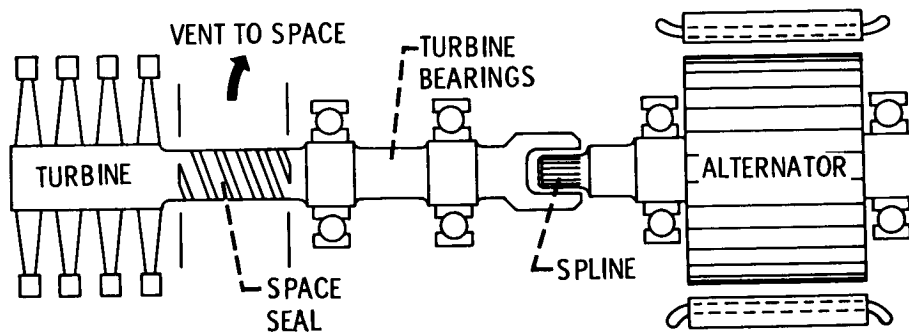
CS-40221

Figure VI-8. - SNAP-8 condenser. Sodium-potassium and mercury flow in opposite directions; shell dimensions: outside diameter, 4.4 to 7 inches; length, 52 inches; tube dimensions: inside diameter, 0.44 to 0.20 inch; length, 51.5 inches; wet weight, 120 pounds.



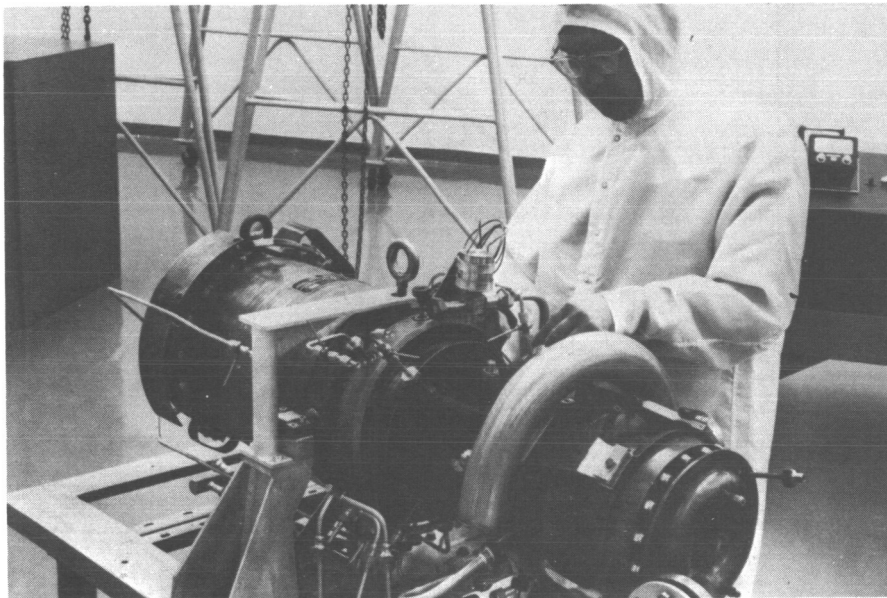
CS-40180

Figure VI-9. - Temperature profile of SNAP-8 condenser. Mercury flow rate, 12 500 pounds per hour; sodium-potassium flow rate, 41 500 pounds per hour; mercury inlet temperature, 678° F; mercury outlet temperature, 490° F; sodium-potassium inlet temperature, 486° F; sodium-potassium outlet temperature, 672° F.



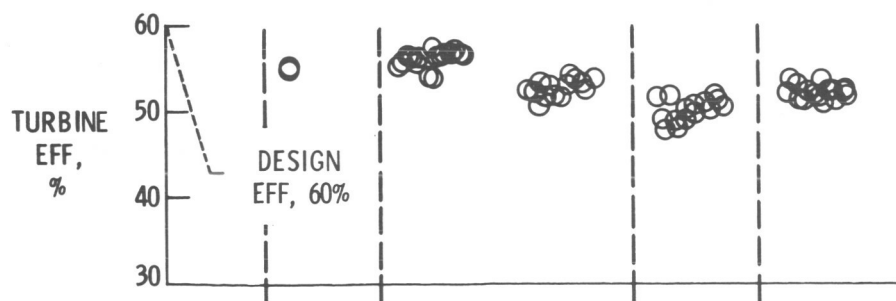
CS-40590

Figure VI-10. - Schematic drawing of turbine-alternator assembly. Turbine design conditions: output, 63 kilowatts; efficiency, 60 percent; weight, 151 pounds; speed, 12 000 rpm; alternator design conditions: output, 80 kilovolt-amperes; power factor, 0.75; efficiency, 87 percent; frequency, 400 cps; weight, 430 pounds.



CS-40188

Figure VI-11. - Turbine-alternator assembly in clean room.



TAA UNIT	1	2	3	4
TOTAL TEST TIME, HR	820	141	42	117
NO. OF STARTS	43	3	2	3

CS-40178

Figure VI-12. - Performance comparison of SNAP-8 turbine assemblies.

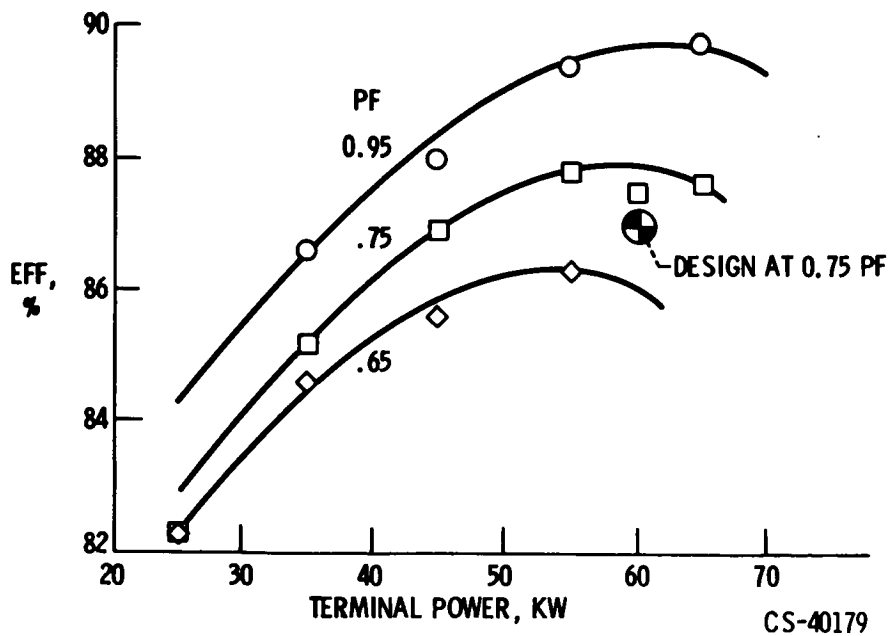


Figure VI-13. - SNAP-8 alternator efficiency as function of power.

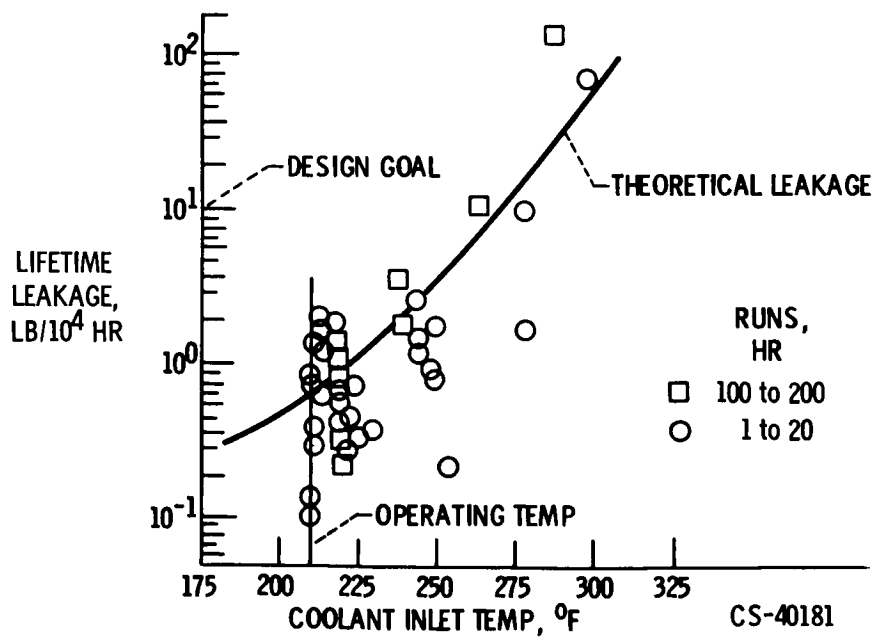
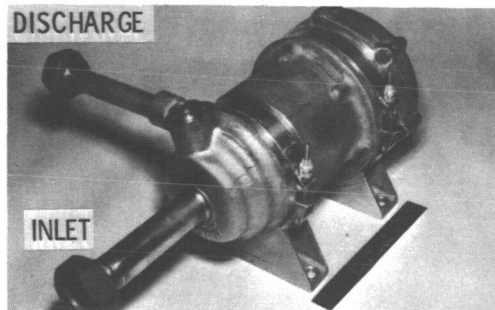
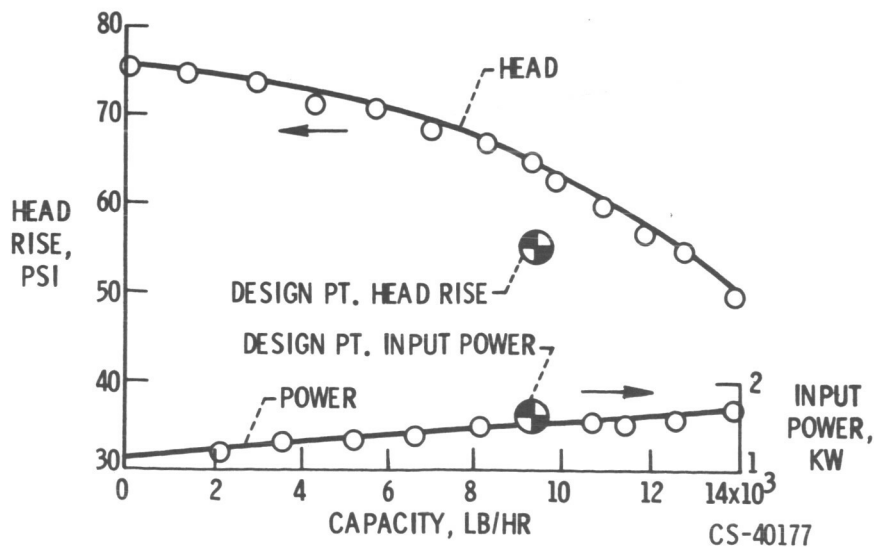


Figure VI-14. - SNAP-8 seal-to-space leakage.



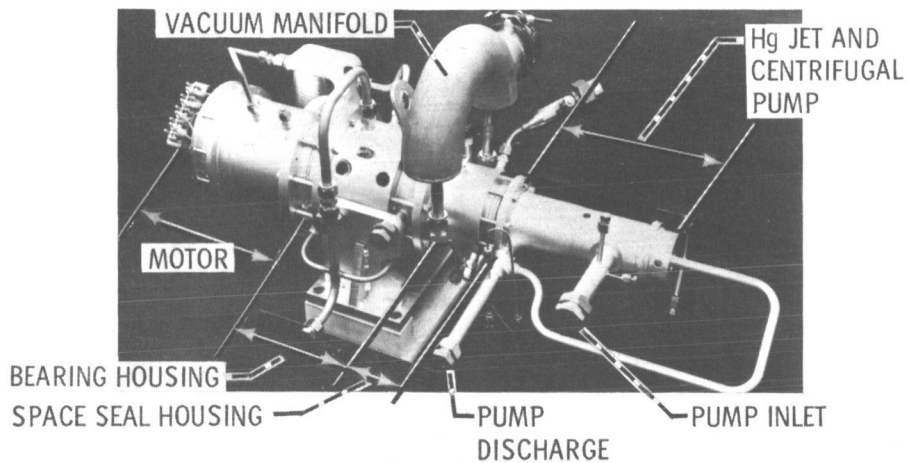
CS-40219

Figure VI-15. - Lubricant-coolant-pump - motor assembly. Design conditions: speed, 7800 rpm; head rise, 57 pounds per square inch; flow, 9400 pounds per hour; input power, 1.6 kilowatts; overall efficiency, 27 percent; carbon journal and thrust bearings lubricated with polyphenyl ether.



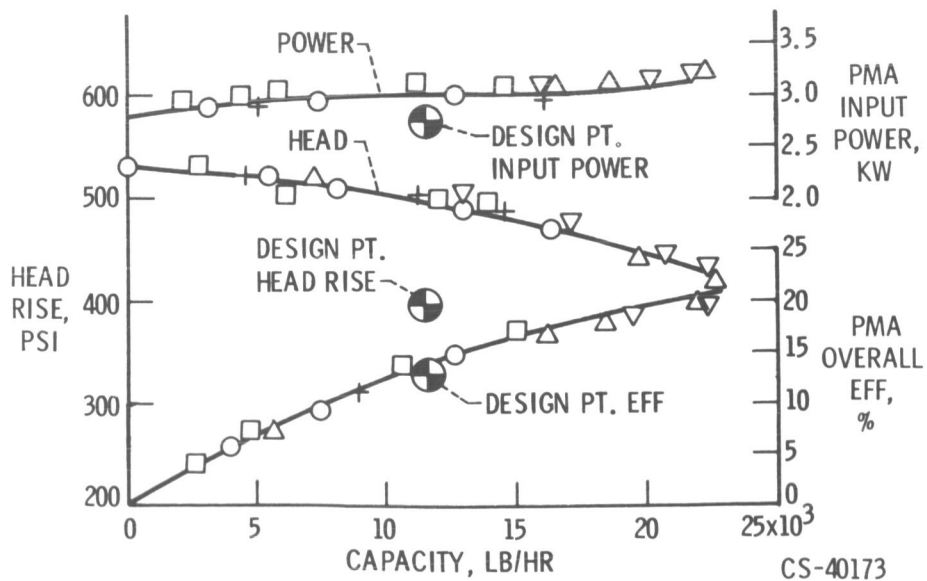
CS-40177

Figure VI-16. - Performance of lubricant-coolant-pump - motor assembly. Fluid, polyphenyl ether.



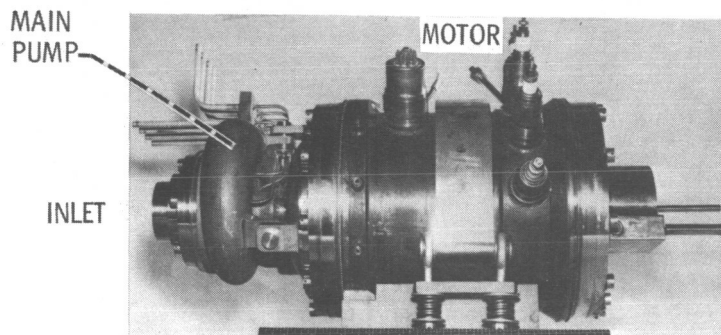
CS-40222

Figure VI-17. - Mercury-pump - motor assembly. Design conditions: speed, 7800 rpm; head rise, 394 pounds per square inch; flow, 11 500 pounds per hour; input power, 2.8 kilowatts; overall efficiency, 14 percent; ball bearings lubricated with polyphenyl ether.



CS-40173

Figure VI-18. - Performance of mercury-pump - motor assembly.



CS-40217

Figure VI-19. - Sodium-potassium-pump - motor assembly.
Design conditions: speed, 5800 rpm; head rise, 35 pounds per square inch; flow, 35 300 pounds per hour; input power, 4.6 kilowatts; overall efficiency, 35 percent; sodium-potassium-lubricated, tilting-pad journal and thrust bearings.

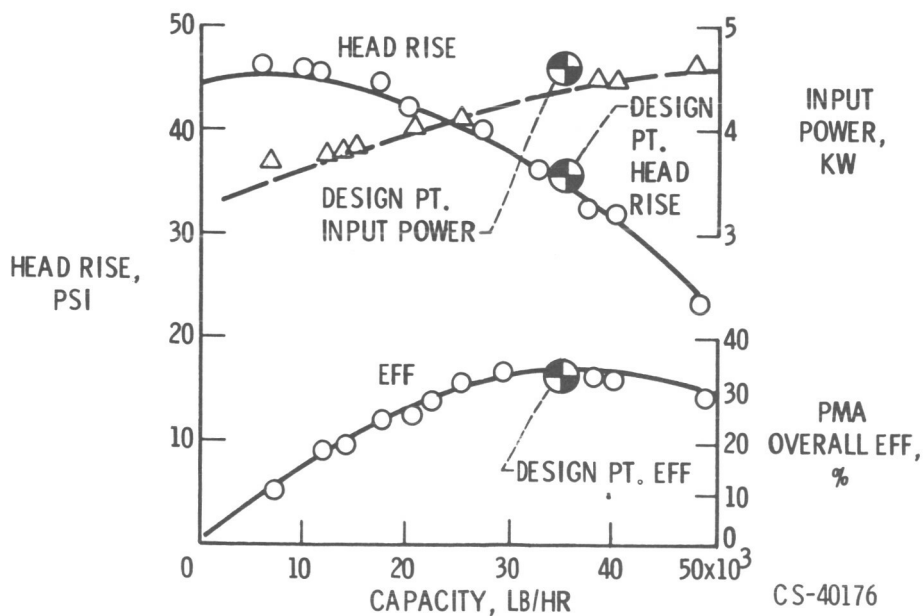


Figure VI-20. - Performance of sodium-potassium-pump - motor assembly operating at 1170° F.

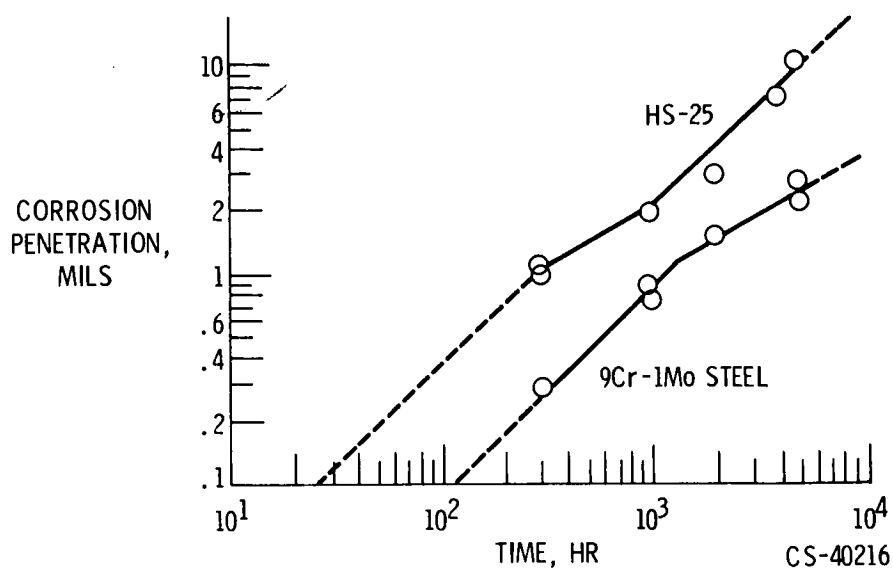


Figure VI-21. - Corrosion rate of selected materials in refluxing mercury capsules at 1100° F.

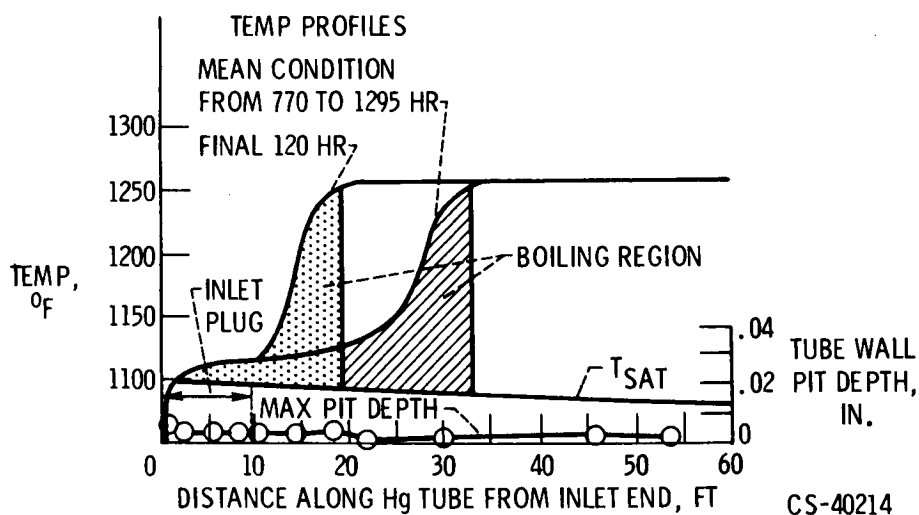


Figure VI-22. - Temperature rise and pitting in mercury tubes during 1425-hour test of full-scale boiler.

VII. POTASSIUM RANKINE SYSTEM MATERIALS TECHNOLOGY

Louis Rosenblum, David R. Englund, Jr., Robert W. Hall,
Thomas A. Moss, and Coulson Scheuermann

INTRODUCTION

The discussion of the materials technology for advanced Rankine cycle systems presented herein mainly concerns the working fluid, potassium, and the containment materials, alloys of the refractory metals columbium and tantalum. Some of the problems inherent in the application of these materials to space power systems are presented, and the more significant results of recent materials investigations are summarized.

Before materials are considered in detail, however, the temperature regime of operation of the potassium-Rankine system should be defined. The working fluid can be used as a guide to delimit the temperature regime for the advanced Rankine cycle system. In figure VII-1 the vapor pressure is shown as a function of temperature for several liquid metals of interest: mercury and the alkali metals (cesium, rubidium, potassium, sodium, and lithium). The shaded area to the left is the area of operation of the SNAP-8 mercury system discussed in paper VI; the shaded area on the right is the operational regime of the advanced system discussed herein. The boundaries of the shaded areas are fixed by both system operation and materials considerations. The upper pressure limit, for example, is set by design stress limitations; the lower pressure limit reflects such operational considerations as vapor velocity, pump cavitation, and subcooling. The higher temperature boundary at approximately 2200° F for the advanced system is established by temperature limitations of available refractory alloys. The lower temperature boundary at 1400° F is determined by such operational considerations as optimum radiator temperature and cycle efficiency. Obviously, these maximum temperature and pressure limits can be extended as new materials with improved properties are developed.

There are four common refractory metals that can be considered for use in potassium Rankine systems: tungsten, tantalum, molybdenum, and columbium. Some of the important properties of these metals are listed in table VII-1. Tungsten has the highest melting point (over 6000° F) and columbium the lowest (about 4500° F). Even this temperature, however, is about 2000° F higher than the operating temperatures anticipated in potassium Rankine systems. Columbium has the lowest specific gravity (about the same as common nickel-base superalloys), while tantalum and tungsten are much heavier.

Columbium and tantalum are highly fabricable, ductile metals, while tungsten and molybdenum are relatively brittle, particularly in the welded condition. The poor fabricability of tungsten and molybdenum renders them unsuitable for use as containment materials for the complex

pipng systems needed in Rankine systems; thus, columbium and tantalum alloys were selected for this application.

OXIDATION OF COLUMBIUM, TANTALUM, AND THEIR ALLOYS

Although tantalum and columbium alloys appear to be suitable containment materials, their use poses an unusual problem because of their high reactivity with contaminants, in particular with oxygen. At the high temperatures of system operation, oxygen is highly soluble in these refractory metals; they literally act as sponges and tend to absorb available oxygen from the environment. Since the addition of relatively small amounts of oxygen to a refractory metal alloy can produce marked changes in strength, ductility, and corrosion resistance of the alloy to potassium, the use of these materials hinges on the control exerted over the contamination reactions. Oxygen contamination, its control, and its effects on the properties of the structural materials are discussed throughout this paper. Concern with contamination of system materials that are expected to operate in space may seem somewhat peculiar, since there is little source of contamination in space. However, most of the research and development on these power systems will be carried out in ground-test vacuum facilities in which oxygen contamination is a real possibility. Therefore, if contamination is to be limited and controlled, the manner in which the oxidation process occurs must be understood and a quantitative determination of the oxidation rates made under test environment conditions.

The low-pressure oxidation of columbium and tantalum refractory metal alloys can be visualized as occurring in three consecutive steps. The overall rate of reaction is determined by that step which occurs at the slowest rate, called the rate-controlling step. The proposed steps, or processes, in the low-pressure oxidation of columbium, tantalum, and their alloys are shown in the simplified model given in figure VII-2. The first process is gaseous diffusion of oxygen molecules to the surface, wherein the number of molecules per second that impinge on the surface of the metal is described by the well-known kinetic theory of gases. The second process, surface reactions, covers the reactions of the molecules on the surface, such as adsorption of the molecules and dissociation of the molecules into atoms. The third process is simply the diffusion of oxygen atoms into the bulk solid. When gaseous diffusion is rate controlling, the oxygen weight gain w is directly proportional to time t :

$$w \propto t$$

When a surface reaction is the rate-controlling process, the weight gain is proportional to time to the n^{th} power:

$$w \propto t^n$$

For thin-walled specimens, comparable with tube thicknesses that would be employed in space power systems,

$$n < 1$$

When diffusion in the solid is rate controlling, the weight gain is proportional to the square root of time:

$$w \propto \sqrt{t}$$

An investigation to establish the rate-controlling process and to obtain quantitative data on oxidation rates was conducted. In this investigation, a novel method was used which has a sensitivity two orders of magnitude greater than available gravimetric methods. The experimental apparatus is shown in figure VII-3. Oxygen is admitted to the vacuum system through the controlled leak; it is simultaneously removed by means of two pumps. One is a conventional vacuum ion pump and the other is the heated refractory metal specimen itself. The oxygen pressure over the specimen P_2 can be set at the desired level by adjusting the oxygen leak rate. The value of P_2 is obtained from a measurement of P_3 , which is then corrected for thermal transpiration effects. The rate of oxygen pickup by the specimen can be readily calculated from the oxygen pressure drop between P_0 and P_1 (as measured by the ionization gages and the mass spectrometers) and the known vacuum conductance. The oxygen weight gain rate R of the specimen is given by the relation

$$R = (P_0 - P_1)C$$

where C is the conductance. This relation is analogous to Ohm's law for electrical current flow. With this apparatus, continuous measurements of oxidation rate have been made for columbium, tantalum, and seven columbium and tantalum alloys of interest. Tests were run over the pressure range of 10^{-8} to 10^{-5} torr and over the temperature range of 1600° to 2000° F. Shown in figure VII-4 is a plot of the experimental data for the oxidation of columbium at a temperature of 1800° F and an oxygen pressure of 3×10^{-8} torr. The weight gain was linear with time for a test run of over 200 hours. This result is typical of the refractory metals tested, inasmuch as all these metals exhibited a linearity between oxygen weight gain and time. These results are significant because they identify gaseous diffusion as the probable rate-controlling process in the oxidation of refractory metals over the range of conditions covered in these tests.

Further, since flux of oxygen molecules to the surface controls the oxidation rate and since this flux is proportional to pressure, the rate of oxygen weight gain for the refractory metals tested should be directly proportional to the oxygen pressure. This conclusion is confirmed as indicated in the typical case given in figure VII-5. Shown is a plot of oxidation rate as a function of oxygen pressure for the columbium-zirconium alloy Cb-1Zr over the temperature range of 1600° to 2000° F. The weight gain rate is, in fact, linear with pressure. The equation of the oxidation rate - pressure line is shown on the figure. The quantity in the parentheses is the kinetic theory of gas expression for the flux of oxygen molecules to the surface of the specimen under the test conditions. The factor ϵ is termed the "pumping efficiency" of the material. The value of ϵ of 0.15 determined for the Cb-1Zr alloy indicates that for every 100 molecules of oxygen that hit the surface of the alloy, 15 penetrate into the bulk metal. Values of pumping efficiency obtained

for columbium, tantalum, and the columbium and tantalum alloys tested were between 0.02 and 0.20; the columbium alloys had generally higher values than comparable tantalum alloys.

In regard to the problem of oxygen contamination of refractory alloys during operation in ground-test vacuum facilities, it is evident that the pumping efficiency values can be used to calculate test vacuum requirements as a function of alloy wall thickness and test time. As an illustration, oxygen pressure is plotted against the time needed to pick up the indicated oxygen contamination in figure VII-6 for T-111 (Ta-8W-2Hf) alloy with one side of the 20-mil-wall tube exposed to the vacuum environment and operated at 2000° F. If, for example, it is desired to limit contamination to no more than 100 ppm oxygen during a 1000-hour test, the oxygen partial pressure must be no more than 1×10^{-8} torr.

The pressures discussed so far have been oxygen partial pressures; however, vacuum gages measure the total system pressure. The oxygen partial pressure is approximately a decade or more lower than the total pressure. In the example just given, in order to ensure a contamination pickup of less than 100 ppm in 1000 hours, the total system pressure should be maintained at 1×10^{-7} torr or less, as measured by the vacuum gage.

SPACE POWER SYSTEM CONTAINMENT MATERIALS

Requirements

The prime requirements for a containment material are as follows. First, it must have good high-temperature creep strength. Second, since the containment material will be utilized primarily in the form of thin-wall tubing which must be welded into a highly reliable, leak-tight piping system, the material must be readily fabricable and possess good ductility in the welded condition. Finally, the containment material must be resistant to corrosion by boiling potassium.

Creep Strength

The first requirement, creep strength, is particularly important since space power systems must operate at high temperatures for long times. Allowable creep deformation, for example, might be limited to less than 1 percent in 10 000 hours. Although there are many columbium and tantalum alloys which could be considered for use as containment materials, no long-time creep data for these alloys were available when Rankine system feasibility studies were initiated. Thus, the first goals were to identify the most promising alloys and to generate the long-time creep information required for preliminary design studies.

The chemical compositions of some of the alloys evaluated are shown in table VII-2. Colum-
bium - 1-percent zirconium is a highly fabricable but relatively weak columbium-base alloy which was in the most advanced stage of development when the study was initiated. The other four materials listed are newer alloys which attempt to combine the good fabricability and weldability of columbium - 1-percent zirconium with better high-temperature strength. The alloys FS-85 and D-43 are columbium-base alloys while T-111 and T-222 are tantalum-base materials.

There are two basic strengthening mechanisms utilized in these alloys. First, other high-melting-point metals, such as tungsten, are added as solid-solution strengtheners; that is, the tungsten replaces columbium or tantalum in the base metal lattice. The difference in atomic sizes produces strains in the lattice and increases strength. Second, smaller amounts of the very reactive metals, zirconium or hafnium, are added to promote dispersion or precipitate strengthening. These metals react with residual or intentionally added interstitial elements such as carbon, oxygen, or nitrogen to form a very fine dispersion of second-phase particles which act as barriers to the high-temperature deformation process.

The high reactivity of these columbium and tantalum alloys with oxygen and other interstitials poses a problem in high-temperature creep testing of these materials. If the test environment is not sufficiently pure, the creep specimen will absorb contaminants such as oxygen from it. This continuous contamination would progressively change the composition of the material and thus affect the creep properties being measured. In general, contamination with oxygen in amounts greater than 200 or 300 ppm makes the material stronger but less ductile. Such contamination during high-temperature creep testing in the laboratory could lead to an overly optimistic estimate of the strength of the material in service. In the high vacuum of space where contamination is absent, the material would be weaker than in the laboratory test.

In order to minimize the problem of oxygen contamination in creep tests, strict limitations were imposed on the vacuum level at which tests were conducted and on the test duration. For an initial screening study which was used to identify the most promising alloys, for example, the tests were limited to durations of a few hundred hours and conducted at total pressures of 10^{-6} to 10^{-7} torr. For tests with durations of thousands of hours, ultrahigh-vacuum creep equipment was designed and constructed.

In the screening program, the creep behavior of twelve columbium alloys and three tantalum alloys was evaluated at temperatures from 2000⁰ to 2400⁰ F and at a constant stress of 4000 psi. This stress was selected as being in the range of interest for typical components of the containment system. Some of the results from the 2200⁰ F screening tests are shown in figure VII-7. Plotted is creep strain in percent against the test time in hours. Under these test conditions, Cb-1Zr crept 1 percent in only 30 hours. The strongest alloys were the tantalum alloys, T-222 and T-111, and the columbium alloys, FS-85 and D-43. These alloys all crept less than 1/2 percent in 300 hours. The other 10 alloys generally fell in the intermediate region between the strongest alloys and Cb-1Zr, although a few were even weaker than Cb-1Zr. On the basis of these results, attention was focused for longer time tests on the four alloys, FS-85, D-43, T-111, and T-222.

The ultrahigh-vacuum creep units developed for these tests are shown in figure VII-8. These creep units are bakeable stainless-steel systems which utilize copper gaskets for all demountable joints. They are evacuated by ion pumps and routinely operate at total pressures of 10^{-8} to 10^{-9} torr. With such units, contamination of 30-mil tantalum alloy sheet has been held to less than 100 ppm in 10 000-hour creep tests.

Although extensive long-time creep data are not yet available, a preliminary comparison of the creep properties of the selected tantalum and columbium alloys at 2200⁰ F are shown in figure VII-9. Since weight is an important consideration in space power systems, the tests were conducted at a constant ratio of stress to density. The actual stresses are indicated in paren-

theses. Despite the fact that the tantalum alloys were tested at higher stress levels to compensate for their higher density, they are significantly more creep resistant than the columbium alloys. The T-222 alloy ran for 7500 hours at 8000 psi before exceeding the 1-percent creep limit. At somewhat lower stresses or temperatures, this alloy would meet the goal of less than 1-percent creep in 10 000 hours.

The effect of stress on the creep rate of the T-222 alloy at 2200° F is shown in figure VII-10. Plotted is the creep curve at 8000 psi which was shown in figure VII-9 and the creep curve at 12 000 psi. Increasing the stress level to 12 000 psi decreases the time for 1-percent creep from 7500 hours to approximately 2500 hours. For low stresses and small strains, the stress dependence of creep appears to follow the relation

$$\dot{\epsilon} = \sigma^n$$

where $\dot{\epsilon}$ is the creep rate, σ is the applied stress, and n is a constant. From available data on tantalum and columbium alloys, the value of the exponent n is approximately 3.

As is known, creep strength is strongly dependent on metallurgical structure. Heat treatments which alter the size and distribution of oxide or carbide precipitates in these alloys will affect their creep strengths. The effect of annealing temperature on creep strength is illustrated in figure VII-11 for the tantalum alloy T-111, creep-tested at 2200° F and 8000 psi. The material annealed for 1 hour at 3000° F before testing was approximately three times as creep resistant as the material annealed at 2600° F for 1 hour before testing. This effect is attributed to the residual carbon present in the alloy. At temperatures between 2800° and 3000° F, the carbon in the alloy is taken into solution, and relatively rapid cooling traps the carbon in the dissolved state. Subsequent testing at elevated temperatures allows the carbide to precipitate from the matrix during creep testing. It is this precipitate which enhances the creep properties of the alloy.

The results of these long-time creep studies to date indicate that existing commercial tantalum-base alloys have adequate creep strength for use as potassium containment materials to temperatures approaching 2300° F. For higher temperatures, stronger alloys will be required. Shown in figure VII-12 is a Larson-Miller creep-strength plot for one of the more promising advanced alloys, Astar 811C, and the two tantalum alloys just discussed, T-111 and T-222. On figure VII-12 the stress for 1-percent creep is plotted against the Larson-Miller time-temperature parameter ϕ . The temperatures indicated correspond to those for the Larson-Miller parameter at a 10 000-hour test time. The Astar 811C alloy (Ta-8W-1Re-1Hf-0.025C) is solid solution strengthened with rhenium as well as with tungsten and is also precipitation strengthened since it contains hafnium and carbon. This new tubing alloy, at comparable stresses and times, has a temperature advantage of about 150° F above commercially available tantalum alloys.

Fabricability

The strength situation for the refractory metal alloys seems promising. However, as was previously mentioned, another prime requirement for a containment material is that it be fabricable. As of the present time, all alloys discussed herein with the exception of the advanced

tantalum-base alloy, Astar 811C, have been fabricated into small-diameter tubing, which is a practical measure of fabricability.

One quantitative measure of the fabricability of an alloy is its ductile-to-brittle transition temperature. It is a characteristic of these columbium and tantalum alloys that they exhibit a change from ductile to brittle behavior over a relatively narrow temperature range, as illustrated in figure VII-13. The transition temperature is easily determined by bending sheet specimens over a radius equivalent to the thickness of the sheet until brittle failure occurs or until a maximum angle of 100° is reached.

Bend transition tests of this type have recently been run on the refractory alloys of interest, and the results are shown in figure VII-14. The transition temperatures for the base material and for tungsten - inert-gas (TIG) arc-welded material are presented. A number of weld variables, such as welding speed, heat input, and spacing, were evaluated. The length of the black bars represents the temperature range over which the transition temperature occurred.

Although the Cb-1Zr alloy does not have the requisite strength characteristics, it is included for comparison since it is known to be readily fabricable. The FS-85 base material had a relatively low transition temperature, but in the as-welded condition the transition temperature was near room temperature. The relatively long bar for the as-welded D-43 alloy indicates the high sensitivity of this columbium alloy to the welding variables investigated; this sensitivity is one reason why it was dropped from further consideration. The alloys with the short bars are preferred since they indicate a low sensitivity to the welding variables. The tantalum-base alloys, as a class, exhibited very low transition temperatures and little sensitivity to the welding variables.

At Lewis special procedures have been developed to minimize contamination and to control welding variables. Personnel are required to put on clean-room coats and shoe covers before entering the welding room. The parts to be welded are chemically and ultrasonically cleaned and carefully handled so as to prevent contamination. Tungsten - inert-gas welding is performed in a controlled environment chamber. After the pieces to be welded are placed into the chamber, it is sealed and evacuated to a pressure of less than 1×10^{-5} torr. The chamber is then backfilled to atmospheric pressure with dry argon or helium containing less than 2 ppm oxygen. During the welding process, water vapor and oxygen levels are continuously monitored and controlled to assure a contaminant level of less than 5 ppm oxygen and 10 ppm water vapor. Electron-beam welding is performed in a large vacuum chamber at pressures below 1×10^{-4} torr. In this welding facility, electron beam welds have been made of refractory metals and alloys in thicknesses ranging from 5 mils to 1/8 inch. With the use of such procedures, high-quality welds with a minimum amount of contamination can be obtained with all the alloys discussed.

In addition to the problem of obtaining good as-welded ductility, however, the problem of embrittlement of the weld zone as the result of precipitation during long-time service must be considered. This precipitation phenomenon, called age hardening or simply aging, has led to serious problems in earlier systems. During long-time ground testing of space power systems, scheduled or inadvertent shutdowns often occur, and it is essential that the weld joints be ductile enough to accommodate the resulting thermal strains.

An experimental program is currently being conducted to determine if the more promising

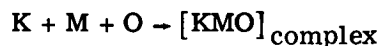
columbium and tantalum alloys are susceptible to this aging embrittlement. In these tests, welded sheet specimens are aged at temperatures and times of interest and the bend transition temperatures determined after this exposure. Available results for the alloys FS-85 and T-111 are shown in figure VII-15, where the bend transition temperature is plotted as a function of aging temperature. Aging time, in all cases, was 1000 hours. Both alloys were postweld-annealed at 2400⁰ F before aging. For FS-85, the bend transition temperature of the as-welded material is about -200⁰ F. However, on aging for 1000 hours at 1800⁰ F, the transition temperature increases to approximately 75⁰ F; that is, the weld is likely to be brittle at room temperature. On the other hand, however, although the alloy T-111 also exhibits the aging phenomenon, the transition temperature is always well below room temperature. No problems from aging of welds would thus be anticipated for this alloy.

As refractory metal test facilities are run on the ground, another practical consideration encountered is the necessity of cutting into the facilities after numerous hours of operation and then rewelding. Since some contamination is bound to occur during thousands of hours of operation, even at pressures as low as 10⁻⁸ torr, the effect of contamination on the properties of the alloys must be considered. Shown in figure VII-16 is the effect of preweld oxygen content on the as-welded transition temperature of the alloys T-111, T-222, and FS-85. Materials evaluated in these tests were doped with oxygen prior to welding, and the welding was performed with the procedures previously described. The T-111 alloy is relatively insensitive to the oxygen content over the range investigated. The FS-85 alloy shows a relatively gradual increase in the transition temperature with increased oxygen and reaches room temperature at 600 ppm oxygen. The T-222 alloy shows a relatively high sensitivity to the increased oxygen. This difference between the two relatively similar tantalum alloys, T-111 and T-222, may be ascribed to the intentional addition of 100 ppm carbon to the T-222 and 10 percent tungsten in T-222 as against the 8 percent in T-111. Additions of tungsten to tantalum appear to reduce the solubility of all interstitials (carbon, oxygen, and nitrogen) in the alloy. It is expected that oxygen additions above 300 ppm to the T-111 alloy will result in an increase in its transition temperature.

Up to this point, the strength characteristics and fabrication and weldability properties of several columbium and tantalum alloys have been discussed. Attention is now given to a critical materials area, that of compatibility of the refractory alloys with potassium.

Corrosion

It is now commonly accepted that corrosion by potassium, and alkali metals in general, is highly dependent upon the presence of oxygen. It has been proposed that oxygen (O) present in the metal will react with the refractory metal (M) and potassium (K) to form a complex oxide, such as potassium columbate or tantalate:



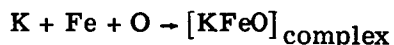
These complex oxides are believed to be highly soluble in potassium and thus are taken rapidly into solution. The potassium - refractory-metal - oxygen reaction is therefore expected to continue until all available oxygen is consumed.

Some alloys contain an element called a gettering element, which is a highly reactive element such as zirconium or hafnium which tends to form a very stable oxide. When a gettering element is present in the alloy, the getter reacts and combines with the oxygen. A reduction in the amount of available oxygen results in the formation of less of the complex oxide, which thereby imparts a degree of corrosion resistance to the alloy.

This mechanism is supported by several observations. First, oxygen distribution studies indicate that oxygen migrates from columbium to potassium, contrary to the expected behavior based on the free energies of formation of the respective oxides. These results imply the formation of an intermediate compound. Second, solubility studies show a high dependency of refractory metal solubility on oxygen content, which indicates the active role of an oxide. Third, complex refractory-metal - alkali-metal oxides are known and have been identified as corrosion products. Last, the nature of the corrosive attack is consistent with this mechanism.

In regard to the subject of solubility, as was just discussed, the amount of oxygen available for the formation of a complex oxide should control the amount of metal taken into a solution by potassium. The solubility of iron in potassium in the presence of materials with different gettering potentials can be used to illustrate this point. The solubility of iron in potassium was measured with a capsule similar to that shown in figure VII-17. The body of the capsule was made of iron and the sampling cup, of a different metal. The sampling cup was positioned within the capsule body as indicated in figure VII-17(c). After equilibration of the potassium with the iron, the capsule was inverted while still at temperature. Then the capsule was allowed to cool, and a sample was removed for analysis. The cup not only served to isolate the potassium sample but in this series of experiments also acted as an oxygen getter.

In figure VII-18 measured iron (Fe) solubility is plotted against estimated available oxygen. As indicated at the bottom of the figure, the cup metals used were nickel, molybdenum, tantalum, columbium, and zirconium. Because of their differing gettering abilities, each material sets a unique value for the amount of oxygen available for the reaction,



The expected variation in measured solubility was indeed obtained; the oxygen effect for iron is quite significant, with approximately two orders of magnitude difference between the solubility results with sampling cups of nickel, a relatively poor getter, and zirconium, a good getter.

This example illustrates the point of enhanced solubility of iron in the presence of oxygen. Presently, similar data are being sought for the refractory metals. Preliminary results of solubility tests, with Cb-1Zr alloy and pure columbium, have shown that the presence of zirconium in the alloy reduces the measured columbium solubility by about one order of magnitude below that obtained for the ungettered columbium. Thus, the information obtained for iron also appears to apply to columbium.

Now that the fundamental processes behind the corrosion reaction have been outlined, attention can be turned to material screening tests which are employed to determine the compatibility of possible containment materials with potassium. Inasmuch as oxygen appears to have a serious effect on corrosion, adequate precautions must be taken to ensure that oxygen is not inadvertently

introduced into the test. Careful handling and control of all test conditions are needed to minimize oxygen contamination so that test results will be meaningful.

Material screening tests were carried out in capsules with 0.5-inch diameter, 1.75-inch length, and 0.040-inch wall thickness. The capsule wall served as the test specimen. To minimize contamination of the metals during loading and capsule sealing, a special vacuum-handling facility was constructed, containing a potassium extruder, a work table, a remote manipulator to position the capsules within the vacuum enclosure, a welding fixture, and an electron beam welder. A measured amount of potassium was extruded from a sample tube and dropped into a capsule. The capsule was placed in the welding fixture and capped. The welding fixture was rotated and the electron beam welder was activated to seal the capsule. Since the entire operation was carried out rapidly and in a vacuum of less than 10^{-5} torr, contamination was minimized.

The capsules were then instrumented with thermocouples and inserted into individually controlled heaters clustered on a test bed. The capsules were tested in a vacuum chamber at a pressure of less than 1×10^{-7} torr, an acceptable vacuum level for the test times and temperatures. Heat input to the capsule was such that the potassium refluxed within the capsule. Potassium vapor rose to the upper part of the capsule where it condensed and then streamed down the wall of the capsule to produce a continuous circulation of fluid. At the end of the tests, the bed was removed from the chamber and the capsules were prepared for metallographic and chemical analyses to determine the extent of corrosion.

Thirteen columbium and tantalum tubing alloys were screened in this manner in the temperature range of 1800° to 2400° F for times up to 10 000 hours. The materials tested are given in table VII-3; both gettered and ungettered columbium and tantalum alloys were included. The potassium used in these tests was of high purity and contained less than 20 ppm oxygen.

The results of tests run on columbium alloys can best be shown by comparing the zirconium gettered alloy FS-85 with the ungettered alloy SCb-291. Figure VII-19 shows a sectioned capsule of SCb-291 which has been tested for 1000 hours at 2200° F. As shown in the accompanying photomicrographs, general dissolution occurred at the top of the capsule and attack along grain boundaries at the bottom of the capsule. Figure VII-20 shows a sectioned FS-85 capsule tested for 2000 hours at 2300° F. Despite the more severe test conditions imposed upon FS-85, it shows essentially no corrosive attack.

A comparison of reflux corrosion capsule results for an ungettered tantalum alloy, Ta-10W, with a hafnium gettered alloy, T-111, is given in figures VII-21 and VII-22, respectively. The ungettered Ta-10W alloy was tested at 1800° F. Termination of the test occurred at 128 hours, after the potassium had leaked out by penetrating the grains in the weld area. This penetration is shown in the bottom photomicrograph on figure VII-21. Intergranular attack was also found in the fine-grained structure at the top of the capsule. In contrast, the gettered alloy, T-111, under more severe test conditions, showed essentially no attack in the weld zone and only a slight roughening at the top of the capsule.

With larger capsules than those previously described, encouraging results were also obtained in long-time tests on the gettered columbium alloys AS-55, D-43, and Cb-1Zr. The results for D-43 are typical of these alloys. As indicated in figure VII-23, there was no detectable corrosion after 10 000 hours at 2000° F.

The effect of both stress and strain on corrosion of columbium alloys in potassium was

investigated. For this purpose, the standard corrosion capsule was altered as shown in figure VII-24. Just above the midregion of the capsule, the wall thickness was machined down to provide a highly stressed region. The capsule was then heated to 2300⁰ F for 1000 hours. Internal pressure in the capsule resulting from the vapor pressure of potassium imposed an initial hoop stress of about 4000 psi on the thin-wall section, which caused it to bulge. The maximum strain in this test after 1000 hours was approximately 37 percent.

After the test, the capsule was sectioned and examined metallographically. A typical photomicrograph from the highly stressed section is shown in figure VII-24(c). There is no evidence of stress corrosion despite the high temperature and large amount of strain. These results are for the columbium alloy D-43, but similar results were also noted for other alloys. Thus, it is believed that stress corrosion is not likely to be a problem in potassium Rankine systems constructed from columbium or tantalum alloys.

The initial screening of the alloys and the determination of basic properties such as solubility limits are most readily obtained in capsules of one type or another as described. The alloy finally selected for a system, however, should be proof-tested in an engineering test loop specifically designed to simulate the proper temperature and flow conditions of the actual system. Since experience has been limited in the construction and operation of such complex test loops, a prototype loop was fabricated from the Cb-1Zr alloy. The choice of this alloy was dictated by the fact that it was the only refractory metal alloy available as tubing in 1963 when the test program was initiated. This loop is shown in figure VII-25. The vacuum chamber in which the loop is mounted was capable of maintaining a vacuum better than 2×10^{-8} torr during loop operation.

Shown in figure VII-26 is a schematic diagram of the corrosion loop. The two-loop system consisted of a primary sodium heater loop and a secondary potassium boiling and condensing loop. In the primary circuit, the sodium is discharged from a pump and flows through an electrical resistance heater to a tube-in-tube counterflow boiler, where heat is transferred to the potassium. The sodium loop operated at a maximum temperature of 2130⁰ F, a minimum temperature of 1990⁰ F, and a flow rate of 2.6 gallons per minute.

In the boiling and condensing secondary loop, the potassium is discharged from the pump through an electrical resistance preheater, where the temperature of the potassium is increased to a temperature near the saturation temperature before it flows into the boiler. In traveling through the boiler, the potassium is converted from liquid to superheated vapor and then passes through the first nozzle of the turbine simulator. Heat is rejected in the crossover line of the turbine simulator, and wet vapor then passes through stages 2 to 10 of the turbine simulator to the condenser. Condensed vapor is returned through the subcooler to the pump. Potassium in this circuit was boiled at 1850⁰ F, superheated to 2000⁰ F, and condensed at 1425⁰ F. The potassium circuit had a flow rate of 0.1 gallon per minute.

The loop was operated stably at these conditions for 5000 hours. Posttest metallurgical evaluation of the potassium circuit revealed no significant corrosion.

Since the design and operation of the Cb-1Zr prototype corrosion loop was successful, additional corrosion loops are now being constructed from the T-111 tantalum alloy.

Test Instrumentation

With a test of the complexity of that just described, success rests heavily upon instrument performance. The instrumentation used must not only be able to operate reliably for long periods, but in some applications must be capable, in terms of materials, of withstanding high temperatures and contact with potassium.

In the consideration of pressure measurements, the pressure-pickup material in direct contact with the potassium must be corrosion resistant. This requirement precludes the use of stainless steel in the pressure instrumentation, even in the low-temperature portions of the loop. A successful technique of solving this problem is the use of the well-known slack-diaphragm pressure transmitter, shown schematically in figure VII-27. The slack diaphragm forms a separating membrane between the potassium of the loop and the NaK which fills the rest of the pressure measuring system; yet it allows the pressure to be transmitted to the pressure pickup. The spring properties of this high-temperature diaphragm have little effect on the pressure measurement; all that is required is that the stiffness be low compared with that of the pressure transducer. The choice of material for the diaphragm and its housing can therefore be dictated by a materials consideration without regard to its characteristics as a spring. Further, because the precision-spring measuring element of the transducer can be maintained at room temperature, the accuracy of the technique is good. Probable errors of the order of 1 percent of full scale are typical.

An example of a Cb-1Zr alloy slack-diaphragm assembly is shown in figure VII-28. This pressure pickup was used on the corrosion loop previously described. Comparable assemblies of T-111 alloy are being made for the T-111 corrosion loops presently under construction.

Response time is the major limitation of this slack-diaphragm technique. The relatively long NaK-filled line that allows the transducer to operate at room temperature also limits the frequency response of the system to the order of 0.1 cps. Making transient pressure measurements generally requires the use of very short connecting tubing, which results in requirements for high-temperature pressure transducers. A transducer of the type shown in figure VII-29 was used on the previously described corrosion loop to measure boiler inlet pressure and indicate loop stability. This transducer is a commercial design, which was modified by the substitution of refractory alloys for the stainless steel normally used. The diaphragm and its housing are made of tantalum alloys. The diaphragm deflection is measured with a differential transformer. The transducer is restricted to operation at temperatures no more than 900° F because of temperature limitations on this differential transformer. The usable frequency response was limited to about 20 cps by the nature of the installation.

A more truly high-temperature transducer is shown schematically in figure VII-30. This transducer is being developed for operation at 1800° F. The pressure capsule is about 1 inch in diameter and made from W-25Re alloy. A vacuum diode operated in the space charge limited mode is used to measure capsule deflection. A linear output signal can be obtained by utilizing a double-diode technique, with one diode a variable-spacing collector-emitter combination and the second, a built-in fixed-spacing reference diode. As stated, this transducer is in development; prototype models are being built for testing in a two-phase potassium loop.

Since the material tests described earlier involve thousands of hours of operating time, thermocouple drift can be a serious problem. In a recent test at 2200° F, for example, a ther-

thermocouple drift of 100°F was observed in 150 hours. There are a great many interrelated factors that affect thermocouple stability. These factors include choice of material, purity of material, wire size, handling and assembly techniques, and the environment to which the thermocouple is subjected. With proper control of these factors, good stability can be achieved, as indicated by recent high-vacuum stability tests summarized in table VII-4. In one set of 1000-hour tests, stability was within $\pm 18^{\circ}\text{F}$ for temperatures ranging from 2200° to 2600°F . The alloys tested included both platinum-rhodium (Pt-Rh) and tungsten-rhenium (W-Re) alloys. In another test at 3200°F for 4000 hours, stability to within 30°F was obtained. The alloys used in this test were W-3Re/W-25Re. In all these tests 20-mil-diameter thermocouple wires were insulated with very high purity alumina. These results reflect the state of the art attainable with proper care in fabricating and using available high-temperature thermocouples.

System Working Fluid

In the past few years, property measurement programs supported by NASA and other government agencies have bridged the last of the engineering property gaps. Currently, the major engineering properties of potassium, such as vapor pressure, density, thermal conductivity, and viscosity, are known over the temperature range of interest to the advanced space power system. For the most part, small amounts of oxygen impurities appear to have a negligible effect on the engineering properties of potassium. This effect, however, is not negligible in relation to corrosion.

As has been previously described, the presence of oxygen enhances the corrosion attack. It is therefore of the greatest importance (1) that the impurity concentration of the potassium be low (preferably 20 ppm or less), (2) that special handling procedures be employed to preclude contamination of the potassium, and (3) that there be a reliable method for the analysis of oxygen in potassium at concentrations below 20 ppm.

Currently, the first requirement can be met. Purification procedures such as distillation and hot gettering allow the routine production of potassium with oxygen concentrations between 5 and 15 ppm.

The second requirement can also be satisfied if rigid standards of cleanliness and handling are maintained. With the use of clean metallic transfer lines which have been vacuum-leak-checked for integrity, potassium has been transferred from system to system and from apparatus to apparatus without introducing measurable contamination.

The third requirement, a reliable analytical method for measuring low concentrations of oxygen, has proved to be the most difficult of the potassium problems. Currently, three principal methods are employed in the analysis of oxygen in potassium: amalgamation, distillation, and neutron activation. The amalgamation method uses the principle of selective solubility to separate the potassium from the oxygen impurity. The potassium is dissolved in mercury; the insoluble oxygen impurity is thus allowed to float to the surface of the mercury. In the distillation method, the volatile potassium is distilled from the less volatile oxide impurity. In the neutron activation method, an encapsulated potassium sample is irradiated with fast neutrons followed by a measurement of the activity of the decay products from the neutron-oxygen reaction.

Until recently, little was known of the accuracy and precision of these methods, in spite of the fact that two of these methods, amalgamation and distillation, have been in use for over a

decade. This state of affairs was further apparent in the results obtained between laboratories. When two or more laboratories performed analyses on equivalent samples of potassium, the results were usually in poor agreement.

Investigations at Lewis have indicated that the major cause of these difficulties is the inadvertent contamination of the potassium during the act of sampling, transfer, and analysis. To minimize such contamination, special vacuum analytical techniques and equipment were devised. The results obtained with two such techniques, vacuum amalgamation and vacuum distillation, on replicate samples are given in table VII-5. For batch 3, a neutron activation analysis was obtained in addition to the amalgamation and distillation analyses. As is apparent, the oxygen values obtained by all three independent methods show good agreement. Thus, for the first time, a high degree of confidence may be had in the accuracy of these methods.

Establishment of the accuracy and precision of results, however, does not complete the analytical situation. The matter of the lack of agreement between different laboratories must still be considered. This problem was attacked through a series of Round Robin Analyses, sponsored by Lewis, the AEC, and the ASTM. Standard samples prepared by Lewis were distributed to 15 participants in government and industrial laboratories throughout this country. The results of the third and most recent Round Robin Analysis were as follows. Amalgamation was the method used by most of the 15 participants; however, a few used distillation or neutron activation. The total number of determinations made was 77; the mean value obtained was 14.7 ppm oxygen; the range of values was 4 to 26 ppm with a standard deviation of 5.1 ppm. These results of this third Round Robin Analysis are encouraging, for they show that reasonable agreement can be obtained among laboratories. Also, these results indicate a more general awareness of the need for environmental control and careful handling.

SUMMARIZATION

Reviewed in this paper are some of the more significant results of recent potassium Rankine system materials investigations. In summary, the oxidation problem, present in all ground-test operations, has been brought into focus: in terms of fundamentals, the probable rate determining process in the low-pressure oxidation of columbium and tantalum alloys has been identified; in terms of engineering, the requirements for vacuum test environments have been defined. As for the structural properties of container materials, test results indicate that the creep strength of available commercial columbium and tantalum alloys is adequate for system operating times and temperatures, as currently envisioned. Moreover, newer tantalum-base alloys such as Astar 811C promise as much as 150⁰ F increased temperature capability, if needed. The fabricability and weldability of the high-strength alloys, such as T-111, appear to be satisfactory, if care is taken to minimize contamination and proper heat treatment is employed. The important question of compatibility of container materials with potassium has been investigated by means of solubility, screening, and pumped loop tests. The results to date indicate that the gettered columbium and tantalum alloys have adequate corrosion resistance. Further, instrumentation for the variety of material tests described, with suitable response and reliability, appear attainable with the proper choice of materials and installation techniques. Finally, as for the working fluid, potassium, the engineering properties are known over the temperature range of interest to the Rankine system, and, in the main, techniques have been established for purification, handling, and oxygen analysis

TABLE VII-1. - PROPERTIES OF REFRACTORY METALS

Metal	Melting point, °F	Specific gravity	Fabricability
Tungsten	6170	19.3	Poor
Tantalum	5400	16.6	Good
Molybdenum	4750	10.2	Fair
Columbium	4470	8.6	Good

TABLE VII-2. - COMPOSITIONS OF TYPICAL
COLUMBIUM AND TANTALUM ALLOYS

Alloy	Composition, wt %					
	Cb	Ta	W	Zr	Hf	C
Cb-1Zr	Bal.	----	--	1	---	----
FS-85	Bal.	28	10	1	---	----
D-43	Bal.	----	10	1	---	0.1
T-111	----	Bal.	8	--	2	----
T-222	----	Bal.	10	--	2.5	.01

TABLE VII-3. - POSSIBLE COLUMBIUM
AND TANTALUM TUBING ALLOYS

Alloy	Composition
Columbium base	
B-33	Cb-4V
SCb-291	Cb-10Ta-10W
Cb-1Zr	Cb-1Zr
D-14	Cb-5Zr
AS-55	Cb-5W-1Zr-0.2Y-0.06C
B-66	Cb-5Mo-5V-1Zr
D-43	Cb-10W-1Zr-0.1C
FS-85	Cb-27Ta-10W-1Zr
Cb-752	Cb-10W-2.5Zr
C-129	Cb-10W-10Hf
Tantalum base	
Ta-10W	Ta-10W
T-111	Ta-8W-2Hf
T-222	Ta-9.6W-2.4Hf-0.01C

TABLE VII-4. - RECENT THERMOCOUPLE STABILITY DATA

	Test duration, hr	
	1000	4000
Measured stability, °F	Within ±18	Within +0, -30
Temperature, °F	2200 to 2600	3200
Thermocouple alloy	Pt-10Rh/Pt, Pt-6Rh/Pt-30Rh W/W-26Re, W-5Re/W-26Re	W-3Re/W-25Re
Configuration	Bare wires in ceramic insulator	
Insulator	Recrystallized Al ₂ O ₃ , 99.5 percent pure	
Wire diameter, in.	0.020	
Vacuum environment, torr	10 ⁻⁶ to 10 ⁻⁸	10 ⁻⁸

TABLE VII-5. - ANALYSIS FOR OXYGEN IN POTASSIUM

[Results from three independent methods corrected for systematic errors.]

Potassium batch	Analytical method	Number of determinations	Mean amount of oxygen, ppm	Standard deviation
1	Vacuum distillation	14	6.1	4.7
	Vacuum amalgamation	7	7.2	2.7
2	Vacuum distillation	7	8.7	2.7
	Vacuum amalgamation	3	6.9	2.5
3	Vacuum distillation	5	16.1	4.8
	Vacuum amalgamation	4	15.6	4.1
	Neutron activation	3	16.1	8.4

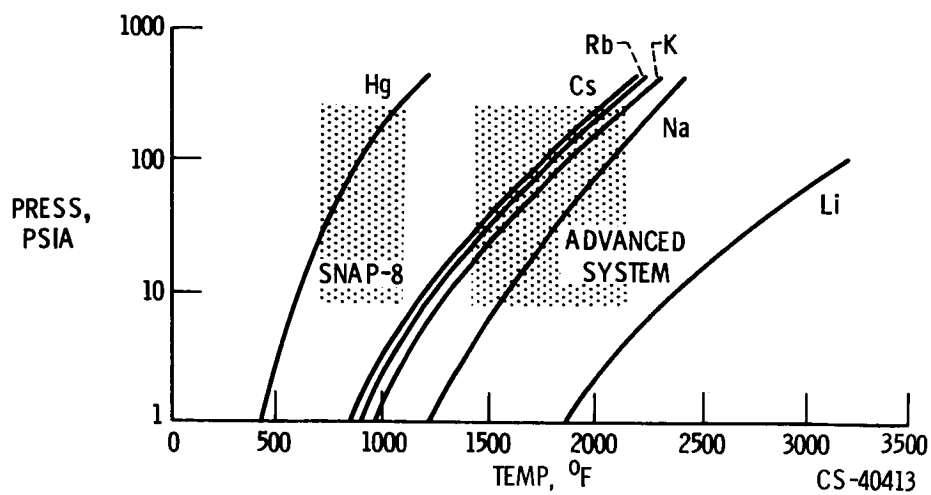


Figure VII-1. - Operational regimes for selected Rankine cycle systems.

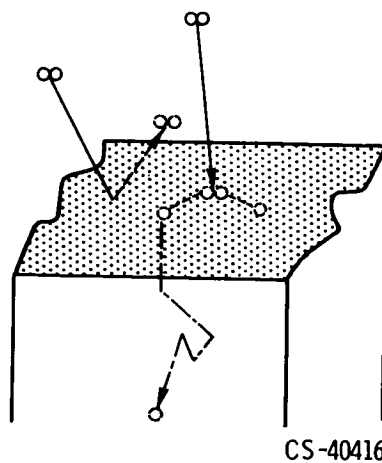


Figure VII-2. - Low-pressure oxidation model for columbium, tantalum, and their alloys.

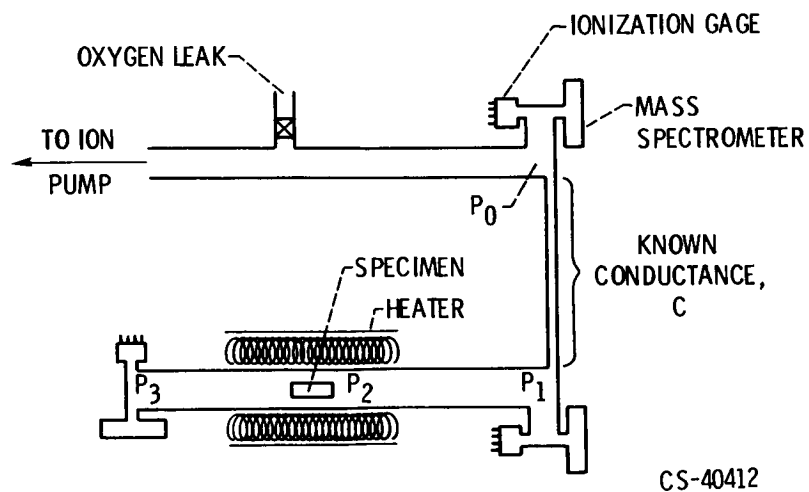


Figure VII-3. - Vacuum pressure-drop oxidation apparatus.

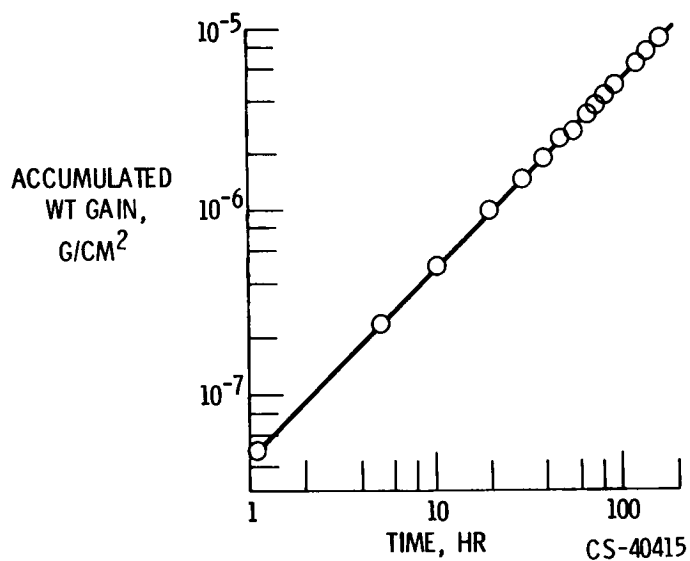


Figure VII-4. - Oxidation rate for columbium. Temperature, 1800° F; oxygen pressure, 3×10^{-8} torr.

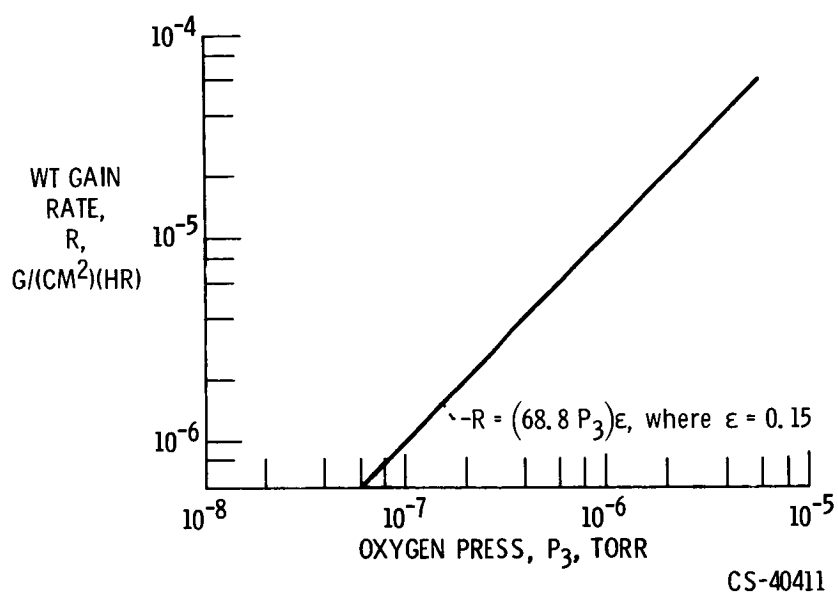


Figure VII-5. - Oxidation rate for columbium - 1-percent-zirconium alloy as function of oxygen pressure at 1600° to 2000° F.

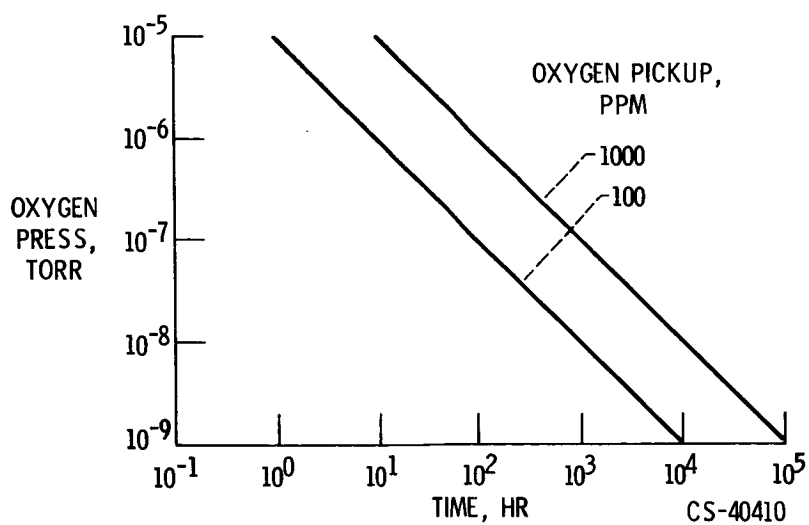


Figure VII-6. - Contamination of T-111 alloy. Temperature, 2000° F; 20-mil-wall tube; exposed on one side to vacuum environment.

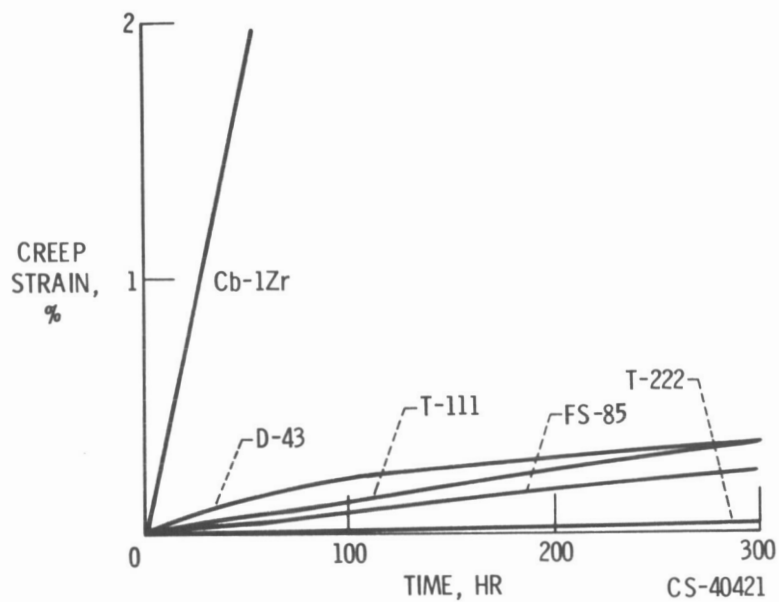


Figure VII-7. - Creep of columbium and tantalum alloys. Temperature, 2200°F; stress, 4000 psi; pressure, 10^{-6} torr.



Figure VII-8. - Ultrahigh-vacuum creep units.

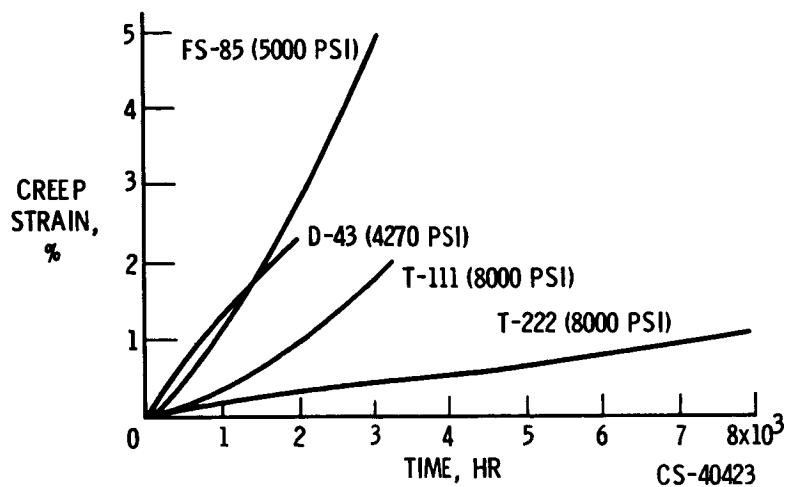


Figure VII-9. - Long-time creep for columbium and tantalum alloys. Temperature, 2200° F; pressure, 10^{-8} torr; constant ratio of stress to density.

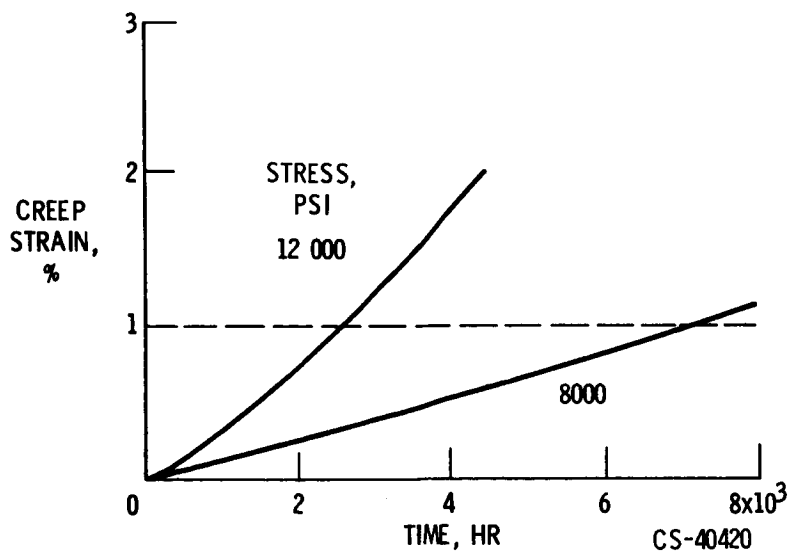


Figure VII-10. - Effect of stress on creep. Alloy, T-222; temperature, 2200° F.

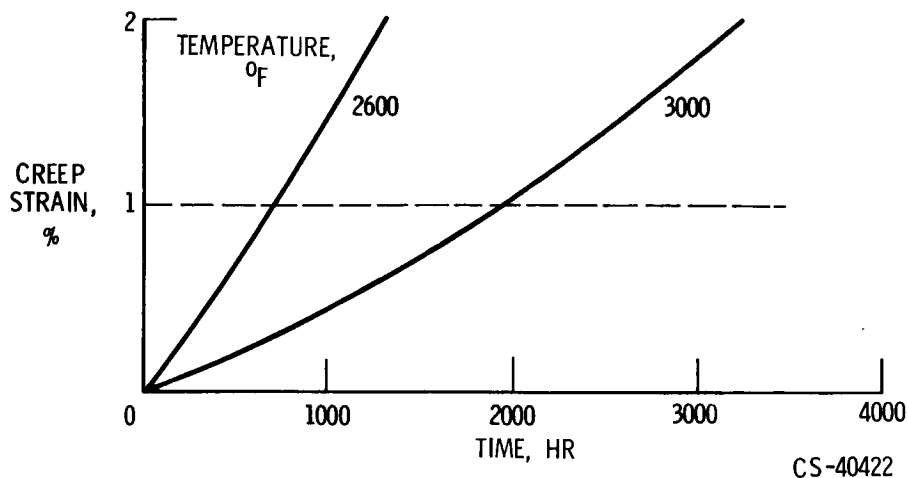


Figure VII-11. - Effect of annealing temperature on creep. Alloy, T-111; temperature, 2200° F; stress, 8000 psi; annealing time, 1 hour.

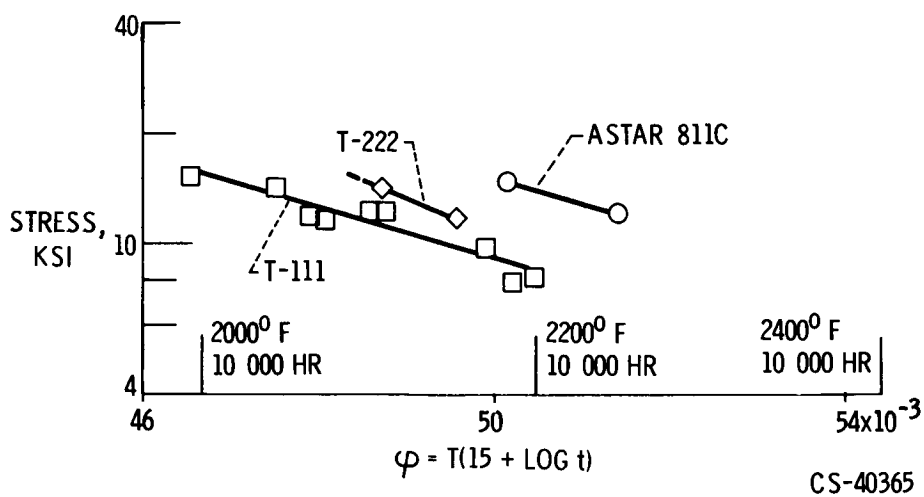


Figure VII-12. - Stress for 1 percent creep in tantalum alloys. Temperature, 3000° F; annealing time, 1 hour.

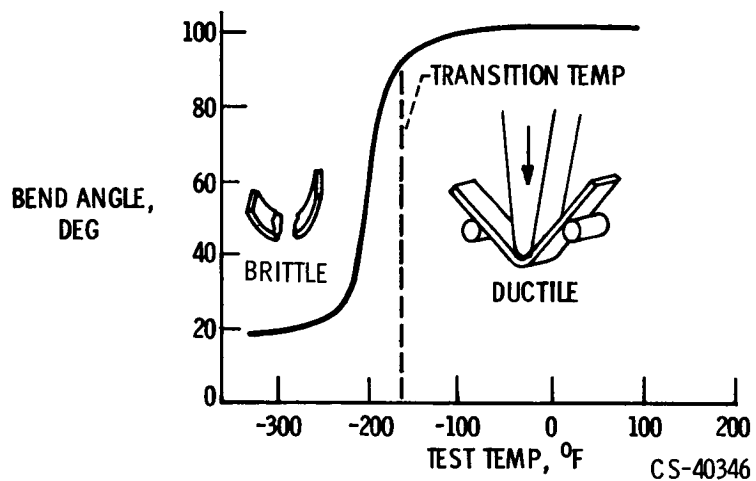


Figure VII-13. - Determination of ductile to brittle bend transition temperature.

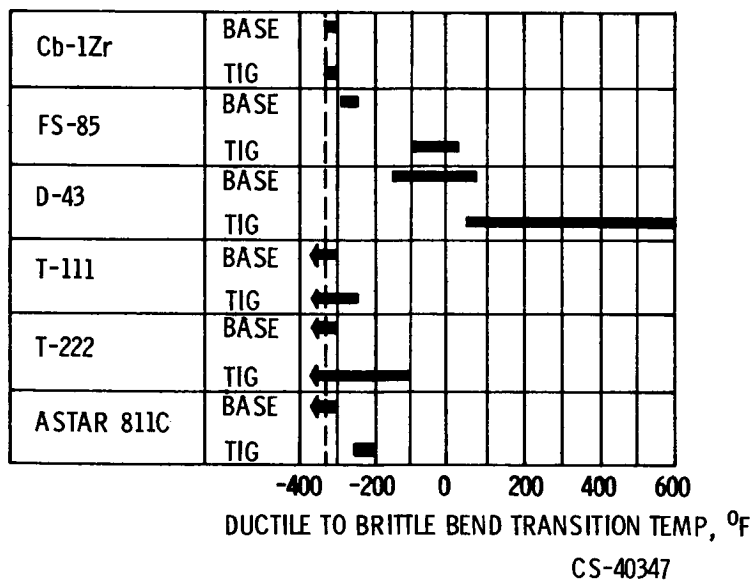


Figure VII-14. - Weld bend ductility for 0.035-inch refractory-alloy sheet with 1t bend radius.

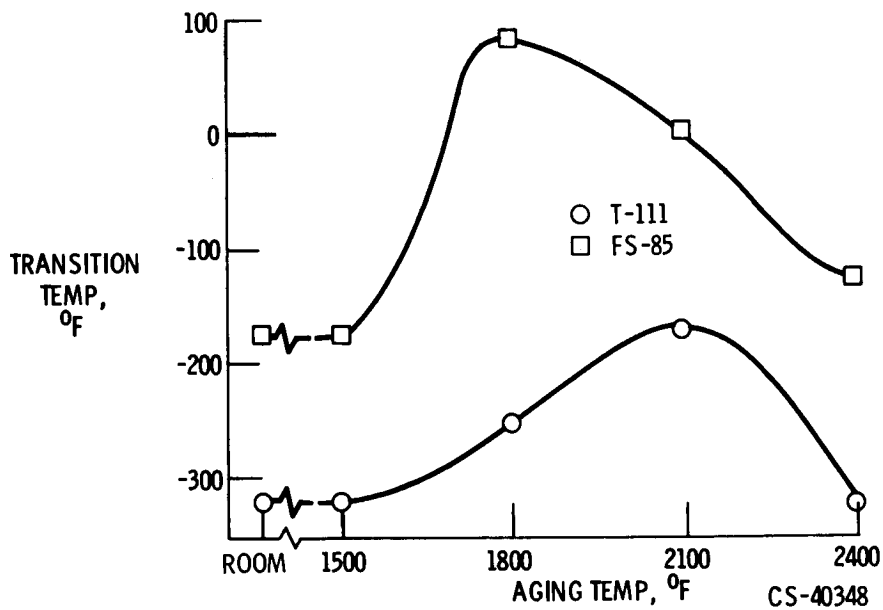


Figure VII-15. - 1000-Hour aging of welded alloys. Tungsten - inert-gas weld; temperature, 2400° F; annealing time, 1 hour.

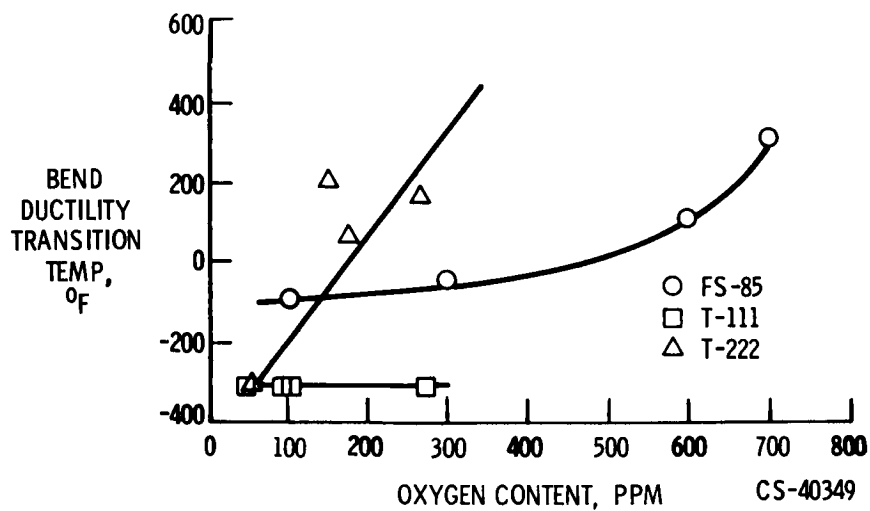
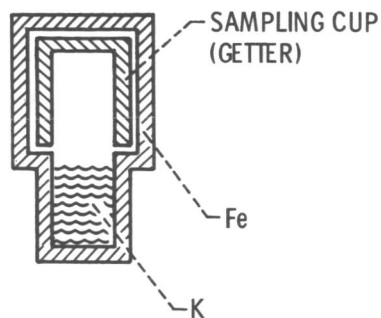
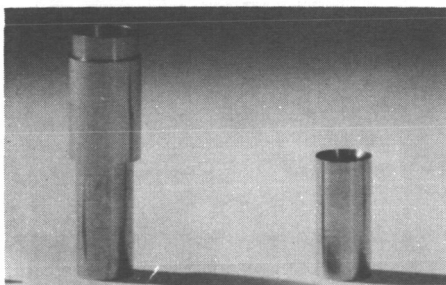


Figure VII-16. - Effect of preweld oxygen content on as-welded transition temperature.



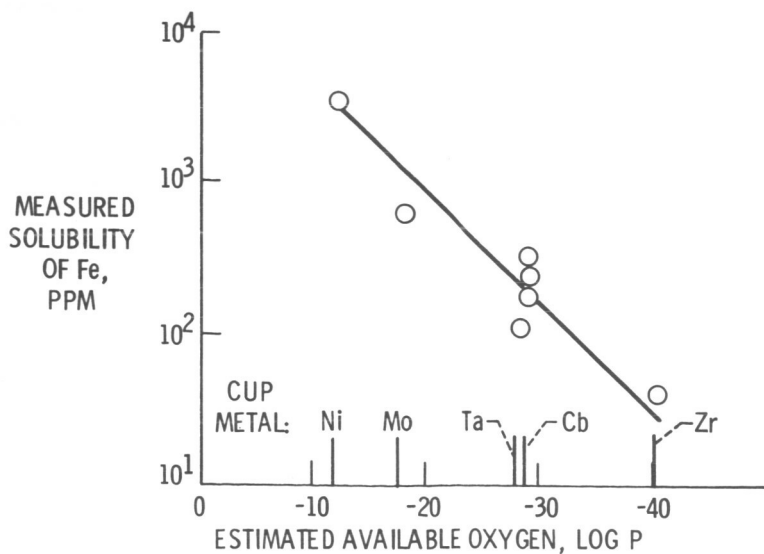
CS-40494

(a) Body.

(b) Sampling cup.

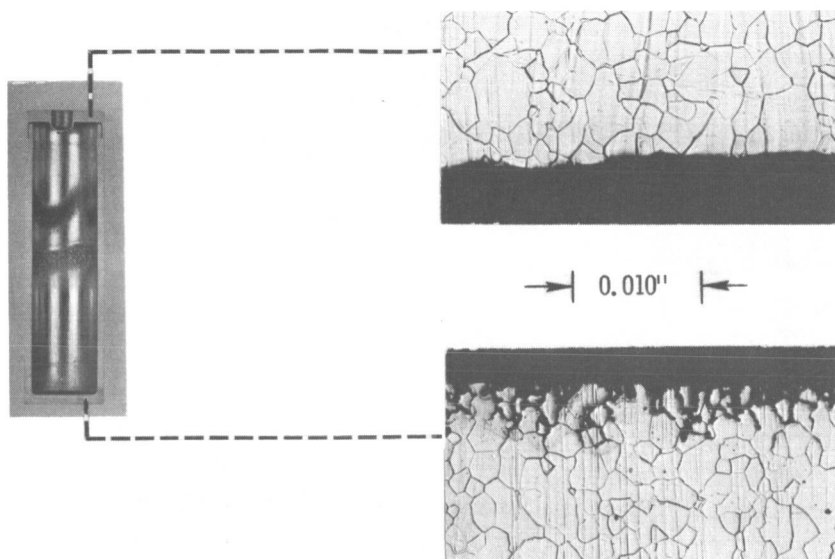
(c) Assembled capsule.

Figure VII-17. - Solubility capsule.



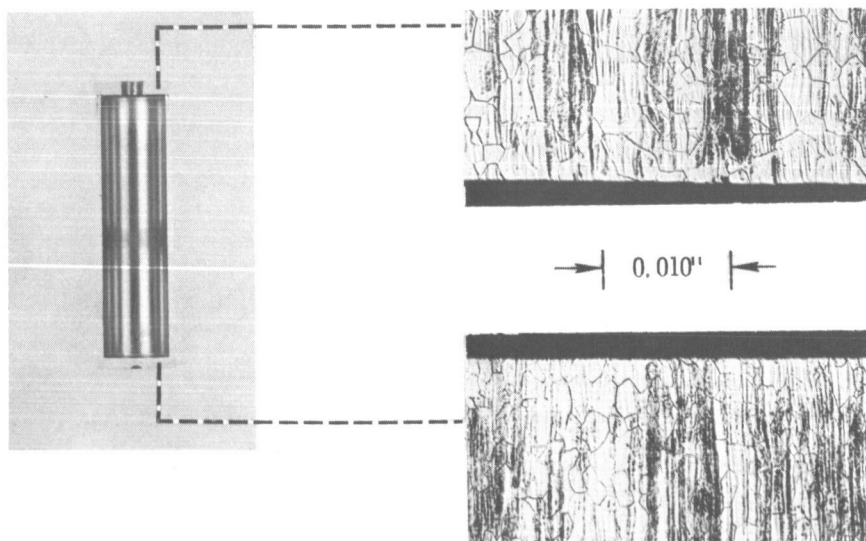
CS-40493

Figure VII-18. - Effect of sampling cup metal on measured solubility of iron in potassium at 1600°F.



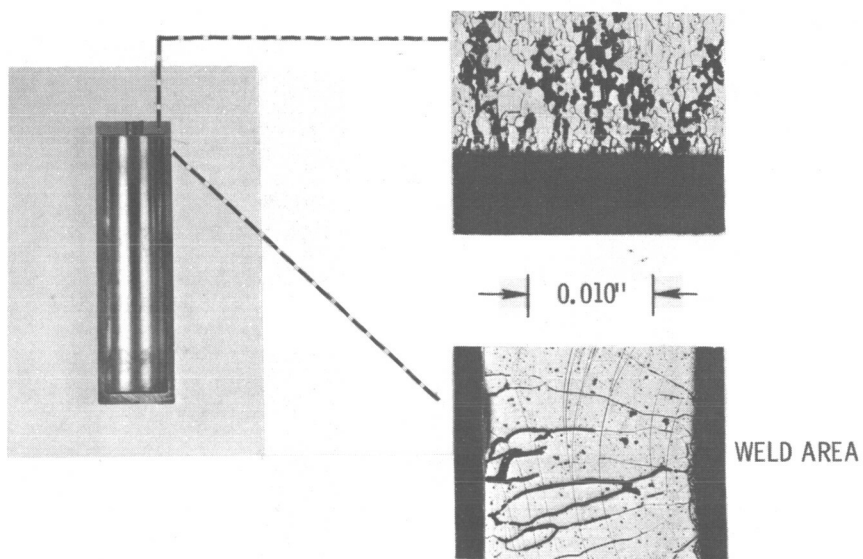
CS-40459

Figure VII-19. - Corrosion of ungettered alloy SCb-291 by potassium. Temperature, 2200°F ; time, 1000 hours.



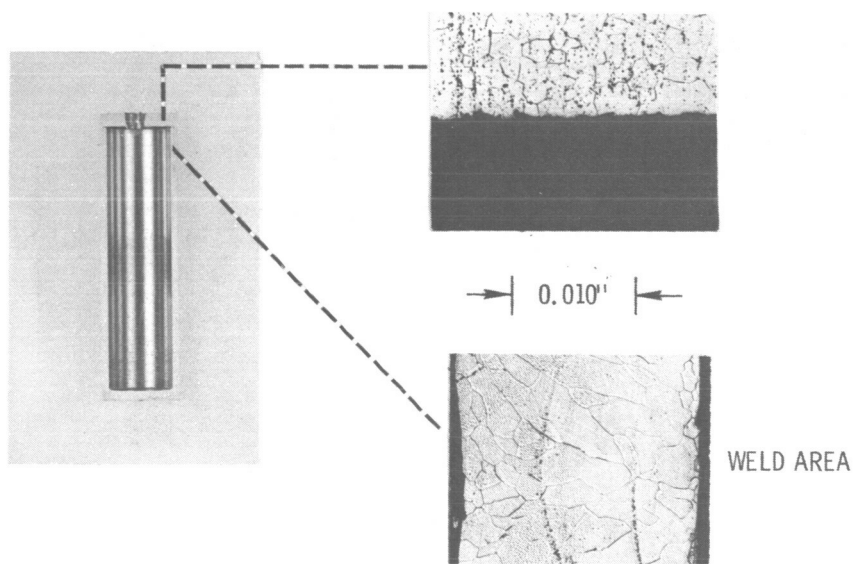
CS-40458

Figure VII-20. - Corrosion of gettered alloy FS-85 by potassium. Temperature, 2300°F ; time, 2000 hours.



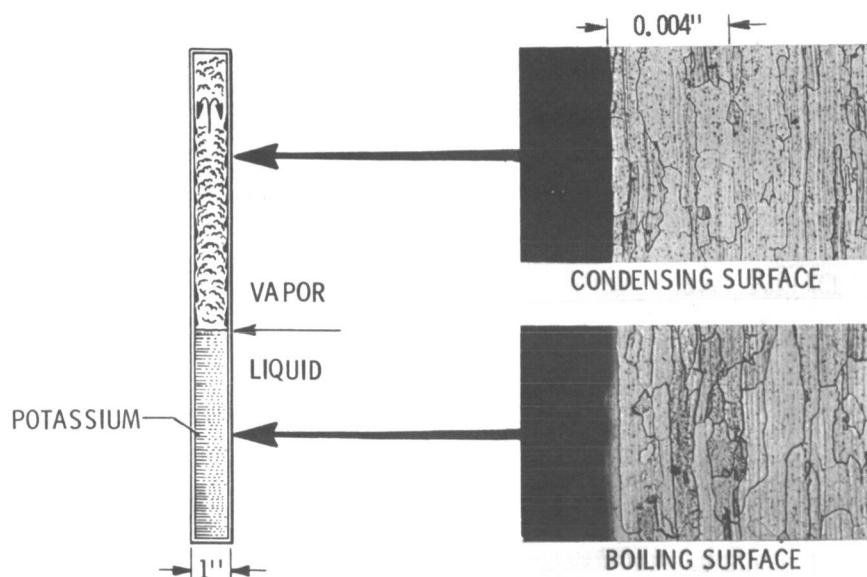
CS-40461

Figure VII-21. - Corrosion of ungettered alloy Ta-10W by potassium. Temperature, 1800° F; time, 128 hours.



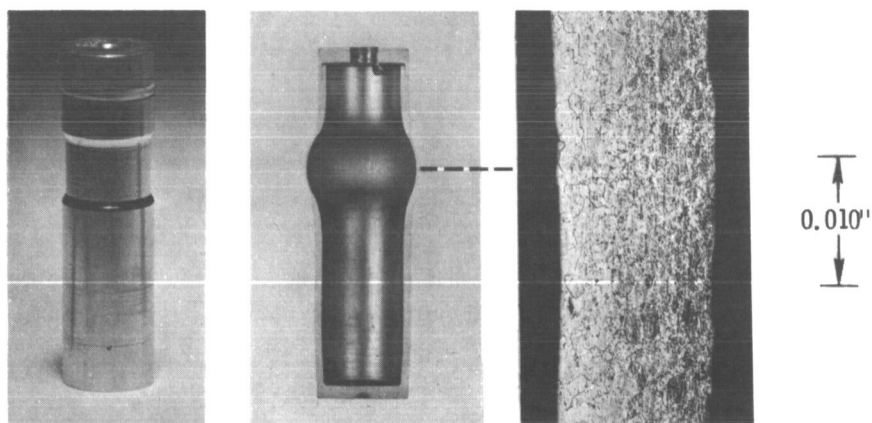
CS-40462

Figure VII-22. - Corrosion of gettered alloy T-111 by potassium. Temperature, 2400° F; time, 2000 hours.



CS-40351

Figure VII-23. - Alloy D-43 after 10 000-hour exposure to refluxing potassium at 2000⁰ F.



CS-40460

- (a) Before test. (b) Sectioned capsule after test. (c) Highly stressed area after test.

Figure VII-24. - Test for stress corrosion in D-43 alloy. Temperature, 2300⁰ F; time, 1000 hours.

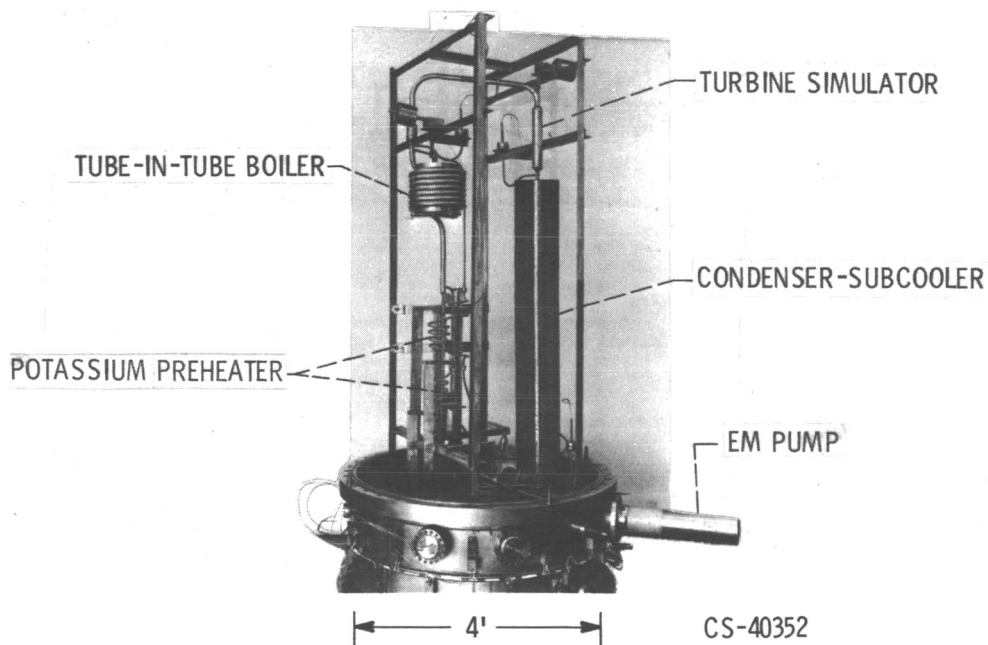


Figure VII-25. - Corrosion loop of Cb-1 Zr.

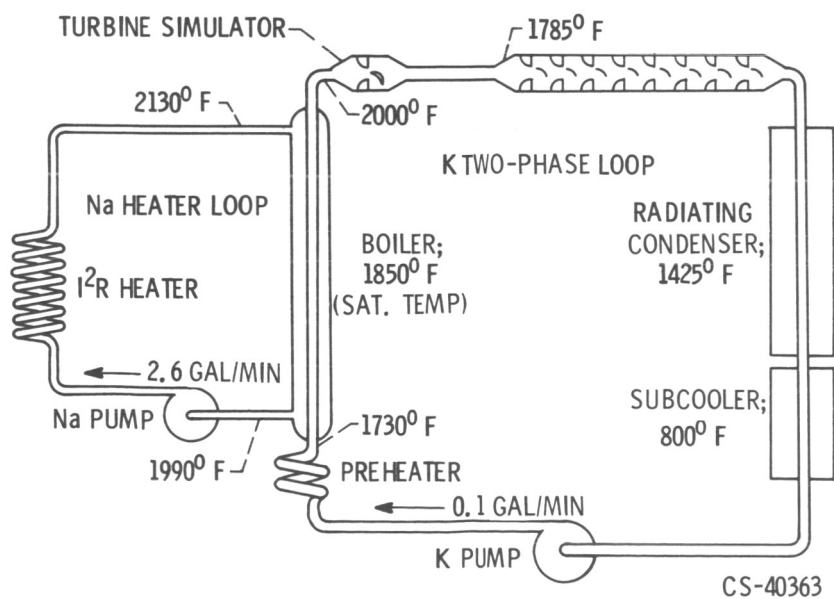


Figure VII-26. - Schematic diagram of Cb-1Zr corrosion loop.

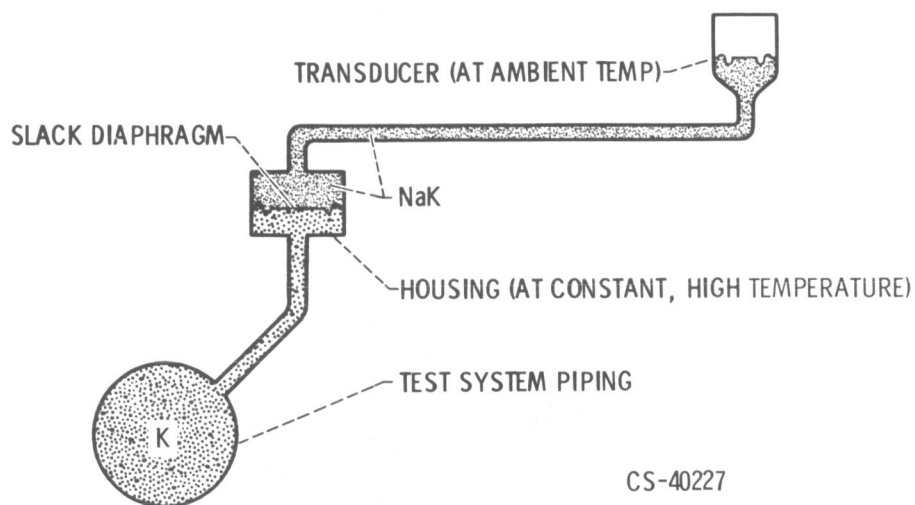


Figure VII-27. - Slack-diaphragm pressure transmitter.

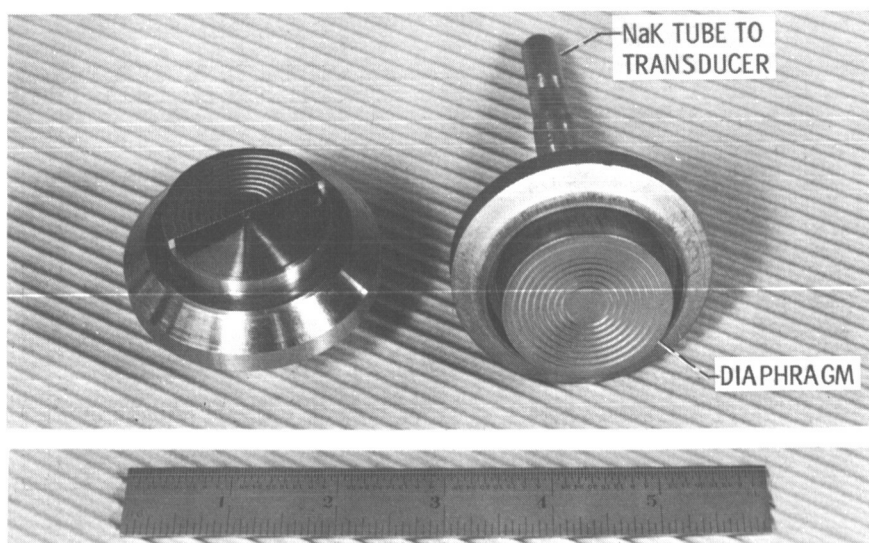
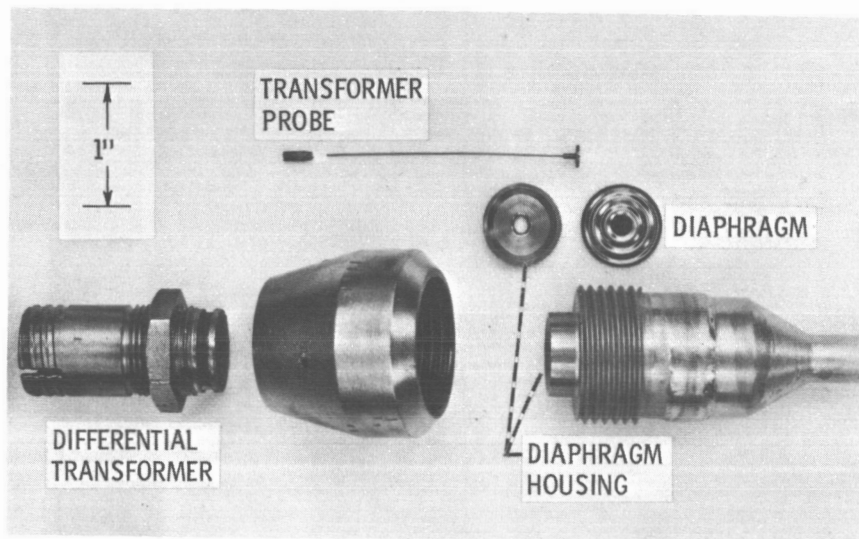
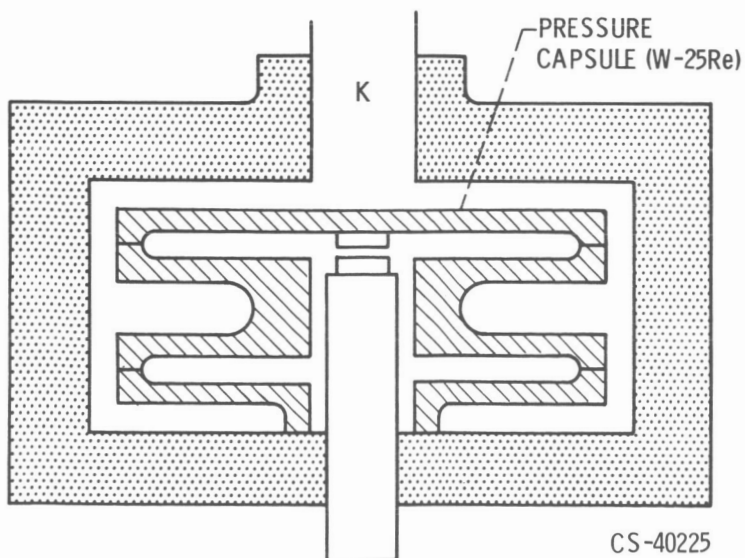


Figure VII-28. - Slack-diaphragm pressure transmitter of Cb-1Zr alloy.



CS-40228

Figure VII-29. - 900⁰ F pressure transducer.



CS-40225

Figure VII-30. - 1800⁰ F vacuum-diode pressure transducer.

VIII. POTASSIUM RANKINE SYSTEMS TECHNOLOGY

Robert E. English, Robert L. Cummings, Robert L. Davies,
Thomas P. Moffitt, and Uwe H. von Glahn

INTRODUCTION

The type of potassium Rankine system considered (fig. VIII-1) in this paper contains four fluid loops, namely, a reactor loop, a power loop, a heat-rejection loop, and a cooling loop. The basis for system operation is like that of SNAP-8, the main differences being that here the temperatures are higher and that potassium rather than mercury is used in the power loop. The particular temperatures shown illustrate the levels that might be used; these temperatures, although high, are within the capabilities of the alloy T-111 discussed in paper VII. The reactor outlet temperature is taken to be 2200° F. The reactor coolant will drop 100° or 200° in passing through the potassium boiler and will be heated an equal amount in the reactor.

One of the main reasons for use of a separate loop for the reactor is to diminish the problems of shielding against nuclear radiation. If some of the reactor fuel elements develop small cracks, the reactor might well be capable of continued operation, but some fission products could then leak into the reactor coolant stream. In the case of the separate reactor loop, as shown in figure VIII-1, the resulting increased radioactivity would be confined to the reactor, the boiler, and the pump in the reactor loop. If a separate reactor coolant loop were not used, this radioactivity would contaminate the entire power loop, thereby complicating the problems of shielding, inspection, and maintenance of the power system.

At the turbine inlet, the potassium vapor can be superheated somewhat. In general, the boiling temperature will be approximately equal to the temperature at the reactor inlet, and the resulting vapor can be superheated to nearly the temperature at the reactor outlet. In this way, the amount of superheat at the turbine inlet might typically be 50° to 150° F.

The condensing and radiating functions are separated for two reasons. First, the design calculations indicate that system weight is thereby diminished. And second, the design of the power loop is then almost independent of the manner in which the power system integrates with the spacecraft and mission. Radiator geometry can be adapted to each spacecraft and mission with only minor alterations in pumping power. The fourth, or cooling, loop provides low-temperature coolant to those system components that require it.

Such a system has a considerable number of components and a substantial diversity of the problems. The program has so far been an investigation of the various constituent problems of these several components, that is, the general technology of such a power system. For this reason, the following discussion covers a variety of problems that are seemingly independent. The

characteristic that ties all these problems together is that they must all be solved in order for such a system as this to function.

In the following discussion, various constituent problems are treated successively. For a period of time, the reactor problems were investigated by Pratt & Whitney CANEL in an AEC sponsored program. More recently, the responsibility for space-power reactors was transferred to the Livermore laboratory, thus the reactor program is presently in the formative stage. Additional study is required before the reactor concept is selected; for this reason, the reactor is not discussed.

BOILER AND CONDENSER

To obtain good performance of the boiler and the condenser in a Rankine cycle space-power system, the heat-transfer processes associated with two-phase flow of liquid metals must be understood. To obtain an efficient and reliable power system, stable operation of these two components must be obtained, both by themselves and by their interactions with other parts of the system.

Boiler

Study of two-phase flow problems with liquid metals has been aided greatly by parallel studies with conventional fluids, such as Freon and water. Thus, the results of heat transfer and pressure drop research with conventional fluids in relatively inexpensive rigs can be applied to liquid-metal systems by considering the pertinent physical properties of each fluid. Furthermore, the conditioning problem encountered with the SNAP-8 mercury system does not exist with alkali metals because of their excellent wetting characteristics, as well as the great care taken to keep alkali metal systems clean and free of contamination. Analysis of experimental liquid-metal data has shown that the two-phase heat-transfer resistance is generally very low.

Typical data obtained with a single-tube heat-exchanger boiler with potassium as the working fluid are shown in figure VIII-2, where the boiler thermal resistance is plotted as a function of boiler exit quality and superheat. The boiler thermal resistance is used instead of its reciprocal, the heat-transfer coefficient, because resistances can be added to each other directly. The thermal resistance of the boiler is made up of the following three resistances: the heating fluid, the tube wall, and the boiling fluid. The heating-fluid resistance and the tube-wall resistance can be readily calculated and are shown by the crosshatched regions in the figure. The boiling resistance is then determined from the difference between the sum of these two calculated resistances and the measured overall values shown by the data points. For the most part, the boiling-fluid resistance is much less than the sum of that for the wall and heating fluid and, therefore, is not the controlling thermal resistance in a liquid-metal boiler. Only in the region of very low quality, and again at vapor superheat, is the boiling-fluid resistance of a magnitude that might be considered controlling. The low values of boiling-fluid thermal resistance obtained for these data

represent very high boiling heat-transfer coefficients, generally in the range of 8000 to 30 000 Btu per hour per square foot per °F.

From these and other studies, it can be concluded that the heat transfer and associated pressure drops for liquid-metal boilers present no serious problems for designers. Then what does constitute the problem area for boilers?

The main area of concern is stable operation of a system that includes two-phase flow in some of the components, and, in particular, the boiler. A system is stable if, when it is disturbed from its operating point, it inherently returns to the same point. The stability of the system depends not only on the stability of each of the components, but on the manner in which the components interact. Although two-phase components may be stable by themselves, component interactions may cause the system to become unstable. Stable operation of two-phase components, therefore, is as much a system problem as it is a component design problem.

Boiler stability problems are many and complex. Two primary problem areas are described: the flow patterns that may exist in a boiler tube, and the "negative-resistance" characteristic of a boiler.

The complicated flow patterns that result from forced-convection boiling within a hollow-tube boiler are shown in figure VIII-3. The boiling fluid flows within a tube and is heated by a second fluid that moves in a surrounding shell. At the beginning of the boiler tube, the fluid is all-liquid and at a temperature below the boiling point (the saturation temperature). The graph in the lower part of the figure illustrates the heating flux being transferred into the boiler tube. In the all-liquid region, the heat transfer is relatively low, since it occurs by ordinary forced convection. As the liquid is heated, the portion near the wall reaches the boiling point. Bubbles are then formed near the wall with the core of the fluid remaining liquid. Here the heat transfer begins to increase because of the boiling action. The bubbly flow regime is reached when the core of the liquid approaches the boiling point and bubbles extend over the entire tube cross section. These bubbles then coalesce, forming large vapor masses. The result is the slug-flow regime, with the flow alternating rapidly between liquid and vapor. Liquid is still flowing along the wall and the heat transfer is very high. The vapor slugs then merge together and annular flow results, where an annulus of liquid flows along the wall and vapor flows at high velocity down the center of the tube. The last regime is mist flow, where the wall is essentially dry and vapor is carrying entrained liquid droplets. Somewhere prior to the region of a dry wall, the heat transfer experiences a transition and very abruptly decreases to a low heat flux rate. This transition point may fluctuate up and down the tube in a rapid, uncontrolled manner.

A number of inherent boiler stability problems are tied to these flow regimes. The slug-flow regime is inherently very unstable and causes violent surges in pressure and flow. These surges are believed to be largely responsible for the fluctuations in the heat-transfer transition point that occurs further downstream in the tube.

Another instability occurs at the very start of the boiling process. The initiation of boiling in liquid metals is erratic because of a bubble-nucleation problem. While most liquids begin to boil when heated only a few degrees above their normal boiling temperature, liquid metals can be heated to several hundreds of degrees above their normal boiling temperature and still remain entirely liquid. Then, at some point, the liquid in the boiler will suddenly break to form an interface and flash into vapor. Flash vaporization results in a sudden release of energy that causes

violent bumping, geysering, and water hammer in the fluid. The outrush of vapor may send a surge of flow and pressure around the power conversion loop, thereby forcing cooler liquid back into the boiler tube, refilling the tube with liquid and setting up another superheating and geysering cycle.

The highly superheated liquid state that can be obtained with alkali metals is caused by conditions that are unfavorable for bubble formation. Studies have shown that bubbles originate at gas- or vapor-filled cavities or nucleation sites, such as pits and scratches in the boiler-tube surface. Under such conditions, boiling can be initiated and maintained with only a few degrees of superheat. With alkali metals, however, the systems are highly degassed to help reduce corrosion and oxidation, thus depleting the gas available at the nucleation sites. Also, these fluids wet the surface exceedingly well, thereby tending to fill many of the larger cavities and render them inactive. These combined effects are the primary cause of the bubble-nucleation problem with liquid metals.

In addition to these flow-pattern instabilities, a forced-flow boiler has, in general, a "negative-resistance" characteristic in its operating range. Some data that illustrate the negative-resistance characteristic of a boiler are shown in figure VIII-4. Here, the pressure drop for a hollow boiler tube is plotted as a function of the weight flow of the fluid. While the data shown are for sodium, similar data are obtained with other fluids. The solid lines show the pressure drops for all-vapor and all-liquid flows, while the dot-dash parallel lines between these limits represent nominal exit vapor quality values. A negative resistance is characterized by a decrease in pressure drop with increasing flow, that is, a negative slope of the curve. The slope of the curve can become negative because an increase in total flow results in a decrease in exit quality, and, hence, a decrease in vapor velocity and pressure drop.

On the negative slope portion of the curve, any flow disturbance tending to increase the flow would lead to a reduction in pressure drop, which, in turn, would cause a further increase in flow rate. An increased flow rate creates an unstable region of boiler operation that leads, in many cases, to severe boiler and system instabilities. The magnitude and location of this negative slope are a function of many variables including liquid subcooling, heat input, fluid pressure level, boiler internal configuration, etc. Thus, a whole family of such curves can be generated to cover the operating range of a particular boiler tube.

It is important to realize that the region of negative slope does not necessarily indicate that the boiler is unstable in this operating range, but does indicate that, when the boiler is coupled with an unsuitable feed-system resistance, an energy source exists which could become a driving force for a system instability.

The negative slope of the boiler operating curve (fig. VIII-4), discussed previously, can be eliminated by adding a high-resistance device at the inlet of each boiler tube. An orifice (fig. VIII-5), whose pressure drop increases with the square of the weight flow, has frequently been used for this purpose. The overall boiler pressure drop is then made up of the sum of the boiler-tube and orifice pressure drops. This combined pressure drop of the sodium boiler tube and an orifice is shown in figure VIII-6 as a function of weight flow. It is apparent that the combined pressure-drop curve has only a positive slope and thus the negative-resistance characteristic of the boiler tube has been eliminated as an instability source. An orifice, being a high-resistance element, also tends to decouple the boiler from disturbances originating upstream in other compo-

nents. By itself, however, an orifice at the boiler inlet does not solve the slug-flow and the bubble-initiation problems.

Of the various inlet devices presently being used for space boiler applications, the central plug and helical spring shown in figure VIII-7 merit discussion. In this configuration, the plug, by reducing the flow area, increases the liquid velocity and thus enhances the heat transfer, while the spiral flow path moderates the slug flow by centrifuging the heavier liquid to the wall of the tube. With this device, however, the point of initiation of boiling is uncertain, and slug flow, depending on the operating conditions, may or may not occur. The device does not by itself solve the bubble-initiation problem; however, artificial nucleation sites in the form of re-entrant cavities could circumvent this shortcoming.

An advanced technique that attempts to solve all the previously discussed instability problems is shown in figure VIII-8. At the top of the figure, a schematic drawing of the proposed boiler-tube inserts is shown. The inserts consist of a small center-tube device at the boiler inlet followed by a helical spring. The lower portion of the figure shows a photograph of a transparent tube test section in which hot water was used to study the flow patterns obtained with these inserts. The flow patterns obtained with these inserts are shown in more detail by the use of close-up photographs. Upstream of the small center tube (fig. VIII-9), the flow is all liquid. The center tube creates a significant pressure drop near the tube outlet where the incoming liquid approaches its saturation or boiling temperature and then provides a spray-type, flashing discharge. The vaporization of a small portion of the flow by flashing provides the vapor required to initiate boiling, and thereby eliminates the bubble-nucleation problem. Furthermore, since the flashing location is fixed by the center-tube outlet, initiation of boiling is fixed and known. Downstream of the spray (fig. VIII-10), an annular flow pattern is quickly established, with the liquid spiraling along the tube wall and the vapor flowing down the center of the tube. The liquid-vapor interface is wavy but apparently unbroken.

In summary, a center-tube insert should eliminate the bubbly and slug-flow regimes entirely, decouple the upstream feed components, provide positive resistance, and forcibly initiate boiling at a fixed location with a prescribed flow regime.

At the boiler-tube outlet it is desirable to provide droplet-free vapor with vapor superheat of the order of 100° F to ease turbine operating problems. To provide for droplet-free, superheated vapor, boiler tubes can be designed to centrifuge the heavier droplets in the mist flow regime to the tube walls. Typical inserts that have been used to accomplish this include twisted tapes, spiral ribbons, and helical springs, as shown in previous figures.

Representative heat-transfer data for a potassium boiler tube illustrating the effectiveness of such a device in achieving vapor superheat are shown in figure VIII-11 as a function of vapor quality and superheat. Data are shown for a hollow tube and for a twisted tape insert. With a hollow tube, a quality of less than 90 percent could be achieved. Use of a twisted tape with a pitch-to-diameter ratio of 2 resulted in a vapor superheat of about 200° F. The heat-transfer coefficient in the midquality region was roughly the same for the two configurations.

Of the high-quality region inserts, the helical spring appears to be most advantageous because liquid drops have no opportunity to stream along a surface that extends to the center of the tube, as has been observed with twisted tapes. Curving the boiler tube, such as in the SNAP-50

boiler design, will also aid in separating the two phases. All the inserts, however, penalize the system by increasing the pressure drop for the boiler, generally by a factor of 2 or more over that for a hollow tube.

Stability studies of two-phase components, particularly boilers, have historically been hampered by lack of dynamic data with which to evaluate mathematical models and analyses. Lewis has begun research in component and system dynamics with water and Freon as convenient working fluids. Briefly, the technique used in this research consists of varying by a small amount a parameter such as weight flow, sinusoidally over a range of frequencies. The response of one variable with respect to another can be obtained solely in terms of frequency. Comparison with analytical models then allows possible sources of instability to be pinpointed. Considerably more experimental data are needed before generalized models of two-phase dynamic behavior can be developed and verified.

Condenser

In general, more is known about the condenser than about the boiler. Successful operation of both convectively cooled and radiantly cooled multitube potassium condensers has been achieved over a range of vapor temperatures that exceeds the 1350°F called for in figure VIII-1. No serious instabilities were encountered over the wide range of operating conditions covered, even when the pressure drop across the units was essentially zero.

Views of the seven-tube, convectively cooled, potassium condenser are shown in figure VIII-12. The condenser was of a "hockey stick" design to facilitate thermal expansion and was 72 inches long. The condenser was made of 316 stainless steel. NaK was used as the coolant fluid, and flowed countercurrent in the shell. Data were obtained up to 1500°F .

Temperature profiles of both the condensing fluid and coolant shell for one run are shown in figure VIII-13 as a function of distance downstream from the vapor inlet. The vapor (flowing from left to right) entered the condenser at 1400°F with an inlet quality of 86 percent. The pressure drop, and hence the saturation temperature change, was negligible for these data. Thus, the temperature of the condensing vapor can be assumed to remain constant at the inlet value until the vapor is completely condensed, indicated as the interface in the figure. Thereafter, the condensed fluid temperature subcools rapidly, reaching substantially the temperature of the coolant shell within a few inches downstream from the interface.

The coolant fluid, flowing countercurrent to the condensing fluid (right to left in the figure), enters the condenser at 1284°F . The shell temperature is substantially constant at this value until the interface is reached, then it increases as condensing occurs, reaching a value of 1348°F at the coolant flow outlet.

Typical coolant-shell temperature profiles for various coolant inlet temperatures are shown in figure VIII-14 again as a function of length from the vapor inlet. These data were obtained with constant inlet conditions (1400°F inlet vapor temperature), a constant coolant flow rate, and a measured pressure drop across the condenser of less than 1 pound per square inch. The vapor temperature profiles are not shown. They are similar to those discussed in figure VIII-13, namely, constant temperature of 1400°F during condensing and temperature approaching that of

the coolant just downstream from the liquid-vapor interface. The locations of the liquid-vapor interfaces are indicated by the arrows. The condensing length, measured from the vapor inlet, increases rapidly with increases in coolant inlet temperature, changing from $9\frac{1}{2}$ to 44 inches for a change in the coolant inlet temperature from 1194° to 1304° F. With a coolant inlet temperature of 1315° F, complete condensing of the vapor was not obtained in the 72-inch length of the condenser.

The two lower curves (fig. VIII-14) represent typical data for high heat flux values near the vapor inlet. The condensing lengths for these two conditions, in which large temperature differences between the vapor and coolant fluid exist, can be predicted by very simple analyses. On the other hand, the two upper curves indicate a near absence of heat transfer (low heat flux) near the vapor inlet due to the small temperature difference between the vapor and coolant. The condensing lengths obtained with small vapor-to-coolant temperature differences cannot, as yet, be predicted. The problem is that the local pressure, and hence local vapor saturation temperature, in the entrance region of the condenser tubes cannot be accurately predicted for the prevailing two-phase flow. Thus, an accurate vapor-to-coolant temperature difference cannot be calculated when small differences are involved with the result that significant errors in calculated condensing lengths can be made.

TURBINE

Turbine-Rotor Materials

The materials problems in the turbine rotor are substantially different from those of just containing liquid potassium as discussed in paper VII. In particular, there is very little liquid potassium in the turbine, the turbine rotor is highly stressed because of its high rotational speed, and the turbine rotor is not required to have the same levels of ductility and weldability as does most of the power system. Materials having high density such as tantalum would increase the stress on a rotating component. Hence, there has been an increased emphasis on materials of lower density, such as molybdenum and columbium.

The high stress in the turbine rotor is an item of concern because high stress produces creep. For highest efficiency, potassium turbines are designed with small operating clearances. Therefore, to maintain the original clearances, the selected material must undergo only small amounts of creep during the life of the turbine at the elevated operating temperature.

Thus, alloys for this application are usually the most creep resistant that can be fabricated from a particular alloy base. In general, the alloy must be forgeable and exhibit some ductility; generally, 5 or 6 percent elongation at room temperature will suffice. Other important requirements include corrosion and erosion resistance.

In the selection of materials for high creep strength, many alloys were screened in high-temperature creep tests in high vacuums. In figure VIII-15, creep data are shown for the molybdenum base alloy TZC, which was the most creep resistant of the candidate turbine materials. The figure illustrates the creep as a function of time at three different stresses and temperatures. After 10 000 hours, an applied stress of 20 000 pounds per square inch at 2000° F results in

0.5 percent creep, 19 000 pounds per square inch at 2056° F leads to 0.25 percent creep, and 25 000 pounds per square inch at 1856° F gives 0.18 percent creep.

It is also desirable and important that allowable stress to limit creep to a low value be predictable for other temperatures and times. In figure VIII-16, the data are presented in terms of stress as a function of the Larson-Miller parameter, which relates temperature and time to stress for a given percentage creep, in this case, 0.5 percent creep.

Of the several alloys that have been considered as turbine rotor materials, three are presented in this plot: the previously discussed TZC, a columbium alloy Cb-132M, and the molybdenum base TZM. Typical allowable stresses for 0.5 percent creep for TZC in 10 000 hours are 20 000 pounds per square inch at 2000° F and 30 000 pounds per square inch at 1800° F. The strength of the columbium alloy Cb-132M degrades more rapidly at high temperature than TZM and TZC.

A turbine material must also be resistant to corrosive attack by potassium vapor. Figure VIII-17 shows the results of a 5000-hour test in potassium vapor at 2000° F. The TZM alloy was tested in the form of segmented ring inserts located internally in the columbium - 1-percent-zirconium capsule. From the microstructures shown, no attack occurred as evidenced by the smooth surface of both the inside and outside diameters of the ring segment and the lack of any penetration either at the surface or at the grain boundaries. Also, the weight change in the five segments tested was less than 0.07 percent of the total weight. From this test and other supporting investigations, it is believed that the stronger molybdenum alloy TZC will also be compatible with the potassium vapor since there are only minor changes in composition from the TZM.

Potassium Expansion Process

The expansion of potassium vapor through the turbine is similar to the expansion of steam. When the expansion takes place in the wet vapor region, the question arises as to where condensation takes place initially. In addition, potassium vapor is composed of both monatomic and diatomic species, the amount of each varying with temperature. When the vapor expands through the turbine with decreasing temperature, the proportion of monatomic to diatomic vapor could change. This poses an additional question as to the type of nozzle expansion process experienced by potassium. A knowledge of this process is required to size the flow passages within the turbine. It is this sizing that determines the pressure distribution and work split between the turbine stages.

Consequently, nozzle expansion data have been accumulated for initially saturated vapors at temperatures to 1600° F. Although not a perfect gas, it was determined that, for practical purposes, the expansion follows the polytropic process equation $pv^n = c$. The value of the exponent n fell between 1.4 and 1.5. For the temperature range considered, condensation did not take place before the throat, or minimum area, of the nozzle. Independent measurements of pressure distribution and weight flow indicate that both flow and pressure distribution are predictable for potassium turbines.

Two-Stage Potassium Turbine Test

Description. - A two-stage turbine was fabricated and tested under contract by the General Electric Company. Figure VIII-18 is a photograph of the rotor prior to testing. The diameter of this rotor is about 10 inches. The buckets were constructed of the nickel-base alloy Udimet 700. Figure VIII-19 shows a partial assembly of the turbine with the rotors installed. Two types of tests were conducted, namely, a short-time performance test to determine blade performance, and an endurance test to determine the erosion characteristics of the turbine.

Performance. - For the performance test, potassium vapor was used at an inlet temperature of 1550° F. The inlet vapor was essentially saturated, in that the inlet quality was considered to be 99.5 percent. Figure VIII-20 presents the performance results in terms of static efficiency as a function of turbine pressure ratio for a constant speed of about 19 000 rpm. The solid curve was predicted prior to testing by using standard gas turbine practice and perturbing the results for moisture effects. At design pressure ratio the efficiency is seen to be approximately 70 percent. The experimental trend at off-design conditions follows closely the predicted curve. In general, then, there appears to be no particular problem in predicting the performance of potassium turbines.

Endurance. - The potassium turbine operating conditions for the endurance test are as follows:

First stage:

Inlet temperature, °F	1500
Inlet quality, percent	99.5

Second stage:

Inlet temperature, °F	1390
Inlet quality, percent	96.7
Tip speed, ft/sec	770

Exit:

Temperature, °F.	1260
Quality, percent	92.5

As the vapor expands through the turbine, both temperature and quality decrease. The lowest quality (or highest moisture) and maximum blade speed occur in the second stage. If erosion takes place, it would be expected to show up on the second-stage wheel. Tip speed is shown rather than rotative speed because it is indicative of the impact velocity between the heavy drops of liquid traveling at relatively low speed and the wheel buckets. Eight of the Udimet 700 nickel buckets were removed from the second-stage wheel and replaced with molybdenum-base buckets, four each of TZM and TZC. The turbine was then assembled and the endurance test begun. Data taken periodically throughout the test showed that the turbine performance remained constant.

The endurance test was interrupted at the end of 2000 hours, and the turbine was dismantled. Figure VIII-21 is a photograph of the second-stage wheel after 2000 hours of operation. The wheel was vapor blasted to remove small amounts of residual potassium that had clung to the sur-

faces. Little or no erosion resulted from the 2000-hour test. The leading edges and bucket tips were still sharp and retained their original shape. Some of the original machining marks were still visible. The buckets were then removed from the wheel and weighed. The average weight change of the buckets was as follows:

Material	Average change, percent
U-700	-0.019
TZM	-.105
TCZ	-.102

The loss in weight amounted to about 0.1 percent for the molybdenum specimens and even less for the nickel alloy. These minute changes in weight and the condition of the buckets led to the conclusion that erosion was not a factor for the given conditions of operation for any of these materials. The turbine was then reassembled, and the endurance test continued. When the total elapsed time amounted to about 4300 hours, the performance of the turbine remained unchanged, which would indicate that if any erosion had occurred, it had been tolerable.

Low Exit Quality

Recent experience has shown that a turbine exit quality of 93 percent, or a liquid content of 7 percent, results in negligible blade erosion. However, the cycle in figure VIII-1 results in a liquid content of 10 to 15 percent at the turbine exit. Whether or not this increased liquid content results in acceptable blade erosion has yet to be investigated. For this reason, the two-stage potassium turbine just discussed will be modified to have three stages. This three-stage turbine will be subjected to performance and endurance tests the same as those given the two-stage turbine. At the conclusion of the tests, it will be known more definitely if the desired liquid contents of 10 to 15 percent at the turbine exit are acceptable.

TURBOGENERATOR PROBLEMS

To obtain a satisfactory configuration for the potassium turbogenerator, the design constraints imposed by all its components must be considered. As shown in figure VIII-22, this unit will consist of four major parts, namely, (1) an axial-flow turbine with five to eight stages, (2) a solid-rotor inductor alternator with an externally cooled stator, (3) a set of bearings, and (4) the necessary seals.

Bearings and Seals

A number of different designs and arrangements can be chosen for each of these major components and, as a result, a number of different turbogenerator configurations are possible. These different approaches may be explained by referring to table VIII-1 where the designs that may be used for the lubricant system, the seals, and the generator are listed.

Because potassium vapor is passing through the turbine, it is natural to consider using liquid potassium as the lubricant in the bearings. Both the shaft bearings would thus be supplied with liquid potassium. Between the turbine rotor and the bearings a labyrinth seal would be required to separate the potassium vapor in the turbine from the liquid in the bearing cavity. If a similar seal is used between the bearings and the generator rotor, there would also be potassium vapor in the generator rotor cavity. Then a special seal would be required to keep the potassium out of the generator windings. The nature of this seal is discussed further later in the section Generator Materials.

It would also be possible to avoid the problems associated with potassium in the generator rotor cavity by venting this chamber to space vacuum. In this case, a potassium-to-space seal, such as the one described for mercury in the SNAP-8 system, will be required for the generator seals to prevent excessive loss of working fluid. Although there are complications associated with the potassium-space seal, this arrangement would have the major advantage of avoiding the possibility of potassium vapor damage to the generator stator.

Another design approach for the turbogenerator unit is to use oil as the lubricant for the bearings. If this approach is chosen, there will be oil in the bearing just adjacent to the turbine, and special precautions must be taken to avoid contamination of the potassium working fluid with the oil and also to avoid contamination of the oil with potassium. The seal between the turbine and the bearings would consequently consist of two seals, one seal between the potassium and the space vacuum, and another between the oil lubricant and the space vacuum. Such seals between oil and space vacuum have been developed for the SNAP-8 unit (see paper VI). This seal technology may also be utilized in the design of the potassium-space seal. With oil lubrication in the bearings, it is necessary to vent the generator rotor cavity to space vacuum in order to prevent oil vapor from coming into contact with the high-temperature rotor and stator parts and causing thermal decomposition of the oil vapor. An oil-to-space seal is therefore also required for the generator seal if oil lubrication is used.

Thus, the turbogenerator configuration will indeed be affected substantially by the choices made for its bearings and seals. There are two main approaches: for the first approach, conventional oil bearings and the space seal technology developed under the SNAP-8 program can be used (see paper VI). For the second approach, potassium-lubricated bearings with rotating space seals can be used, or a special static seal can be used to keep potassium out of the generator stator.

Liquid-Metal Bearing Experience

If potassium is chosen as the lubricant for the turbogenerator, fluid-film bearings will be used. In this type of bearing the load-carrying capacity is provided by pressures generated within

the fluid film, and rolling, or rubbing, contact does not occur. Direct bearing material wear or fatigue is, therefore, not a problem. When potassium is used as a lubricant, these fluid-film bearings can also develop a large load-carrying capacity with a moderate bearing power consumption. The power loss for such bearings for a 300-kilowatt turbogenerator unit, for example, is not expected to exceed a few kilowatts. The potassium lubricated bearing is also well suited for high-temperature operation.

Now that the advantages have been described, the following questions remain to be answered:

- (1) What are the problems for this type of bearing?
- (2) What results are available to indicate selecting it for the space power system?

The problems that must be solved for a potassium-lubricated bearing for this use are as follows:

- (1) Bearing instability must be avoided under the light loads associated with zero-gravity operation of the turbogenerator.
- (2) Differential thermal expansion and housing distortion must be accommodated by special flexible or pivoting mounts.
- (3) Materials are required that are compatible with high-temperature liquid metals.

These problems are the same in general as those for Brayton cycle turbomachinery discussed in paper V. This is indeed the case as shown by a comparison of the results. To solve the problem of obtaining stable liquid-metal bearings, numerous tests have been run at Lewis and other research centers on different bearing configurations. From those tests, the preloaded pivoted pad bearing (fig. VIII-23) is attractive. A tilting pad bearing, the cylindrical journal, and a pivot are shown at the bottom of the figure, and the assembled bearing with three pads installed is shown at the top. This bearing is the most stable type at very small applied loads since the tilting pad is inherently stabilizing. This type of bearing also has advantages for service in the high-temperature turbogenerator because the individual pads are self-aligning and can correct for housing distortion.

Several types of full cylindrical bearings have also been investigated for liquid-metal use. This type of bearing employs different types of grooves and other modifications to obtain stable operation at light loads. Figure VIII-24 shows the herringbone groove bearing, which is a smooth cylindrical bearing with a journal containing herringbone grooves. This type has proved to be the most stable bearing in tests at Lewis. Other cylindrical-bearing configurations, however, have also been operated stably at high speed and light loads.

The bearing for use in the potassium turbogenerator must accommodate differential thermal expansion and housing thermal distortion. Figure VIII-25 therefore illustrates use of a flexible-mounting diaphragm to allow for differential motion of shaft and bearing. The pivots that provide bearing stability are also shown. This approach is the same as that used for the gas Brayton cycle system (paper V). If a full cylindrical bearing were used, a flexible mount to accommodate misalignment would also be needed.

A summary of the accomplishments of NASA and other agencies and their contractors shows that substantial experience has been accumulated with liquid-metal-lubricated bearings. Results obtained with a number of different fluids are as follows:

- (1) Water has been used extensively to study the hydrodynamic characteristics of bearings, because water closely simulates liquid metals in this respect.
- (2) For NaK, 3200 hours of endurance operation on pivoted-pad bearings has been achieved at 325° F. Additional tests were run on pressurized and hydrostatic journals in pumps at 1200° F.

(3) For sodium, high-speed tests were made at 800° F, and tests of the pivoted-pad and the herringbone-groove-type bearings showed the best stability. Low-speed tests have also been conducted for periods of 20 000 hours at temperatures up to 1100° F.

(4) Bearing tests have also been made on lithium to 800° F extending to 2100 hours.

(5) Potassium bearings have operated continuously for 1500 hours at temperatures to 600° F, and endurance tests on these bearings are presently continuing. Additional tests have been run at temperatures as high as 1200° F.

In the high-temperature sodium tests on pivoted-pad bearings, one possible problem encountered was the rapid pivot wear. A flexible-diaphragm mount has also been used for elimination of the pivots and thus elimination of the problem of pivot wear. This is a matter that will require continued investigation.

Bearing Materials

Not only must bearings be selected that are stable and that can accept the thermal transients of power system operation, but also bearing materials must be selected that are compatible with one another and with the alkali-metal lubricant. In selecting materials for liquid-metal-lubricated bearings, it is necessary first to see under what conditions the bearings must operate and what material properties will allow such operation. First, the bearings must operate in liquid metals, and thus corrosion resistance is required. Second, smooth lubricant flow passages are necessary; the material must be fabricated with a smooth surface that must be maintained. To maintain the surface, the material must resist abrasive damage; thus a high hardness is required. A high hardness of bearing materials has also been shown necessary in actual bearing tests.

Because the clearances in these bearings are very close, it is necessary for the materials to be dimensionally stable. Since the clearances are so small, a close match in thermal expansion between the bearing and shaft material is desirable since this would ease the design problems.

The last property to be considered here is the thermodynamic stability of the material. While dynamic stability is not a design requirement, it is a materials requirement because any elements transferred out of the material could ruin its structural integrity and make it unacceptable.

Many materials have been evaluated for this application, and table VIII-2 lists the properties that have been discussed, namely, coefficient of thermal expansion, Vickers hardness number, and material stability, both dimensional and thermodynamic. Three candidate bearing materials and two potential shaft materials are indicated. The bearing materials are titanium carbide - 10 columbium and two tungsten carbide materials, one bindered with a refractory metal and the other with cobalt. The shaft materials are the molybdenum base TZM and the cobalt-base Nivco.

The coefficient of thermal expansion, where a close match is desired, is shown for the materials; they do match well for the TZM and the tungsten carbide bearing materials, while there is some difference in the titanium carbide - 10 columbium. The Nivco is considerably different from all the other materials. Design studies are yet to be made on actual hardware to define what can be accomplished with these materials.

The Vickers hardness numbers for all the bearing materials have been measured and are

quite high for the candidates in table VIII-2; thus they would be expected to resist abrasion. The dimensional stability of materials tested in potassium at 1200° F for 1000 hours was evaluated, and all the candidates had negligible changes.

A measure of thermodynamic stability is the amount of carbon transferred from the bearing material to a columbium - 1-percent-zirconium capsule. The carbon transfer was very low for all the materials tested at 1200° F. At 800° F, no transfer of carbon was observed for any of the materials listed. Corrosion resistance was evaluated in this test also, and there was no observed attack; this evaluation is based on visual, chemical, and metallographic examinations.

Generator Materials

The design features of an electrical generator for space applications are discussed in paper V. Just as for the Brayton system, the potassium Rankine generator will have a solid rotor. The differences are the higher operating temperature of the Rankine cycle generator and the possible presence of potassium vapor in the rotor cavity. Because of the meager information on electrical materials above 400° F, various candidate materials were tested in order to determine their electrical capabilities at high temperatures.

The cobalt-base alloy Nivco is a candidate rotor material. Nivco has a combination of high creep strength and acceptable magnetic properties. Figure VIII-26 shows creep curves for various temperatures and stresses. After 7000 hours at 1100° F with an applied stress of 37 500 pounds per square inch, Nivco has undergone only 0.8 percent creep. The creep curves provide design data in the 1100° F temperature range.

The next functional part of the generator to be considered is the stator. The laminations were made of the iron-base magnetic material Hyperco 27. Insulations were typically high-purity alumina except for that on the nickel-clad silver conductor. That insulation was Anadur-E glass plus refractory oxides, and the end-turn potting compound was phosphate-bonded zirconium silicate.

Figure VIII-27 shows a statorette constructed of the following electrical materials:

Component	Material
Magnetic material	Fe-27Co
Interlaminar insulation	Alumina
Slot insulation	Alumina
Electrical conductor	Nickel-clad silver
Conductor insulation	Anadur-E glass plus refractory oxides
Potting compound	Phosphate-bonded zirconium silicate

The assembly shown is representative of a 15-kilovolt-ampere 3-phase generator stator and has been tested in vacuum for 5000 hours with a hot-spot temperature of 1100° F. The photograph was taken after the 5000-hour test; the appearance of the assembly was unchanged by the test.

The properties measured were the conductor resistance and insulation resistance. Figure VIII-28 shows that the conductor resistance for the 5000-hour test was constant for the duration of test, which is indicative of material stability and lack of metallurgical interactions.

The insulation resistance (fig. VIII-29) was measured for both phase to phase and phase to ground. The resistance did not degrade; in fact, it actually improved. This improvement is the result of outgassing of water vapor and other volatile residuals that are being removed by the high vacuum.

Two solenoids and a transformer constructed of these same materials are shown in figure VIII-30. These units were tested in vacuum for 5000 hours with a hot-spot temperature of 1100° F. The two solenoids operated for 5000 hours, with one continuously energized and the other energized at 170-hour intervals to check for the occurrence of diffusion bonding. Continuously energizing the solenoid added a direct-current voltage to the thermal effects in a nonenergized solenoid. No diffusion bonding occurred, and both solenoids were operating satisfactorily at the end of the test. The transformer test was lessened in value by a voltage surge from a power supply. The transformer exhibited electrical continuity after the test, and evaluation will determine the full extent of the failure and what data may still be obtained.

With potassium-lubricated bearings and conventional shaft seals, potassium vapor would be present in the generator rotor cavity (see section on Bearings and Seals). While the solid rotor will not be attacked by the vapor, the insulation in the stator windings will be attacked, and therefore, potassium vapor must be excluded from the stator assembly. The ceramic bore seal shown in figure VIII-31 performs this function. A ceramic bore seal is used because any metallic materials will give eddy current losses. These losses result in heat buildup and a loss of efficiency in the generator.

The ceramic is likely to be beryllia mainly because of its high thermodynamic stability. An added benefit of beryllia is its high thermal conductivity in comparison with other oxides. A high thermal conductivity will reduce temperature differentials and thus diminish the likelihood of cracking the bore seal.

To exclude potassium vapor from the stator totally, other vapor paths to the stator must also be blocked off by attaching the ceramic bore seal to the generator housing and thus indirectly to the bearing and seal housing. This attachment is made by a metal member that must be thin and flexible to allow for thermal expansion mismatches between the ceramic and the generator housings. This construction requires a ceramic-to-metal braze joint that must be leak tight.

This joint is one of the major problems in bore seal construction. A ceramic-to-metal joint is usually made by using an active metal braze, that is, a braze alloy that contains elements which, when molten chemically, react with the surface of the ceramic. This reaction then allows the braze material to wet the surface and thus promotes a good braze joint.

Tests have been conducted on a number of braze alloys. The joint efficiencies range from 60 to 98 percent, that is, the joint strength can be 98 percent as strong as the ceramic beryllia which typically has a modulus of rupture of 25 000 pounds per square inch.

It has been stated that the ceramic-to-metal joints must be leak tight. To check this, assemblies were made with 2-inch-diameter beryllia cylinders fitted with columbium - 1-percent-zirconium end caps. The assemblies tested showed no leakage within the limits of sensitivity of measurement.

PUMPS

The four-loop system shown in figure VIII-1 requires four pumps, one in each loop. For the SNAP-8 program, considerable experience has been gained with motor-driven pumps. Figure VIII-32 shows a motor-driven centrifugal pump described in paper VI. It pumps NaK in the reactor loop of the SNAP-8 system at 1100°F and has accumulated 3000 hours of endurance on a single pump. A pump of this type is thus a candidate for use in three of the four loops. The operating conditions are as follows:

Speed, rpm	5800
Head rise, psi	35
Flow, lb/hr	35 300
Input power, kW	4.6
Overall efficiency, percent	35

In the reactor loop (fig. VIII-1) the fluid temperature is quite high at the pump inlet, about 2000°F . Use of a motor-driven centrifugal pump at this point in the system would require thermal isolation of the motor from the pump in order to limit the motor temperature to the 1100°F for which considerable experience has been gained with electrical materials. Although such thermal isolation has been successful in the SNAP-8 program, a motor-driven pump for this application has not actually been built.

Electromagnetic Pumps

The electromagnetic induction pump is also a candidate for this service. One of the attractive features of the electromagnetic pump is that it is mechanically simple; it has no shaft, bearing, or seal. However, it is not without problems. On the good side of the ledger is the considerable experience obtained to date with electromagnetic pumps in ground installations. They have operated for thousands of hours at fluid temperatures to 2000°F . For example, in one of the corrosion loops, a helical induction pump has circulated sodium at 1990°F for 5000 hours (paper VII, fig. VII-25).

The experience with pumps of this type does not mean, however, that a 2000°F pump is available for use in the reactor loop. The purpose of the pumps to date has been simply to pump liquids at high temperature in a pipe that will contain it. Consequently, the pumps are heavy with much external cooling to eliminate temperature problems. Efficiencies have been typically less than 5 percent, compared with 35 percent for the SNAP-8 mechanical pump just described. What is required, then, is to increase the performance level, while at the same time decreasing the weight.

Figure VIII-33 shows a pump that is designed to have an acceptable level of performance. It is a helical induction pump under development as a boiler feed pump. The operation of this pump is exactly the same as an induction motor. The stator is wound to produce a rotating magnetic field. The core of the pump is an annular pipe containing a helix and liquid potassium, which is

electrically conductive. The rotating field causes the potassium to follow a helical path through the duct, in this case from right to left. The pressure of the potassium is continuously increased as it passes through the helical passage within the field of the stator. The stator is thermally insulated from the high-temperature-pump cell. The pitch of the helix is larger on the inlet side of the annulus to avoid cavitation by lowering the velocity at the pump inlet. It should be possible to design such pumps to accept near-boiling fluid at the pump inlet.

The pertinent design point data for the pump under development are as follows:

Head rise, psi	240
Flow, gal/min	33
Temperature, °F	1000
Efficiency, percent	20

The 20-percent efficiency is a considerable improvement over present high-temperature electromagnetic pumps, but it is still lower than that obtainable from mechanical pumps. It is a trade-off, then, between simplicity and efficiency. The pump is to develop a pressure rise of 240 pounds per square inch with a flow equal to that required for a 300-kilowatt system. Although the design fluid temperature is 1000° F, the pump is to accommodate liquid potassium to 1400° F, and it will be tested at this higher temperature.

In order to increase the temperature level of electromagnetic pumps, use will be made of the advancements in magnetic materials such as those previously described for the generator. Also, the versatility of remotely inducing an electrical force on the conductive potassium makes other types of electromagnetic pumps worth considering. Such studies are underway.

RADIATOR

For the waste-heat rejection system, the liquid coolant from the condenser is pumped to the radiator where it rejects the waste heat by thermal radiation to space. One problem of the radiator is that the pipes through which this liquid flows must be protected against meteoroid penetration. Early meteoroid penetration estimates were based on indirect measurements such as the audible clank or flash of light produced by an impacting meteoroid or the visible light and ionization produced by a meteor in the Earth's atmosphere. A considerable amount of interpretation and speculation was required in order to use these data to predict the amount of meteoroid armor required. Recent data from the Explorer and Pegasus satellites have substantially improved our knowledge of this meteoroid problem. The satellites now yield data in the desired final form, namely, on the frequency of penetration of metallic surfaces, as shown in figure VIII-34. Although the Pegasus data and much of the Explorer data were obtained on aluminum surfaces, they have here been converted to stainless steel by use of the correlating equation of Summers.

The solid line represents a 1963 projection of the data available at that time. The new data lie substantially on this line for thicknesses of a few mils, but for thickness less than 1 mil, the data are below this early prediction. In the range significant for radiator design, the early prediction is still valid.

On the other hand, the ideas of radiator design have been changing (fig. VIII-35). The armored tube and fin is an early approach. Liquid coolant passes through the tubes. The armor surrounding the tubes protects them from meteoroid penetration. Heat from the liquid is conducted through the armor and into the fins. Both the upper and the lower surfaces then radiate this heat to space. If a meteoroid punctures a fin, a very small amount of surface area is lost, and the ability of the radiator to radiate waste heat drops by a negligible amount. On the other hand, puncture of a tube would allow the coolant to leak out, a generally catastrophic event. For this reason, the tubes are heavily armored and spaced far apart. Because tube spacing is limited by the temperature drop resulting from heat conduction through the fins, copper clad with stainless steel is a good material from which to build the fins.

The bumper-fin concept protects the tubes by a meteoroid bumper. A meteoroid that strikes the radiator surface is shattered with the result that only a diffuse spray of smaller particles impinges on the vulnerable tubes. Because this concept employs thermal conduction to carry the heat from the tubes to the radiating surfaces, the problem of temperature drop in the fins is much the same as in the armored tube and fin.

The vapor-chamber-fin concept retains the ability of the bumper-fin to protect the tubes from meteoroid penetration, but it improves the heat-transfer characteristics by adaptation of the ubiquitous heat pipe. Heat is transferred in the following way: The radiator contains a large number of box-like compartments, one of which is shown in figure VIII-35. This box is lined with a wick that is a thin layer of porous material such as wire cloth or sintered metal powder. Enough liquid metal is put into each compartment to saturate the wick. The central cavity contains only the vapor from this liquid metal. Heat from the tubes is conducted to the wick, and thereby some of the liquid in the wick is vaporized. Vapor within this cavity condenses on the two radiating surfaces of the radiator. The condensate thus formed is then transported by capillary forces back to the heating surface, where it is again vaporized. By this convection of metallic vapor and liquid, heat is transferred from the tubes to the radiating surfaces. Because the effective thermal conductivity of the vapor chamber fin is high, not only may the tubes be far apart but also the radiator size may be reduced.

For the vapor-chamber-fin concept, the entire radiator surface is vulnerable to meteoroid penetration. This vulnerability would be a detriment if it were not for the compartmentization of the radiator. A typical radiator might contain of the order of 100 such compartments of which 10 percent might be sacrificed during the mission; in other words, 10 punctures during the mission would result in a 10-percent loss of heat-rejection capacity, a factor easily adjusted for by making the radiator just a bit larger than required. By the combination of improved meteoroid protection and improved lateral heat transfer within the radiator, radiator weight is approximately halved.

Emissive coatings are required for the radiating surfaces. Bare stainless steel radiates only 20 percent as much heat as does a blackbody, therefore, investigations have been made of coatings that have high emissivity. Calcium and iron titanates are the two best coatings to date. Their characteristics are shown in figure VIII-36. The iron titanate has now been endurance tested for $22\frac{1}{2}$ months and the calcium titanate for a full 2 years. The two specimens still have an emissivity of 0.88.

Coatings have also been subjected to additional tests. For example, each test specimen has endured 88 thermal cycles between room temperature and 1350° F. Fatigue specimens have been tested in a standard fatigue machine for as many as 10⁶ stress cycles. For some of the fatigue specimens, the cyclic stress was high enough to fracture the stainless steel. Through all these thermal and stress cycles, the coatings have tenaciously adhered to the metal surfaces, even right up to edge of a fracture. The enduring qualities of these coatings give every indication of their suitability for use on these high-temperature radiators.

CONCLUDING REMARKS

In both this discussion and the discussion in paper VII the technology of potassium-vapor Rankine-cycle turbogenerator power systems has been reviewed, and our work on a variety of constituent problems of these systems has been discussed. On the bases of corrosion and strength, maximum temperatures of 2200° to perhaps 2400° F appear practical (paper VII). Satisfactory thermodynamic data for design of such a powerplant are now available. Adequate information has been obtained on the heat-transfer coefficients and pressure drops of boiling and condensing potassium, and our general knowledge of the problem of boiling stability is advancing. Tolerable turbine blade erosion has been experienced at qualities as low as 93 percent, and investigation of lower values is planned in the near future. Design information on bearings, seals, pumps, and electrical materials is accumulating. The thermal design of radiators is improving, and the meteoroid satellites provide additional confidence that reliable radiators can be designed.

The program at Lewis is now beginning to change in its general character by a shift from the general accumulation of design data into component demonstration. Over the next few years, the major components of such a power system should be ready for testing.

Considerable effort lies ahead in building and testing the first real refractory components typical of advanced Rankine power systems. These components will draw on the fabrication procedures described in paper VII, and special facilities will be required in order to provide the high vacuum specified. Testing of these components and testing of the complete power system will undoubtedly reveal problems presently unknown. In order to obtain the performance and long life required for the high-power missions of the future, extensive design and testing of these advanced components are planned over the next 10 years, drawing on the base of technology described herein.

TABLE VIII-1. - LUBRICANT, SEALS, AND
GENERATOR DESIGN

Bearing lubricant	Turbine seal	Generator seals	Generator cavity
Potassium	Potassium - potassium	Potassium - potassium	Potassium vapor
Potassium	Potassium - potassium	Potassium - space	Vacuum
Oil	Potassium - space Oil - space	Oil - space	Vacuum

TABLE VIII-2. - PROPERTIES OF BEARING MATERIALS AT 1200° F

Materials	Coefficient of thermal expansion, °F ⁻¹	Vickers hardness number	1000 hr in potassium	
			Dimensional change, percent	Carbon increase in Cb-1Zr capsule, ppm
Bearing				
TiC-10Cb	4.00×10 ⁻⁶	810	0.008	0
90WC-2CbC-8Mo	2.62	1800	.07	40
74WC-20TaC-6Co	2.97	1020	.014	45
Shaft				
TZM	2.98×10 ⁻⁶	205	-0.04	0
Co-23Ni-1.1Zr-1.8Ti	7.4	----	-----	--

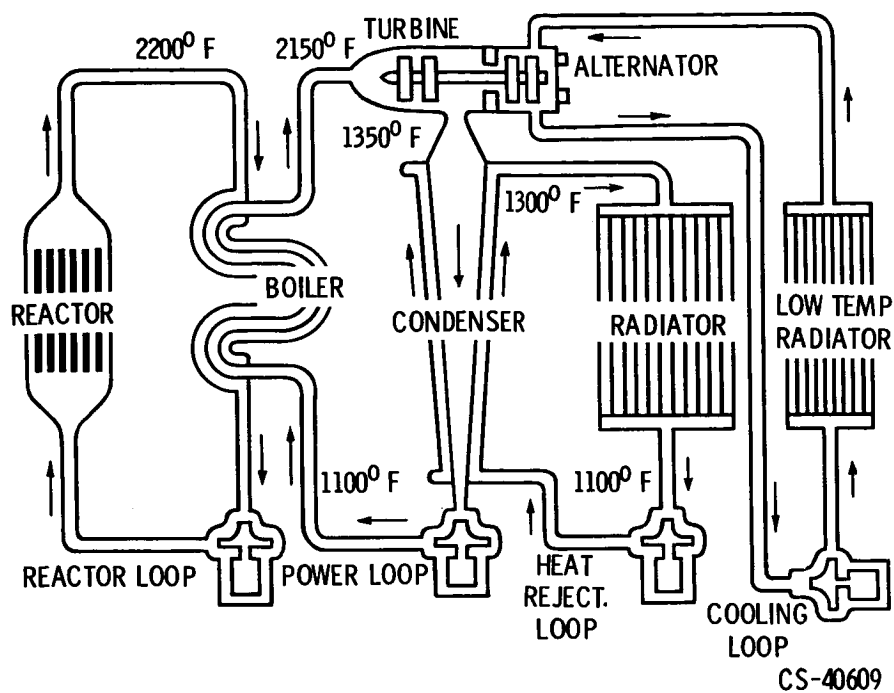


Figure VIII-1. - Potassium Rankine system.

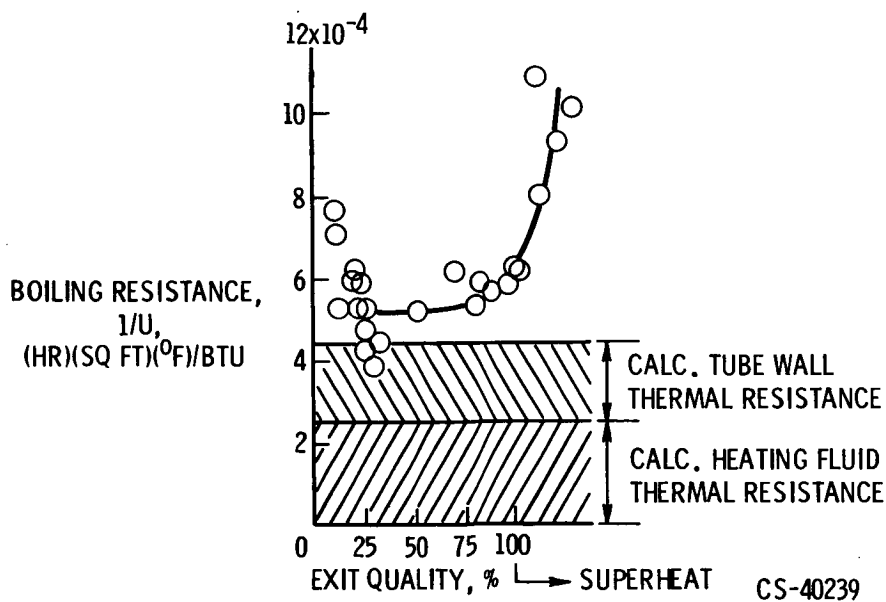


Figure VIII-2. - Overall boiler thermal resistance as function of exit quality.

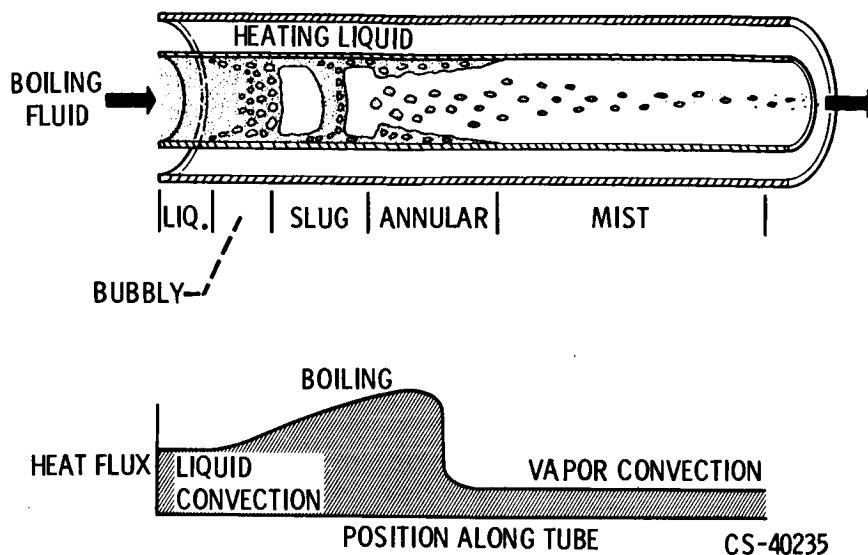


Figure VIII-3. - Two-phase boiling flow regimes.

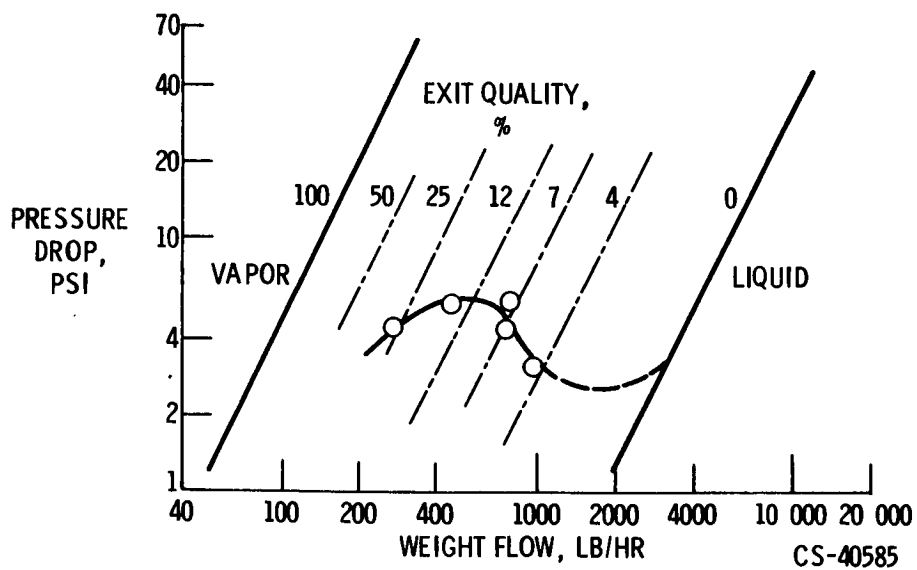


Figure VIII-4. - Boiling pressure drop for sodium.

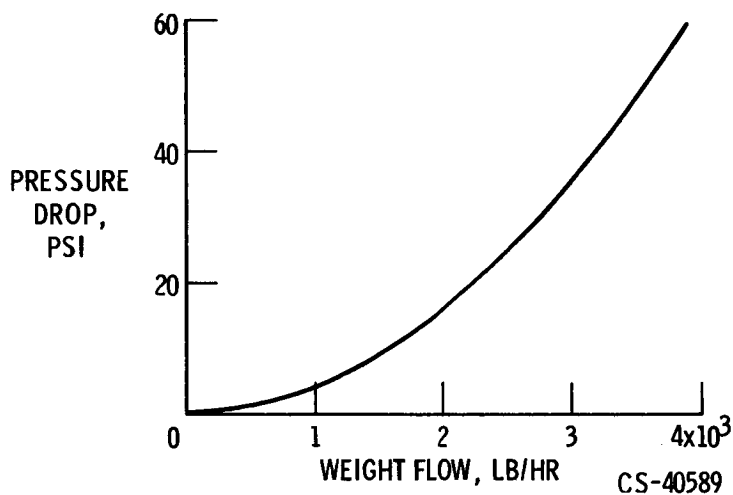


Figure VIII-5. - Orifice pressure drop. Square-law inlet resistance.

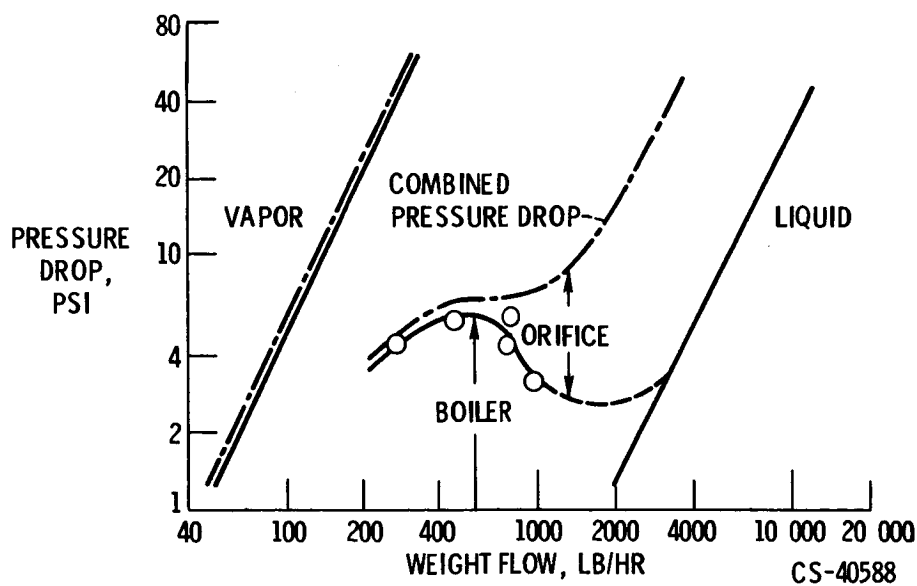


Figure VIII-6. - Boiling pressure drop for sodium.

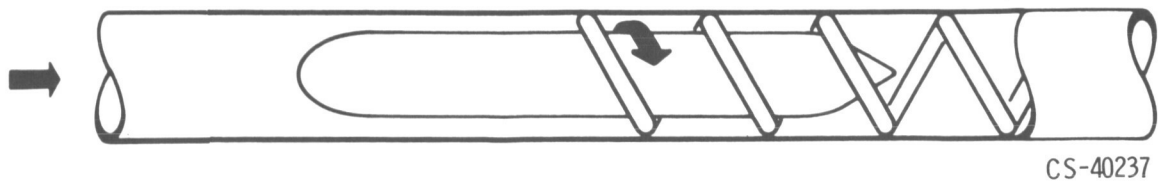
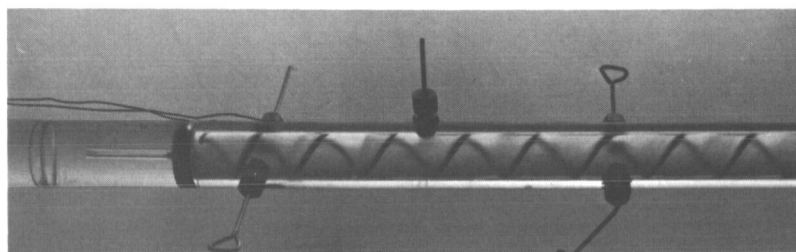
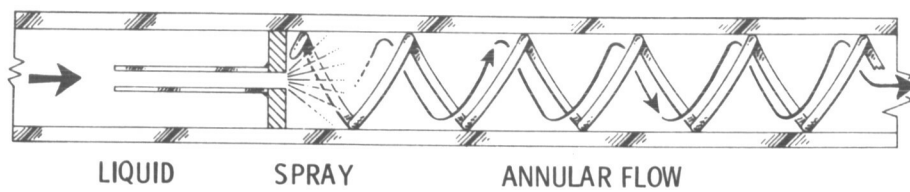
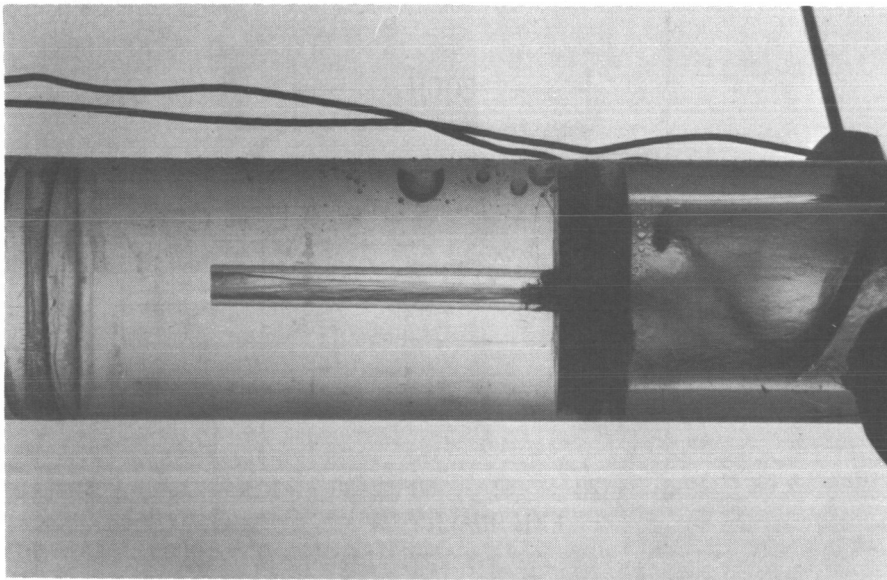


Figure VIII-7. - Center plug and spring boiler inlet insert.



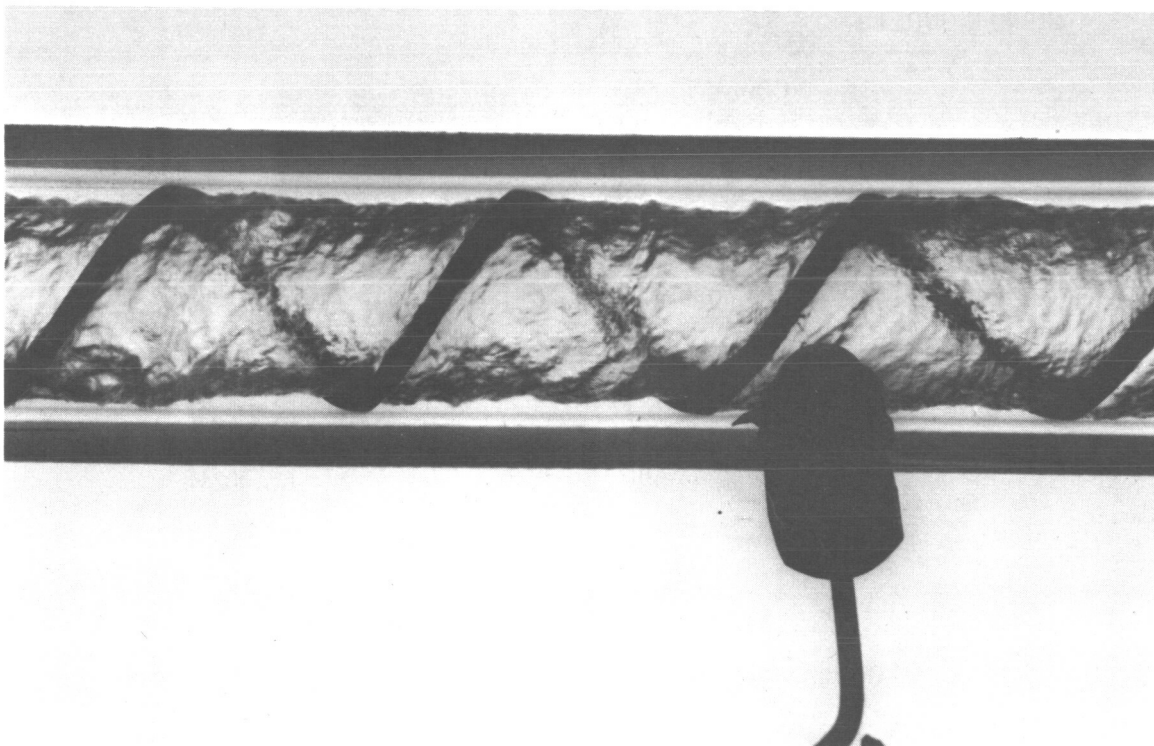
CS-40479

Figure VIII-8. - Center tube and spring boiler tube inlet inserts.



CS-40476

Figure VIII-9. - Closeup of center tube.



CS-40478

Figure VIII-10. - Closeup of annular region.

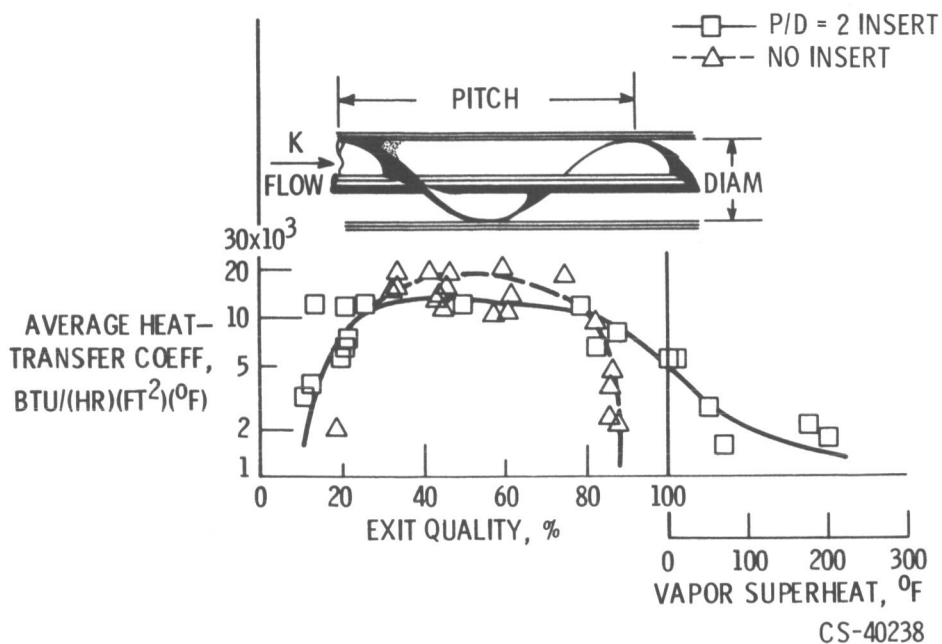
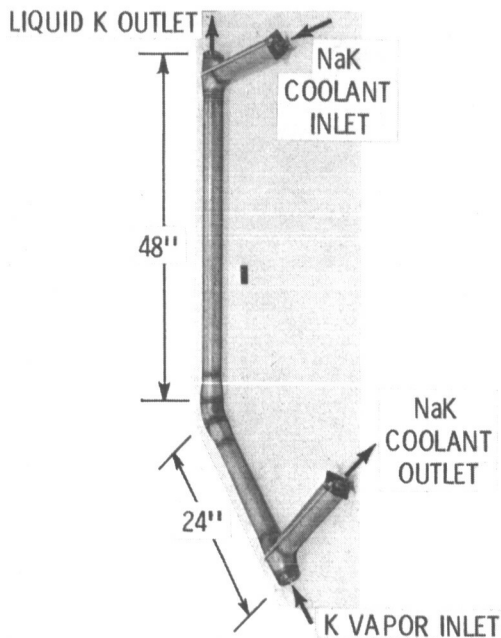
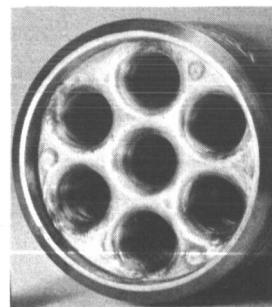


Figure VIII-11. - Boiling potassium heat transfer.



(a) Overall view.



CS-40244

(b) Detail of vapor inlet. Tube outside diameter, 1/2 inch; shell inside diameter, 2 inches; material, 316 stainless steel.

Figure VIII-12. - Seven-tube potassium condenser.

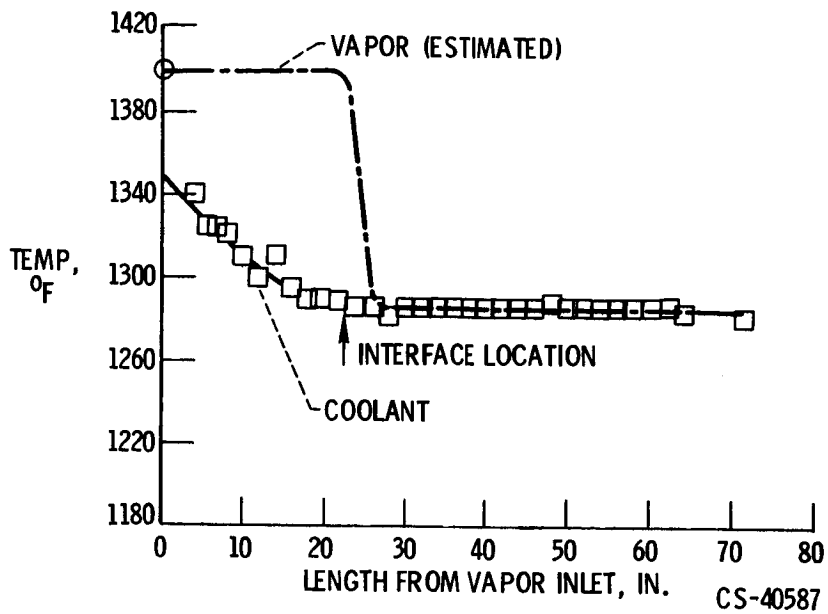


Figure VIII-13. - Condenser temperature profiles.

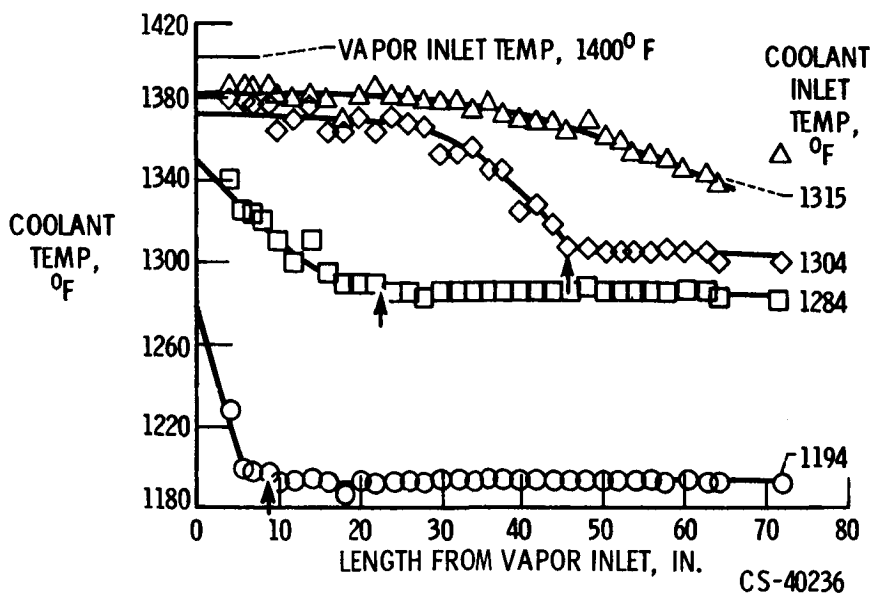


Figure VIII-14. - Seven-tube condenser performance.

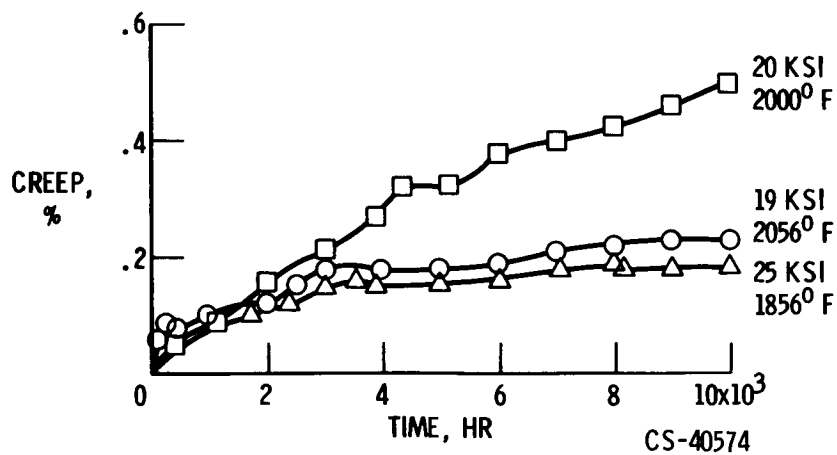


Figure VIII-15. - Creep of TZC (Mo-1.25Ti-0.15Zr-0.12C).

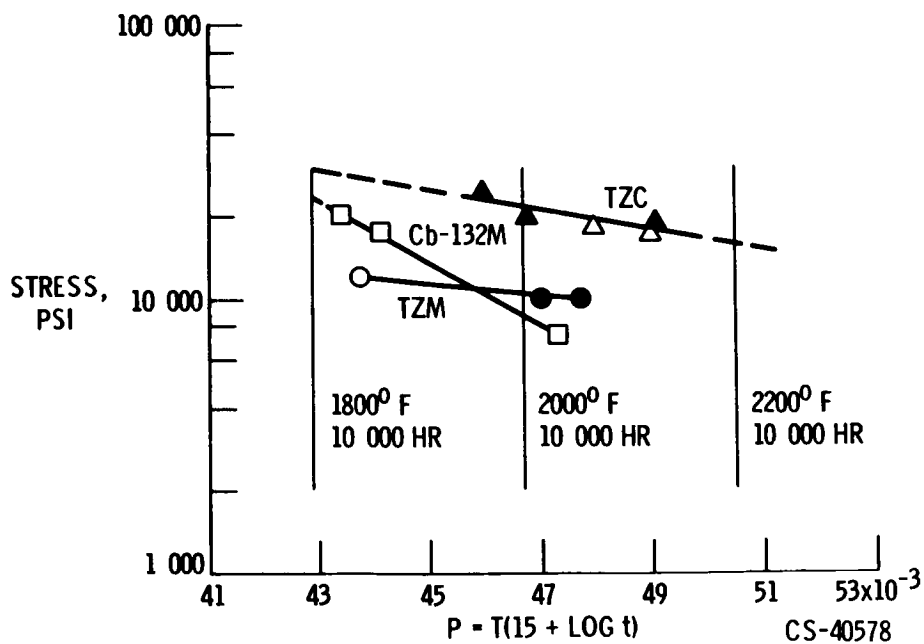
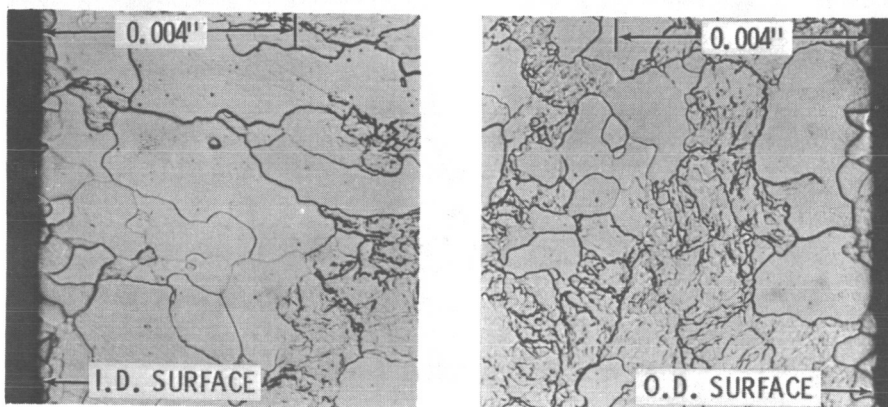
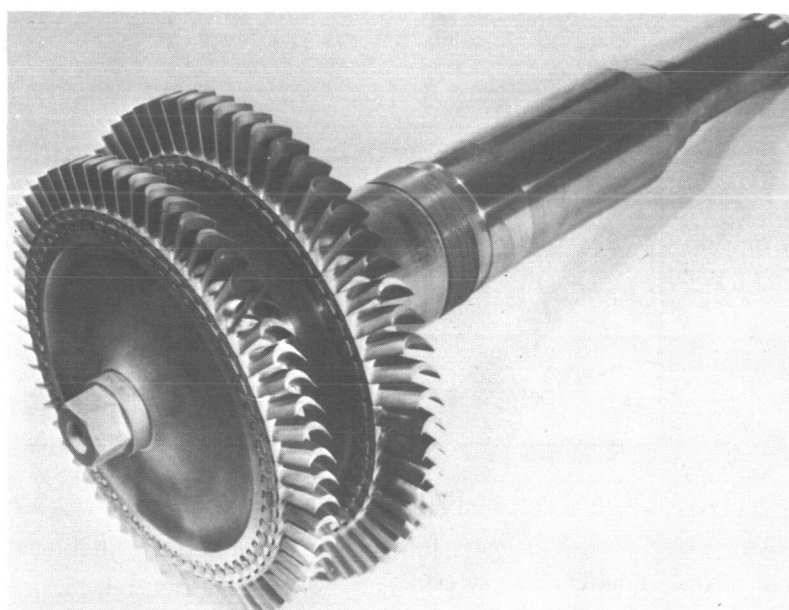


Figure VIII-16. - Strength of turbine alloys for 0.5 percent creep.



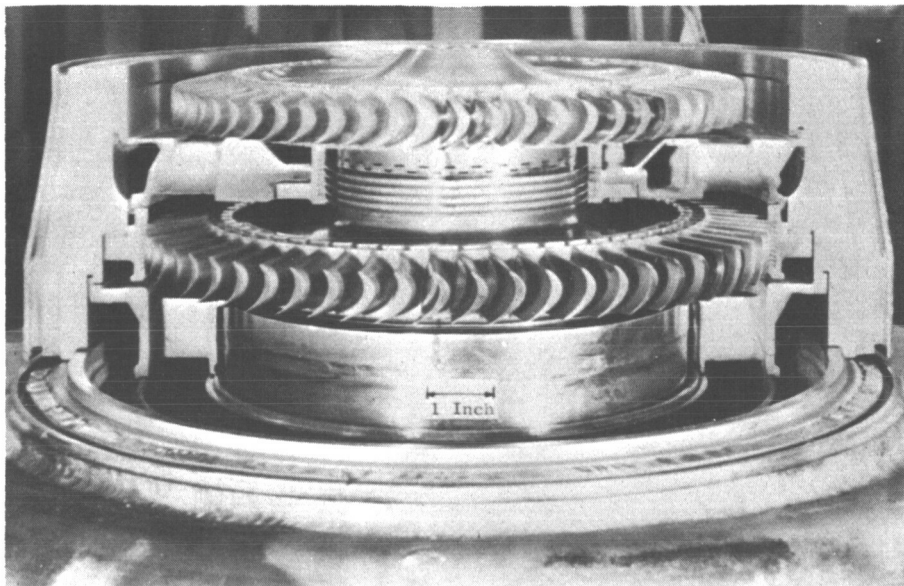
CS-40580

Figure VIII-17. - TZM compatibility with potassium vapor for 5000 hours at 2000° F.



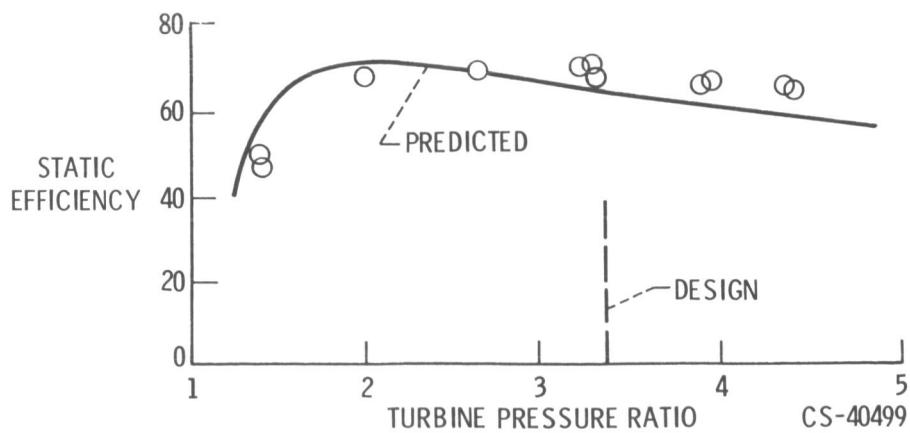
CS-40618

Figure VIII-18. - Potassium turbine rotor.



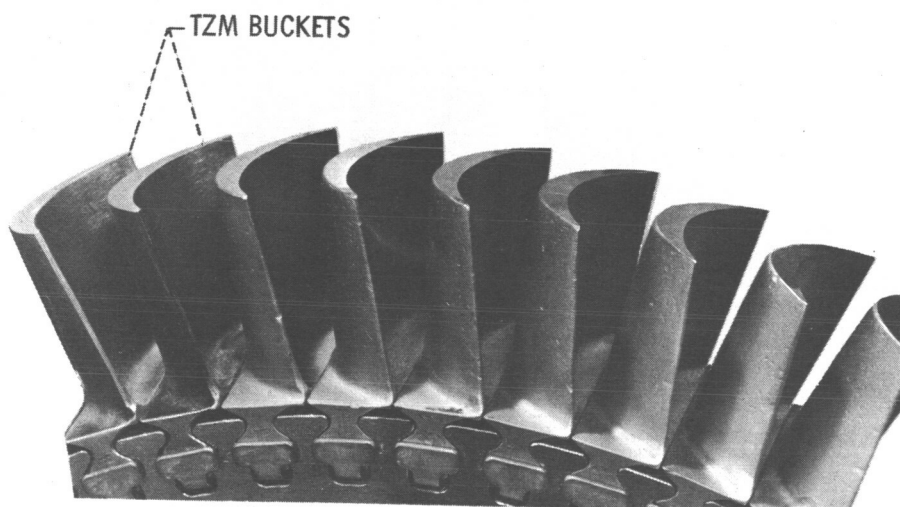
CS-40619

Figure VIII-19. - Turbine partial assembly.



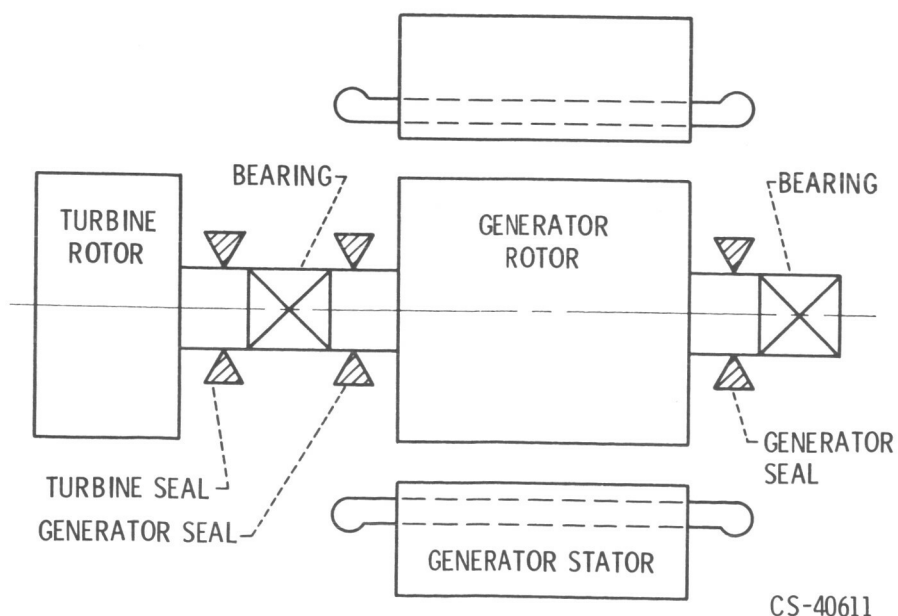
CS-40499

Figure VIII-20. - Two-stage potassium turbine performance. Inlet temperature, 1550° F; quality, 99.5 percent.



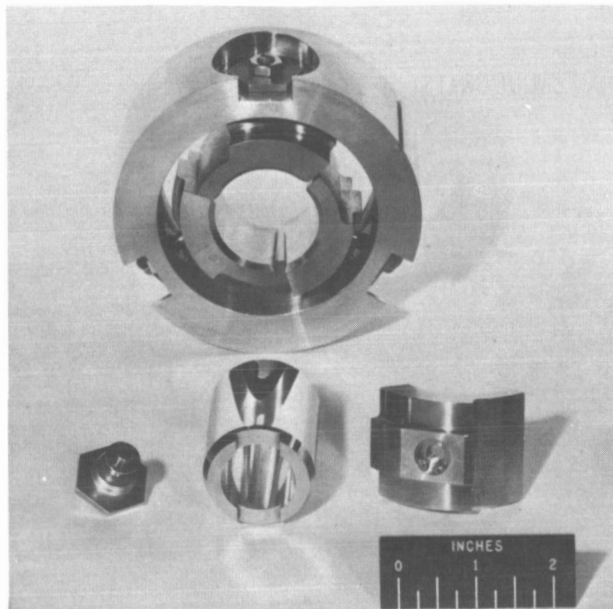
CS-40502

Figure VIII-21. - Second-stage wheel after 2000-hour endurance test.



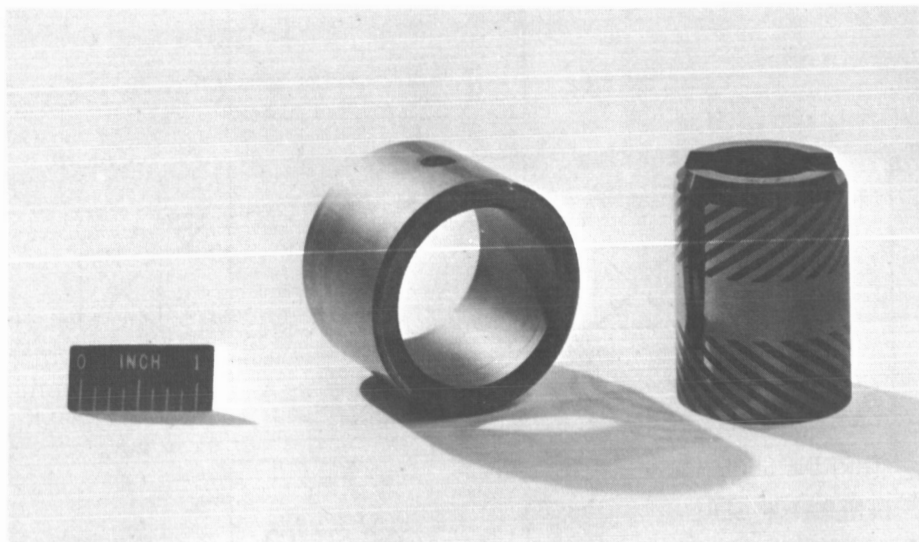
CS-40611

Figure VIII-22. - Turbogenerator bearing-seal arrangement.



CS-40621

Figure VIII-23. - Pivoted-pad-bearing assembly.



CS-40617

Figure VIII-24. - Herringbone groove bearing tested in sodium to 800° F.

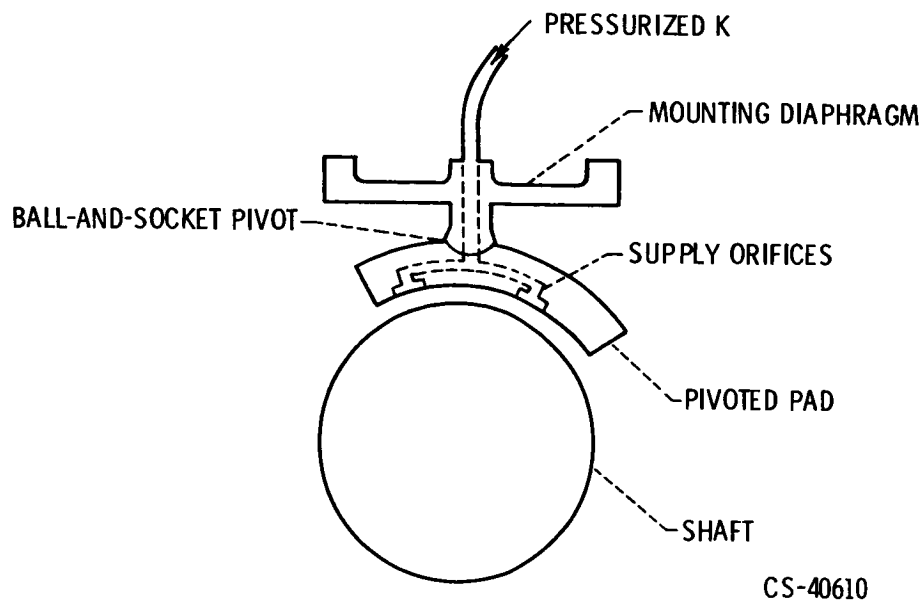


Figure VIII-25. - Mounting arrangement for pivoted-pad bearing.

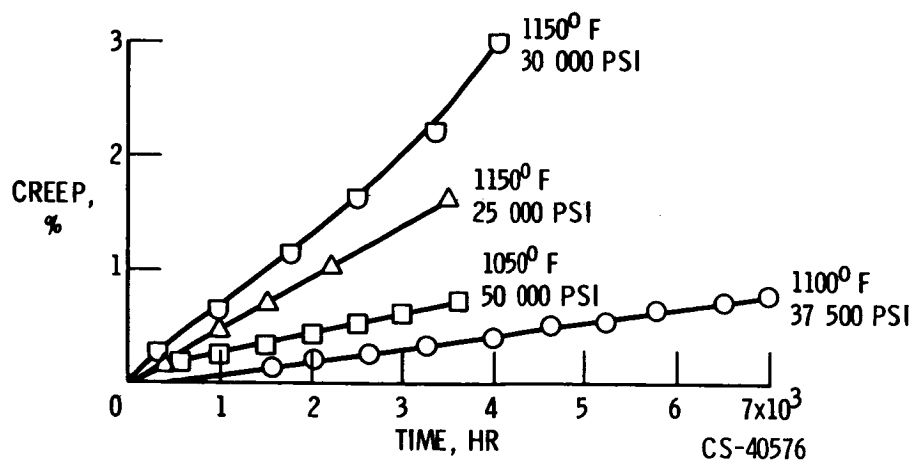
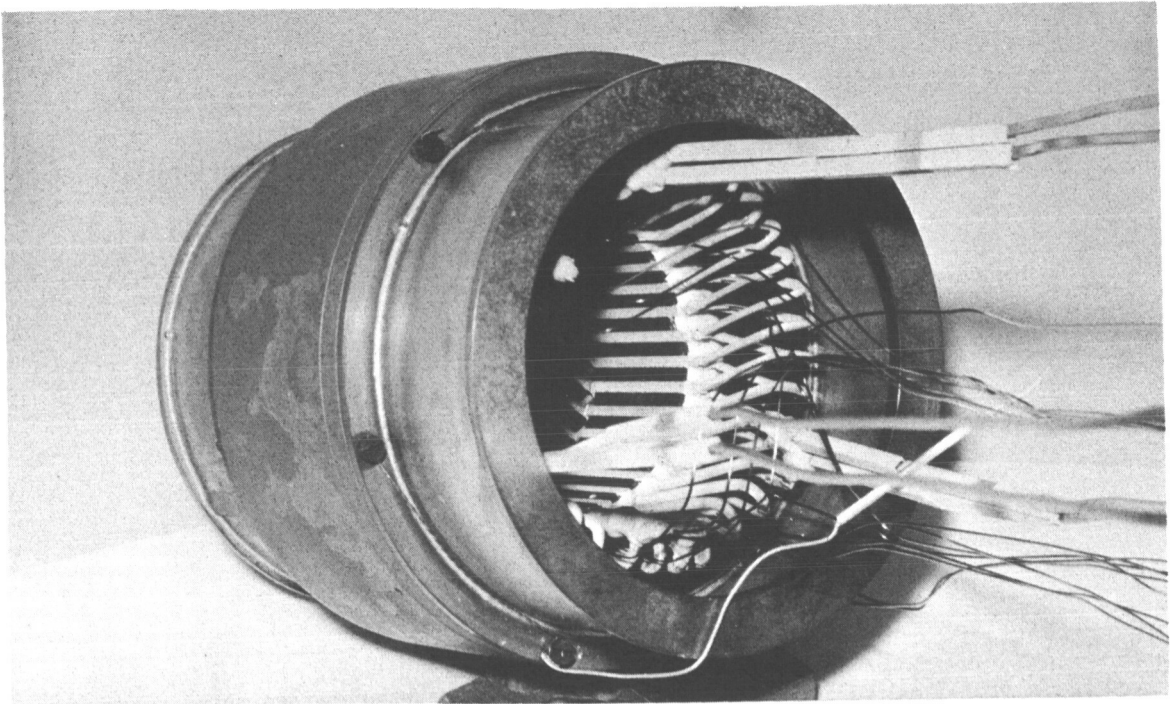


Figure VIII-26. - Creep of Nivco (Co-23Ni-1.1Zr-1.8 Ti).



CS-40558

Figure VIII-27. - Stator assembly tested in vacuum for 5000 hours at 1100° F.

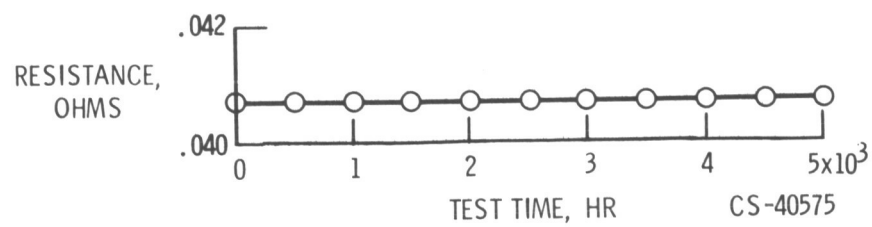


Figure VIII-28. - Conductor resistance at 1100° F.

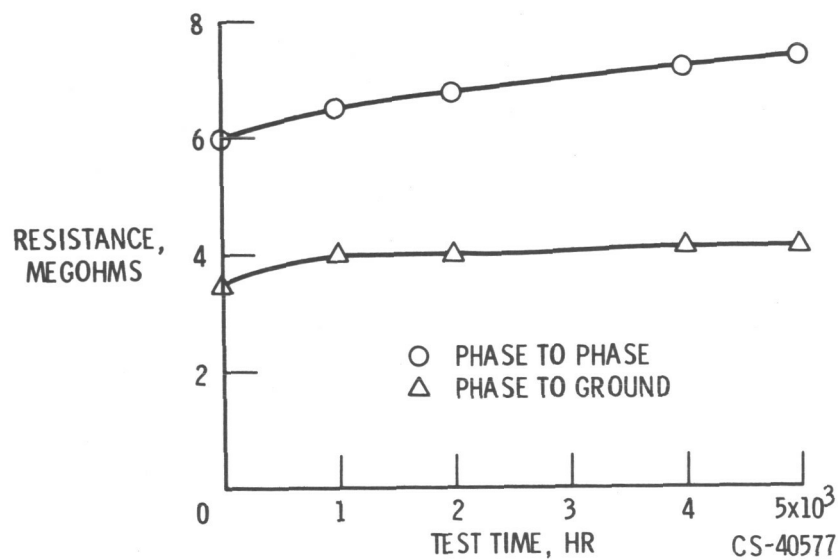
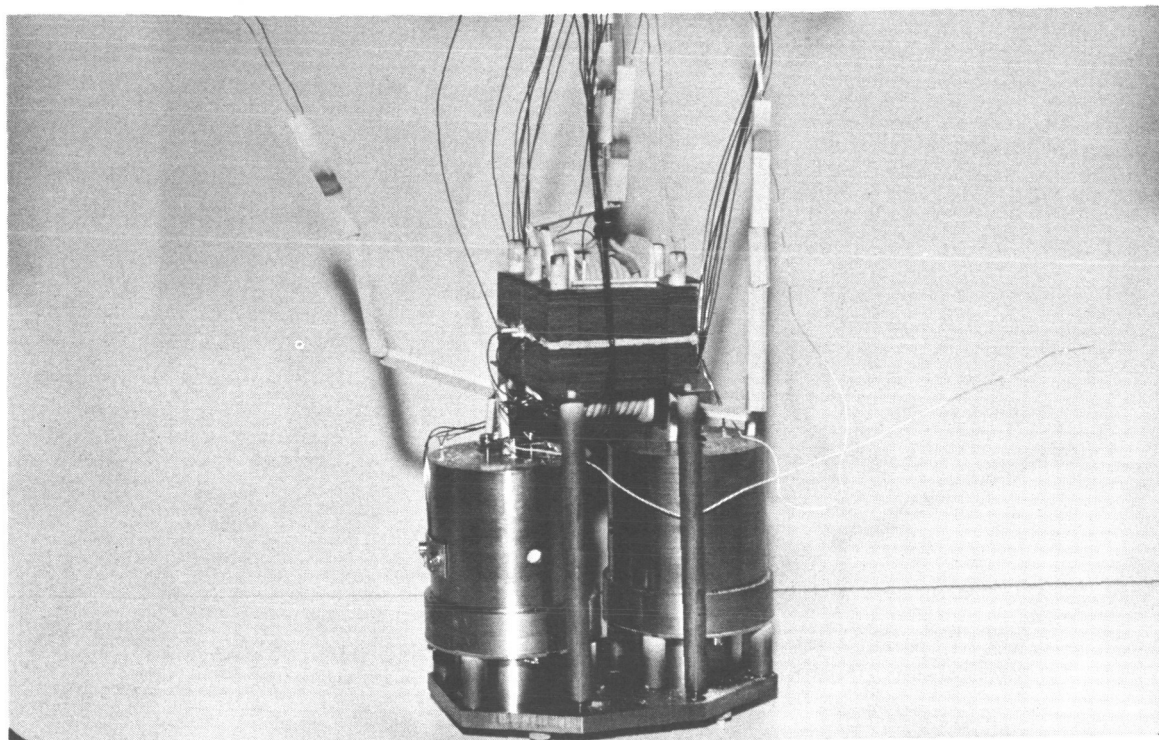


Figure VIII-29. - Statorette insulation resistance at 1100° F.



CS-40557

Figure VIII-30. - Solenoid and transformer assembly tested in vacuum for 5000 hours at 1100° F.

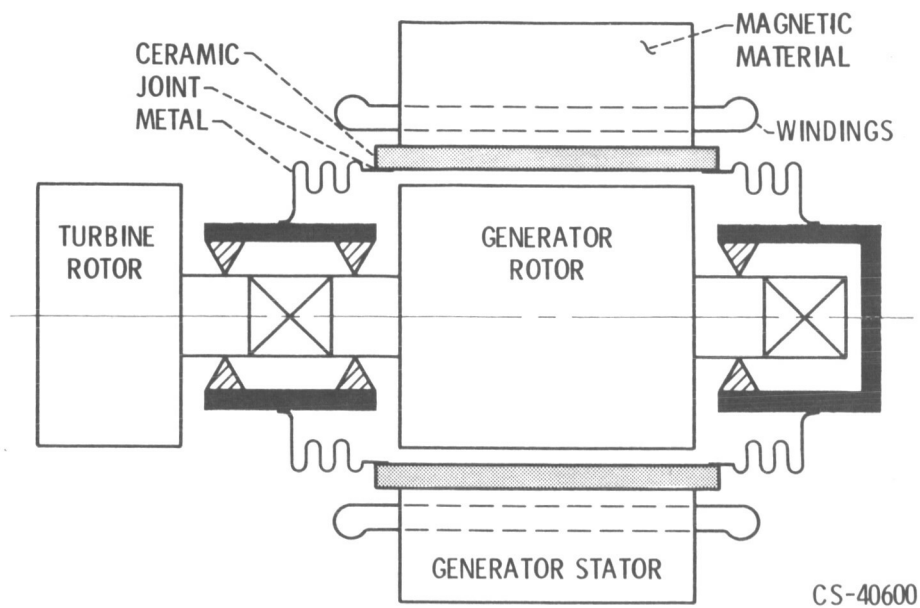


Figure VIII-31. - Generator bore seal.

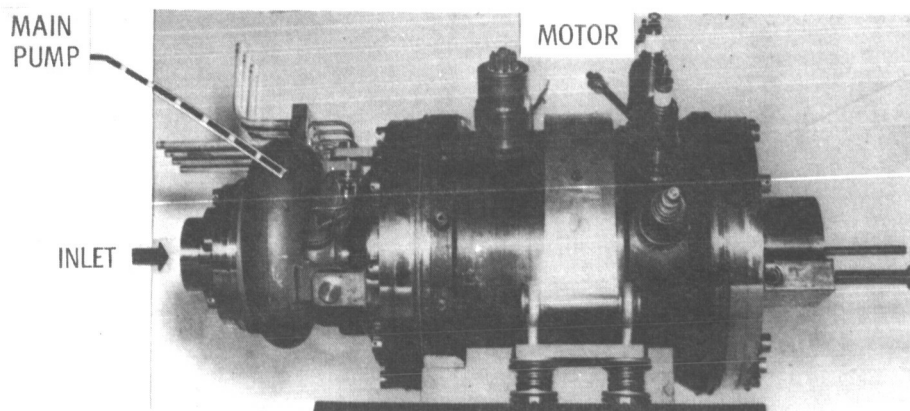


Figure VIII-32. - NaK pump-motor assembly with NaK lubricated, tilting-pad journal and thrust bearings.

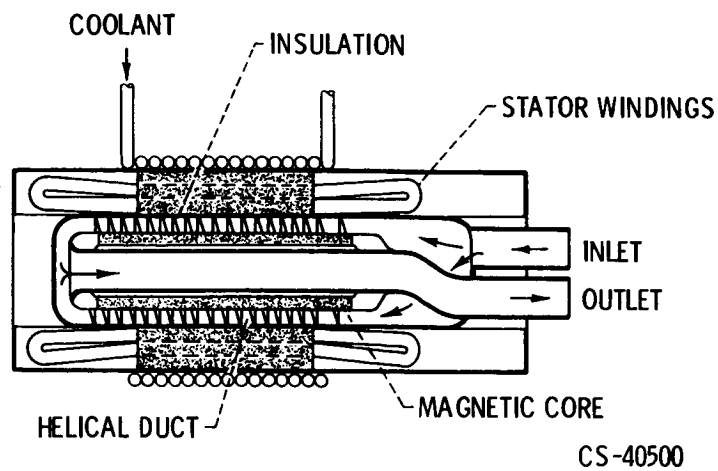


Figure VIII-33. - Electromagnetic helical induction pump.

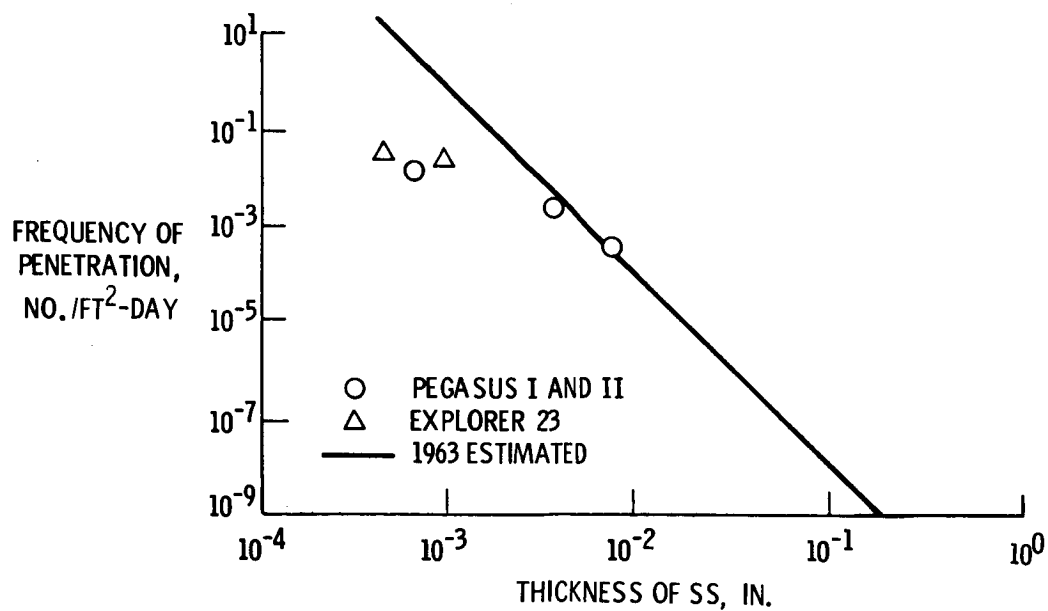
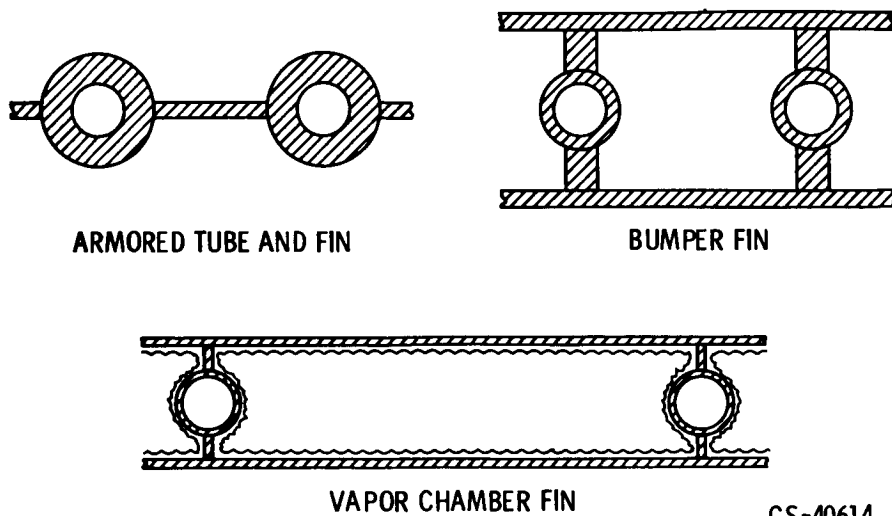


Figure VIII-34. - Meteoroid fluxes for Earth orbit.



ARMORED TUBE AND FIN

BUMPER FIN

VAPOR CHAMBER FIN

CS-40614

Figure VIII-35. - Radiator concepts.

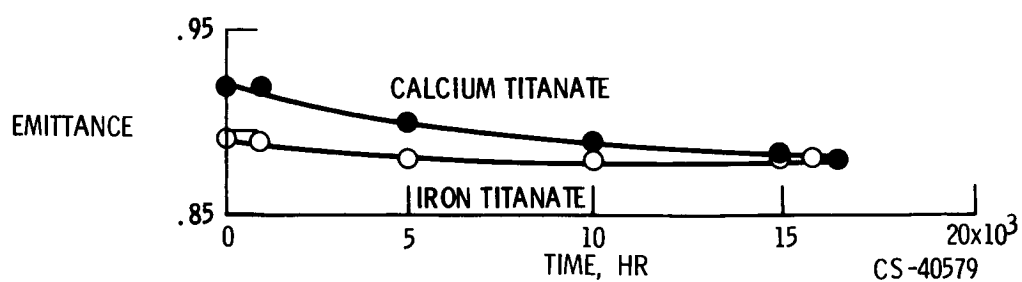


Figure VIII-36. - Endurance test of emissive coatings. Substrate, 310 stainless steel; temperature, 1350° F.

IX. THERMIONICS

Roland Breitwieser and Herman Schwartz

INTRODUCTION

The state of art of several aspects of thermionics as it is considered in the framework of a space power system is reviewed herein. NASA contractual and in-house efforts are emphasized. The principle of thermionics is discussed, and a brief exposure to some pertinent characteristics of thermionic converter systems is introduced. Primary emphasis is placed on (1) establishing the major performance constraints based on fundamental surface and plasma physics, (2) illustrating empirical performance, (3) introducing a few reactor-converter interface considerations, and finally (4) reviewing some limitations of prospective thermionic nuclear reactor fuels. It should be noted, since the NASA sponsored work is stressed, that many excellent references relating to these subject areas have been excluded from this report.

EFFICIENCY CONSIDERATIONS AND THERMIONIC REACTOR SYSTEMS

Figure IX-1 illustrates the basic principle of thermionic conversion. The converter is simply two metal electrodes separated by a small gap. Heat is applied to one metal electrode from an energy source such as a nuclear fuel. As the metal temperature increases, electrons are boiled out and are captured on the cooler electrode. The emission and capture of electrons provide the current flow through the external load. The voltage that can be obtained is depicted in the potential diagram. The hotter electrode, the emitter, has a relatively large population of electrons in the higher energy levels compared with the cooler electrode, the collector. The variation in the electron density is the driving force that permits the development of a useful voltage. Characteristically this is about 3/4 volt. The thermionic converter is a unique heat engine since it is one of the few energy conversion methods that produces electric power directly from heat over a large temperature interval in a single step. It is also unique in its ideal efficiency. A simplified expression for the efficiency is

$$\eta_{el} = \frac{J_{net}(V_1 - V_2)}{J_{net}V_1} \approx \eta_{Carnot} \quad (V_1 \gg kT) \quad (1)$$

where the output term, electric power, is the net current times the difference in the emitter and collector voltage barriers. The input term is simply the energy involved in elevating the elec-

trons to the higher energy levels so that the current can flow over the potential barrier. If the potential barrier is large in comparison with the kinetic energy of the electrons in transit, and if the barriers V_1 and V_2 are adjusted to match the absolute temperature ratio, the Carnot cycle efficiency is approached. These highly idealized conditions neglect the ever-present loss terms. Figure IX-2 removes us from this never-never land of ideality into the reality of the actual thermionic device.

The dictates of the energy source require high power densities, thus, high current densities. At the present time, the high current densities require high emitter temperatures to produce the necessary flow of electrons. In order to sustain the high current densities, a partially ionized gas must be introduced into the interelectrode space. Electron scattering then exists. Radiation transport becomes significant because of the large temperature difference. Gaseous thermal conduction in the interelectrode space also results. Ion flow negates some of the electron current and also transports energy. In order to extract the electric power, leads must be attached to the hot and cold electrodes. Excessive heat is conducted if the lead is too big, or excessive voltage losses if the lead is too small.

The expression for efficiency departs from the Carnot-like expression of equation (1) to the practical expression of efficiency of equation (2):

$$\eta_{el} = \frac{(J_{net})(V_1 - V_2 - \Delta V)}{J_1(V_1 + 2kT_1) - J_2(V_1 + 2kT_2) + \Sigma \dot{Q}} \neq \eta_{Carnot} \quad (2)$$

The difference between the expressions in the numerator involves a voltage drop and a correction to the net current that accounts for electrical leakages. The denominator increases because of the need to recognize kinetic energy of the electrons and the summation of the many losses enumerated above.

The highly optimistic approach, in which only the first-order constraints of the various physical constants of the materials available to thermionics are used, predicts an efficiency somewhere between one-half and two-thirds of the Carnot-cycle efficiency. In practice, because of some yet inescapable plasma voltage losses, practical converters are achieving only a bit over one-third of the Carnot-cycle efficiency. Even though the present-day fraction of Carnot efficiencies of thermionic energy conversion are not amongst the highest, certain features of thermionics are attracting interest for the potential application to a nuclear energy source, particularly for space application.

Some of these qualities are illustrated in the next few figures. An elaborate nuclear thermionic design is not illustrated. Instead a simplified design has been selected, mainly to demonstrate the basic principles and problems of in-pile nuclear thermionics. However, some of the details of the converter element design do employ practices found useful in research converters. The three main parts of the system are reactor, shield, and radiator (fig. IX-3). The radiator is considerably smaller than other space power systems, since the operating temperatures are higher. Segmented radiators coupled with similar segmented reactor elements are suggested. Each one of the reactor segments is further subdivided into unit thermionic cells (fig. IX-4). The cells are mounted in a tray and are cooled by liquid metal flowing across the tray similar to the

usual crossflow heat exchanger. The arrangement shown has two cells connected in series in each cylindrical station. Each double converter module should develop about $1\frac{1}{2}$ volts. Conceptually, one can visualize the thermionic reactor as a group of $1\frac{1}{2}$ volt batteries connected in some series, parallel network to provide both the necessary voltage and current and to provide reliability through redundant cross connections.

The detail of an individual cell is shown in figure IX-5. Nuclear fuel such as uranium dioxide is introduced in the center. A vented fuel capsule is shown. The encapsulated fuel is electrically isolated by an insulator. The fuel cladding then serves as an electron emitter. The electrons flow to the collector, which is typically a trilayer tube constructed of a thin layer of aluminum oxide sandwiched between layers of niobium. The trilayer tube simultaneously serves as the collector surface, current lead, and heat-exchanger surface. It is cooled by liquid metal as was discussed previously. Cesium gas is introduced into interelectrode space by the use of a cesium reservoir or cesium dispenser material.

The main advantage of the in-pile thermionic conversion system is the high source temperature of this heat engine. The nemesis of most space power is the temperature limit imposed by the liquid-metal corrosion limit and/or the high-temperature strength characteristics of materials. This limitation is avoided by not exposing the liquid metal to the high-temperature source. Instead, the liquid metal is only exposed to the collector, which is at the point of heat rejection. The high-temperature zones can be lightly stressed since the high-temperature surfaces are exposed only to a very low pressure ionized gas. The other attractive feature of this system is the modular design. The modular design offers reliability through redundancy and eases testing problems. The system subdivides into a series of building blocks such as radiators, reactor compartments, and individual cells. Designs like the one illustrated permit out-of-pile testing of the individual cells and groups of cells. The individual thermionic cells can also be introduced into a test reactor for studies of the nucleonic interactions. It has been said that the scaling by multiplicity feature of thermionics permits the development of a power system with a nuclear source that has many of the advantages photovoltaics has provided the solar source. The disadvantages are fairly obvious. The reactor design and fabrication certainly are not simple.

The reactor complexity can be avoided by an alternate approach in which the thermionic converters are external to the reactor, as shown in figure IX-6. A conventional compact liquid-metal-cooled reactor is used. The hot liquid metal is circulated through a thermionic heat exchanger. The heat is rejected through an additional liquid-metal loop to the radiator. Thermionic conversion is achieved in a multipassage heat exchanger. The system illustrated uses an insulated trilayer inner tube that houses the high-temperature liquid metal and also acts as the electron emitter (fig. IX-7). The second trilayer tube houses the ionized gas needed for the converter, serves as a collector, and is sectioned to provide a series of individual thermionic converters. The annulus formed by the outside tube and the second trilayer tube contains the liquid-metal coolant. Many variations of external thermionics exist. This system is not necessarily advocated but merely illustrates some of the more obvious features of external thermionics. The advantages of a simple reactor approach coupled with modular thermionics exist but, unfortunately, the liquid-metal loop is exposed to the reactor fuel temperature. Thus, the system is limited to low source temperatures, a region somewhat unattractive to the electronics of thermionics. Also, from a safety view, if the fuel cladding ruptures, the liquid-metal loop may be con-

taminated with fission products.

If a system analysis is made for either the in-pile or out-of-pile thermionic approach, the performance levels for the converters required to make the system competitive to other power systems becomes established. Roughly, the net power (numerator of eq. (3)) should exceed 5 watts per square centimeter at 2600° F and should exceed 10 watts per square centimeter at 3000° F. The efficiency should approach or exceed 30 percent of the Carnot cycle efficiency, as shown in equation (3):

$$\eta_{el, av} = \frac{(J_{net})(V_1 - V_2 - \Delta V)}{J_1(V_1 + 2kT_1) - J_2(V_1 + 2kT_2) + \Sigma \dot{Q}} \gg 30 \text{ percent of Carnot} \quad (3)$$

The remainder of this paper treats the probability of achieving the required efficiency indicated in equation (3), the power densities, and the operating life (at the high temperatures involved) from the viewpoint of basic surface and plasma physics, empirical converter performance, reactor interface problems, and thermionic reactor limitations.

SURFACE PHYSICS

The physics of thermionic energy conversion reduce to the problem of getting the electrons out of the emitter, across the interelectrode gap, and into the collector efficiently. Figure IX-8 shows the problem of getting the electrons out of the emitter. The high temperatures involved in thermionics require the use of refractory metals. Unfortunately, the same interatomic forces that hold a metal together also bind the electrons to the surface. This electron affinity is described quantitatively by the electron work function, which is so named because the term expresses the work required to extract an electron from the surface. The electron emission rate equation, $J = 120T^2 \exp - \phi/kT$ ampere per square centimeter, is the Richardson-Dushman equation. Using a typical work function for tungsten and plugging in a temperature of 1923° K (3000° F) results in an emission current density of only 0.4 milliampere. Therefore, the work function must be lowered to provide for more emission. This is achieved usually by depositing a partial layer of a low work function metal over the surface of the refractory emitter. Practical thermionic converters usually use cesium. The low work function layer is maintained by continuously flooding the emitter surface with cesium gas.

An interesting and fortunate characteristic of the adsorption process is that the higher the work function, the more refractory the metal, the stronger the cesium attachment to the surface (refs. 1 and 2). An experimental correlation recently noted by the Field Emission Corporation (ref. 3) illustrates this effect (fig. IX-9). The bare work function, that is, the metallic surface, free of any adsorbed particles is the abscissa. The maximum change in work function that can be produced by adsorbing cesium on the surface is given in the upper ordinant. The change in work function overcompensates for the initial high value of the substrate, so that the lowest value of work functions of cesiated surface are achieved with the surfaces that have the highest initial bare work function. The field emission experiments used in obtaining these data permitted

the identification of individual crystal planes. It was noticed that this correlation held for individual crystal index planes of the same metal, and indeed a tungsten surface, oriented to expose a 110 Miller index plane, is one of the more desirable surfaces for the cesium adsorption and retention process. This field emission study and other similar research (refs. 1, 2, and 4) indicate that high work functions are desired not only for the minimum work function but at the intermediate work function values used in practical thermionic converters.

Some idea of the nature of the substrate surface as a function of the crystallographic orientation can be obtained from simple models of the surface. Figure IX-10 shows some of the results of a model based on interaction of a test particle with an array of substrate atoms arranged to give a particular surface orientation (ref. 5). Two surfaces of a body-centered cubic crystal typical of tungsten, tantalum, and molybdenum are shown. The surfaces treated are a 110 surface that corresponds to a slice through the crystal that intercepts the center atom in the crystal. The 100 plane corresponds to the face of a cubic crystal. If an interaction potential corresponding to an attractive and repulsive force that is inversely proportional to the sixth and twelfth power of the distance between particles, respectively, is assumed to exist between the test particle and all the atoms of the substrate and, if a lattice constant and test particle size of σ/a are chosen to match the surface and adsorbate dimensions, topographical potential plots of the surface can be generated. Each contour line corresponds to a constant adsorption energy. The 110 plot shown is not for the entire surface of a unit cell but only for that fraction outlined by the dashed lines in the crystal. The rest of the pattern is repetitive across the 110 face. From these contour plots, relative surface diffusion barrier heights, relative adsorption energies, and number of adsorption sights can be deduced. Various interactions potentials can be assumed. The 6-12 interaction potential used is a convenient mathematical expression that satisfies many of the physical experimental observations.

The results of this analysis indicates the 110 tungsten plane is of interest to thermionics because it provides a large number of adsorption sights with relatively strong adsorption energies and, furthermore, should be thermally stable in terms of self-diffusion.

Recent experimental developments permit a detailed examination of the stability of the surface layer. Table IX-1 presents the results of some of these studies of surface layers by the low-energy electron diffraction (LEED) technique (ref. 6 and data obtained by H. E. Farnsworth et al. under NASA Grant Nsg 373). Information on the initial surface layer and adjacent sublayers can be obtained by changing the energy of the incident electron and observing the intensity of the diffracted beam pattern. Several monocrystals of tantalum, molybdenum, and tungsten have been examined. The crystals were cut so that the 110 and 130 Miller index planes were parallel to the surface. Several temporary surface structures were produced on these crystals. The 130 and 310 surfaces on the tantalum were developed by ion bombardment. The 130 surface of molybdenum was produced by cutting followed with appropriate surface treatment. The 110 surface of molybdenum appeared naturally after heating because of the substrate orientation. The tungsten sample was ion bombarded, and a random surface orientation resulted. The crystals that had a bulk orientation of 110 reoriented to a 110 surface after thermal annealing in vacuum at temperatures close to those experienced in a practical thermionic converter. The molybdenum sample with a 110 bulk orientation maintained a 110 orientation through to the surface even after extensive heat treatment. The crystal with a 130 bulk orientation relaxed

back to the 100 and 110 surface planes as would be expected from free-energy considerations of the surface and crystal. Therefore, it appears that the 110 oriented surface can be produced and maintained in vacuum if the bulk orientation is 110. Although these encouraging results can be obtained from small zoned refined monocrystalline samples, the question remains can we reduce this approach to actual practice? For example, can the oriented surfaces be established on the surface of a cylinder?

Recently developments in tungsten fabrication by vapor phase deposition of tungsten is one approach that is quite promising in this regard. Tubes such as shown in figure IX-11 have been routinely, though not always reproducibly, fabricated by vapor deposition. The vapor-deposited tubes are near theoretical density, leak tight, exhibit good structural properties, and, if required, can be deposited in quite complex shapes. The vapor deposition involves hydrogen reduction of a tungsten halide on the heated mandrel. It has been observed that if tungsten hexachloride is used, the bulk sample exhibits a strong 110 orientation parallel to the surface of the mandrel. For tungsten hexafluoride, a 100 bulk orientation results. Photomicrographs (obtained by L. Yang, General Atomic Div. General Dynamics Corp., under NASA Contract NAS 3-8504) of the chloride and fluoride tungsten products after heat treatments are shown in the lower part of figure IX-11. The tungsten hexafluoride samples with their small columnar grain structures should exhibit superior mechanical properties except that the noninterrupted columnar grain boundaries that propagate through the metal may enhance mass diffusion, as will be discussed later in this paper. A series of preliminary tests were performed on a group of vapor-deposited disks (ref. 7) to see if the bulk orientation affected the surface orientation in the same manner as observed in the small zone refined monocrystalline studies (table IX-2). The surface was characterized in terms of the thermionic emission work function. The vapor-deposited tungsten surfaces produced by careful grinding, polishing, and thermal treatment reflected the bulk orientation as determined by work function measurement. Consistently the tungsten fluoride product samples of the 100 orientation gave the lower work functions than the samples with a 110 bulk orientation. A series of surface treatments was made on samples, including additional thermal treatment, chemical etch and electrochemical etch. The various treatments changed the surface work function but, after high-temperature thermal treatment, all samples relaxed back to the initial work function with the exception of one. Thus, the results on practical surfaces were consistent with the LEED studies. The duplex sample was a single exploratory test to determine if the desirable structural properties of the fluoride product could be combined with the desired surface properties of the chloride product. Some hope exists, for this approach, as evidenced by the high surface work function.

It is assumed herein that the desired thermionic emitter possesses a high substrate work function because of the consistent observations that better cesium adsorption properties result with the high substrate work functions.

Additional adsorption studies are being conducted as part of the NASA thermionic program. The analytical work includes calculations of the binding energies of various adsorbates (refs. 5, 8, 9, and 10), two-species adsorption theory (ref. 11)(e.g., tungsten on cesium), and multiple-species adsorption, where the adsorption of cesium, barium, or strontium on oxidized and fluorided surfaces has been analyzed (refs. 12 to 14). Experimentally, adsorption has been studied by field emission, as was shown in figure IX-9. Molecular beams of cesium, oxygen,

and fluorine have also been utilized to examine the details of dual-species (ref. 15) and multi-species (ref. 16) adsorption. It is interesting to note that oxidizing or fluoriding the surface of refractory metals tends to increase work functions which, in turn, improve cesium adsorption characteristics. The observation that high substrate work functions improve cesium adsorption is again verified even for complex surfaces, a point noted in the development of photoemissive surfaces many years ago. Reproducibility of the additive studies of oxygen and fluorine in the high-temperature, high-current conditions found in thermionic converters is extremely difficult to obtain, however.

The final evaluation still resides in tests in the actual environment of the thermionic converter. Figure IX-12 illustrates experimental results of the now well-documented tungsten-cesium adsorption system obtained in a research-type thermionic converter. A tungsten emitter whose bulk orientation is basically 110 was used. Current density is plotted as a function of cesium pressure. The curves presented for two emitter temperatures are based on experimental data and are fared through the use of an analytical expression (unpublished data of R. Breitwieser of Lewis Research Center). Current densities as high as 100 amperes per square centimeter have been observed by pulse measurements at the higher cesium pressures.

PLASMA CONSIDERATIONS

The unambiguous demonstration of the stability of a 110 tungsten surface at high-temperature, high-current conditions has not been established. It has been verified, however, that more than adequate emission currents are available in a diode if the cesium pressure is sufficiently high. In terms of relative particle flux, it is interesting to note that, at the high-current conditions, 3 to 6 cesium atoms must arrive at the surface per unit time for every electron that is emitted from the same surface. Spacings in a converter, therefore, must be small to avoid electron-atom scattering. Methods exist for getting electrons out of the emitter. The problem remains, however, of getting electrons across the interelectrode space. Figure IX-13 illustrates some of the problems in getting electrons across, and the following outline presents part of the associated research program:

Space charge:

- (1) Application of Langmuir theory to electrons and ions
- (2) Two-species theory
 - (a) Ion and electron current - voltage curves
 - (b) Stability analysis

Elastic scattering including space charge:

- (1) Isotropic collisions
- (2) Energy-dependent and angular-dependent collisions

Cross section:

- (1) Atom-atom
- (2) Atom-ion
- (3) Atom-electron

If no ions are present in the interelectrode space, a large space-charge barrier develops, so that the electron flow is reduced to a mere trickle. For example, an emitter that has an emission capability of over 100 amperes per square centimeter will have all but 1 milliamperes of its

current reflected back to the emitter by the space-charge barrier if the interelectrode space is 1 millimeter, if no ions are present, and if the acceleration potential across the surfaces is restricted to 1/2 volt. Ions formed at the surface will reduce the space-charge barrier but, with the exception of thermionic converters which use very high source temperatures, the rate of surface ionization does not produce enough ions to permit the transfer of significant electron currents. The surface ion formation mechanism is now quite well understood (ref. 17), as are the modifications to the space-charge theory which include ions as well as electrons. The ion and electron transport is understood for steady-state conditions (refs. 18 and 19) and in terms of transient stability analyses (ref. 20).

The transmission of a substantial fraction of the emitted current requires that ions be produced in the interelectrode space. It follows, therefore, that some of the energy of the emitted electrons must be diverted to produce the ions. A voltage drop results because of both elastic and inelastic electron scattering. The elastic scattering randomizes the directed velocity of the electron, whereas the inelastic collisions absorb energy of the incoming electron by the excitation or ionization of the target atoms. The elastic scattering process is at a reasonable level of understanding. A new technique exists by which the complexity of the simultaneous effects of space charge, energy-dependent cross sections, and angular-dependent elastic cross sections can be treated to generate theoretical current-voltage curves for thermionic converters (ref. 21 and unpublished data of C. M. Goldstein). A variation of a Monte Carlo transport analysis is used.

As mentioned, experimental and analytic information on the various collision cross sections are being obtained in support of this effort. The atom-atom (ref. 22), atom-ion (refs. 23 and 24), and atom-electron (ref. 24) cross sections are under study. The application of cross section data can be seen in the effect of argon on the elastic scattering of electrons, presented in figure IX-14. Argon exhibits an electron-neutral cross-section minimum in the near-thermal energy range; this effect is called the Ramsauer effect. This strongly energy-dependent cross section provides a stringent analytic exercise when used in electron transport analysis as well as an interesting possible gaseous additive for a thermionic converter. Argon minimizes ion losses by reducing mobility and, thus, wall recombination. Relatively large ion-neutral cross sections compared with the small electron-neutral cross sections in the Ramsauer region provide the needed mechanism.

The current voltage characteristics (in dimensionless units) have been compared with the noncollisional space-charge solution. The collision parameter refers to the product of pressure (in torr) and distance (in cm). These data were calculated by the aforementioned Monte Carlo analytical method (unpublished data of C. M. Goldstein). The slight negative current-voltage slope is caused by the Ramsauer minimum in the energy-dependent cross section. The current reduction of argon is small in comparison with gases such as cesium because of the small cross section in the near thermal range. The analyses in their present forms are merely a first step in the attempt to provide a rigorous, analytical treatment for electron transport that can account for the detailed nature of the electron-neutral collisions and space-charge interactions. As yet, the method has not been used in treating the inelastic portion of the scattering processes although, with additional effort, the approach appears to be completely feasible, although more experimental information on the nature of the emitter sheath would be helpful. Since the details

of getting the electrons across the interelectrode space are not understood as yet because of the yet undetermined inelastic effects, the thermionic field has relied on empirical observations of plasma drops. Lewis results (unpublished data of R. Breitwieser and W. Rush), which are quite consistent with the results of others (ref. 25), indicate that voltage drops of greater than 0.4 volt are always present in the volume ionization mode of practical converters. Voltage drops greater than this minimum exist when the collisional activity is high and can be correlated with the electron-neutral atom collision frequency or, more simply, with the product of gas pressure and interelectrode spacing.

COLLECTOR EFFECTS

Figure IX-15 summarizes a portion of the previous discussion and introduces the problem of getting electrons into the collector. It indicates the approximate type of work function required to achieve the required electron current density from the emitter. The type of plasma sheath and the minimum plasma drop involved in the ignited or volume ionization mode of operation, which involves the aforementioned inelastic collisions, is also in figure IX-15, as well as the type of collector sheath and collector work functions that are needed for the output voltages of a practical thermionic diode. The following collector problems relate first to the confusion of the nature of the collector sheath:

Collector sheath:

- Emission spectroscopy (line shift)
- Laser diagnostics (improved spatial resolution)
- Langmuir probe studies

Adsorption processes:

- Analytical (emphasis on low work function region)
- Experimental (field emission, molecular beam, and diode work)
- Contamination (collector surface "cold" trap impurities)

At times, the ineffectiveness of thermionic conversion is attributed to the collector surface although it is actually because of the properties of the plasma sheath adjacent to the collector. Attempts to strengthen the analysis of the sheath problem are being made by evolving new diagnostic tools that provide the spatial resolution needed to probe the sheath. This first step relates to a definition of the central plasma properties. The line shift method of emission spectroscopy suggests some simplifications in this regard (ref. 26). The laser, with its excellent optical resolution, is being developed as a probe (ref. 27). Recognition of the relation of the refractive index of a plasma to electron density is the principle of the laser plasma probe. Advances in Langmuir probes through miniaturization are being made also (ref. 28). In addition to the problems related to the uncertainties of the sheath at both the collector and emitter, all the adsorption processes must be controlled again to produce the desired collector work function. The emphasis is on a lower work function for the collector. If the allowed operating temperatures, the various potential barrier heights required for the emission of the current densities of interest, and the plasma drops present in the group of converters of the day are considered, the collector work function should be less than 1.8 electron volts to prevent serious in-roads into the output potential of the

devices; for low-temperature thermionics, the lower the better. The adsorption processes are complicated since a single gas pressure exists in the interelectrode space, and it is necessary to attempt to optimize the coverages on both the emitter and collector surfaces with a closely linked arrival rate of the adsorbing species. The inability to achieve low work functions (less than $1\frac{1}{2}$ eV) is one of the contributing reasons for the rapid decay of the performance of thermionics at low operating temperatures. An additional serious collector problem is related to the fact that the collector is the major cool surface in a converter. The collector not only collects electrons, but the various contaminants in the diode as well. The collection of diode debris may seriously affect the adsorption processes, as illustrated in figure IX-15; the debris is represented by the black dots.

The sketch is not pure fiction. Examination of many thermionic converters gives strong visual evidence of collector deposits. The severity of the collector deposits is of course related to the outgassing techniques used in diode preparation, emitter and collector materials, possible nuclear fuel clad interactions, and, in general related to the entire physical-chemical high-temperature stability of the converter assembly.

Diffusion of the nuclear fuel through the emitter clad is a source of collector contamination that has received major attention, since the fuel cladding may not exhibit long-time, high-temperature stability with some of the proposed fuels.

The electron reception characteristics of the collector are affected by extremely small amounts of contamination, since a fraction of an atomic monolayer of contaminant may influence the collector adsorption process. Carefully controlled out-of-pile tests have been used to obtain quantitative information on the rates of diffusion through simulated fueled emitters (table IX-3). The amount of uranium contamination on a cold surface adjacent to a simulated thermionic emitter containing nuclear fuels was measured by either activation analysis or alpha counting. The amount of uranium deposited expressed in terms of equivalent atomic monolayers is shown for 90 mole percent uranium carbide - 10 mole percent zirconium carbide (ref. 30) and uranium dioxide (ref. 31). Two tungsten clads were evaluated for the uranium dioxide. The greatest rate of diffusion was observed for the uranium carbide - zirconium carbide fuel. A possible problem in the use of vapor-deposited tungsten is suggested by the higher rates of uranium diffusion as compared with the powder metallurgy product tungsten. The vapor-deposited tungsten was produced from tungsten hexafluoride and possessed the usual columnar grain structure. The large number of columnar grain boundaries propagating through the clad undoubtedly enhanced fuel diffusion rates. Proper selection of fuel type and cladding promises to minimize the amount of contamination to levels where the use of getters, or natural absorption characteristics of collector materials can accommodate low rates of material transport.

CONVERTER PERFORMANCE

Having traced our way across the converter and having established some of the thermionic converter problems, the next few figures deal with the reduction to practice of the aforementioned research. Figure IX-16 shows the latest type of research converter, which is undergoing preliminary orientation tests prior to in-pile evaluation. The planar configuration was chosen to provide for ease in instrumentation and ease in evaluating new design approaches. The emitter

consists of duplex vapor-deposited tungsten bonded on tantalum. The emitter is essentially identical to the duplex sample referred to in table IX-2. The tungsten formed from the tungsten chloride (WCl_6) is on the outer surface to provide for the beneficial adsorption properties of a high work function material. The inner layer formed from tungsten fluoride (WF_6) is presumed to give better structural properties. The collector is a niobium - niobium alumina cermet - niobium trilayer. The niobium cermet serves as an electrical insulator between the emitter and the collector and as an electrical insulator between the collector and the heat sink. The niobium cermet is only 23 mils thick; thus, it is a good thermal conductor. The cermet is made by hot isostatic pressing of niobium spheres that were precoated with high-purity alumina. The vapor-deposited alumina coatings were graded to provide for an increasing alumina concentration toward the center of the cermet. The dark areas in the photomicrograph in figure IX-16 correspond to the alumina, and the light areas correspond to the niobium. The cold resistance of the cermet is typically greater than 10 megohms for a 1-square-centimeter sample. Initial tests of the diode are in process. The collector properties, in terms of structural reliability, and thermal and electrical characteristics are very encouraging. The emitter has indicated favorable structural stability during the initial series of thermal annealing and degassing processes. To date, cesiated performance has not been obtained.

Figure IX-17 presents results of the electrical performance of converters that reflect the technology of the 1964 - early 1966 time period. Power densities observed at conditions corresponding to maximum efficiency are shown as a function of emitter temperature for the converters. The higher performance corresponds to data obtained in a research-type converter built in late 1965 and early 1966 (obtained by J. Lawrence under NASA Contract NAS 3-8511). The lower performance data, indicated by data points, are typical of converters fabricated about 2 years ago and used in tests evaluating the life of thermionic converters (ref. 32). Tungsten emitters and niobium collectors were used for both groups of converters. Insufficient documentation of the detailed properties of the emitter and collector processing, as well as some questions of data accuracy in the life-test converters, precludes a quantitative explanation of the difference in performance. The performance curve is typical of the carefully processed thermionic converter being tested presently and is a conservative example. Several performance mappings of converters tested during the first half of 1966 indicate even higher performance.

Typical performance values of the research converter are: output voltage at 2000°K is 0.7 volt, efficiency of approximately 15 percent. At the temperature ratios used, the efficiency is about 30 percent of Carnot cycle efficiency. The ability to produce single converters that exhibit useful power levels and efficiencies has been demonstrated. The ability to assemble large groups of high performance diodes, as projected in systems studies, remains to be proven.

The problem of reliable operation has undergone examination in both in-pile and out-of-pile thermionics. Tables IX-4 and IX-5 present typical out-of-pile results. The results (ref. 32) summarized in table IX-4 are from cylindrical diodes electrically heated to 2100°K with a power density of 7 to 11 watts per square centimeter and an efficiency of 12 to 13 percent throughout the tests.

The 300 series diodes used vapor-deposited tungsten emitters supported on tantalum sleeves.

All failed for the same reason, fracture of a tantalum sleeve. The 400 series diodes used a tungsten - 25-percent-rhenium alloy emitter and included unenriched uranium dioxide sandwiched into the emitter structure. These diodes shorted because of deformation of the emitter structure. A similar set of tests conducted at General Atomic (ref. 30) explored further the effect of unenriched fuel sandwiched in cylindrical emitters (table IX-5). The operating conditions and method of heating were essentially the same as the table IX-4. LC-1, LC-5, and LC-6 incorporated uranium carbide - zirconium carbide fuel and suffered from significant performance degradation. LC-2 and LC-3 contained a tungsten - uranium dioxide cermet, and LC-4 was a fuel-free control diode. Although performance levels could be maintained for the noncarbide tests, the cesium reservoir temperature had to be reset to maintain peak performance. No self-consistent major failure mode was observed. The collector deposits resulting from the uranium carbide emitter interaction increased radiation heat transfer and increased the collector work function and, thus, degraded performance consistently.

REACTOR FUEL

In order to broaden the perspective of nuclear fuel - thermionic converter interactions, table IX-6 presents some of the gross features of typical fuels. High uranium content implies reduced reactor core size, high thermal conductivity reduces temperature gradients in the fuel, and high vapor pressure may induce fuel loss. Uranium carbide has the desirable characteristics of high uranium density, high thermal conductivity, low vapor pressure, and it is quite refractory. A highly refractive, fully dense fuel tends to inhibit fission gas release and cause fuel swelling. Fission gas evolution will probably be treated through controlled porosity of the uranium carbide fuel so that the fission gas can be released and vented.

Uranium dioxide has a moderate uranium density, a low thermal conductivity, and a higher vapor pressure than the carbide fuel. At high temperatures, uranium dioxide is somewhat plastic and does not contain fission gas; thus, the fission gas may be released and vented.

The uranium content of the uranium dioxide - tungsten cermet is lowered by the tungsten, the conductivity is improved, and, if the tungsten is used to enshroud the uranium dioxide, vapors are contained. Fission gas containment is also aided by the tungsten.

Some of the nuclear fuel problem can be directly deduced from the fuel and clad properties without in-pile testing. Subsequent figures illustrate a few of the problems.

Emitter clads for thermionics operate in the temperature range where the clads have low strength. It is necessary, therefore, to consider methods for minimizing the pressure buildup of the fission gases. For a fuel such as uranium carbide - zirconium carbide, a fuel body is developed that has a fine-grain, interconnecting pore structure. The fission gases generated in the fuel can then diffuse to the pores and subsequently vent out of the fuel body. The problem with this approach is that, at high temperatures, materials tend to sinter and fill voids. Figure IX-18 shows the results of the preliminary tests in which the uranium carbide fuels tend to sinter (private communication from L. Yang). The interconnected porosity determined by a gas adsorption method was measured for two fuels at 1000 and 2000 hours at 2100° K. The results

indicate that considerable and unattractive dilution of the uranium content of the fuel by the highly refractory zirconium carbide is required to stabilize porosity. Unless thermionic converters can be built to operate effectively at lower temperatures, the tendency to sinter with the consequent threat of fuel swelling exists for uranium carbide.

Uranium dioxide releases its fission gases at high temperatures in the plastic flow range. At these conditions, however, vapor loss of uranium dioxide poses a problem. If a 2100° F cylindrical emitter fueled with uranium dioxide were only partly encapsulated so that one end was left open to vent fission gases, most of the fuel would be lost in an operating time of 1 year. Figure IX-19 presents calculations (data obtained by R. Breitwieser) of uranium dioxide vapor loss through orifices and tubes sized to prevent fission gas pressure buildup and at the same time sized to reduce uranium dioxide vapor loss to an acceptable level. The suggested method notes that the stable location for void volume in uranium dioxide is in the highest temperature zone. A small orifice at the end of a tube penetrating this void volume is presumed to remain open for the temperature-time relations shown in figure IX-19. A 10-mil orifice will restrict the weight loss to low values over an appreciable range of temperatures. The weight loss can be reduced further by the use of a capillary tube in place of an orifice, and minimized still further by reducing the mobility of the uranium dioxide through the use of an inert cover gas such as argon. If the reliability of the small vents is questionable, the cover gas and or tube approach permits the use of significantly larger inside diameter tubes within the framework of acceptable uranium dioxide losses.

The alternate to venting uranium dioxide is the containment of fission gases. A cermet, consisting of small uranium dioxide particles clad in tungsten in which the tungsten and the uranium dioxide share the burden of containing the fission gases, is such a possibility. Also, the tungsten in the cermet increases the thermal conductivity and, therefore, reduces the temperature variation across the cermet fuel, which in turn improves uranium dioxide fission gas retention. An estimate of the temperature where it may be possible to retain the fission gases at useful power density and burnup is given in figure IX-20.

The calculation is based on the local stress limits of the tungsten wrapped around the uranium dioxide particle. The fuel volume is reduced by increasing the proportional amount of tungsten as stress limits are encountered. Additional assumptions include the following:

- (1) Spheres of uranium dioxide coated with 3 microns of tungsten
- (2) Tungsten fraction increased by decreasing uranium dioxide particle size
- (3) Coated spheres arranged in a closely packed hexagonal array
- (4) Creep limit of 1 percent for tungsten in 10 000 hours
- (5) Fission gas releases of 5 and 50 percent in uranium dioxide at 1800° and 1900° K, respectively

Figure IX-20 shows that, at the limiting fuel temperature for either of the two fuel burnups, an increase of 70° K requires that tungsten be added in the amount to drop the fuel volume fraction 30 percent. The reason for this strong dependence is the increased release of fission gases with increasing temperature and the rapid dropoff of the creep strength of tungsten with temperature. As expected, burnup is an important factor in the determination of limiting fuel temperature.

An additional problem with uranium dioxide - tungsten cermet has been its dimensional

stability on thermal cycling. This characteristic is often present in composite materials of mixed tensile and yield strengths. Uranium dioxide - tungsten cermet specimens clad with tungsten have been thermally cycled by electric heating from room temperature to approximately 2000° K for 100 cycles. Insufficient data have been obtained to correlate cracking with fabrication procedure. Figure IX-21 gives the extent of dimensional change for three specimens (data obtained from Battelle Memorial Institute under NASA Contract NAS 3-4255). One of the nonfractured specimens exhibited less than 1 percent growth but, again, the insufficient experimental statistics exist to define specific fabrication procedures that would ensure dimensional stability.

These results reflect the uncertainties in much of thermionics. No fundamental roadblocks to a successful system development are apparent. There are many individual cases of excellent structural characteristics, fuel stability, and converter performance, which all lead to logical system design and testing concepts. However, the small number of tests and the statistical scatter of results certainly indicate the need for more extensive and more controlled testing of many subparts of this potentially attractive space power system.

REFERENCES

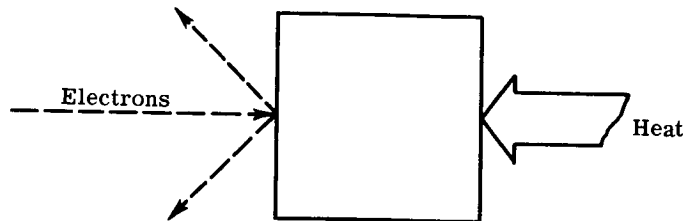
1. Levine, J. D.; and Gyftopoulos, E. P.: Adsorption Physics of Metals Partially Covered by Metallic Particles. III. Equations of State and Electron Emission. *Surface Sci.*, vol. 1, no. 4, 1964, pp. 349-360.
2. Razor, Ned S.; and Warner, Charles: Correlation of Emission Processes for Adsorbed Alkali Films on Metal Surfaces. *J. Appl. Phys.*, vol. 35, no. 9, Sept. 1964, pp. 2589-2600.
3. Bennette, C. J.; Strayer, R. W.; Swanson, L. W.; and Cooper, E. C.: Behavior of Various Adsorbates on Metal Substrates. Final Rep. (NASA CR-54704), Field Emission Corp., Feb. 18, 1966.
4. Houston, J. M.; and Webster, H. F.: Thermionic Energy Conversion. *Advance in Electronics and Electron Physics*. Vol. 17. L. Marton and Claire Marton, eds., Academic Press, 1962, pp. 125-206.
5. Bacigalupi, Robert J.; and Neustadter, Harold E.: Dependence of Adsorption Properties on Surface Structure for Body-Centered-Cubic Substrates. NASA TN D-3141, 1965.
6. Boggio, J. E.; and Farnsworth, H. E.: Low-Energy Electron Diffraction and Photoelectric Study of (110) Tantalum as a Function of Ion Bombardment and Heat Treatment. *Surface Sci.*, vol. 1, no. 4, 1964, pp. 399-406.
7. Anon: Studies of Thermionic Materials for Space Power Applications. Rep. No. GA-7244 (NASA CR-72043), General Atomic Div., General Dynamics Corp., July 15, 1966.
8. Neustadter, Harold E.; and Luke, Keung P.: Low-Coverage Heat of Adsorption. I - Alkali Metal Atoms on Tungsten; Atom-Metal Interaction Theories. NASA TN D-2430, 1964.

9. Neustadter, Harold E.; Luke, Keung P.; and Sheahan, Thomas: Low-Coverage Heat of Adsorption. II - Alkali Metal Atoms on Tungsten; Lennard-Jones Atom-Atom Interaction Theory. NASA TN D-2431, 1964.
10. Neustadter, Harold E.; and Luke, Keung P.: Low-Coverage Heat of Adsorption. III - Alkali Metal Ions on Tungsten; Atom-Metal Interaction Theory. NASA TN D-2460, 1964.
11. Luke, Keung P.; and Smith, John R.: Theoretical Study of Zero-Field Electron Work Function of Metal Immersed in Gas-Direct Application to Cesium Thermionic Diode. NASA TN D-2357, 1964.
12. Tower, Leonard K.: The Erected Dipole Model in the Adsorption of Cesium on Fluorinated Molybdenum. NASA TN D-3223, 1966.
13. Tower, Leonard K.: A Preliminary Analysis of the Process of Desorption of Multiple Additives from Metals. Paper Presented at the IEEE Thermionic Conversion Specialists Conference, San Diego, California, Oct. 25-27, 1965.
14. Tower, Leonard K.: Desorption Kinetics of Multiple Adsorbates - Cesium with Fluorine on Molybdenum and Tungsten. NASA TN D-3596, 1966.
15. Stickney, R. E.; and Bergman, J. G.: Effect of Fluorine and Oxygen on Thermionic Emission from Polycrystalline Tungsten. 26th Annual Conference on Physical Electronics, Massachusetts Institute of Technology, Mar. 21-23, 1966.
16. Stickney, R. E.; and Fehrs, D. L.: Retarding Potential Measurements of the Work Function of Tantalum as a Function of Cesium Coverage. 26th Annual Conference on Physical Electronics, Massachusetts Institute of Technology, Mar. 21-23, 1966.
17. Breitwieser, Roland; and Rush, Wayne: Saha-Langmuir Surface Ionization Relation. Paper Presented at the IEEE Thermionic Conversion Specialists Conference, San Diego, California, Oct. 25-27, 1965.
18. Goldstein, C. M.: Theoretical Current-Voltage Curve in Low-Pressure Cesium Diode for Electron-Rich Emission. J. Appl. Phys., vol. 35, no. 3, pt. 1, Mar. 1964, pp. 728-729.
19. Goldstein, C. M.: Theoretical Current-Voltage Curve in Low-Pressure Cesium Diode for Ion-Rich Emission. Paper Presented at the IEEE Thermionic Conversion Specialists Conference, Gatlinburg, Tennessee, Oct. 7-9, 1963.
20. Burger, P.: Computer Simulation Methods for Plasma Diodes with Collisions. Paper Presented at the IEEE Thermionic Conversion Specialists Conference, San Diego, California, Oct. 25-27, 1965.
21. Goldstein, Charles M.: Monte Carlo Method for the Calculation of Transport Properties in a Low-Density Ionized Gas. NASA TN D-2959, 1965.
22. Sheldon, John W.; and Manista, Eugene J.: Atomic Beam Determination of the Cesium-Cesium Total Scattering Cross Section. NASA TN D-3160, 1965.

23. Sheldon, John W.: Semiclassical Calculation of the Differential Scattering Cross Section with Charge Exchange: Cesium Ions in Cesium Vapor. NASA TN D-2484, 1964.
24. Bullis, R. H.; and Flavin, R. K.: Research on the Collision Probabilities of Electrons and Cesium Ions in Cesium Vapor. Rep. No. A-920057-5 (NASA CR-50301), United Aircraft Corp., May 31, 1963.
25. Kitrilakis, Sotiris: Correlation of Internal Voltage Loss in Optimized Thermionic Converters. A Symposium on High Temperature Conversion - Heat to Electricity, Univ. of Arizona, Feb. 19-21, 1964. Earl W. Phelan, ed., AEC Rep. No. TID-7687, pp. 214-219.
26. Majkowski, R. F.; and Donohue, R. J.: Cesium Plasma Spectroscopy-Electron Number Density Measured by Stark Shift of Spectral Lines. Final Rep. (NASA CR-54997), General Motors Research Lab., Jan. 14, 1966.
27. Verdeyen, J. T.; Cherrington, B. E.; and Fein, M. E.: Investigation of the Basic Processes Occurring in Gaseous Plasmas in Various Charge Density and Energy States. Second Semiannual Prog. Rep., May 1, 1965 thru Oct. 1, 1965, University of Illinois, Gaseous Electronics Lab., 1965.
28. Morris, J. M.: Small Plasma Probes with Guard Rings and Thermocouples. NASA TM X-1294, 1966.
29. Horner, M. H.: Post-Operation Examination of Thermionic Life-Cells. Rep. No. GA-7131, General Atomic Div., General Dynamics Corp.
30. Anon: Studies of Thermionic Materials for Space Power Applications. Rep. No. GA-6860 (NASA CR-54980), General Atomic Div., General Dynamics Corp., May 6, 1966.
31. Kaznoff, A. I.; and Sanderson, M. J.: Diffusion and Interactions in the Urania-Tungsten and Urania-Molybdenum Systems. Paper Presented at the International Conference on Thermionic Electrical Power Generation, London, Sept. 20-25, 1965.
32. Anon: Research Program for the Long Term Testing of Cylindrical Diodes and the Irradiation of Fuel and Insulator. Rep. No. GEST-2049 (NASA CR-54656), General Electric Co., Apr. 18, 1965.

TABLE IX-1. - STABILITY OF MONOCRYSTALLINE SURFACES

(FROM LEED STUDIES, BROWN UNIVERSITY)



Material	Basic crystal orientation	Initial surface orientation	Surface after heat treatment
Tantalum (BCC)	110	^a 130 and 310	110
Molybdenum (BCC)	130	130	110 and 100
Molybdenum (BCC)	110	110	110
Tungsten (BCC)	110	^a Random	110

^aProduced by ion bombardment.

TABLE IX-2. - STABILITY OF VAPOR-DEPOSITED TUNGSTEN SURFACES

(FROM GENERAL ATOMIC)

Process	Initial ϕ	Etch	Treated ϕ	Thermal aging		Final ϕ
				$^{\circ}\text{K}$	Hr	
Tungsten fluoride (WF_6)	4.52	Thermal	4.52	2073	600	4.52
Tungsten fluoride (WF_6)	4.52	Chemical	4.67	2273 to 2673	18	4.54
Tungsten fluoride (WF_6)	4.51	Electrochemical	4.72	2173 to 2573	36	4.50
Tungsten chloride (WCl_6)	5.01	Thermal	5.01	2073	1040	5.01
Tungsten chloride (WCl_6)	4.93	Chemical	4.85	2673	7	4.94
Tungsten chloride (WCl_6)	5.05	Electrochemical	4.89	2173 to 2673	39	4.85
Duplex tungsten chloride - tungsten fluoride ($\text{WCl}_6\text{-WF}_6$)	4.86	Thermal	4.86	2073	720	4.86

TABLE IX-3. - URANIUM DIFFUSION THROUGH

TUNGSTEN-CLAD EMITTER

[Cladding, 20 mils; test time, 1000 hr.]

Fuel	Temperature		Clad	Number of monolayers
	^o K	^o F		
90 mole percent uranium carbide - 10 mole percent zirconium carbide	2170	3432	Vapor-deposited tungsten (GA)	230
Uranium dioxide	2100	3320	Vapor-deposited tungsten (GE)	15
Uranium dioxide	2070	3252	Powder metallurgy tungsten	4

TABLE IX-4. - GENERAL ELECTRIC THERMIONIC

CONVERTER LIFE TESTS

[Emitter temperature, 2100^o K (3320^o F); power density, 7 to 11 W/cm²; efficiency, 12 to 13 percent; electrically heated emitter; percent degradation, none.]

Designation	Duration, hr	Failure mode
301	3754	Emitter support sleeve ↓
302	100	
303	916	
311	6413	
312	8055	
313	3775	
431	405	Short
432	151	Short

TABLE IX-5. - GENERAL ATOMIC THERMIONIC

CONVERTER LIFE TESTS

[Emitter temperature, 2000° to 2100° K (3140° to 3320° F);
power density, 7 to 9 W/cm²; efficiency, 11 to 13 per-
cent; electrically heated emitter.]

Designation	Duration, hr	Failure mode	Degradation, percent
LC-1	7 174	Metal-ceramic seal	60
LC-2	3 235	Crack in emitter stem	None
LC-3	10 406	Short	None
LC-4	7 345	Braze joint	None
LC-5	7 558	Braze joint	15
LC-6	2 300	Continuing	^a 40

^aLow initial power.

TABLE IX-6. - CHARACTERISTICS OF THERMIONIC FUELS

	Uranium carbide	Uranium dioxide	Uranium dioxide - tungsten cermet
Uranium density	High	Medium	Low
Thermal conductivity	High	Low	High
Vapor pressure	Low	High	Not applicable
Probable fission gas management	Release and vent	Release and vent (high tempera- ture)	Retain

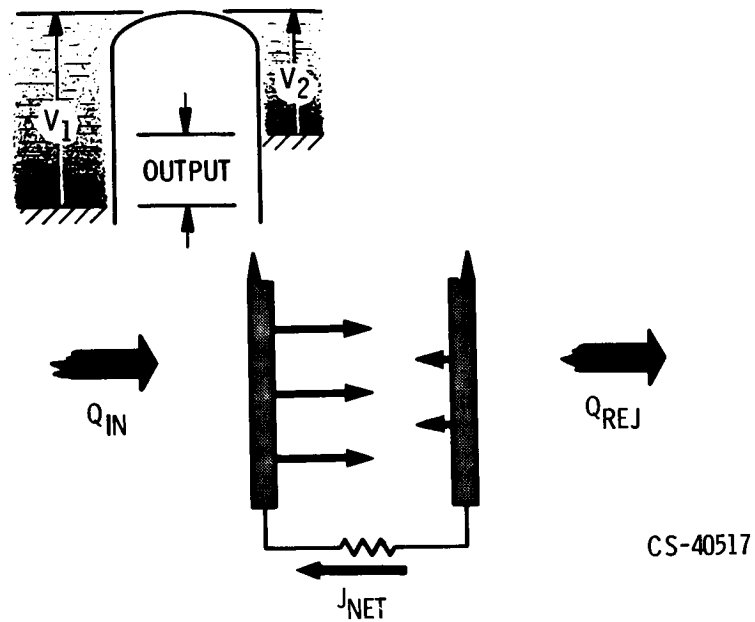


Figure IX-1. - Ideal thermionics.

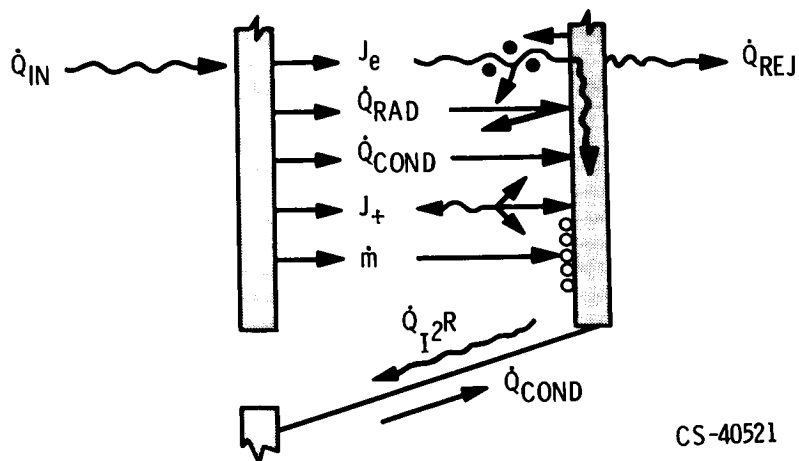


Figure IX-2. - Actual thermionics.

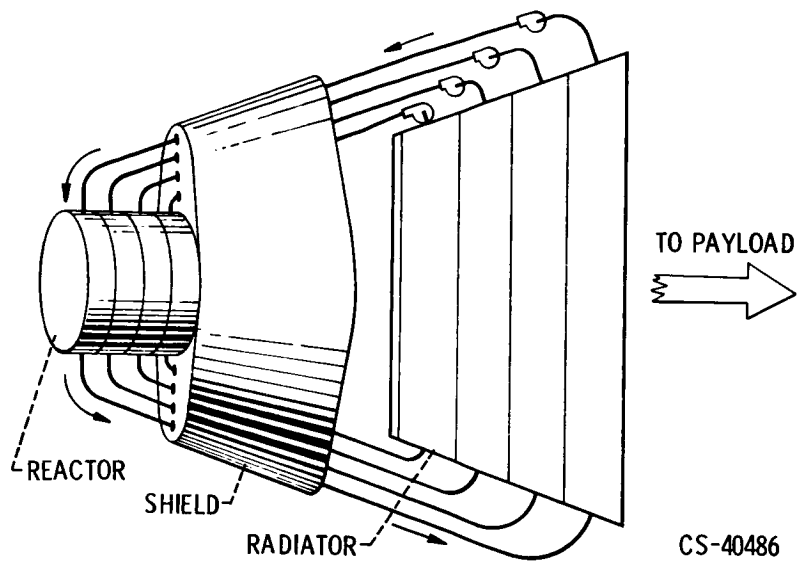


Figure IX-3. - In-pile thermionic system.

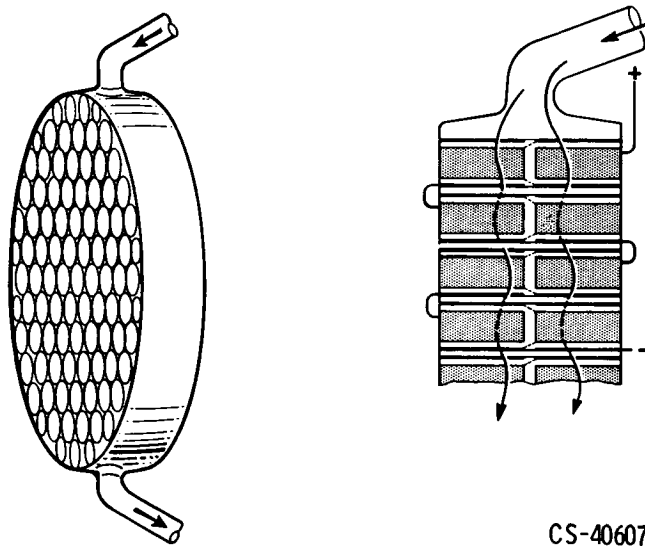


Figure IX-4. - In-pile thermionics crossflow heat exchanger.

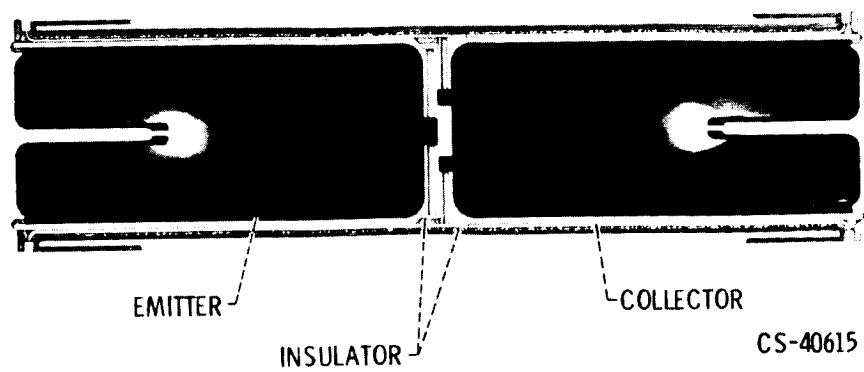


Figure IX-5. - In-pile thermionics unit cells.

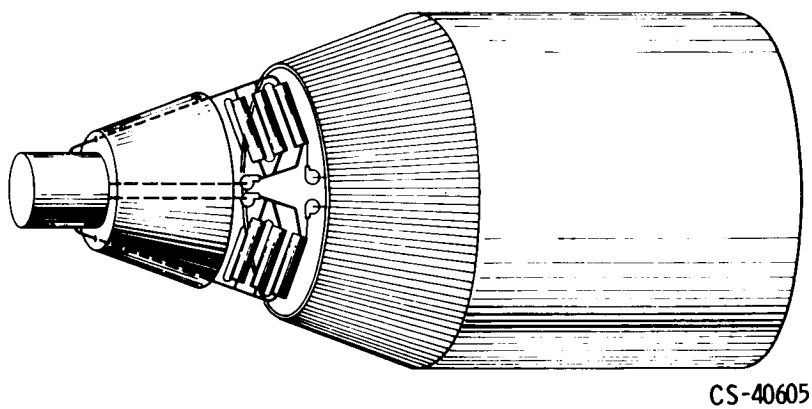


Figure IX-6. - Out-of-pile thermionic system.

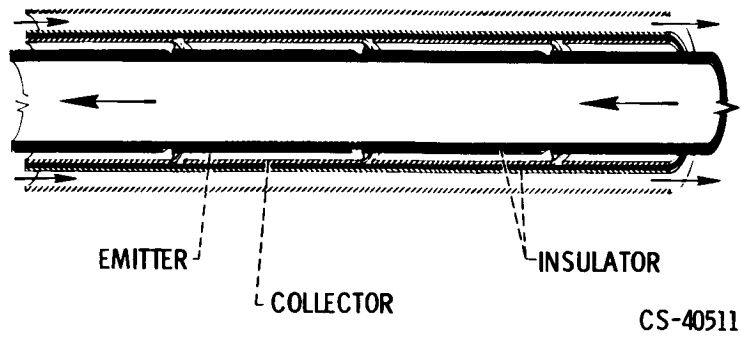


Figure IX-7. - Out-of-pile thermionic converter.

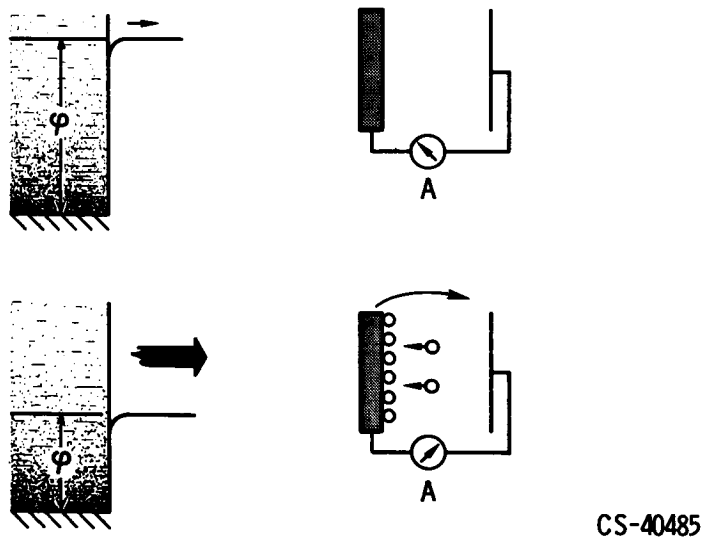


Figure IX-8. - Removal of electrons from emitter.

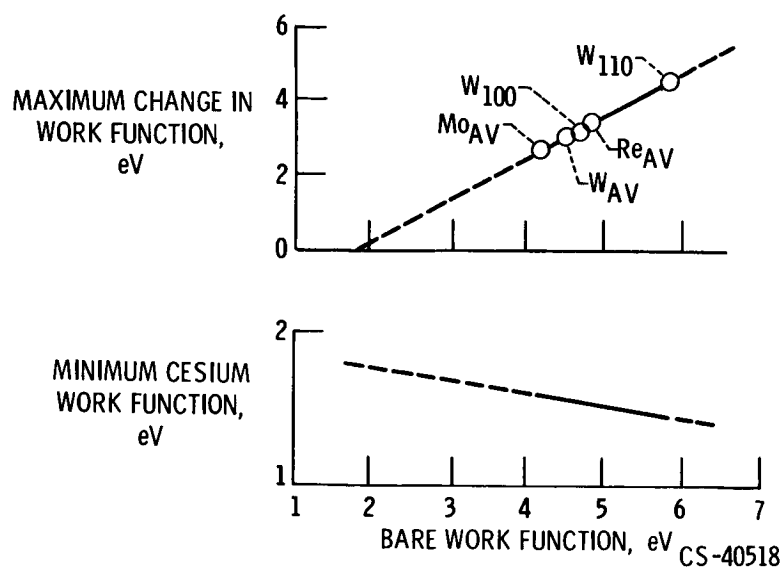


Figure IX-9. - Experimental work function correlation of bare and cesiated surfaces. (From Field Emission Corp.)

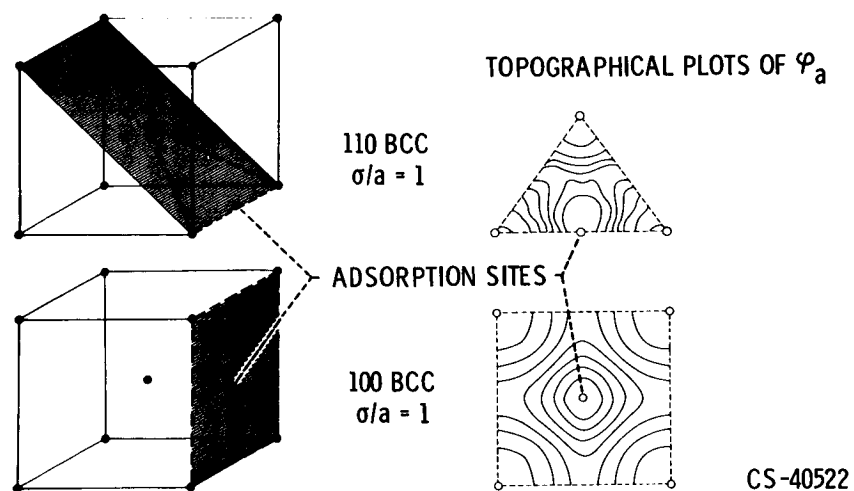
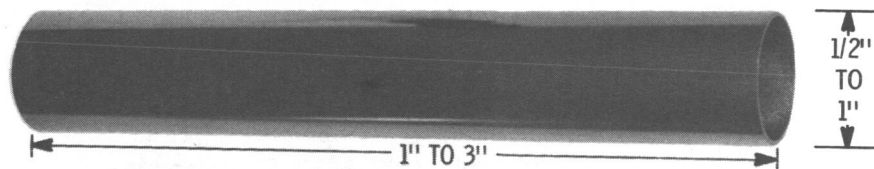
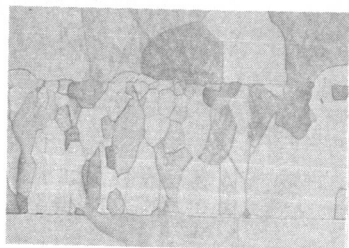


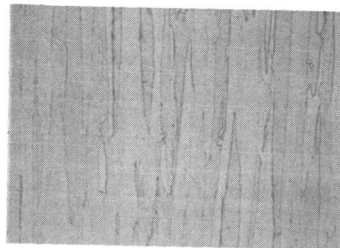
Figure IX-10. - Nature of ideal surface.



(a) Typical fuel containment cylinder.



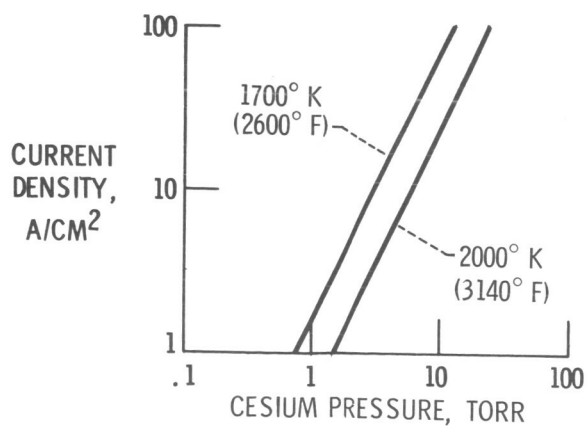
(b) Tungsten from hydrogen reduction of WCl_6 . Approximately 110 plane.



(c) Tungsten from hydrogen reduction of WF_6 . Approximately 110 plane.

CS-40523

Figure IX-11. - Vapor-deposited tungsten emitters.



CS-40480

Figure IX-12. - Effect of cesium pressure on electron emission (based on data from diode using 110 oriented tungsten emitter).

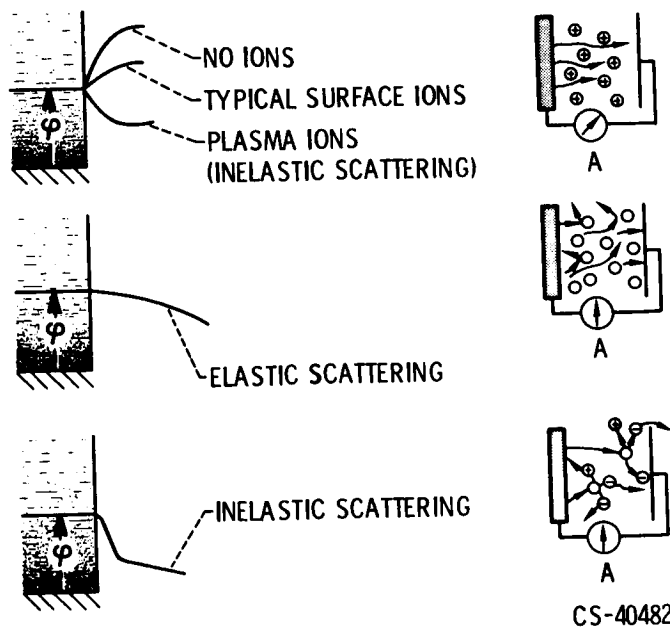


Figure IX-13. - Moving electrons across interelectrode space.

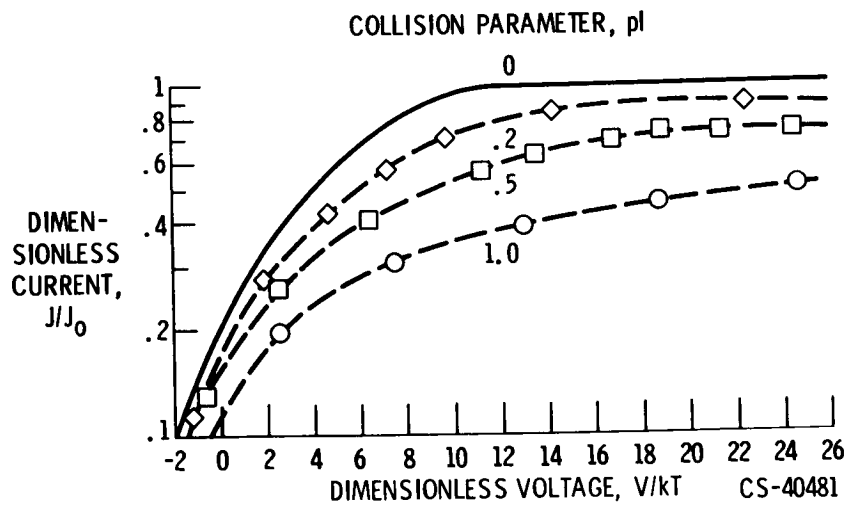


Figure IX-14. - Effect of argon on transmission of electrons in planar diode (including angular and velocity dependent elastic cross section).

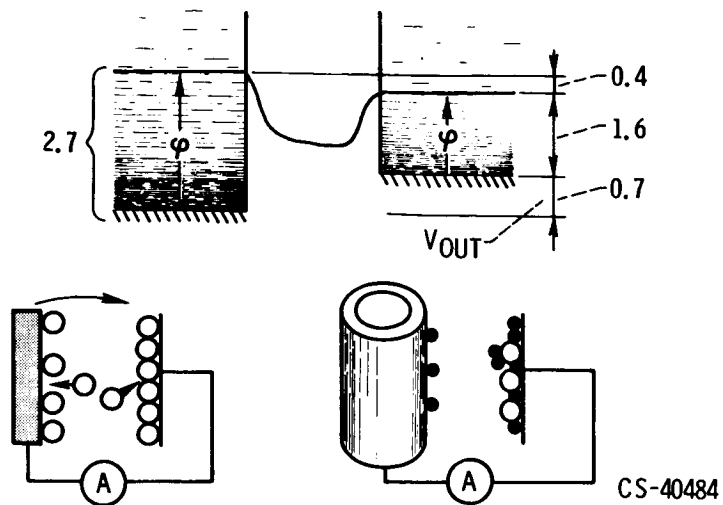


Figure IX-15. - Moving electrons into collector.

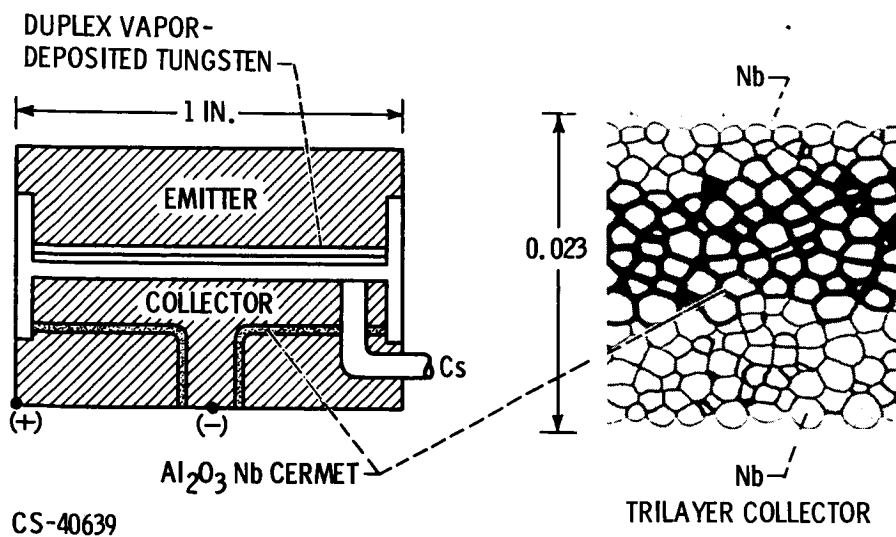


Figure IX-16. - Research converter.

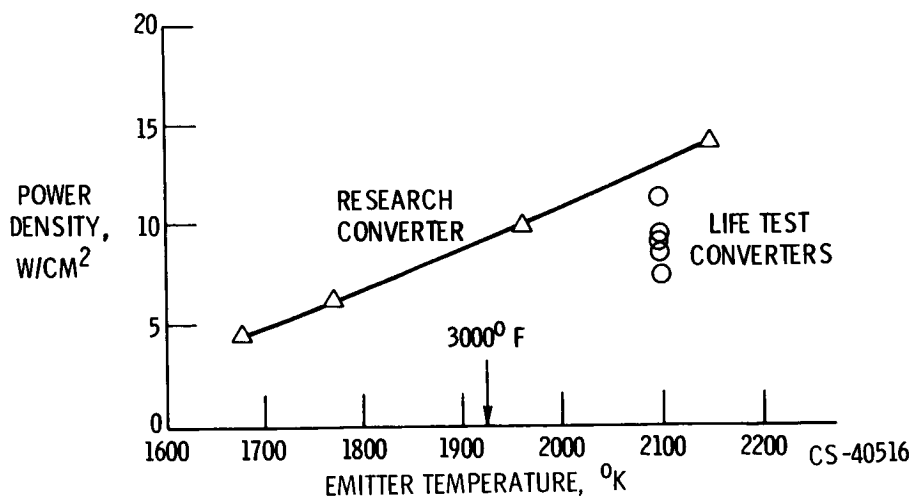


Figure IX-17. - Thermionic converter performance for electrically heated tungsten emitters. (From General Electric.)

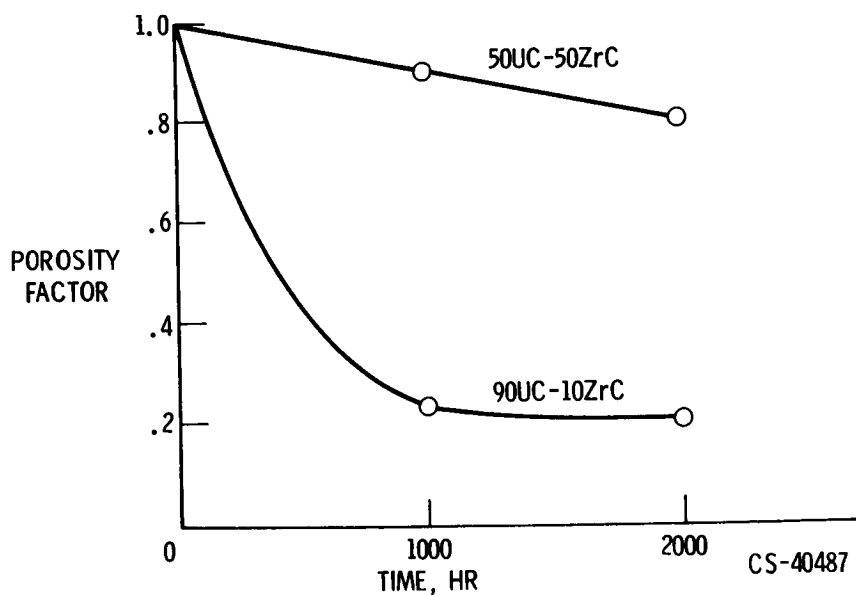


Figure IX-18. - Variation of uranium carbide - zirconium carbide porosity at 2100° K (3320° F). Isostatically cold pressed at 90 000 pounds per square inch; sintered 15 hours at 2300° K (3680° F). (From General Atomic.)

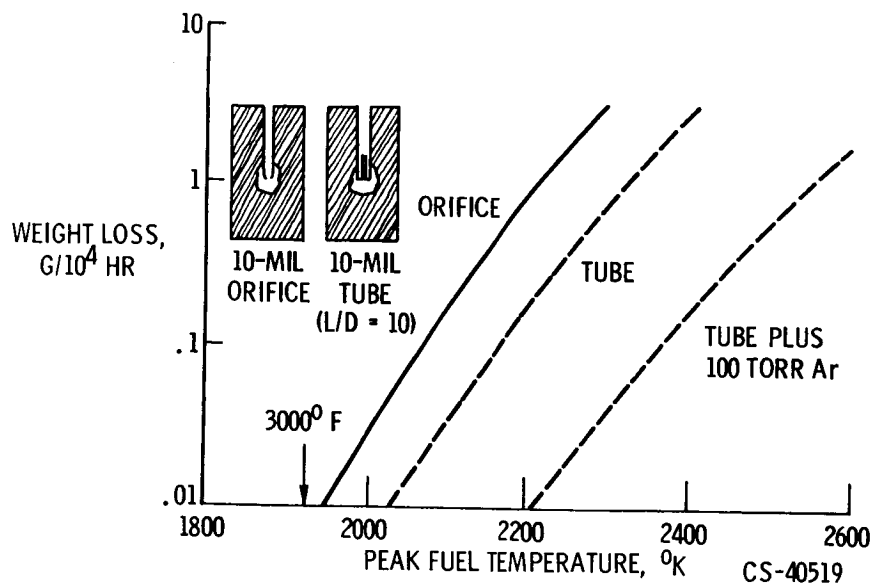


Figure IX-19. - Uranium dioxide vapor loss in vented fuel capsules.

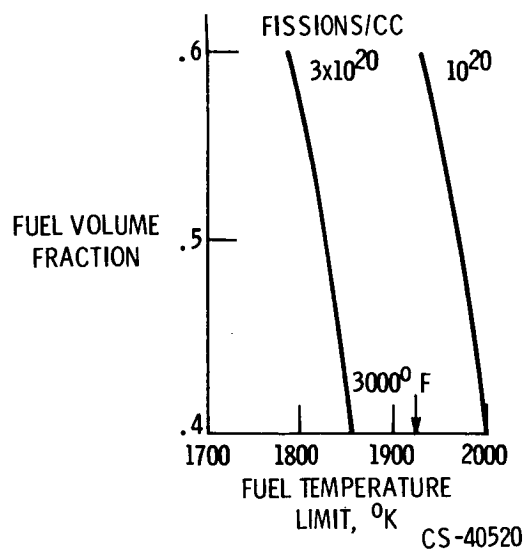


Figure IX-20. - Fuel volume fraction for uranium dioxide - tungsten cermet, 1 Percent creep for tungsten in 10^4 hours; 5 percent fission gas release at 1800°K ; 50 percent fission gas release at 1900°K .

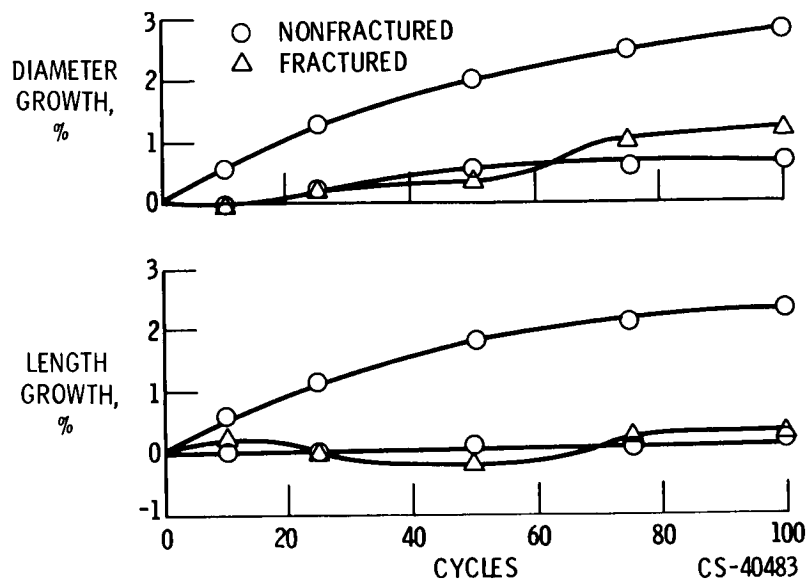


Figure IX-21. - Growth for thermal cycle specimens.

X. APPLICATIONS OF POWER SYSTEMS TO SPECIFIC MISSIONS

Bernard Lubarsky and Lloyd I. Shure

The new power systems, previously described, are discussed in terms of typical mission applications. A comparison of the use of these new powerplants is made with existing systems, such as photocells. The relative interest in different kinds of power systems varies greatly from mission to mission. In a survey of power-system applications to future missions, an important feature is breadth of coverage. If a broad range of presently unapproved missions is covered, the depth of coverage cannot, of necessity, be very great. Therefore, the numbers given for the various systems are only approximate and not definitive because details have not been sufficiently established for these advanced missions. Many of these comparisons are made with two significant figures, but these figures are only the product of the assumptions used in each case.

The missions discussed begin with near-Earth orbital and progress outward to the planetary missions. The first mission, the near-Earth, large, manned, orbiting laboratory, is one of considerable interest to NASA at this time.

A summary of the weights and area characteristics of solar power systems for manned orbiting stations is shown in table X-1. These solar power uses are divided into what are called day and night applications. Day-power weight is the weight of photocell panels required to provide a kilowatt of power while exposed to the Sun. Night-power weight is the sum of two weights, namely, the weight of photocell panels required in sunlight to charge batteries plus the weight of the batteries required to deliver power during the night, or shade, part of the orbit. For day power, the conventional photocell system is quite light, about 50 pounds per kilowatt. This number represents the probable lower limit of what can be achieved in large lightweight multikilowatt solar arrays based on technology work that has just begun and is of the order of half the weight of arrays currently in use. The 1.5-kilowatt array described in paper I and flown by the Air Force on the Agena vehicle weighed approximately 130 pounds per kilowatt; hence, the weight shown for conventional photocells is fairly optimistic. This is done for comparability, that is, in order to compare future photocell systems with other advanced power systems. Hence, for the photocell-and-battery system, which is fairly well developed today, optimistic weights are shown in order to reflect the inevitable improvement that will occur. In the case of other advanced systems, the weights shown are representative of the first flight system; that is, they are conservative in the sense that future developments beyond that time could undoubtedly produce still lighter systems.

The night-power computations are based on the Sun and shade times for a 260-nautical-mile ecliptic orbit. A typical value of 55-percent charge-discharge efficiency for the batteries was assumed. The discharge voltage obtained from the batteries is about 55 percent of the voltage required to charge them, and, of course, the ampere-hours are the same. Also included is a 95-percent efficiency for the battery charger. From these assumptions, the photocell power re-

quired for the night power is obtained. Battery weights were based on 2 watt-hours per pound, a value typical of nickel-cadmium cells from which an extremely large number (thousands) of charge-discharge cycles is obtained. Currently, nickel-cadmium batteries flying in low-altitude orbit normally produce about 1 watt-hour per pound so that, again, current systems weigh about twice what is shown in table X-1. When all these assumptions are added, a specific weight of 450 pounds per kilowatt is obtained. The collector area shown in the table is the photocell array for both day and night power.

In the case of thin-film photocells and batteries, a range of weights is presented. This range corresponds to two efficiencies: a 5-percent efficiency, which is an average of presently demonstrated technology, and a 7-percent efficiency, which is currently typical of occasional cells as produced, although they do not retain this 7-percent efficiency for a long time. Thus, this 7-percent efficiency represents the upper range of what can reasonably be anticipated for advanced development. The weight of structure assumed ranges from 0.1 to 0.2 pound per square foot for the thin-film array. In a conventional photocell array for which the cells are heavier and more brittle, the structural weight is about 1/3 pound per square foot. For the thin-film cells with their lighter weight and greater flexibility, a lower structural weight was chosen. In spite of this, there really is no significant difference in weight between conventional and thin-film photocells for this particular application. This result was anticipated since the predominant weight of the system has little to do with the weight of the photocell array, but is primarily involved in the energy-storage requirement for night power. This characteristic applies throughout nearly all the missions discussed herein. Therefore, wherever any kind of substantial energy-storage requirement is concerned, the weight of photocell systems, both conventional and thin film, will be approximately the same. The choice then between these two systems will be based on other factors, such as the ease of packaging, or lower cost of the thin-film system, or the lower collector area of the conventional photocell array. For the remainder of this discussion, since the weights of these two systems are nearly the same, only the conventional photocell system is considered.

The Brayton cycle, instead of using batteries for energy storage, stores energy in the form of heat of fusion, in this case, of lithium fluoride. This method results in lighter weights for low-altitude orbit than battery storage. The Brayton cycle system thus shows a significant weight advantage. Therefore, where energy-storage requirements are high, such as in this application, the Brayton cycle is expected to offer some advantage in weight. However, whenever energy-storage requirements are low, the Brayton cycle is less attractive on a weight basis. Of course, it does offer an advantage in reduced collector area because of its higher efficiency.

Figure X-1 shows a 30-kilowatt conventional photocell array on a three-spoke orbiting manned station of the kind that might be put into orbit by a Saturn V. The approximate dimensions are 100 feet from the middle of the hub to the tip of the spoke and approximately 80 feet in width across the photocell array. The weight capability of the Saturn V for this mission is approximately 250 000 pounds. Figure X-2 shows a typical 30-kilowatt solar Brayton system on the same space station to the same scale as shown in figure X-1. Here, three 10-kilowatt solar Brayton systems are shown, one at the end of each spoke. The mirror diameter for this system is 30 feet.

Table X-2 is a summary of nuclear power systems for this same application. In the solar

power system, energy storage for night power was a predominant feature in system weight. In the nuclear power systems, a different feature becomes very important and prevails in many instances, namely, shielding. In this table, four different nuclear power systems are given with their weights and radiator areas. The weights have been broken down into unshielded weights and the weight of the shield itself. The unshielded isotope Brayton system weighs about 350 pounds per kilowatt, and because it uses plutonium 238 with its relatively low level of emitted radiation, the shield weight required is small, of the order of 0 to 50 pounds per kilowatt, where the shield weight depends on isotope location and shielded area.

The 35-kilowatt SNAP-8 system includes a completely redundant power-conversion system. These two complete systems are connected to one reactor. This redundancy was necessary in order to assure the high reliability usually associated with manned missions. Either of these power-conversion systems is capable of producing 35 kilowatts. The isotope Brayton system does not have redundant machinery since it is assumed that a 30-kilowatt system could utilize three 10-kilowatt modules; if some redundancy were required, a fourth standby system could be provided. In any event, the weights can be adjusted from the values given in table X-2. The SNAP-8 thermoelectric system has a lower efficiency than the SNAP-8 mercury Rankine system and is also heavier; hence, it produces less electric power from the same thermal power of the SNAP-8 reactor and accordingly weighs more unshielded. The large increase in shield weight for the SNAP-8 thermoelectric reactor system is a result entirely of the lower power; the shielding is the same as that required for SNAP-8, but because of the lower power output of the SNAP-8 thermoelectric system, the unit weight (lb/kW) is higher. The reactor systems are significantly heavier for this mission than the corresponding isotope systems because the large amount of penetrating radiation put out by the reactor requires reactor shields that are thicker and correspondingly heavier than isotope shields.

Currently, three advanced reactor power systems are being evaluated, namely, Rankine, Brayton, and thermionic systems. The numbers shown in table X-2 are representative of the potassium Rankine system. For the thermionic system, the weights would be quite similar, but the radiator area would be still smaller. For the Brayton system, the weights would probably be of the order of 50 percent larger, and the radiator area would be larger by a factor of perhaps 5. In comparison with the other reactor systems, there is a substantial reduction in shield weight per kilowatt due primarily to the higher power level of the advanced reactor system. This reactor, although producing nine times the power of the SNAP-8 reactor, would only be slightly larger with the result that total shield weight would increase only slightly, while the unit weight (lb/kW) would decrease markedly.

Figure X-3 is a conceptual view of SNAP-8 on a manned space station. The reactor is at the apex of the cone in the lower right of the figure. The distance from the reactor to the nearest occupied point in the space station is 125 feet. The base of the cone containing the SNAP-8 system is approximately 22 feet in diameter. This configuration is typical of a SNAP-8 configuration for space-station application.

As shown in figure X-3, the station could be assembled from two launches of a Saturn IB, which has an orbital capability of the order of 30 000 pounds. The space station would be taken up by one launch, and the SNAP-8 system with its shield would be taken up on the second launch for rendezvous with the space station. If a Saturn V were used for this type of mission, there

would be a much larger orbital weight capability, and a much larger space station similar to the three-spoke version in figure X-2 would probably be used.

It is now possible to draw several conclusions related to advanced power systems for the manned orbiting space station. The Brayton cycle system, either solar or isotope powered, would have low weight. The photocell systems would be next, and the SNAP-8 system would be the heaviest. Although the advanced reactor system is the lightest, the technology of such a system (papers VII and VIII) is considerably behind that of the Brayton and SNAP-8 systems. Although the SNAP-8 and Brayton cycle systems will be available for missions in the 1970's, the earliest that the advanced Rankine system will be ready is the very late 1970's or the 1980's.

If an advanced reactor system were available, it would probably be the most attractive of those compared in table X-2. Among the other systems, it appears that, since the Brayton cycle is the lightest, it would be the system of choice. However, if a 30-kilowatt manned orbiting space station is the application, these unit weights can be multiplied by 30 to obtain the total power-system weight that would be required. The SNAP-8, even at 900 pounds per kilowatt, is of the order of 30 000 pounds. On a Saturn V class of space station with a 250 000-pound total weight, this 30 000 pounds represents a little over 10 percent of the total weight. Hence, there is ample weight and surface area to accommodate any of these power systems at the 30-kilowatt level. The weight constraint in this particular mission is not as significant as that which will be shown for others. Weight is certainly not unimportant and, all other things being equal, the lightest power system would be selected. In a mission for which there is ample weight capability and many power systems to choose from, other characteristics besides weight can prevail. For example, availability is an important factor in any mission planning. If during mission planning, one power system is not fully developed or its safety has not been fully demonstrated and if sufficient weight capacity is available, the system of choice will more than likely be the one that has been proved. Another feature that can be important is the spatial orientation associated with solar power systems. The mission manager may be happy to be relieved of the requirements to orient continuously any of these solar supplies. In such a case, a nuclear power system may be chosen.

Cost might also be an important factor. Plutonium 238 for the 10-kilowatt isotope Brayton system could cost \$20 to 25 million; for a 10-kilowatt isotope thermoelectric system, between \$60 and 75 million worth of plutonium 238 would be required. This cost difference is certainly significant. Of course, plutonium 238 has an 86-year half-life, and since only a small amount would actually be consumed, it can be argued that the isotope can be recovered for reuse and costs can thereby be reduced; however, just how the bookkeeping would be handled is not certain. The photocell array of 30 kilowatts would cost between \$10 and 15 million. SNAP-8 or thin-film photocells would be much cheaper, as would the solar Brayton system.

An additional penalty associated with the solar power systems on this mission is atmospheric drag. In a 260-nautical-mile orbit, the drag of a 30-kilowatt conventional photocell array is sufficiently high that, if bipropellant rockets are used to counterbalance the drag, about 5000 pounds of fuel would be required each year.

Ample weight capability characterizes such a mission. Any of these power systems could be chosen. The choice will depend on the details of just how the mission will be performed and to some extent the preference of the project manager involved. The selection will more than

likely not be dominated by weight considerations alone.

Up to this point, the discussion has centered around a manned orbiting space station with a nominal 30-kilowatt electric power requirement, and as noted earlier, the high-powered advanced reactor systems would not be available until the 1970's at the earliest. It is anticipated, however, that eventually powers of the order of 300 kilowatts, which could be supplied by the advanced reactor system, will be required for these missions. Figure X-4 illustrates the kinds of power systems that might be considered for this application in this time period. A conventional photocell-and-battery system is compared with an advanced reactor system. Both systems produce 300 kilowatts for a large manned orbiting station, the same three-spoke station described earlier. At the 300-kilowatt level, the performance of an advanced reactor system far exceeds the capability of any of its competitors. If an advanced reactor system is available in this time period, it can provide very large powers for weights with which no other system can compete. It is interesting, however, that if the need for a 300-kilowatt conventional photocell system were great enough, it could conceivably be built. However, the weight of this system is such that it would more than likely require the separate launch of a Saturn V class vehicle.

In low-altitude orbit, NASA programs specify a much larger number of unmanned than manned missions. The unmanned missions are characterized by power requirements from much less than 1 kilowatt up to a fraction of a megawatt. The two power systems currently in use are the solar photocell and isotope thermoelectric system. These systems will be difficult to displace by any of the advanced systems discussed herein. The Brayton and Rankine systems are both mechanical. At very low powers, a fraction of a kilowatt, the parasitic losses of machinery become dominant, and they become unattractive. The only potential contender for these low-power missions of the three new power-conversion techniques discussed here is the thermionic system; as yet, not enough is known concerning temperature levels attainable with isotope fuels for any real prediction to be made. There is, however, the possibility that the isotope thermionic system might someday be attractive for this application.

At higher altitudes, the next class of missions is a 24-hour, or synchronous, orbit. The remarks made previously relevant to the solar photocells and isotope thermoelectric systems apply without change to this class of missions. For those missions that require higher power levels, solar and nuclear power systems are again compared for the 24-hour orbit (table X-3). In this orbit, there are about 80 dark periods per year. The longest of these is 72 minutes and they diminish to zero. For this reason, the energy-storage requirements for the photocell-and-battery system are much reduced. Instead of the thousands of cycles required for the low-Earth-orbital missions, only a few hundred cycles are required for a very long-life space station. It should be noted from paper II that the energy (W-hr/lb) available from batteries increases rapidly as the number of cycles is decreased. For this application, it appears reasonable to assume an energy capacity of 10 watt-hours per pound instead of the 2 watt-hours per pound utilized for the low-altitude orbit, which are probably equally optimistic numbers. It is reasonable to assume that by the time this mission is flown, some increase beyond this 10 watt-hour per pound capability can be anticipated. The net result is a significant reduction in the weight required for the shade or night power. Also, the shade-to-sun ratio becomes much more favorable since there are approximately 23 hours of light and 1 hour of darkness in the worst circumstances; hence, the additional weight of extra photocells for charging batteries is also decreased. Thus, the importance of energy storage on overall system weight is diminished. In the case of the

Brayton cycle, its biggest advantage as noted previously in low-altitude orbit was its lighter energy storage. For the 24-hour orbit, the energy-storage requirements are about the same as in the low-altitude orbit. There is slightly less weight of collector required because the light-dark ratio is more favorable, but there is somewhat more weight of heat-storage material required because the longest time period is extended from 35 to 72 minutes. When both these effects are included, the weight remains nearly the same; hence, the weight advantage has shifted decidedly in favor of the photocell system.

Table X-3(b) is a summary of nuclear power systems for this 24-hour-orbit television-broadcast satellite. For this mission, the shield weights are significantly lower than those discussed earlier for the low-altitude orbits. This marked reduction in shield weight derives from the unmanned character of the mission. Men and photofilm are probably the two most radiation sensitive "devices" that exist, and the payload in this case is considerably more radiation resistant; consequently, for this and other unmanned applications, relatively lightweight shields are possible. The characteristics of the basic power-conversion system without shielding are not affected by the change to a higher orbit and hence are the same as those shown earlier (table X-2) for the manned orbiting station. It is interesting to note that, with the exception of the advanced reactor system, the photocell-and-battery system is by far the lightest.

The importance of weight will be a significant factor for this 24-hour television-satellite mission. For example, if a Saturn V were selected as the booster for this mission, the cost could well equal the total capitalization of the COMSAT Corporation. As a result, there is a strong incentive to utilize smaller and cheaper boosters. The next largest vehicle to the Saturn V would be the Saturn IB. The Saturn IB with the Centaur upper stage has a weight capability of approximately 9000 pounds in the 24-hour orbit. Comparable to this would be the Titan 3C-Centaur, which would have about the same weight capability. The Titan 3 with its trans-stage is comparable to the Atlas-Centaur kick-stage combination, each having a weight capability of approximately 2200 pounds in a 24-hour orbit. Thus, in this case of vehicles, the total payload capability will range from 2000 to 9000 pounds.

To be attractive, however, the direct-broadcast satellite requires substantial power. If each home receiver is equipped with, for instance, a 6-foot-diameter parabolic antenna, several tens of kilowatts will be required to cover one-fourth the United States with television reception of the present quality. If a value of 50 kilowatts is selected to meet this requirement, table X-3(a) shows that the photocell system would approach 10 000 pounds, which, by itself, is beyond the weight capability of the launch vehicles noted previously. Hence, it is clear that there is going to be considerable pressure in this mission to pick the lowest weight system. Therefore, again excepting the advanced reactor systems, which would be very attractive when available, the photocell system appears the most likely candidate. When this mission is examined in greater detail, the orientation problems and penalties associated with the photocell system might be significant enough to warrant selection of either the isotope Brayton or SNAP-8 system in spite of the weight disadvantage. From the two basic missions examined so far, it is apparent that both selection criteria and system characteristics are very sensitive to the mission application.

Manned missions on the lunar surface is the application of power to be considered. Manned missions to the moon with currently existing vehicles will be limited to relatively modest efforts because of the low landed-weight capabilities. The following discussion is based on a cryogenic

hydrogen-oxygen landing stage not currently developed. The present Saturn V plus this hypothetical upper stage could land approximately 26 000 pounds on the lunar surface. The following discussion considers power supplies of interest for manned operations based on this 26 000-pound payload capability.

As noted earlier, a key factor in solar systems is energy storage. In the case of the moon with its 14-Earth-day night cycle, energy storage will be a major factor. Table X-4 summarizes the energy-storage requirements for these systems. It is apparent that the batteries and the heat storage are both prohibitively heavy. Heat storage still shows an advantage over batteries, as was the case in the Earth-orbital missions considered earlier. However, neither is competitive with fuel cells. These fuel cells would operate as follows: During the lunar day, power from the photocell system would be utilized to electrolyze water. The hydrogen and oxygen obtained would be stored for subsequent use during the lunar night. A fuel-cell system of this type is described in paper II. Current fuel cells degrade with use; although some few fuel cells have operated several thousand hours, many others have failed at earlier times. Neither a really long-life fuel-cell system nor the required long-life electrolyzer is currently available. Hence, it is not known whether the weight of the fuel-cell system described herein can really be achieved. It has been assumed that the performance currently obtained from fuel cells and electrolyzers for short periods can be achieved for these very long times.

Another concept for heat storage is a large bed of lunar soil to cover a tube-and-fin heat exchanger (fig. X-5). Above the bed of soil are a series of plastic windows and a reflector-insulator. This reflector-insulator is pulled over the bed at nightfall to preserve as much heat in the bed as possible. In the daytime, the reflector-insulator is rolled aside, and the plastic windows act as a greenhouse to trap heat in the lunar soil bed. Heat removed from the bed by the tube-and-fin heat exchanger might provide an energy supply to a thermal power system. Preliminary analysis of this idea indicates that its value is heavily dependent on the thermal conductivity that can actually be achieved for the lunar soil bed. For this preliminary analysis, the thermal conductivity of lunar soil was assumed to be that of sand in a vacuum and indicated that not much heat could be gotten into or out of the bed. Investigations are continuing on schemes for enhancing this conductivity in some practical way.

Nuclear power supplies for this mission on the lunar surface will have essentially the same unshielded weight as shown earlier. For this manned mission, shield weight will again be a significant factor. However, lunar material may play an important role. The extent to which this lunar material can be counted on for shielding, if at all, will then determine the shield weight required to be launched with the powerplant.

Two basic approaches were used to evaluate power systems for manned lunar operations. First is the lunar shelter concept that utilizes the photocell system (fig. X-6(a)). The 26 000-pound capability of the cryogenic lander is utilized to land a single complete shelter that includes the power supply, life support, living space, and experiments that would be required for a small lunar station. In the case of the isotope Brayton system (fig. X-6(b)), approximately 1000 to 1500 pounds of the total system weight would consist of shielding. These relatively high weights would be required because of the proximity of the power supply to the men for long periods. If lunar material could be utilized for shielding, or if the power supply could be removed from the vehicle and placed at some distance from the men, the weight of this system could be reduced to approximately 2000 pounds. The isotope power supply is considerably lighter than

the photocell system for this application, and weight will be quite important since 26 000 pounds is the weight limitation on a Saturn V launch vehicle. The Saturn V itself is estimated to cost approximately \$100 million. On this basis, weight is quite significant, and the nuclear power systems are the more attractive.

The second approach to evaluating power systems for manned lunar operations is shown in figures X-7 and X-8. In this case, it was assumed that the entire payload of a cryogenic lander could be devoted to the power system for an advanced and relatively elaborate lunar base. With this weight capability, a 20-kilowatt photocell - fuel-cell power system could be landed. In the case of the SNAP-8 power system, the unshielded weight with one set of redundant power-conversion equipment is shown. For SNAP-8, it was assumed that advantage would be taken of local topographical features such as the crater rim shown in figure X-8 and that lunar material could provide a substantial portion of the shielding requirements. On this basis, the 35-kilowatt SNAP-8 would only use half the weight capability of the cryogenic lander if no shielding were required. Thus, once again, because of the severe energy-storage requirements for solar power systems in the lunar environment, it appears that the nuclear system is the more attractive.

One additional manned lunar mission was considered, that of the three-man roving vehicle; figure X-9 illustrates this concept. The deployed panels on the top of the vehicle are radiators for the hydrogen-oxygen fuel-cell system for motive power. The phantom outline represents the radiators for an isotope Brayton system to provide this same power requirement. Figure X-10 shows the weight requirements as a function of propulsion time. The weight of the fuel-cell power system is nonlinear because, as the weight of reactants increases with propulsion time, the horsepower required to drive the vehicle increases. The weight of the isotope system is, of course, constant with time because of the long half-life of the isotope. For relatively short propulsion times (of the order of 100 hr), the fuel-cell system offers a weight advantage. However, for longer propulsion times, the nuclear system becomes more attractive.

The interplanetary missions comprise the next group of applications considered. For the unmanned exploration of the inner solar system (anywhere from Mercury to Mars), it appears that either solar photocells or an isotope thermoelectric system can provide the power. This application will not be considered further; however, table X-5 compares power systems for a manned Mars mission. The day-power weight shown for photocells is more than twice that shown earlier for this system because the design power here is that generated at Mars, and the diminished solar flux at Mars results in increased photocell weight. No night power is required for this planetary mission because the trajectory can be selected to be in the Sun continuously. Normally, some batteries would be required to furnish peak power with the photocells providing a constant average power; however, the greatest requirement for batteries on this mission is likely to occur at planetary entry. This mission would probably use atmospheric drag in the planetary entry either at Mars or at Earth return, or perhaps at both. For this phase of the mission, the solar panels would have to be folded. It is assumed that this period of time would be approximately 1 hour. This portion of the mission has not been analyzed in sufficient detail for this time period to be accurately estimated; however, the penalty in table X-5 of 70 pounds per kilowatt for batteries is indicative of this requirement. The weight penalty would be linear with the time required for aerodynamic breaking; hence, if it were 5 hours, a 350-pound-per-kilowatt penalty would be incurred. Thus, as far as weight is concerned, it is again an impor-

tant feature on this manned planetary mission, photocells and batteries will be the most attractive system provided that the energy-storage requirement is not severe. If the planetary entry period is protracted, interest might very well shift to the isotope Brayton, which would require no orientation or deployment.

Figure X-11 compares power systems for unmanned outer-planetary missions. At Jupiter, for example, the solar flux is only 4 percent of that occurring at Earth. While use of solar photocells is theoretically possible, it appears that the solar photocell system will be unattractive for this mission. The radioisotope thermoelectric generator would, however, be a logical choice. As the distance from Earth increases, however, the communication bit rate diminishes rapidly. For example, with the 210-foot dish (the largest ground antenna under construction today) and an 8-foot vehicle antenna, a power supply of approximately 500 watts could furnish about 4 bits per second from the orbit of Jupiter. From Neptune, this bit rate would diminish to perhaps 1/2 bit per second. Typical Surveyor pictures of the moon contain about 10^6 bits of information. Thus, if pictures are desired, it is theoretically possible to obtain them, but the continuous times required (days or weeks) do not appear practical. In order for the bit rate to be increased, and hence, for the information to be obtained more quickly, a method for augmenting power at planetary encounter was considered and is shown in figure X-11. The 500-watt radioisotope thermoelectric generator would provide power on the way out when not much power is required; a 10-kilowatt hydrogen-oxygen fuel-cell system is also provided in order to increase the information rate when required, as at planet encounter, for example. This hybrid system is then compared with a 10-kilowatt isotope Brayton system that would have the 10-kilowatt power available over the entire mission. If all the information desired can be returned in a few days or less, a chemical supplement, such as the hydrogen-oxygen fuel cell, to a 500-watt thermoelectric generator would seem an acceptable power system. However, if longer periods are desired, once again, the isotope Brayton appears to be the system of choice.

There is one other mission that has not been considered in this discussion and that is electric propulsion. For the electric propulsion missions of interest, both very high power and very light weight will be required. The chances are good that the advanced reactor system is the only power supply really suitable for electric propulsion. Because of their light weight, if energy storage is not a requirement, photocells have been considered, and it is conceivable that solar cells might be of some interest for electric propulsion.

This concludes the mission survey. Throughout this discussion, it is apparent that the interesting powerplants depend heavily on the mission itself. Energy-storage requirements, the amount of sunlight available, shielding requirements, and the extent to which lunar material can be utilized all have their effect on the attractiveness of these powerplants. The general conclusion that can be drawn from this discussion is that there is clearly a place for both solar and nuclear power systems for the missions discussed here and probably a place also for the advanced systems described in this conference.

TABLE X-1. - SOLAR POWER SYSTEMS

FOR MANNED ORBITING STATION

System	Weight, lb/kW			Total collector area, ft ² /kW
	Day power	Night power	Total	
Conventional photocells and batteries	50	400	450	230
Thin-film photocells and batteries	30 to 70	380 to 420	410 to 490	400 to 600
Brayton cycle	240	60	300	70

TABLE X-2. - NUCLEAR POWER SYSTEMS

FOR MANNED ORBITING STATION

System	Power, kW	Weight, lb/kW			Radiator area, ft ² /kW
		Unshielded	Shield	Total	
Isotope Brayton	10	350	0 to 50	350 to 400	80
SNAP-8	35	350	250 to 550	600 to 900	35
SNAP-8 thermoelectric	20	550	450 to 950	1000 to 1500	100
Advanced reactor	300	30	30 to 70	60 to 100	4

TABLE X-3. - TELEVISION-BROADCAST SATELLITE

IN 24-HOUR ORBIT

(a) Solar power systems

System	Weight, lb/kW			Total collector area, ft ² /kW
	Day power	Night power	Total	
Photocells and batteries	50	140	190	120
Brayton cycle	240	60	300	50

(b) Nuclear power systems

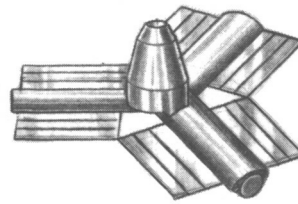
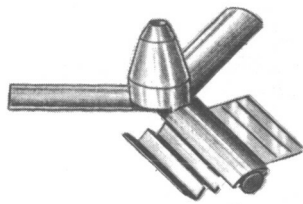
System	Power, kW	Weight, lb/kW			Radiator area, ft ² /kW
		Unshielded	Shield	Total	
Isotope Brayton	10	350	0	350	80
SNAP-8	35	350	50	400	35
Advanced reactor	300	30	5	35	4

**TABLE X-4. - ENERGY STORAGE
FOR SOLAR POWER SYSTEMS
ON MOON**

System	Weight, lb/kW
Batteries	34 000
Fuel cells	1 000
Heat storage (Brayton)	15 000

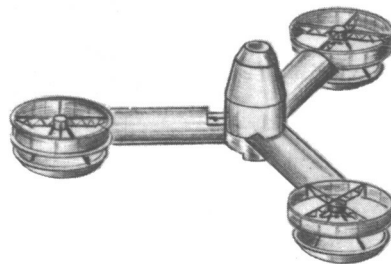
**TABLE X-5. - POWER FOR
MANNED MARS MISSION**

Day power, lb/kW	Planet entry power, lb/kW	Total, lb/kW
Photocells and batteries		
120	70	190
Isotope Brayton		
Unshielded, lb/kW	Shield, lb/kW	Total, lb/kW
350	0 to 150	350 to 500



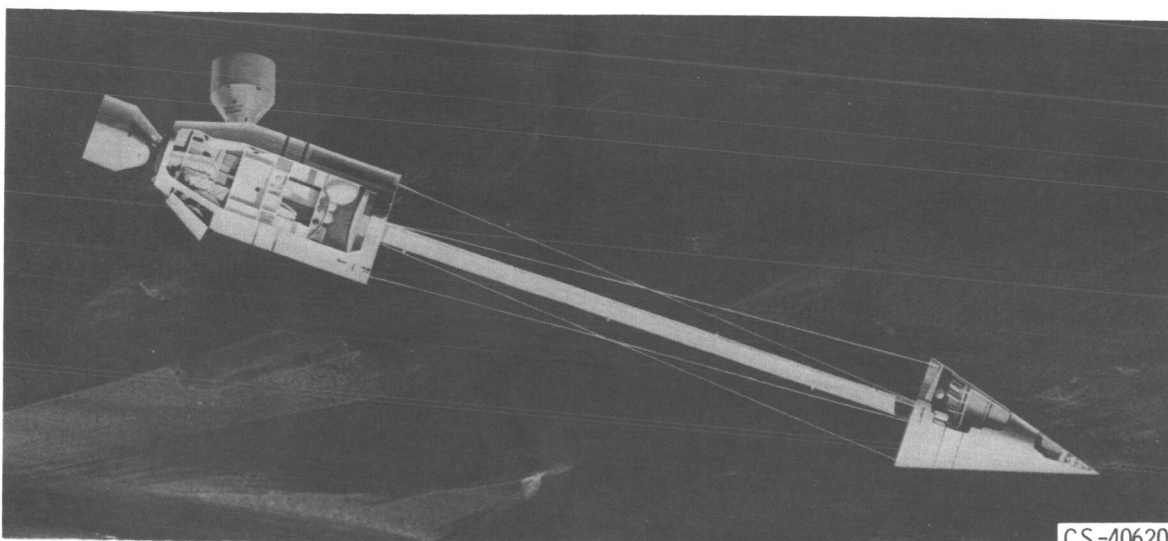
CS-40370

Figure X-1. - 30-Kilowatt conventional photocell system for manned orbiting station.



CS-40372

Figure X-2. - 30-Kilowatt solar Brayton system for manned orbiting station.



CS-40620

Figure X-3. - SNAP-8 power system for manned orbiting station.

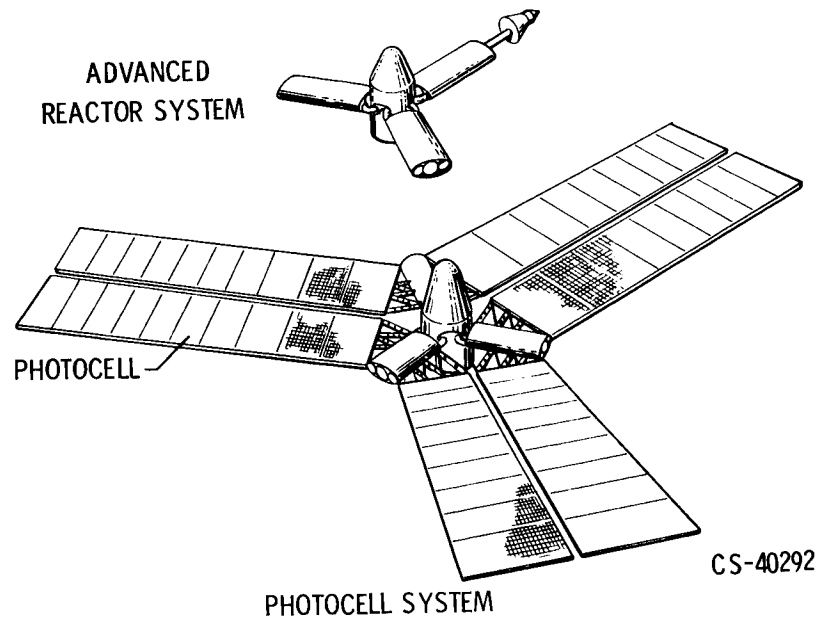


Figure X-4. - 300-Kilowatt power systems for manned orbiting station. Photocell-and-battery system: weight, 138 000 pounds; area 69 000 square feet. Advanced reactor system: weight, 24 000 pounds; area, 1200 square feet.

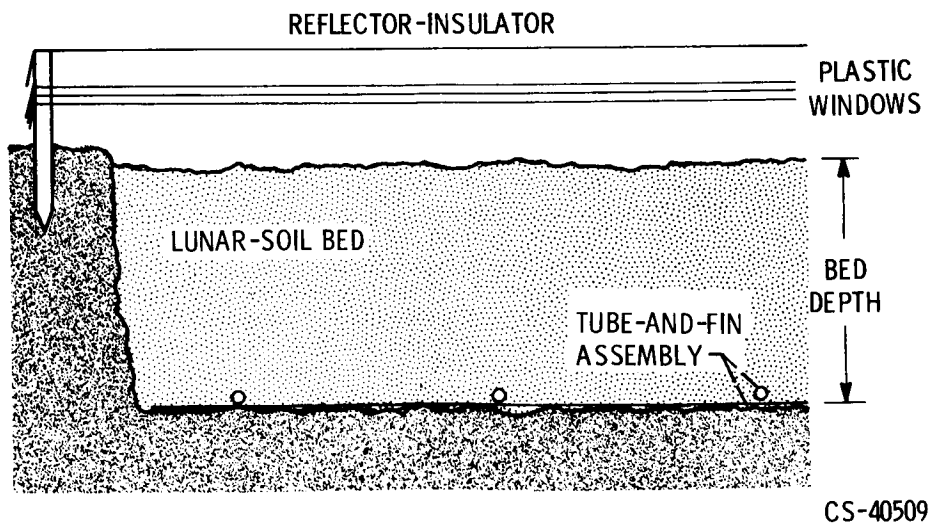


Figure X-5. - Conceptual lunar-soil heat-storage device.

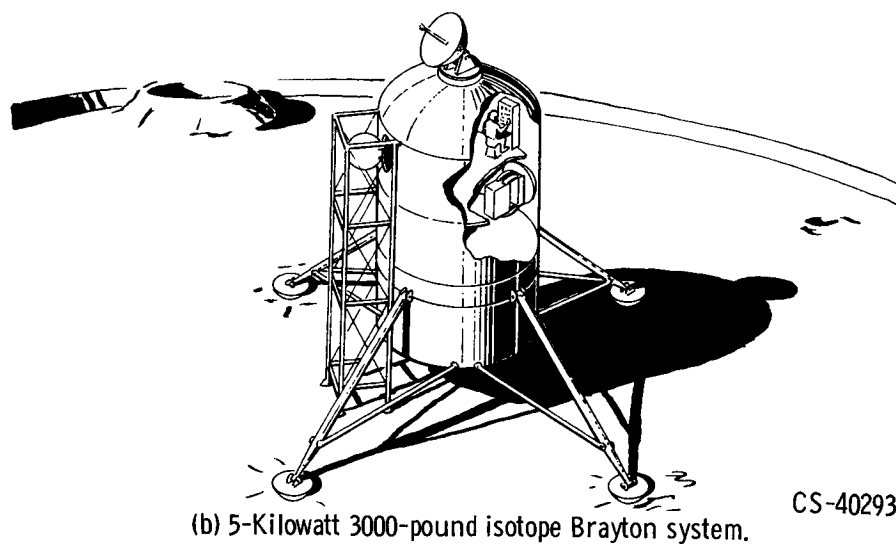
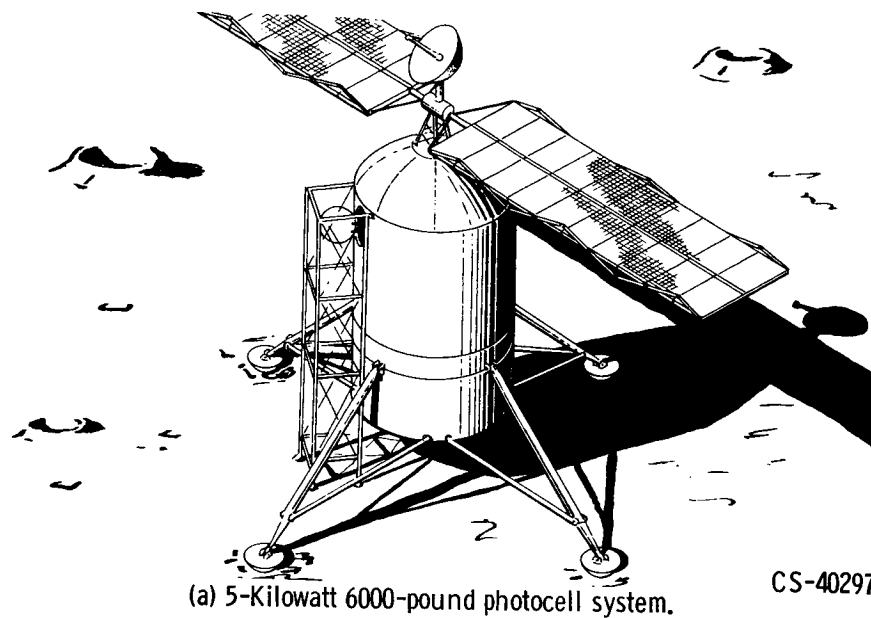


Figure X-6. - Lunar shelter.

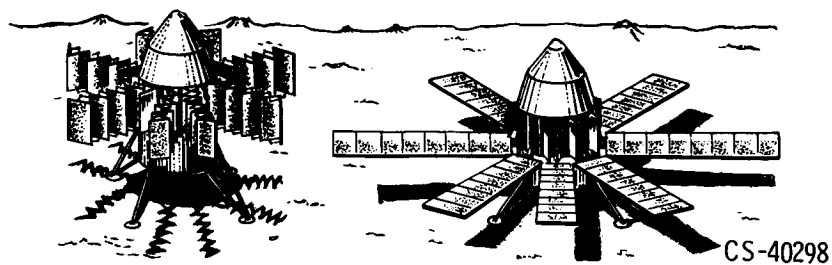
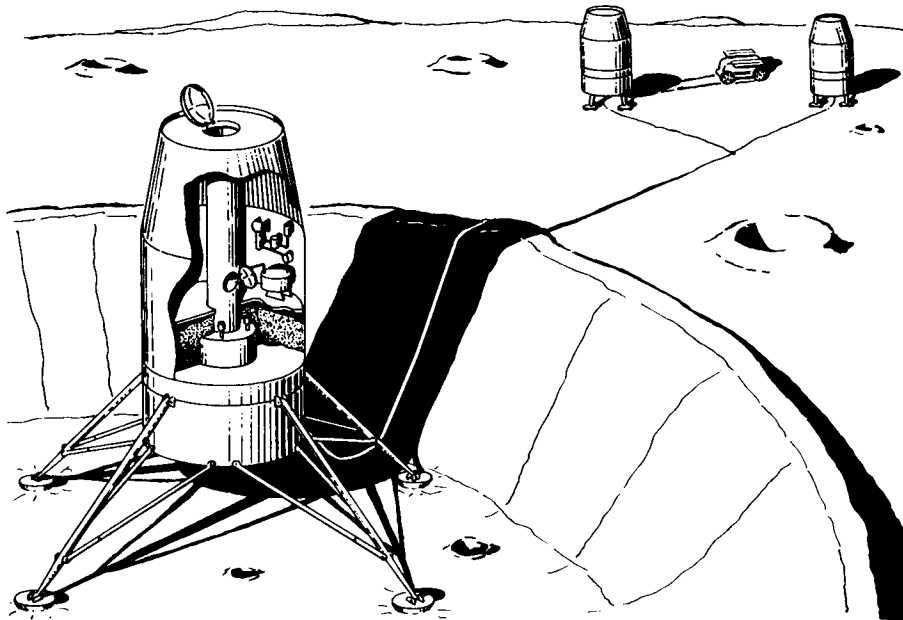
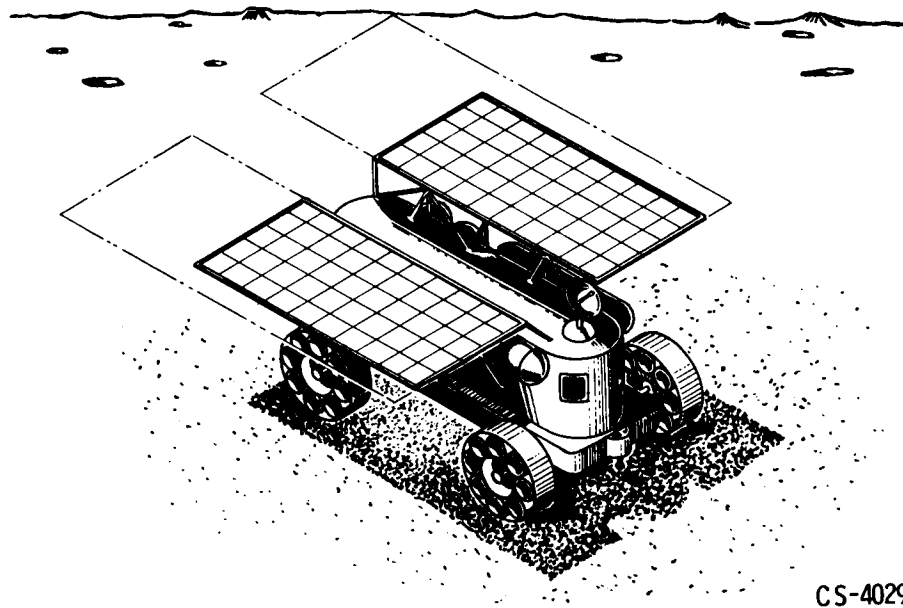


Figure X-7. - Lunar base 20-kilowatt, 26 000 pound photocell - fuel-cell power system.



CS-40536

Figure X-8. - Lunar base 35-kilowatt, 12 000-pound (plus shielding) SNAP-8 power system.



CS-40294

Figure X-9. - Three-man lunar roving vehicle.

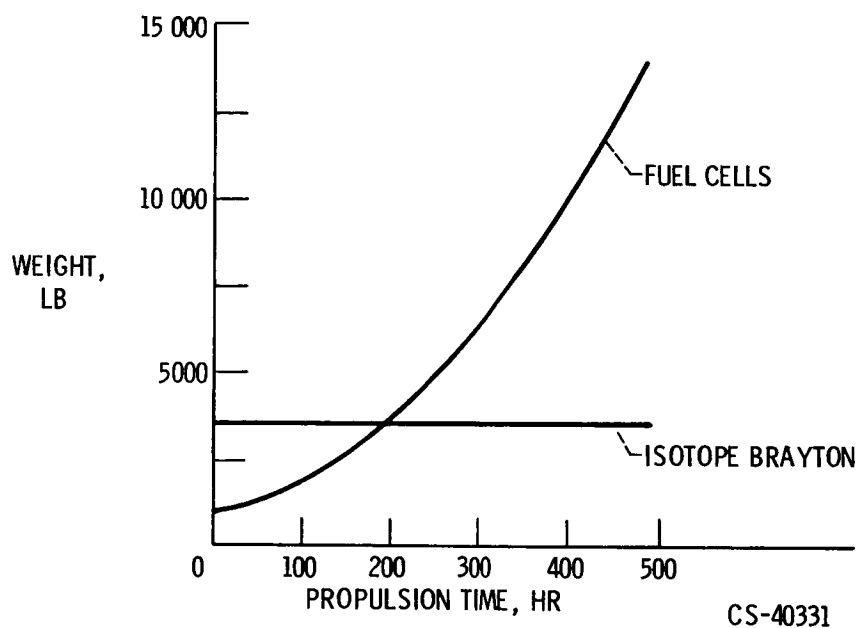


Figure X-10. - Three-man lunar roving vehicle power supply weights. Speed on level terrain, approximately 5 miles per hour.

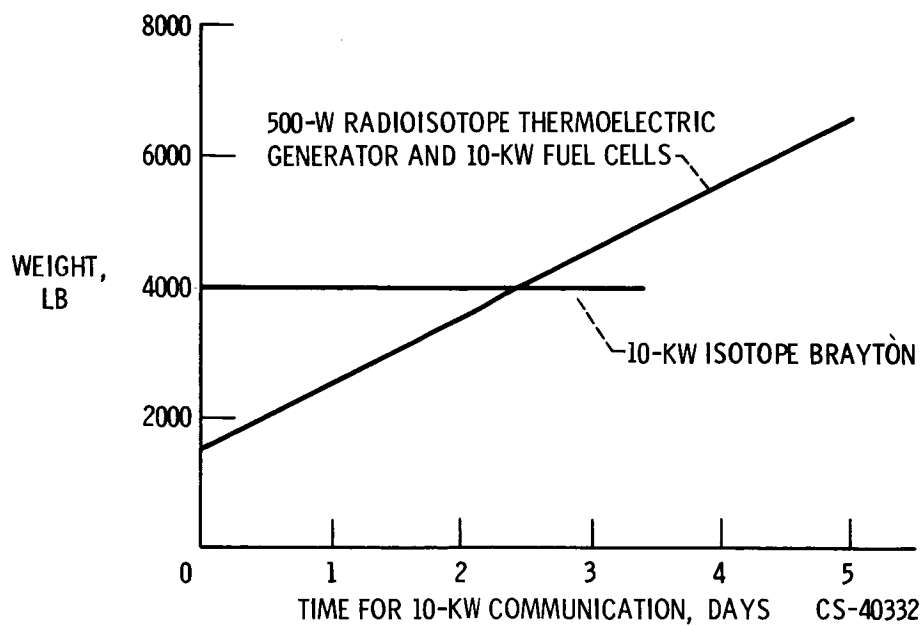


Figure X-11. - Power for unmanned outer-planetary missions.